Dissertation

Zur Erlangung des Grades
eines Doktors der Naturwissenschaften
(Dr. rer. nat.)

vorgelegt von

M.Sc. Katja Kleeberg

Gießen, 2019

Institut für Theoretische Physik
-Fachbereich 07-

Dyson-Schwinger Equations for strongly interacting fermions on the hexagonal graphene lattice

Referent: Prof. Dr. Lorenz von Smekal
Koreferent: Prof. Dr. Christian Fischer

Abstract

The development of two-dimensional materials in order to realize certain valuable electronic properties is a rapidly ongoing process. In this context, Dirac materials which exhibit low-energy Dirac-like excitations are of special interest, with graphene being the most famous representative. In order to understand existing phenomena and to extend application possibilities, new phases are constantly considered, leading to a rather rich phase diagram containing distinct ordered phases of matter. Here the competition between those phases with regard to the most preferred realization becomes important.

In this thesis we address the semimetal-insulator phase transition where the insulating phase can either be realized in terms of an antiferromagnetic phase or a staggered charge density configuration. To this end we establish the Dyson-Schwinger formalism on the hexagonal lattice without the common low-energy approximations, taking the whole band structure of graphene into account. These collective phenomena are then studied under the influence of an extended Hubbard interaction within several truncation schemes. Furthermore, the impact of varying temperature and chemical potential on the phase transition is investigated. Additionally we also address the corresponding critical exponents characterizing the phase transition in terms of specific universality classes.

Zusammenfassung

Die Entwicklung zweidimensionaler Materialien, um bestimmte nützliche elektronische Eigenschaften zu realisieren, ist ein schnell voranschreitender Prozess. In diesem Zusammenhang sind Dirac Materialien, die Dirac-ähnliche Anregungen im Niederenergie-Bereich aufweisen, von besonderem Interesse, mit Graphen als den bekanntesten Vertreter. Um existierende Phänomene zu verstehen und Anwendungsmöglichkeiten zu erweitern, werden stetig neue Phasen in Betracht gezogen, was zu einem eher vielfältigen Phasendiagramm führt, das unterschiedlich geordneten Phasen von Materie beinhaltet. Hier wird der Wettbewerb zwischen diesen Phasen im Hinblick auf eine bevorzugte Realisierung wichtig.

In dieser Arbeit beschäftigen wir uns mit dem Semimetall-Isolator-Übergang, wobei die Isolator-Phase entweder durch eine antiferromagnetische Phase oder eine alternierende Konfiguration der Ladungsdichte realisiert werden kann. Zu diesem Zweck etablieren wir den Dyson-Schwinger Formalismus auf dem hexagonalen Gitter ohne die üblichen Niederenergie Näherungen, wobei die gesamte Bandstruktur von Graphen berücksichtigt wird. Diese kollektiven Phänomene werden dann unter dem Einfluss von erweiterten Hubbard Wechselwirkungen anhand mehrerer Trunkierungen studiert. Außerdem werden die Auswirkung von variierender Temperatur und chemischen Potential auf den Phasenübergang untersucht. Des Weiteren beschäftigen wir uns mit den zugehörigen kritischen Exponenten, die den Phasenübergang bezüglich bestimmter Universalitätsklassen charakterisieren.

Contents

1

Introduction

Before graphene was experimentally synthesized for the first time in 2004 [1], it was theoretically [2,3] as well as experimentally [4] argued that two-dimensional crystals might be thermodynamically unstable [2,3] and a magnetic long-range order in two dimensions was even excluded [5,6]. This discovery of graphene, which gave rise to the nobel prize in 2010 awarded to Novoselov and Geim [1], was the starting point of a rapidly proceeding development and investigation of technologically promising two-dimensional materials. Graphene, consisting of an one atom thick layer of carbon atoms arranged in a hexagonal lattice, turned out to be a surprisingly strong material of high cristal quality [7] and with unique electronic and mechanical properties [8–10].

Even before the experimental realization of monolayer graphene, it was theoretically introduced as a semimetal with an extraordinary band structure [11] and density of states [12]. Suspended graphene was found to exhibit a Fermi surface consisting of two independent points (K^+ and K^-) of the Brioullin zone (BZ) where the conically merging valence and conduction bands touch each other. This enables the theoretical description of quasi-particles of the hexagonal lattice within a relativistic theory of Dirac fermions [13] in the low-energy regime. These quasi-relativistic particles, which were validated experimentally [14], move with an adapted Fermi velocity v_f instead of the speed of light. On this basis, graphene can be mapped into quantum electrodynamics in two spatial dimensions and one time dimension, QED_{2+1} [8,13,15]. Therefore graphene serves as a real probe of QED_{2+1} for example concerning the investigation of the QED analogy to an axial anomaly [13] or effects like the Klein paradox [8, 9, 16, 17].

The introduction of several symmetries on the hexagonal lattice in its continuum description also provides the analogy to phenomena like spontaneous symmetry breaking in QED. Here the sublattice-valley symmetry between the two independent

Dirac points K^+ and K^- represents an analogy of chiral symmetry in QED that can be explicitly or spontaneously broken in relation to the generation of a mass gap, pushing graphene into an insulating phase.

Due to the small Fermi-velocity, $v_f/c \sim 1/300$, suspended graphene exhibits a large effective fine structure constant,

$$\alpha_g = \frac{e^2}{4\pi\epsilon\hbar c} \cdot \frac{c}{v_f} \approx \frac{300}{137} \approx 2.2\,, \tag{1.1}$$

expressing the ratio between Coulomb interaction and kinetic energy. Experimentally, graphene was found to be a good conductor [18, 19] which first was in contradiction to theoretical findings predicting critical couplings for an antiferromagnetic Mott insulator below α_g. This puzzle could be resolved by the introduction of screening effects [20–25] but the critical coupling still seems to be in the vicinity of α_g which gives reason to the assumption that graphene could undergo a phase transition into an insulating phase by a small increase of the electronic interaction.

Based on the analogy to QED_{2+1}, various kinds of insulating phases like the quantum spin or anomalous Hall insulator [26–28], a charge density wave (CDW) or spin density wave (SDW) insulating phase [27, 29–31], or even a quantum spin liquid phase [23, 32, 33] have been suggested. Also magnetic instabilities and superconducting phases are investigated theoretically as well as experimentally [34–36] and indeed, a superconducting phase has recently been found in twisted bilayer graphene [37].

For instance, graphene can be produced by vapour deposition, micromechanical cleavage or exfoliation [16] and provides the basis of bilayer graphene as well as of all carbon like allotropes like buckyballs, nanotubes and of course graphite as the probably most prominent example (see Fig. 1.1) [11, 38]. Graphene is a promising candidate for various technological applications and can be easily modified chemically as well as mechanically [39]. These modifications could solve the lack of a band gap and give rise to the application of graphene in the field of transistor physics or e.g. as replacement for silicon in semiconductor based devices [40].

Another upcoming idea is the realization of composed two-dimensional layers in order to modify optical as well as electronic properties within a kind of construction kit [41, 42]. Beside graphene, also other adequate two-dimensional components can be gained from three-dimensional materials with weak van der Waals forces between the single layers. Here a plenty amount of two-dimensional materials is available [43, 44]. These materials are of high industrial interest regarding the field of optoelectronics or spintronics with a wide range of application possibilities such as new kinds of light sources, displays or foldable touchscreens [42].

In the following, we stick to the investigation of graphene as important basic material. The large coupling constant of suspended graphene as given in Eq. (1.1) requires a non-perturbative treatment of the theory. Therefore functional methods like the functional renormalization group [45–48] or the formalism of Dyson-Schwinger Equations (DSE's) [49–53] can be utilized in order to describe non-perturbative phenomena. Also models on the basis of Monte Carlo simulations provide an appropriate approach [24, 25, 31, 40, 54]. In this work the Dyson-Schwinger equations are chosen to study an emerging Mott insulating phase in regard to a possible CDW or SDW realization [27, 29–31]. The Dyson-Schwinger formalism on the hexagonal

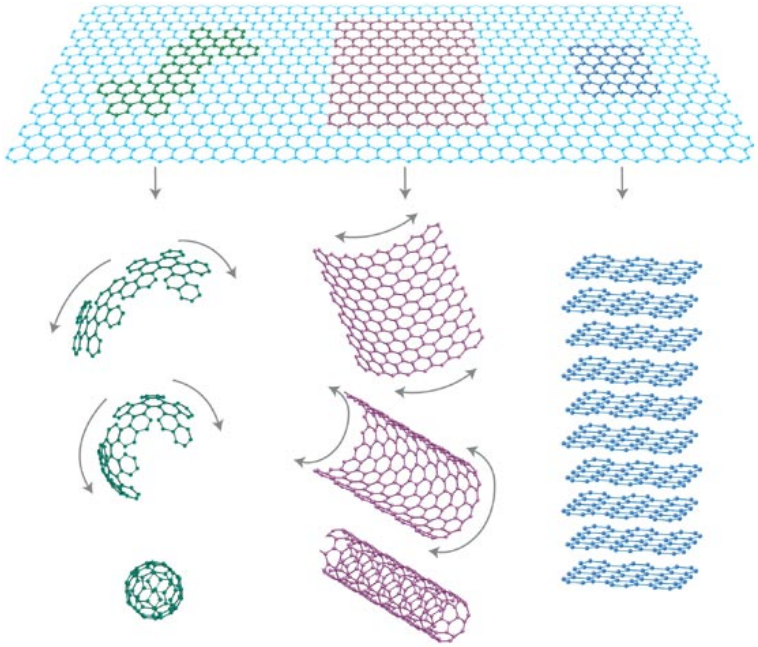

Figure 1.1: Shown is graphene as basis of carbon allotropes like fullerenes (0d), nanotubes (1d) or graphite (3d). Taken from Ref. [7].

lattice is applied without low-energy approximation taking the whole band structure of graphene into account.

This thesis is organized as follows. In Chap. 2 the lattice representation of graphene in position space as well as the corresponding Brioullin zone (BZ) in momentum space will be introduced. On this basis, the formalism of second quantization is introduced and the free Hamiltonian within a tight-binding approach will be constructed. In Sec. 2.3 the sublattice-valley symmetry of the hexagonal lattice is established in analogy to chiral symmetry in continuous QED_{2+1}. The mechanism of chiral symmetry breaking also provides the principle of a spontaneous gap generation turning graphene into an insulating phase.

In Chap. 3 we start with the introduction of the free fermion propagator and formulate an instantaneous interaction matrix in sublattice space. In App. C we will derive the associated Dyson-Schwinger equations in order to describe the effects of the interaction on graphenes band structure non-perturbatively. Subsequently, different possibilities concerning a Mott insulating phase, namely the charge density wave (CDW) and the spin-density wave (SDW) configuration, will be discussed. The extended Hubbard model will be introduced in Sec. 3.4 as an appropriate framework to especially study the competition between the realization of an SDW or CDW state, respectively. At the end of this chapter we will focus on the numerical setup, which enables us to effectively solve the obtained Dyson-Schwinger equations within the Hubbard model for huge lattice sizes.

In Chap. 4 we concentrate on the solution of the Dyson-Schwinger equations within different mean field approaches. In particular, the resulting order parameter identifying the band gap between the valence and conductor band of graphene, is studied for various interaction strengths of the Hubbard model (U and V) serving as

control parameter of the phase transition. In this context the corresponding critical exponents and the influence of finite lattices regarding this phase transition will be discussed. Then the mean field theory is extended by the renormalization effects on the band structure within a so-called Hartree-Fock approximation. At the end of this chapter we will apply the formalism of 2PI effective action to the considered theory in order to determine the transition line between the CDW state and the SDW phase in the U-V coupling plane.

Chap. 5 is based on the derivation of Dyson-Schwinger equations from App. E including a dressed photon propagator that takes mutual screening effects of the π band electrons into account. The vacuum polarization is initially assumed to be static by means of a static Lindhard approximation and the corresponding phase transition is investigated, still for zero temperature and zero chemical potential.

Since the static approximation does not provide reasonable results, the assumption of a frequency independent interaction is rejected in Chap. 6 where the full frequency dependence of the photon and fermion propagator as well as a non-trivial vertex function will be taken into account. The vertex dressing is modeled in terms of a Ball Chiu ansatz including non-trivial wavefunction renormalizations. As we will see, these corrections to the wavefunction renormalization are only marginally relevant concerning the location of the considered semimetal insulator transition. The wavefunction renormalization is thus again fixed to its trivial value. Afterwards we will show results for the semimetal insulator transition including the SDW and the CDW state. Moreover, a finite-size scaling method will be applied in order to extract the critical exponents. Finally the temperature dependence as well as the behavior for varying chemical potential μ is discussed for the SDW phase.

2

Structure and Properties of Graphene

Graphene is a monolayer of carbon atoms arranged in a hexagonal lattice with an interatomic distance of $a \simeq 1.42\,\text{Å}$. Every carbon atom counts four valence electrons, three of them form covalent σ-bonds in terms of an sp^2-hybridization of the atomic orbitals $(2s, 2p_x, 2p_y)$ [8]. These are flexible bonds between the carbon atoms forming the hexagonal lattice. The remaining p_z-electrons are forming two additional π-bands, π and π^*, and are assumed to be primarily responsible for the electronic properties of graphene. These electrons are in rather good approximation assumed to be strongly bound to their atomic kernel [8, 9, 58] which motivates the treatment within a tight-binding model being the basis of all considerations within this work.

2.1 Lattice Representation of Graphene

The honeycomb lattice of graphene can be described by a two-component unit cell with the corresponding basis vectors

$$\boldsymbol{a}_1' = \frac{a}{2}\begin{pmatrix}\sqrt{3}\\ 3\end{pmatrix}, \qquad \text{and} \qquad \boldsymbol{a}_2' = \frac{a}{2}\begin{pmatrix}\sqrt{3}\\ -3\end{pmatrix}, \tag{2.1}$$

as depicted in Fig. 2.1. This certainly represents the standard choice of basis vectors. However, in order to resolve the interatomic distance a between two carbon atoms a smaller unit cell has to be introduced. For that reason, essentially the following basis vectors were used within this work

$$\boldsymbol{a}_1 = a\begin{pmatrix}0\\ 1\end{pmatrix}, \qquad \boldsymbol{a}_2 = \frac{a}{2}\begin{pmatrix}\sqrt{3}\\ -1\end{pmatrix}. \tag{2.2}$$

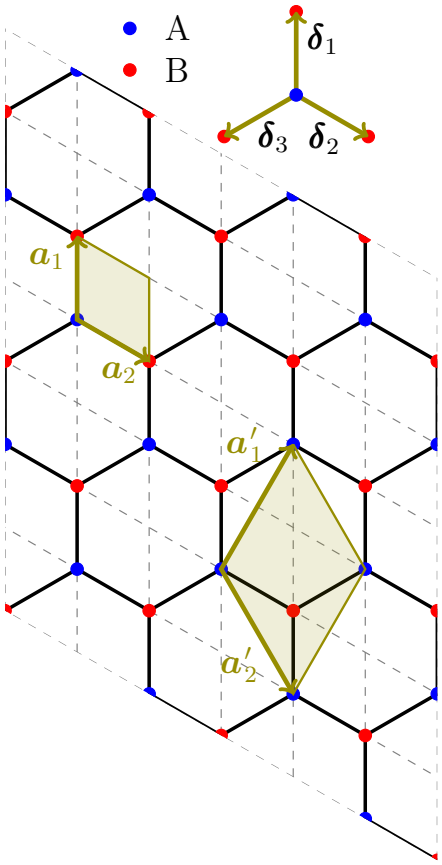

Figure 2.1: The nearest-neighbor vectors $\boldsymbol{\delta}$ and two different choices of basis vectors for the representation of the honeycomb lattice are shown [59].

The nearest-neighbor vectors, each linking to an adjacent carbon atom, are accordingly given by

$$\boldsymbol{\delta}_1 = \boldsymbol{a}_1\,, \qquad \boldsymbol{\delta}_2 = \boldsymbol{a}_2\,, \qquad \boldsymbol{\delta}_3 = -(\boldsymbol{a}_1 + \boldsymbol{a}_2)\,, \tag{2.3}$$

as represented in Fig. 2.1. For clarity, the characteristic quantities for both basis representations are summarized in App. A.1.

Consequently, an arbitrary discrete vector in position space on this finer triangular lattice can be expressed as

$$\boldsymbol{r} = i\,\boldsymbol{a}_1 + j\,\boldsymbol{a}_2\,. \tag{2.4}$$

A distinct disadvantage in comparison to the description in terms of a composition of two independent sublattices and the basis vectors from Eq. (2.1), is the necessity to distinguish between three types of lattice points included by a lattice discretization specified by the basis vectors from Eq. (2.2). The discrete lattice vector of Eq. (2.4) includes sites from sublattice A (blue sites), sites from sublattice B (red sites) as well as empty sites (referred to as sublattice C in the following). Since all carbon core atoms are assumed to be fixed within the framework, C sites are never occupied by a carbon atom. Mathematically this can be expressed in terms of the corresponding

combinations of coefficients i and j as follows,

$$i+j \mod 3 = 0: \quad \text{sublattice } A\,, \tag{2.5}$$

$$i+j \mod 3 = 1: \quad \text{sublattice } B\,, \tag{2.6}$$

$$i+j \mod 3 = 2: \quad \text{unoccupied}\,. \tag{2.7}$$

The associated reciprocal basis vectors are illustrated in Fig. 2.2.

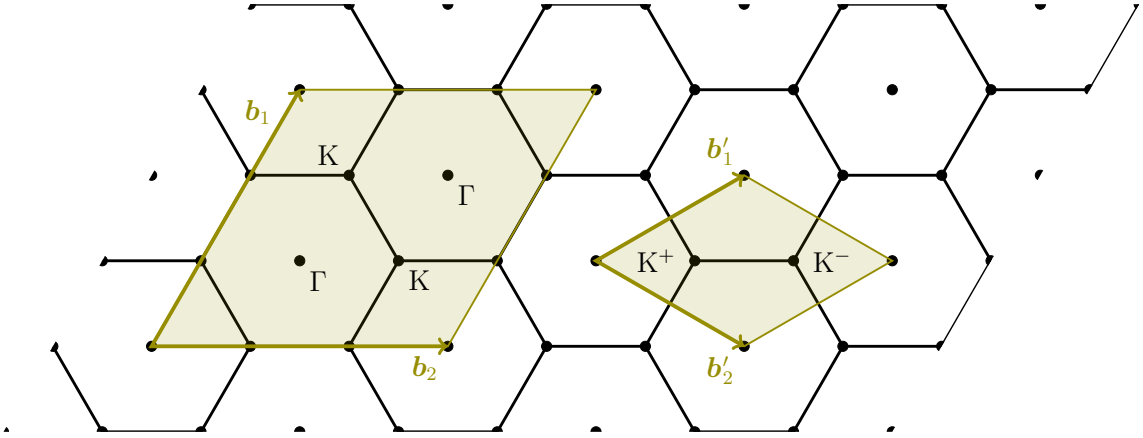

Figure 2.2: The corresponding reciprocal bases for the lattice representations from Fig. 2.1 are represented [59]. In this work mainly the momentum space vectors $\boldsymbol{b}_1$ and $\boldsymbol{b}_2$ are used in order to resolve nearest-neighbor distances while maintaining the periodicity of all correlation functions in momentum space. The BZ spanned by $\boldsymbol{b}'_1$ and $\boldsymbol{b}'_2$ belongs to the commonly used two-component unit cell description.

Due to the finer triangular lattice in position space one has to deal with a three times larger Brillouin zone (BZ) spanned by

$$\boldsymbol{b}_1 = \frac{2\pi}{3a}\begin{pmatrix}\sqrt{3}\\ 3\end{pmatrix}\,, \qquad \boldsymbol{b}_2 = \frac{4\pi}{3a}\begin{pmatrix}\sqrt{3}\\ 0\end{pmatrix}\,. \tag{2.8}$$

In Fig. 2.2, additionally the high symmetry points K and Γ of the honeycomb lattice were sketched. The so-called Dirac points denoted by K, or by K^+ and K^- respectively within the two-component lattice representation, are of special interest regarding the investigation of the electronic properties as elaborated in the next chapter. In the three times larger Brioullin zone one principally counts six K points, two for each sublattice (A, B, C) similar to the representation within the smaller BZ. For convenience all Dirac points are denoted by K.

In order to define momentum modes on sublattices A and B we therefore use Fourier transforms on the fine triangular lattice with constraints

$$\frac{1}{3}\sum_{l=0}^{2} e^{-\frac{2\pi \mathrm{i}}{3}(i+j-s)l} = \begin{cases} 1\,, & i+j \mod 3 = s\,,\\ 0\,, & \text{otherwise}\,. \end{cases} \tag{2.9}$$

Moreover we apply Born-von Karman boundary conditions on the fine lattice (see e.g. Ref. [60]) for a properly defined discrete Fourier transform on likewise discrete momentum vectors

$$\boldsymbol{k} = \frac{m}{N}\,\boldsymbol{b}_1 + \frac{n}{N}\,\boldsymbol{b}_2\,, \tag{2.10}$$

where the considered graphene sheet consists of $N \times N$ unit cells in real space. As already assumed, the number of lattice points in both momentum directions are chosen to be equal throughout the whole work. Furthermore, N is always taken to be even and a multiple of 3 in order to precisely match the high-symmetry points (denoted by K and Γ in Fig. 2.2) within the presented lattice discretization.

The Born-von Karman type of boundary conditions require the relevant functions (denoted by ψ) to be invariant under a shift of N times the basis vectors,

$$\psi(\boldsymbol{r}) = \psi(\boldsymbol{r} + n_1\,N\boldsymbol{a}_1 + n_2\,N\boldsymbol{a}_2) \qquad n_1, n_1 \in \mathbb{Z}\,, \tag{2.11}$$

in momentum space one therefore finds

$$\psi(\boldsymbol{k}) = \psi(\boldsymbol{k} + n_1\,\boldsymbol{b}_1 + n_2\,\boldsymbol{b}_2) \qquad n_1, n_1 \in \mathbb{Z}\,. \tag{2.12}$$

This corresponds to a spatial deformation of the rhombic BZ into a twisted torus by closing opposite edges in agreement with Eq. (2.12).

In order to apply the formalism of second quantization, arguably providing the most intuitive access to solid state problems, we define creation and annihilation operators for electrons on both sublattices A and B of the fine triangular lattice as follows,

$$a_{\boldsymbol{r}} = \frac{1}{N^2}\sum_{\boldsymbol{k}} e^{\mathrm{i}\,\boldsymbol{k}\cdot\boldsymbol{r}}\,a_{\boldsymbol{k}} = \begin{cases} c_{\boldsymbol{r}}\,, & \boldsymbol{r} \text{ on sublattice } A\,, \\ 0\,, & \text{otherwise}\,, \end{cases} \tag{2.13}$$

$$b_{\boldsymbol{r}} = \frac{1}{N^2}\sum_{\boldsymbol{k}} e^{\mathrm{i}\,\boldsymbol{k}\cdot\boldsymbol{r}}\,b_{\boldsymbol{k}} = \begin{cases} c_{\boldsymbol{r}}\,, & \boldsymbol{r} \text{ on sublattice } B\,, \\ 0\,, & \text{otherwise}\,, \end{cases} \tag{2.14}$$

with the creation operators being the hermitian conjugated. For now the spin index σ is suppressed and will be introduced later as a trivial extension of the index space. Sometimes also the shorthand notation

$$c_{\boldsymbol{r}} = \begin{cases} a_{\boldsymbol{r}}\,, & \boldsymbol{r} \text{ on sublattice } A\,, \\ b_{\boldsymbol{r}}\,, & \boldsymbol{r} \text{ on sublattice } B\,, \\ 0\,, & \text{otherwise}\,. \end{cases} \tag{2.15}$$

is used, which can be neatly defined by multiplication of the appropriate constraint from Eq. (2.9). A summary of the conventions regarding the Fourier transform can be found in App. B, note that all annihilation and creation operators of course are time-dependent operators due to the Heisenberg picture [61].

Momentum modes on sublattices A and B are then created and annihilated by applying $a^\dagger_{\boldsymbol{k}}$, $a_{\boldsymbol{k}}$ and $b^\dagger_{\boldsymbol{k}}$, $b_{\boldsymbol{k}}$ with

$$a_{\boldsymbol{k}} = \frac{1}{3}\sum_{\boldsymbol{r}}\sum_{l=0}^{2} e^{-\frac{2\pi\mathrm{i}}{N}\left((m+\frac{Nl}{3})i+(n+\frac{Nl}{3})j\right)}\,c_{\boldsymbol{r}}\,, \tag{2.16}$$

$$b_{\boldsymbol{k}} = \frac{1}{3}\sum_{\boldsymbol{r}}\sum_{l=0}^{2} e^{\frac{2\pi\mathrm{i}}{3}l}\,e^{-\frac{2\pi\mathrm{i}}{N}\left((m+\frac{Nl}{3})i+(n+\frac{Nl}{3})j\right)}\,c_{\boldsymbol{r}}\,,$$

respectively. The nature of a function to exist either on sublattice A or B itself provides a shift symmetry in momentum-space. In general one finds the relation

$$f_s(\boldsymbol{k} + n \cdot \boldsymbol{\Delta}) = e^{-\frac{2\pi \mathrm{i}}{3} n \cdot s} \, f_s(\boldsymbol{k}) \qquad\qquad n \in \mathbb{Z}\,, \tag{2.17}$$

with $\boldsymbol{\Delta} = (\boldsymbol{b}_1 + \boldsymbol{b}_2)/3$ and s defining the sublattice via $i + j \mod 3 = s$. This symmetry is illustrated in Fig. 2.3 where the red-, blue- and green-colored areas are completely independent from each other but all parts with the same color are related to each other by Eq. (2.17).

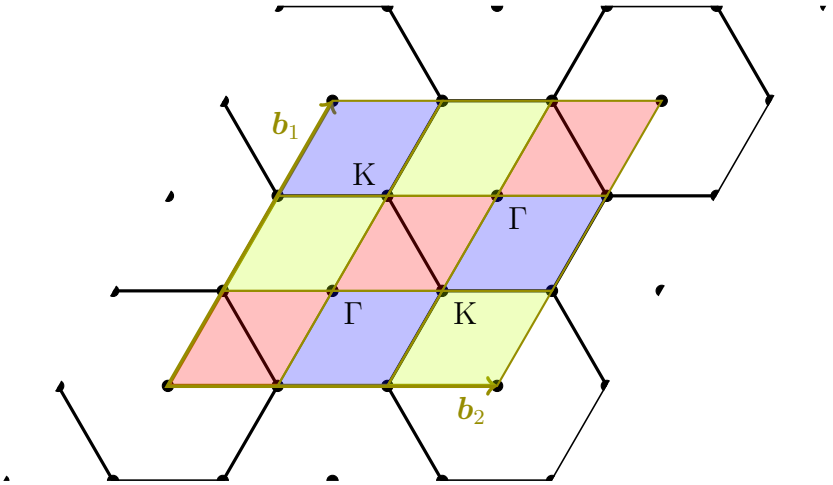

Figure 2.3: Shown is the decomposition of the Brioullin zone into several symmetry contributions. The different colored areas are independent from each other but the same-colored parts can be converted into each other by certain symmetry transformations (see Eq. (2.17)) if the function only exist on one lattice type in position space.

For instance, assuming N to be a multiple of three, the creation operators $\boldsymbol{a}_k$ and $\boldsymbol{b}_k$, are periodic under shifts along the diagonal in momentum space by $\boldsymbol{\Delta}$,

$$a_{\boldsymbol{k}} = a_{\boldsymbol{k}+\boldsymbol{\Delta}} = a_{\boldsymbol{k}+2\boldsymbol{\Delta}}\,, \tag{2.18}$$

and periodic up to a third root of unity,

$$b_{\boldsymbol{k}} = e^{\frac{2\pi \mathrm{i}}{3}} \, b_{\boldsymbol{k}+\boldsymbol{\Delta}} = e^{\frac{4\pi \mathrm{i}}{3}} \, b_{\boldsymbol{k}+2\boldsymbol{\Delta}}\,. \tag{2.19}$$

They are related to the Fourier modes on the fine lattice by

$$a_{\boldsymbol{k}} = \frac{1}{3} \sum_{l=0}^{2} c_{\boldsymbol{k}+l\boldsymbol{\Delta}}\,, \qquad \text{and} \qquad b_{\boldsymbol{k}} = \frac{1}{3} \sum_{l=0}^{2} e^{\frac{2\pi \mathrm{i}}{3} l} \, c_{\boldsymbol{k}+l\boldsymbol{\Delta}}\,, \tag{2.20}$$

which can be obtained by the more general relation

$$\sum_{(i+j) \bmod 3 = s} e^{-\mathrm{i}\,\boldsymbol{k}\cdot\boldsymbol{r}} = \frac{1}{3} \sum_{l=0}^{2} e^{\frac{2\pi \mathrm{i}}{3} s \cdot l} \, \delta(\boldsymbol{k} - l\,\boldsymbol{\Delta}) \tag{2.21}$$

for the Fourier transform on a single sublattice. The equal-time canonical anti-commutator relations then become

$$
\begin{aligned}
[a_{\boldsymbol{k},\sigma}, a^\dagger_{\boldsymbol{k}',\sigma'}]_+ &= \delta_{\sigma,\sigma'} \frac{N^2}{3} \sum_{l=0}^{2} \delta_{\boldsymbol{k}+l\boldsymbol{\Delta},\boldsymbol{k}'} \,, \qquad (2.22)\\
[b_{\boldsymbol{k},\sigma}, b^\dagger_{\boldsymbol{k}',\sigma'}]_+ &= \delta_{\sigma,\sigma'} \frac{N^2}{3} \sum_{l=0}^{2} e^{\frac{2\pi \mathrm{i}}{3} l} \, \delta_{\boldsymbol{k}+l\boldsymbol{\Delta},\boldsymbol{k}'} \,,\\
[a_{\boldsymbol{k},\sigma}, b^\dagger_{\boldsymbol{k}',\sigma'}]_+ &= [b_{\boldsymbol{k},\sigma}, a^\dagger_{\boldsymbol{k}',\sigma'}]_+ = [a_{\boldsymbol{k},\sigma}, b_{\boldsymbol{k}',\sigma'}]_+ = [a^\dagger_{\boldsymbol{k},\sigma}, b^\dagger_{\boldsymbol{k}',\sigma'}]_+ = 0 \,,\\
[a_{\boldsymbol{k},\sigma}, a_{\boldsymbol{k}',\sigma'}]_+ &= [b_{\boldsymbol{k},\sigma}, b_{\boldsymbol{k}',\sigma'}]_+ = [a^\dagger_{\boldsymbol{k},\sigma}, a^\dagger_{\boldsymbol{k}',\sigma'}]_+ = [b^\dagger_{\boldsymbol{k},\sigma}, b^\dagger_{\boldsymbol{k}',\sigma'}]_+ = 0 \,.
\end{aligned}
$$

2.2 The Hamiltonian Formulation

2.2.1 Tight-Binding Model

As mentioned above, graphene is a two-dimensional layer of carbon atoms arranged on a honeycomb lattice and is firmly bound to one and another by strong covalent σ-bonds in terms of an sp^2-hybridization of the atomic orbitals. The remaining valence electrons of the p_z-orbitals are predominantly responsible for the electronic properties of graphene since they are not involved in the structural composition of the honeycomb lattice and are therefore available for the electronic transport [8]. These p_z-orbitals are arranged perpendicularly to the graphene plane forming a π-orbital with weak overlap and could therefore be treated in a tight-binding approach (see Ref. [58]). In the simplest form with only nearest-neighbor hopping, the kinetic part of the Hamiltonian is given by

$$
\mathcal{H}_{tb} = -\kappa \sum_{\langle \boldsymbol{i},\boldsymbol{j}\rangle,\sigma} (c^\dagger_{\boldsymbol{i},\sigma} c_{\boldsymbol{j},\sigma} + c^\dagger_{\boldsymbol{j},\sigma} c_{\boldsymbol{i},\sigma}) \,, \qquad (2.23)
$$

where κ is referred to as the hopping parameter which is given by the orbital overlap of two adjacent wavefunctions under the influence of interaction [11,16,58]. In other words, the hopping parameter determines the probability for an electron to hop from one carbon atom to an adjacent one. It is experimentally fixed to approximately $\kappa \simeq 2.8$ eV [9] and provides a natural unit of energy here. Strictly speaking, the annihilation and creation operators from Eq. (2.13) and Eq. (2.14) exactly describe excitations of these p_z-electrons forming the π-electron systems.

The angle brackets denote the nearest-neighbor sum $\langle i,j\rangle$ and an additional index σ has been introduced to take account for a spin index which plays the role of a flavor number. Generally σ runs from 0 to $N_f - 1$, but N_f is fixed to $N_f = 2$ throughout this work due to the two electronic spin states $\sigma = \uparrow, \downarrow$. Dividing the sum over the sites $\boldsymbol{i}$ of the bipartite honeycomb lattice into two triangular sublattices $\boldsymbol{i}_s$ with $s = 0, 1$ for sublattice A and B explicitly, we can write the symmetry breaking staggered on-site potential as a mass term as follows

$$
\mathcal{H}_m = \sum_{\boldsymbol{i}_s,s,\sigma} (-1)^s m_\sigma \; c^\dagger_{\boldsymbol{i}_s,\sigma} c_{\boldsymbol{i}_s,\sigma} \,. \qquad (2.24)
$$

We additionally introduce a chemical potential μ'_σ for all flavors to assure a finite-charge carrier density. Accordingly, the free Hamiltonian can be written as

$$\mathcal{H}_0 = -\kappa \sum_{\langle \boldsymbol{i},\boldsymbol{j}\rangle,\sigma} (c^\dagger_{\boldsymbol{i},\sigma} c_{\boldsymbol{j},\sigma} + c^\dagger_{\boldsymbol{j},\sigma} c_{\boldsymbol{i},\sigma}) + \sum_{\boldsymbol{i}_s,s,\sigma} (-1)^s m_\sigma \, c^\dagger_{\boldsymbol{i}_s,\sigma} c_{\boldsymbol{i}_s,\sigma} - \sum_{\boldsymbol{i},\sigma} \mu'_\sigma \, c^\dagger_{\boldsymbol{i},\sigma} c_{\boldsymbol{i},\sigma} \,. \quad (2.25)$$

Next we define two-component fermion fields for properly normalized momentum states on the two sublattices,

$$\psi_{\boldsymbol{k},\sigma} = \frac{\sqrt{3}}{N} \begin{pmatrix} a_{\boldsymbol{k},\sigma} \\ b_{\boldsymbol{k},\sigma} \end{pmatrix} , \; \bar{\psi}_{\boldsymbol{k},\sigma} = \psi^\dagger_{\boldsymbol{k},\sigma} \gamma^0 = \frac{\sqrt{3}}{N} \Big(a^\dagger_{\boldsymbol{k},\sigma}, -b^\dagger_{\boldsymbol{k},\sigma} \Big) \,, \quad (2.26)$$

where we used $\gamma^0 = \sigma_3$ in the two-dimensional sublattice space (see App. A) so that the staggered on-site potential can be written as a Dirac-mass term (cf. Eq. (2.28) below). Here the explicit factor of $1/3$ takes formally care of the overcounting of modes on the redundant small triangular lattice with nearest-neighbor base. With the already established conventions in momentum space we obtain the free Hamiltonian, accordingly,

$$\begin{aligned} \mathcal{H}_0 =& -\frac{\kappa}{N^2} \sum_{\boldsymbol{k},\sigma} (a^\dagger_{\boldsymbol{k},\sigma} \varphi_{\boldsymbol{k}} \, b_{\boldsymbol{k},\sigma} + b^\dagger_{\boldsymbol{k},\sigma} \varphi^*_{\boldsymbol{k}} \, a_{\boldsymbol{k},\sigma}) + \frac{1}{N^2} \sum_{\boldsymbol{k},\sigma} m_\sigma \, (a^\dagger_{\boldsymbol{k},\sigma} a_{\boldsymbol{k},\sigma} - b^\dagger_{\boldsymbol{k},\sigma} b_{\boldsymbol{k},\sigma}) \\ & - \frac{1}{N^2} \sum_{\boldsymbol{k},\sigma} \mu'_\sigma \, (a^\dagger_{\boldsymbol{k},\sigma} a_{\boldsymbol{k},\sigma} + b^\dagger_{\boldsymbol{k},\sigma} b_{\boldsymbol{k},\sigma}) \quad (2.27) \\ =& \frac{1}{3\,N^2} \sum_{\boldsymbol{k},\sigma} \bar{\psi}_{\boldsymbol{k},\sigma} \, \gamma^0 \, H^0_\sigma(\boldsymbol{k}) \; \psi_{\boldsymbol{k},\sigma} \,, \quad (2.28) \end{aligned}$$

with

$$\varphi_{\boldsymbol{k}} = \sum_{i=1}^{3} e^{\mathrm{i}\,\boldsymbol{k}\cdot\boldsymbol{\delta}_i} = e^{\frac{2\pi \mathrm{i}}{N} m} + e^{\frac{2\pi \mathrm{i}}{N} n} + e^{-\frac{2\pi \mathrm{i}}{N}(m+n)} \,, \quad (2.29)$$

being the structure function of the tight-binding model. Note that the structure function transforms like $\boldsymbol{b}^\dagger$ under shifts of $\boldsymbol{\Delta}$ (see Eq. (2.19)), i.e.,

$$\varphi_{\boldsymbol{k}} = e^{-\frac{2\pi \mathrm{i}}{3}} \varphi_{\boldsymbol{k}+\boldsymbol{\Delta}} = e^{-\frac{4\pi \mathrm{i}}{3}} \varphi_{\boldsymbol{k}+2\boldsymbol{\Delta}} \,, \quad (2.30)$$

so that the tight-binding Hamiltonian is again invariant under such transformations. The associated Hamilton matrix in sublattice space from Eq. (2.28) is given by

$$H^0_\sigma(\boldsymbol{k}) = \begin{pmatrix} m_\sigma - \mu'_\sigma & -\kappa \, \varphi_{\boldsymbol{k}} \\ -\kappa \, \varphi^*_{\boldsymbol{k}} & -m_\sigma - \mu'_\sigma \end{pmatrix} . \quad (2.31)$$

The corresponding Eigenvalues provide the free single-particle energies $E^{(0)}_{\pm,\sigma}(\boldsymbol{k})$ for the π-band excitations with

$$E^{(0)}_{\pm,\sigma}(\boldsymbol{k}) = -\mu'_\sigma \pm \varepsilon_{\boldsymbol{k},\sigma} \qquad \text{and} \qquad \varepsilon_{\boldsymbol{k},\sigma} = \sqrt{m_\sigma^2 + \kappa^2 |\varphi_{\boldsymbol{k}}|^2} \,. \quad (2.32)$$

This dispersion relation for the non-interacting electron system is represented in Fig. 2.4 for vanishing chemical potential ($\mu'_\sigma = 0$), e.g. for graphene at half filling. The energy relation consists of two energy bands, interpreted as electron and hole

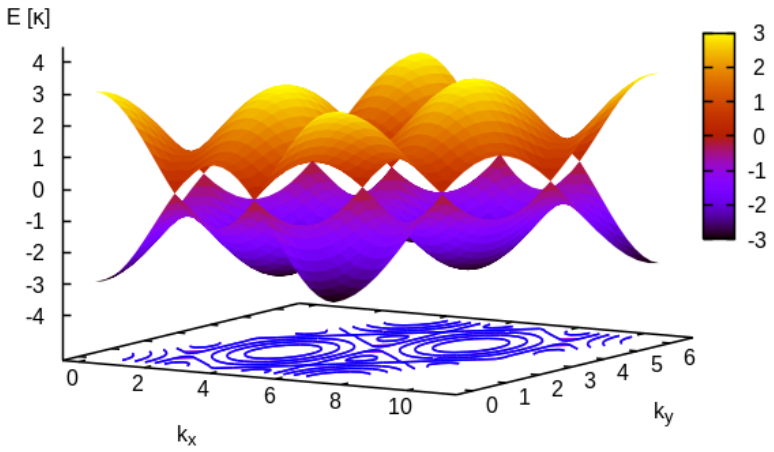

Figure 2.4: The single-particle energies of the non-interacting tightly bound electron system is plotted over the entire Brioullin zone (see Fig. 2.3). Represented are both bands π and π^* related to the electron and hole states of the hexagonal graphene lattice at half filling. Both π-bands touch each other at the Dirac points K indicating a semimetal with zero activation energy.

states. The upper and lower band touch each other in six points at the Fermi level, separating the valence (π) from the conduction band (π^*). These points are the Dirac points K (see also Fig. 2.3) which are crucial for the definition of the order parameter in the next chapter. As indicated in Eq. (2.32), the band gap for now is exactly given m_σ, e.g. the explicitly symmetry breaking mass term.

As it is clear from the energy relation depicted in Fig. 2.4, graphene is a semimetal with zero activation energy, which has already been investigated in 1947 by P. R. Wallace [11] and indeed, experimentally it was found that graphene is a conductor with unique properties.

In Fig. 2.5 (right) the energy-momentum relation from Fig. 2.4 is shown along the high symmetry points of the BZ which are marked in Fig. 2.5 (left). One common approach to handle complicated many-particle interactions on the honeycomb lattice is to expand the structure function near the Dirac points as follows,

$$\kappa\,|\varphi_q| \approx v_f\,q + \mathcal{O}[(q/K)^2], \tag{2.33}$$

with the Fermi velocity $v_f = 3\kappa a/2$ and q being the absolute value of the momentum vector relatively to the Dirac point [8]. This ansatz provides the basis for the so-called Dirac-cone approximation, which works pretty well regarding the low-energy momentum modes around the Dirac points.

In Fig. 2.5 the arrangement of the high symmetry points are illustrated on the left hand side. The Γ point marks the center of the honeycomb, while M identifies the

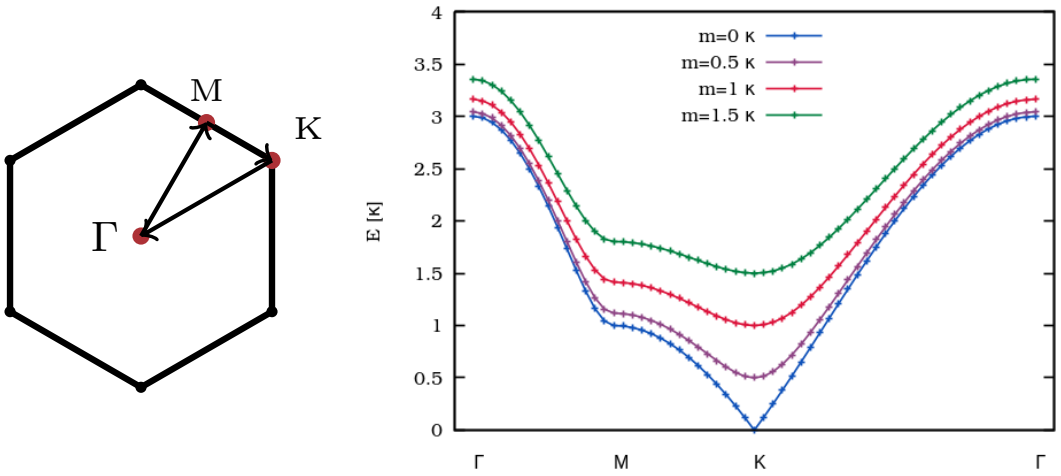

Figure 2.5: On the left hand side the high symmetry points of the BZ are illustrated. On the right hand side the quasi-particle energy relation along the high symmetry points from Eq. (2.32) is plotted.

van Hove singularity at the saddle points in the band structure, and K labels the Dirac points. On the right hand side the energy dispersion function from Fig. 2.4 for the upper π-band is plotted against high symmetry points of the BZ for vanishing chemical potential and varying constant explicit mass terms, as indicated by m_σ in Eq. (2.32). For $m = 0$ the energy dispersion is just equal to the absolute value of the structure factor $|\varphi_{\boldsymbol{k}}|$ specified by Eq. (2.29). For non-zero mass terms a band gap emerges and the energy dispersion is slightly modified. In Ref. [36] it was even shown that the singularity do not change its location in momentum space in the present of interactions. The opening of a band gap indicates an insulator transition which is caused by an explicit mass term in the example of Fig. 2.5. Such a mass term can be directly related to the sublattice symmetry, i.e. the symmetry between sublattice A and B, as can be read off from Eq. (2.31) and will be studied in the following.

2.3 Symmetry Breaking Patterns on the Honeycomb Lattice

In this section the analogy between chiral symmetry breaking in QED_{2+1} [62–66] and the corresponding sublattice-valley symmetry on the hexagonal lattice will be briefly discussed (see Ref. [8, 46, 67] for more details). For simplicity we consider the smaller Brioullin zone containing two independent Dirac points K^+ and K^-. In the larger Brioullin zone we count 6 independent Dirac points, two per sublattice similar to the formulation on the smaller Brioullin zone. The formulation on the larger Brioullin zone additionally requires the inclusion of Eq. (2.21) in order to separate the momentum modes corresponding to one sublattice.

The Lagrangian in Minkowski spacetime is given by

$$\mathcal{L} = \sum_{\sigma=1}^{N_f} \bar{\Psi}_{\omega,\sigma}(\boldsymbol{k}) \left[\gamma^0\omega + \kappa\varphi_{\boldsymbol{k}}\,\gamma^+ + \kappa\varphi^*_{\boldsymbol{k}}\,\gamma^-\right] \Psi_{\omega,\sigma}(\boldsymbol{k})\,, \tag{2.34}$$

derived in App. E.1. The notation in frequency-momentum space is given in App. B. Here, σ labels the spin degree of freedom and the wavefunction $\Psi_\sigma(k)$ is given in two-dimensional sublattice space with its conjugate $\bar{\Psi} = \Psi^\dagger\gamma_0$. The Dirac matrices $\gamma_0 = \sigma_3$ and $\gamma^i \equiv \sigma_3\sigma_i$, with $i = 1, 2$, were introduced in sublattice space in App. A.2. Furthermore we use the shorthand notation $\gamma^\pm = (\gamma^1 \pm \mathrm{i}\,\gamma^2)/2$ in order to resemble a continuum Dirac theory as shown in the following. In the low-energy approximation the Lagrangian can be expanded around the Dirac points K^+ and K^- where the band structure behave linearly, $\kappa\,\varphi(K_\pm + \boldsymbol{k}) = \pm v_f(k_x \mp \mathrm{i}\,k_y)$,

$$\mathcal{L} \simeq \sum_{\sigma=1}^{N_f} \left[\bar{\Psi}_{\omega,\sigma}(K^+ + \boldsymbol{k}) \left[\gamma^0\omega + v_f(\gamma^1 k_x + \gamma^2 k_y)\right] \Psi_{\omega,\sigma}(K^+ + \boldsymbol{k}) \right. \tag{2.35}$$

$$\left. + \bar{\Psi}_{\omega,\sigma}(K^- + \boldsymbol{k}) \left[\gamma^0\omega + v_f(-\gamma^1 k_x + \gamma^2 k_y)\right] \Psi_{\omega,\sigma}(K^- + \boldsymbol{k})\right]. \tag{2.36}$$

By the introduction of a wavefunction in sublattice-valley space,

$$\Upsilon_{\omega,\sigma}(\boldsymbol{k}) = \begin{pmatrix} \Upsilon_{\omega,K_+,\sigma}(\boldsymbol{k}) \\ \Upsilon_{\omega,K_-,\sigma}(\boldsymbol{k}) \end{pmatrix} = \begin{pmatrix} a_\sigma(\omega, K_+ + \boldsymbol{k}) \\ b_\sigma(\omega, K_+ + \boldsymbol{k}) \\ b_\sigma(\omega, K_- + \boldsymbol{k}) \\ a_\sigma(\omega, K_- + \boldsymbol{k}) \end{pmatrix}, \tag{2.37}$$

the Lagrangian can be rewritten as

$$\tag{2.38}$$

$$\mathcal{L} \simeq \sum_{\sigma=1}^{N_f} \bar{\Upsilon}_{\omega,\sigma}(\boldsymbol{k}) \left[\gamma^0\omega + v_f\widetilde{\gamma}^1 k_x + v_f\widetilde{\gamma}^2 k_y)\right] \Upsilon_{\omega,\sigma}(\boldsymbol{k})\,, \tag{2.39}$$

matching the Lagrangian of a Dirac theory where the Fermi velocity v_F takes the role of the velocity of light c. Note the interchange of annihilation operators concerning the A and B sublattice in Eq. (2.37) in order to deal with ordinary gamma matrices in four-dimensional space (Weyl representation),

$$\widetilde{\gamma}^0 = \begin{pmatrix} 0 & \mathbb{1} \\ \mathbb{1} & 0 \end{pmatrix} \qquad \text{and} \qquad \widetilde{\gamma}^i = \begin{pmatrix} 0 & -\sigma^i \\ \sigma^i & 0 \end{pmatrix}, \tag{2.40}$$

with σ^i indicating the standard Pauli matrices as listed in App. A.2. In complete analogy to chirality in QED_{2+1} the theory described by equation (2.39) would be invariant under the following transformations,

$$\Upsilon_{\omega,\sigma}(\boldsymbol{k}) \to e^{i\alpha\widetilde{\gamma}_3}\Upsilon_{\omega,\sigma}(\boldsymbol{k})\,, \qquad \Upsilon_{\omega,\sigma}(\boldsymbol{k}) \to e^{i\alpha\widetilde{\gamma}_5}\Upsilon_{\omega,\sigma}(\boldsymbol{k})\,, \tag{2.41}$$

where the chiral matrix $\widetilde{\gamma}^5$ is constructed as usual, $\widetilde{\gamma}^5 = \mathrm{i}\,\widetilde{\gamma}^0\widetilde{\gamma}^1\widetilde{\gamma}^2\widetilde{\gamma}^3$ [8]. Consequently, there will be a U(2) symmetry generated by $\mathbb{1}, \widetilde{\gamma}_3, \widetilde{\gamma}_5$ and $[\widetilde{\gamma}_3, \widetilde{\gamma}_5]$ for each fermion flavor. We therefore remain with a $\mathrm{U}(2N_f)$ symmetry. A mass term of the form

$$m_\sigma\,\bar{\Upsilon}_{\omega,\sigma}(\boldsymbol{k})\Upsilon_{\omega,\sigma}(\boldsymbol{k}) \tag{2.42}$$

would break this symmetry down to

$$\mathrm{U}(2N_f) \to \mathrm{SU}\left(\mathrm{N}_f\right) \times \mathrm{SU}\left(\mathrm{N}_f\right) \times \mathrm{U}\left(1\right) \times \mathrm{U}\left(1\right). \tag{2.43}$$

This subvalley-lattice symmetry, corresponding to an inversion symmetry on the hexagonal lattice, within a low-energy description mimics a chiral symmetry in its continuum representation. Indeed, the hexagonal lattice only exhibits a discrete rotational invariance what is neglected in the Dirac cone approximation. The existence of a mass term as given in Eq. (2.42) exactly corresponds to the explicit mass of the previous discussion (see Eq. (2.32)). The considered symmetry cannot only be broken by an explicit mass term but also by spontaneous symmetry breaking which is the object of our further considerations within the Dyson-Schwinger framework.

3

The Fermionic Dyson-Schwinger Equations

In this chapter the fermion propagator and its Dyson-Schwinger equation will be introduced, considering a bare Coulomb interaction between the fermions in the solid state system. Moreover, the possibility of different electron configurations, namely the spin density wave (SDW) and the charge density wave (CDW) configuration will be discussed. In this context, the extended Hubbard model will be motivated as an appropriate approach to study the competition concerning these phases. Finally, the basis of the numerical solution procedure is presented in order to solve the obtained DSE's.

3.1 The Free Fermion Propagator

The fermionic Feynman propagator is defined as the usual time-ordered product of the corresponding Heisenberg fields,

$$G_{F,\sigma}(t,\boldsymbol{k}) = \langle T(\psi_{\boldsymbol{k},\sigma}(t)\bar{\psi}_{\boldsymbol{k},\sigma}(0))\rangle = \int \frac{d\omega}{2\pi}\, e^{-\mathrm{i}\,\omega t}\, G_{F,\sigma}(\omega,\boldsymbol{k})\,, \tag{3.1}$$

with spin index σ and thus one independent propagator per spin degree of freedom. More precisely, the fermion propagator is given by the creation and annihilation operators in sublattice space (cf. Eq. (2.26)),

$$G_{F,\sigma}(t,\boldsymbol{k}) = \frac{3}{N^2}\langle\, T \begin{pmatrix} a_{\boldsymbol{k},\sigma}(t)a^\dagger_{\boldsymbol{k},\sigma}(0) & -a_{\boldsymbol{k},\sigma}(t)b^\dagger_{\boldsymbol{k},\sigma}(0) \\ b_{\boldsymbol{k},\sigma}(t)a^\dagger_{\boldsymbol{k},\sigma}(0) & -b_{\boldsymbol{k},\sigma}(t)b^\dagger_{\boldsymbol{k},\sigma}(0) \end{pmatrix}\rangle \tag{3.2}$$

$$= \begin{pmatrix} G^{AA}_{F,\sigma}(t,\boldsymbol{k}) & G^{AB}_{F,\sigma}(t,\boldsymbol{k}) \\ G^{BA}_{F,\sigma}(t,\boldsymbol{k}) & G^{BB}_{F,\sigma}(t,\boldsymbol{k}) \end{pmatrix}, \tag{3.3}$$

where the free fermion propagator, associated to the Hamiltonian from Eq. (2.28), is entailed by the Heisenberg equations (see App. C) and mathematically directly given in terms of the corresponding resolvent,

$$G^0_{F,\sigma}(\omega, \boldsymbol{k}) = \mathrm{i}\left(\gamma_0\left(\omega - H^0_\sigma(\boldsymbol{k})\right)\right)^{-1}, \tag{3.4}$$

with the free momentum-space Hamiltonian from Eq. (2.31).

By the introduction of Dirac matrices $\gamma_0 = \sigma_3$ and $\gamma^i \equiv \sigma_3\sigma_i$, with $i = 1, 2$, fulfilling the Clifford algebra of the pseudospin-1/2 degree of freedom, $\{\gamma_\mu, \gamma_\nu\} = 2g_{\mu\nu}$, the free fermion propagator can be rewritten as

$$G^0_{F,\sigma}(\omega, \boldsymbol{k}) = \frac{\mathrm{i}\left(\gamma^0(\omega + \mu'_\sigma) + \kappa\varphi_{\boldsymbol{k}}\,\gamma^+ + \kappa\varphi^*_{\boldsymbol{k}}\,\gamma^- + m_\sigma\right)}{(\omega + \mu'_\sigma)^2 - \varepsilon^2_{\boldsymbol{k},\sigma} + \mathrm{i}\,\epsilon},$$

using the abbreviation $\gamma^\pm = (\gamma^1 \pm \mathrm{i}\,\gamma^2)/2$. With the infinitesimal shift into the complex plane, Feynman boundary conditions are implemented in Minkowski spacetime, which is indicated by the additional index F. The conventions concerning the introduced Dirac matrices are summarized in App. A.2.

3.2 Instantaneously Interacting Fermions

In the following, we introduce an interaction between the fermionic quasi-particles in terms of a Coulomb interaction. For the sake of generality we want to retain the long-range terms although we will focus on the extended Hubbard-model in the next section. The generalized Coulomb interaction is of the form

$$\mathcal{H}_C = \frac{1}{2}\sum_{i,j}\, q_i\, V_{ij}\, q_j\,, \tag{3.5}$$

where q_i denotes the charge operator at lattice site i,

$$q_i = \sum_\sigma n_{i,\sigma} - \bar{Q} \qquad \text{with} \qquad n_{i,\sigma} = c^\dagger_{i,\sigma}\, c_{i,\sigma}\,, \tag{3.6}$$

and σ labels the sum over all fermion flavors. For the considered case of two fermion flavors, the constant parameter $\bar{Q}$ is set to $\bar{Q} = 1$ in order to account for the positive charged cores (1 per carbon site), providing a neutral graphene sheet. The Hamiltonian can be rewritten as

$$\mathcal{H}_C = -\frac{1}{2}\sum_{i,\sigma} V_{ii}\, n_{i,\sigma} - \sum_{i\neq j,\sigma} V_{ij}\, n_{i,\sigma} + \underbrace{\frac{1}{2}\sum_{i,j,\sigma,\sigma'} V_{ij}\, n_{i,\sigma} n_{j,\sigma'}}_{\mathcal{H}_{tp}} + \frac{1}{2}\sum_{i,j} V_{ij}\,, \tag{3.7}$$

here the constant term can be neglected in the following since it merely represents a shift in the energy distribution and does not contribute to the Dyson-Schwinger equations at all. Additionally the contributions proportional to $n_{i,\sigma}$ are absorbed within the chemical potential μ'_σ, which is therefore relabeled by μ_σ.

In App. D.2 it is explicitly shown that the demand for fermion number conservation entails $\mu = 0$. Generally, a contribution from $\mu \neq 0$ causes an effective electric field that tends to push fermions out of the solid-state body. Experimentally, this

can be realized for instance by chemical doping, the application of a back voltage or the application on an additional substrate [9]. As starting point, we first of all investigate the case of suspended graphene for zero temperature.

For the interacting case we then formally set $\mu' \to \mu = 0$ to keep the system at half filling. The normal ordered two-particle operator reads

$$\begin{aligned}\mathcal{H}_{tp} =& \frac{1}{2} \sum_{s,s',\boldsymbol{i},\boldsymbol{j},\sigma,\sigma'} V_{\boldsymbol{ij}}^{s,s'}\; c^\dagger_{s,\boldsymbol{i},\sigma}(t)\, c^\dagger_{s',\boldsymbol{j},\sigma'}(t')\, c_{s',\boldsymbol{j},\sigma'}(t')\, c_{s,\boldsymbol{i},\sigma}(t) \qquad (3.8)\\ =& \frac{1}{2} \sum_{\boldsymbol{i},\boldsymbol{j},\sigma,\sigma'} \Big(V_{\boldsymbol{ij}}^{AA}\, a^\dagger_{\boldsymbol{i},\sigma} a^\dagger_{\boldsymbol{j},\sigma'} a_{\boldsymbol{j},\sigma'} a_{\boldsymbol{i},\sigma} + V_{\boldsymbol{ij}}^{AB}\, a^\dagger_{\boldsymbol{i},\sigma} b^\dagger_{\boldsymbol{j},\sigma'} b_{\boldsymbol{j},\sigma'} a_{\boldsymbol{i},\sigma}\\ &+ V_{\boldsymbol{ij}}^{BA}\, b^\dagger_{\boldsymbol{i},\sigma} a^\dagger_{\boldsymbol{j},\sigma'} a_{\boldsymbol{j},\sigma'} b_{\boldsymbol{i},\sigma} + V_{\boldsymbol{ij}}^{BB}\, b^\dagger_{\boldsymbol{i},\sigma} b^\dagger_{\boldsymbol{j},\sigma'} b_{\boldsymbol{j},\sigma'} b_{\boldsymbol{i},\sigma} \Big)\,, \qquad (3.9)\end{aligned}$$

where s and s' include sublattice degrees of freedom and σ and σ' refer to spin indices. Note the independence of the interaction from the spin degree of freedom in contrast to the dependence from the sublattice degree of freedom, which is actually called the pseudospin degree of freedom since it is treated like a flavor index in common theories.

The time dependence of the operators is suppressed in the following due to a shorter notation, but it should be mentioned that Eq. (3.9) represents an instantaneous interaction. Since the Fermi velocity is about three hundred times smaller than the speed of light, $v_f/c \approx 1/300$ [16], the approach of an instantaneous bare interaction neglecting retardation effects throughout this work is expected to be a very good approximation.

With the Fourier transform of the translationally invariant interaction potential on the fine triangular lattice (see also App. B.1),

$$V_{\boldsymbol{ij}} = \frac{1}{N^2} \sum_{\boldsymbol{q}} e^{\mathrm{i}\,\boldsymbol{q}\cdot(\boldsymbol{i}-\boldsymbol{j})}\, V_{\boldsymbol{q}}\,, \quad V_{\boldsymbol{q}} = \sum_{\boldsymbol{i}} e^{-\mathrm{i}\,\boldsymbol{q}\cdot\boldsymbol{i}}\, V_{\boldsymbol{i0}}\,, \qquad (3.10)$$

we can also extract the single sublattice components via

$$V_{\boldsymbol{q}}^{AA} = V_{\boldsymbol{q}}^{BB} = \frac{1}{3} \sum_{l=0}^{2} V_{\boldsymbol{q}+l\boldsymbol{\Delta}}\,, \qquad (3.11)$$

and

$$V_{\boldsymbol{q}}^{AB} = V_{\boldsymbol{q}}^{BA*} = \frac{1}{3} \sum_{l=0}^{2} e^{-\frac{2\pi\mathrm{i}}{3} l}\, V_{\boldsymbol{q}+l\boldsymbol{\Delta}}\,, \qquad (3.12)$$

as stated out in the last chapter (Eq. (2.21)). The Coulomb interaction can therefore be written as

$$\begin{aligned}\mathcal{H}_{tp} =& \frac{1}{2N^6} \sum_{\boldsymbol{k},\boldsymbol{p},\boldsymbol{q},\sigma,\sigma'} \Big(V_{\boldsymbol{q}}^{AA}\, a^\dagger_{\boldsymbol{p}+\boldsymbol{q},\sigma} a^\dagger_{\boldsymbol{k}-\boldsymbol{q},\sigma'} a_{\boldsymbol{k},\sigma'} a_{\boldsymbol{p},\sigma} + V_{\boldsymbol{q}}^{AB}\, a^\dagger_{\boldsymbol{p}+\boldsymbol{q},\sigma} b^\dagger_{\boldsymbol{k}-\boldsymbol{q},\sigma'} b_{\boldsymbol{k},\sigma'} a_{\boldsymbol{p},\sigma}\\ &+ V_{\boldsymbol{q}}^{BA}\, b^\dagger_{\boldsymbol{p}+\boldsymbol{q},\sigma} a^\dagger_{\boldsymbol{k}-\boldsymbol{q},\sigma'} a_{\boldsymbol{k},\sigma'} b_{\boldsymbol{p},\sigma} + V_{\boldsymbol{q}}^{BB}\, b^\dagger_{\boldsymbol{p}+\boldsymbol{q},\sigma} b^\dagger_{\boldsymbol{k}-\boldsymbol{q},\sigma'} b_{\boldsymbol{k},\sigma'} b_{\boldsymbol{p},\sigma} \Big)\,, \qquad (3.13)\\ =& \frac{1}{18N^2} \sum_{\boldsymbol{k},\boldsymbol{p},\boldsymbol{q},\sigma,\sigma'} V_{\boldsymbol{q}}^{ss'}\; :\bar{\psi}_{\boldsymbol{p}+\boldsymbol{q},\sigma} \gamma^0 \Gamma^s \psi_{\boldsymbol{p},\sigma}\; \bar{\psi}_{\boldsymbol{k}-\boldsymbol{q},\sigma'} \gamma^0 \Gamma^{s'} \psi_{\boldsymbol{k},\sigma'} :\,, \qquad (3.14)\end{aligned}$$

in momentum space, where we have introduced the following sublattice projectors,

$$\Gamma^A = \begin{pmatrix} 1 & 0 \\ 0 & 0 \end{pmatrix}, \qquad \text{and} \qquad \Gamma^B = \begin{pmatrix} 0 & 0 \\ 0 & 1 \end{pmatrix}. \tag{3.15}$$

Here it should be mentioned that the Hamiltonian is again invariant under momentum shifts by $\boldsymbol{\Delta}$ since the third roots of unity from the shift within the interaction exactly cancel with those from the creation (annihilation) operators. So obviously the momentum-space Hamiltonian is periodic on the three-times smaller commonly used BZ (Fig. 2.2), but the structure factor and the interaction between different sublattices are not.

Next, the corresponding fermionic equations of motion for the fermion propagator, namely the Dyson-Schwinger Equations (DSE's), are derived by means of the Heisenberg Equation, see App. C. This is probably a rather unusual approach to obtain the DSE's but very useful and reasonable, particularly with regard to the formalism of second quantization. In this context several approximations were used in order to end up with a simplified and truncated form of the Dyson-Schwinger equations, the so-called Hartree-Fock equations involving only the renormalization of the fermion propagator. For now we stick to an instantaneous bare interaction neglecting renormalization effects to the photon propagator. More generally even a static Coulomb interaction has the nice feature that it provides Dyson-Schwinger equations that close upon theirselves. Due to the mentioned difference in the order of magnitude between Fermi velocity and speed of light only the zeroth component of the photon field is taken into account. Therefore we only have to deal with the zeroth vertex component, here Ward-Takahashi identities require the vertex to be bare for a bare wavefunction renormalization, which is definitely true for a static interaction at zero temperature and zero chemical potential. The resulting DSE's are therefore given in terms of the Hartree-Fock equations and read (see App. C for more details)

$$\begin{aligned} G^{-1}_{F,\sigma}(k^0,\boldsymbol{k}) = G^0_{F,\sigma}(k^0,\boldsymbol{k})^{-1} + \overbrace{\frac{1}{N^2}\int\frac{dq^0}{2\pi}\sum_{\boldsymbol{q},u,u'} D^{0,uu'}(\boldsymbol{k}-\boldsymbol{q})\,\gamma^0\Gamma^u\,G_{F,\sigma}(q^0,\boldsymbol{q})\,\gamma^0\Gamma^{u'}}^{\text{Fock-term}} \\ \underbrace{-\frac{1}{N^2}\int\frac{dq^0}{2\pi}\sum_{\boldsymbol{q},u,u',\sigma'}(-1)^{|u-u'|}\,\mathrm{tr}\left(D^{0,uu'}(\boldsymbol{q}=0)\,\Gamma^u\,G_{F,\sigma'}(q^0,\boldsymbol{q})\,\Gamma^u\right)\Gamma^{u'}}_{\text{Hartree-term}}, \end{aligned} \tag{3.16}$$

where the bare photon propagator denoted by $D^0(\boldsymbol{q})$ can be simply connected to the instantaneous interaction matrix $V(\boldsymbol{q})$ via

$$D^{0,uu'}(\boldsymbol{q}) = \mathrm{i}\,V^{uu'}(\boldsymbol{q}). \tag{3.17}$$

Note that we have $V^{uu'}(\boldsymbol{q}=0) = V^{u'u}(\boldsymbol{q}=0)$ for zero momentum transfer.

Altogether we have to take two contributions into account, see Fig. 3.1: the Fock contribution which is very similar to the fermion self-energy in QED, except the sublattice dependence, and the Hartree contribution. The Hartree term generally

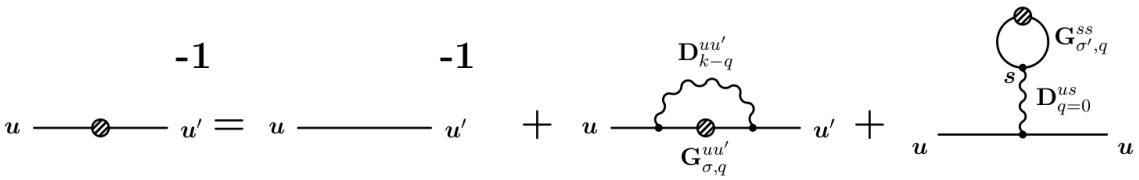

Figure 3.1: Shown is a diagrammatic sketch of the DSE from Eq. (3.16). Within the present truncation scheme only fermion propagators are dressed, which is indicated by the black dot. The last term represents the Hartree-contribution, whereas the term next to it illustrates the Fock-term.

accounts for the interaction of an electron with all charges considered as one background field [68]. Without the distinction between interactions on like sites and different sites, the Hartree-term would naturally cancel as for usual QED studies, where the negative background from all electrons exactly cancel with the positive background from the carbon cores. This will especially depend on the considered charge distribution as we will see in the next chapter.

With an ansatz for the dressed inverse propagator of the same structure as the free propagator, fulfilling the required symmetries, with renormalization functions $M_{\sigma,\boldsymbol{k}}, \phi_{\sigma,\boldsymbol{k}}$ and $Z_{\sigma,\boldsymbol{k}}$,

$$G_{F,\sigma}(k^0,\boldsymbol{k})^{-1} = -\mathrm{i}\begin{pmatrix} (k^0+\mu_\sigma)\,Z_{\sigma,\boldsymbol{k}} - M_{\sigma,\boldsymbol{k}} & \kappa\,\phi_{\sigma,\boldsymbol{k}} \\ -\kappa\,\phi^*_{\sigma,\boldsymbol{k}} & -(k^0+\mu_\sigma)\,Z_{\sigma,\boldsymbol{k}} - M_{\sigma,\boldsymbol{k}} \end{pmatrix}, \tag{3.18}$$

the DSE's can be simplified. The corresponding Feynman propagator is given by

$$G_{F,\sigma}(k^0,\boldsymbol{k}) = \frac{\mathrm{i}}{(k^0+\mu_\sigma)^2\,Z^2_{\sigma,\boldsymbol{k}} - \Omega^2_{\sigma,\boldsymbol{k}} + \mathrm{i}\,\epsilon}\begin{pmatrix} (k^0+\mu_\sigma)\,Z_{\sigma,\boldsymbol{k}} + M_{\sigma,\boldsymbol{k}} & \kappa\,\phi_{\sigma,\boldsymbol{k}} \\ -\kappa\,\phi^*_{\sigma,\boldsymbol{k}} & -(k^0+\mu)\,Z_{\sigma,\boldsymbol{k}} + M_{\sigma,\boldsymbol{k}} \end{pmatrix}, \tag{3.19}$$

where $\Omega_{\sigma,\boldsymbol{k}} = \sqrt{M^2_{\sigma,\boldsymbol{k}} + \kappa^2|\phi_{\sigma,\boldsymbol{k}}|^2}$ is the dressed quasi-particle energy function. The matrix equation from Eq. (3.16) can be decoupled in terms of the single renormalization functions via

$$M_{\sigma,\boldsymbol{k}} = \frac{1}{2\mathrm{i}}\mathrm{tr}\left[G^{-1}_{F,\sigma}(k^0,\boldsymbol{k})\right], \tag{3.20}$$

$$Z_{\sigma,\boldsymbol{k}} = \frac{1}{-2\mathrm{i}\,(k^0+\mu)}\mathrm{tr}\left[\gamma^0\,G^{-1}_{F,\sigma}(k^0,\boldsymbol{k})\right], \tag{3.21}$$

$$\phi_{\sigma,\boldsymbol{k}} = \frac{1}{\mathrm{i}}\mathrm{tr}\left[\gamma^-\,G^{-1}_{F,\sigma}(k^0,\boldsymbol{k})\right], \tag{3.22}$$

$$\phi^*_{\sigma,\boldsymbol{k}} = \frac{1}{\mathrm{i}}\mathrm{tr}\left[\gamma^+\,G^{-1}_{F,\sigma}(k^0,\boldsymbol{k})\right]. \tag{3.23}$$

This yields the following system of coupled equations in terms of the introduced

renormalization functions,

$$M_{\sigma,\boldsymbol{k}} = m_\sigma + \frac{1}{N^2}\int \frac{dq^0}{2\pi}\left(\sum_{\boldsymbol{q}} D_{\boldsymbol{q}}^{0,AA} \frac{M_{\sigma,\boldsymbol{k}+\boldsymbol{q}}}{(q^0+\mu)^2 Z_{\sigma,\boldsymbol{k}+\boldsymbol{q}}^2 - \Omega_{\sigma,\boldsymbol{k}+\boldsymbol{q}}^2 + \mathrm{i}\,\epsilon} + (D_{\boldsymbol{q}=0}^{0,AB} - D_{\boldsymbol{q}=0}^{0,AA}) \sum_{\boldsymbol{p},\sigma'} \frac{M_{\sigma',\boldsymbol{p}}}{(q^0+\mu)^2 Z_{\sigma',\boldsymbol{p}}^2 - \Omega_{\sigma',\boldsymbol{p}}^2 + \mathrm{i}\,\epsilon}\right), \tag{3.24}$$

$$Z_{\sigma,\boldsymbol{k}}\cdot(k^0+\mu) = (k^0+\mu) - \frac{1}{N^2}\int \frac{dq^0}{2\pi}\left(\sum_{\boldsymbol{q}} D_{\boldsymbol{q}}^{0,AA} \frac{(q^0+\mu) Z_{\sigma,\boldsymbol{k}+\boldsymbol{q}}}{(q^0+\mu)^2 Z_{\sigma,\boldsymbol{k}+\boldsymbol{q}}^2 - \Omega_{\sigma,\boldsymbol{k}+\boldsymbol{q}}^2 + \mathrm{i}\,\epsilon} + (D_{\boldsymbol{q}=0}^{0,AB} + D_{\boldsymbol{q}=0}^{0,AA}) \sum_{\boldsymbol{p},\sigma'} \frac{(q^0+\mu) Z_{\sigma',\boldsymbol{p}}}{(q^0+\mu)^2 Z_{\sigma',\boldsymbol{p}}^2 - \Omega_{\sigma',\boldsymbol{p}}^2 + \mathrm{i}\,\epsilon}\right), \tag{3.25}$$

$$\phi_{\sigma,\boldsymbol{k}} = \varphi_{\boldsymbol{k}} + \frac{1}{N^2}\int \frac{dq^0}{2\pi}\sum_{\boldsymbol{q}} D_{\boldsymbol{q}}^{0,BA} \frac{\phi_{\sigma,\boldsymbol{k}+\boldsymbol{q}}}{(q^0+\mu)^2 Z_{\sigma,\boldsymbol{k}+\boldsymbol{q}}^2 - \Omega_{\sigma,\boldsymbol{k}+\boldsymbol{q}}^2 + \mathrm{i}\,\epsilon}, \tag{3.26}$$

$$\phi_{\sigma,\boldsymbol{k}}^* = \varphi_{\boldsymbol{k}}^* + \frac{1}{N^2}\int \frac{dq^0}{2\pi}\sum_{\boldsymbol{q}} D_{\boldsymbol{q}}^{0,AB} \frac{\phi_{\sigma,\boldsymbol{k}+\boldsymbol{q}}^*}{(q^0+\mu)^2 Z_{\sigma,\boldsymbol{k}+\boldsymbol{q}}^2 - \Omega_{\sigma,\boldsymbol{k}+\boldsymbol{q}}^2 + \mathrm{i}\,\epsilon}. \tag{3.27}$$

All renormalization functions remain frequency independent for frequency independent interactions, e.g. if the photon propagator is meant to be static. Consequently, within the approximation of an instantaneous Coulomb potential, the frequency integrals can be solved analytically, also for finite temperature and finite chemical potential. The solution of the required frequency integrals is extensively described in App. D.1.

As can now be clearly seen from the mass renormalization function, the emergence of an effective band gap ($M_\sigma(K) \neq 0$), indicating an insulating phase, can either be induced by an explicitly symmetry breaking mass term ($m_\sigma \neq 0$) or also by dynamical mass generation in the limit ($m_\sigma \to 0$), equivalently to the chiral limit in QED.

Another interesting point that can be read off from Eq. (3.24)-Eq. (3.27) is that the interaction between like sites do not contribute to the Fermi velocity renormalization within this truncation.

3.3 Competing Order - CDW vs. SDW Excitations

Throughout this work we follow the most common assumption of two fermion flavors $N_f = 2$ with $\sigma = \uparrow, \downarrow$, due to spin up and spin down fermions. Of particular interest concerning such a configuration is the preferred constellation of electrons with increasing interaction. In this context we investigate the two possibilities of sublattice breaking, either by equally distributed charges ($m_\uparrow = m_\downarrow$) forming a spin density wave state (SDW) or by equally distributed spins ($m_\uparrow = -m_\downarrow$), where a charge density wave is formed (CDW). These two possibilities can be understood as two different realizations of breaking the same symmetry, namely the sublattice symmetry [8]

$$U(4) \to SU(2) \times SU(2) \times U(1) \times U(1), \tag{3.28}$$

as introduced in Sec. 2.3.

The semi-metal insulator transition can therefore be induced by an alternating charge density (CDW) as well as by an alternating spin density (SDW), corresponding to the same symmetry breaking pattern with different vacuum alignments. These two electronic configurations can be thought of as illustrated in Fig. 3.2 for a strictly localized realization. For a charge-staggered and spin-staggered ground state respec-

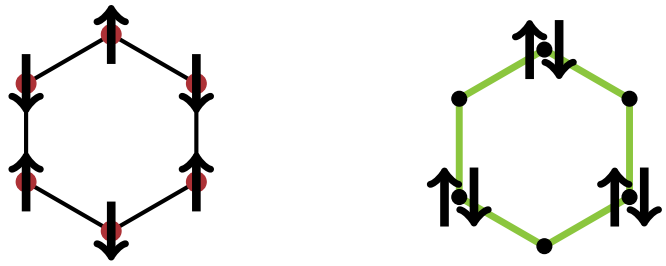

Figure 3.2: On the left hand site a strictly localized SDW distribution is represented. On the right hand side the corresponding counterpart of a CDW state is shown.

tively, we generally define

$$\begin{aligned} m_{\mathrm{cdw}} &= \frac{1}{2}\left(m_\uparrow + m_\downarrow\right), \\ m_{\mathrm{sdw}} &= \frac{1}{2}\left(m_\uparrow - m_\downarrow\right). \end{aligned} \tag{3.29}$$

We adopt this ansatz to the dressed mass functions and assume all other renormalization functions to be equal for different spin states. The resulting mass renormalization function apparently distinguishes between SDW and CDW excitations,

$$M_{\mathrm{sdw},\boldsymbol{k}} = m_{\mathrm{sdw}} + \frac{1}{N^2}\int\frac{dq^0}{2\pi}\sum_{\boldsymbol{q}} D^{0,AA}_{\boldsymbol{q}}\frac{M_{\mathrm{sdw},\boldsymbol{k}+\boldsymbol{q}}}{(q^0+\mu)^2 Z^2_{\boldsymbol{k}+\boldsymbol{q}} - \Omega^2_{\mathrm{sdw},\boldsymbol{k}+\boldsymbol{q}} + \mathrm{i}\,\epsilon}, \tag{3.30}$$

$$\begin{aligned} M_{\mathrm{cdw},\boldsymbol{k}} = m_{\mathrm{cdw}} + \frac{1}{N^2}\int\frac{dq^0}{2\pi}\Bigg(&\sum_{\boldsymbol{q}} D^{0,AA}_{\boldsymbol{q}}\frac{M_{\mathrm{cdw},\boldsymbol{k}+\boldsymbol{q}}}{(q^0+\mu)^2 Z^2_{\boldsymbol{k}+\boldsymbol{q}} - \Omega^2_{\mathrm{cdw},\boldsymbol{k}+\boldsymbol{q}} + \mathrm{i}\,\epsilon} \\ &+ 2\left(D^{0,AB}_{\boldsymbol{q}=0} - D^{0,AA}_{\boldsymbol{q}=0}\right)\sum_{\boldsymbol{p}}\frac{M_{\mathrm{cdw},\boldsymbol{p}}}{(q^0+\mu)^2 Z^2_{\boldsymbol{p}} - \Omega^2_{\mathrm{cdw},\boldsymbol{p}} + \mathrm{i}\,\epsilon}\Bigg), \end{aligned} \tag{3.31}$$

while the Fermi velocity renormalization and the wave-function renormalization are expected to be equal for both spin states,

$$Z_{\boldsymbol{k}} = Z_{\uparrow,\boldsymbol{k}} = Z_{\downarrow,\boldsymbol{k}}, \qquad \text{and} \qquad \phi_{\boldsymbol{k}} = \phi_{\uparrow,\boldsymbol{k}} = \phi_{\downarrow,\boldsymbol{k}}, \tag{3.32}$$

determined by the integral equations from Eq. (3.30) and Eq. (3.32). Now it becomes clear why we emphasize the decisive difference between spin and pseudospin degree of freedom, the Hartree-term exactly makes the difference between CDW and SDW excitations.

Of course one also has to take a stable mixed phase into consideration, this is why we did not only examine to solve Eq. (3.30)-Eq. (3.32) for the SDW and CDW case separately, but we also solve the whole coupled system by doubling the number of renormalization functions without fixing the system either to an SDW or CDW state (see Sec. 3.5 for details).

3.4 Extended Hubbard Model

In order to particularly investigate the competition between the CDW and SDW phase, the bare electron-electron interaction has been reduced to its on-site potential U ($V_{\boldsymbol{ii}} = U = \text{const.}$) and its nearest-neighbor interaction V ($V_{\boldsymbol{ii}+\boldsymbol{\delta}_i} = V = \text{const.}$) within the so called extended Hubbard model. The considered interaction (Eq. (3.10)) hence simplifies to

$$V_{\boldsymbol{i0}} = U \cdot \delta(\boldsymbol{i}) + V \cdot \sum_{i=1}^{3} \delta(\boldsymbol{i} - (\boldsymbol{i} + \boldsymbol{\delta}_i)) \,. \tag{3.33}$$

In momentum space the following sublattice contributions are obtained,

$$V_{\boldsymbol{q}}^{AA} = U, \qquad \text{and} \qquad V_{\boldsymbol{q}}^{AB} = V \cdot \varphi_{\boldsymbol{q}} \,, \tag{3.34}$$

with $\varphi_{\boldsymbol{q}}$ being the bare structure function from Eq. (2.29) and $V_{\boldsymbol{q}}^{BA} = (V_{\boldsymbol{q}}^{AB})^*$.

Evidently, a fermionic many particle system which is dominated by the on-site repulsion is preferably arranged in an SDW formation, whereas the arrangement within a CDW state would be favored if the nearest-neighbor repulsion clearly dominates. Therefore U and V provide excellent control parameters to investigate these competing semi-metal insulator transitions with $M_{sdw,K}$ and $M_{cdw,K}$ as order parameters.

The associated ansatz for the bare bosonic propagator can be summarized in sublattice space as

$$D_{\boldsymbol{q}}^{0} = \mathrm{i} \begin{pmatrix} U & V \cdot \varphi_{\boldsymbol{q}} \\ V \cdot \varphi_{\boldsymbol{q}}^{*} & U \end{pmatrix} . \tag{3.35}$$

Throughout this work we want to consider a repulsive interaction with $U \geq 0$ and $V \geq 0$. Note that the prefactor of the Hartree term, which only appears for the CDW case, is just given by

$$D_{\boldsymbol{q}=0}^{0,AB} - D_{\boldsymbol{q}=0}^{0,AA} = 3\,V - U \,, \tag{3.36}$$

within the extended Hubbard model. For this reason, exactly the same DSE's are obtained for $U = 3\,V$, for both, the SDW and the CDW case, where the factor of three represents the coordination number of the two-dimensional hexagonal lattice. In graphene the effective on-site interaction is about $U_0 = 9.3\,\mathrm{eV} \approx 3.32\,\kappa$ [69], a varying on-site interaction can be simply related to a general Coulomb coupling strength α, identifying the interaction strength in the long-range consideration

$$U = \frac{\alpha}{\alpha_g} U_0 \,. \tag{3.37}$$

The nearest-neighbor coupling of graphene was also determined in Ref. [69] to approximately $V_0 = 5.5\,\mathrm{eV} \approx 1.96\,\kappa$ from first principles within a constrained Random Phase Approximation (cRPA).

Indeed, in HMC studies it turns out that the long-range tail of the Coulomb interaction is not decisively important for the location of the phase transition as pointed out in Ref. [25] in comparison to the outcome of Ref. [24]. A different question is the corresponding kind of phase transition and the related universality class, which depends on the range of the interaction and is still a rather open question [40].

3.5 Numerical Techniques

In principal, the DSE's form an infinite tower of coupled differential equations, namely the equations of motion for Green functions of the considered theory [70]. Since the DSE's resum loop contributions up to infinite order, the Dyson-Schwinger formalism is one of a few suitable tools, among e.g. FRG or Monte-Carlo methods, to overcome non-perturbative phenomena.

With the on-site coupling U and the hopping parameter κ we face a theory with similar orders in the kinetic as well as in the interaction energy, which both can not be handled perturbatively. Therefore the Dyson-Schwinger formalism seems to provide an adequate framework to investigate the phenomena of this theory. In this context the infinite resummation, also contained in Eq. (3.24)-Eq. (3.27), is hidden in a geometric series,

$$G_{F,\sigma}(k^0,\boldsymbol{k}) = G^0_{F,\sigma}(k^0,\boldsymbol{k}) \sum_{n=0}^{\infty} \left(\mathbb{1} + \left(-\Sigma(k^0,\boldsymbol{k})\, G^0_{F,\sigma}(k^0,\boldsymbol{k})\right)^n\right) \tag{3.38}$$

$$= G^0_{F,\sigma}(k^0,\boldsymbol{k})\left(\mathbb{1} + \Sigma(k^0,\boldsymbol{k})\, G^0_{F,\sigma}(k^0,\boldsymbol{k})\right)^{-1}. \tag{3.39}$$

Nevertheless, in order to obtain a numerical accessible set of equations, several truncation schemes are needed. Within the truncation schemes of this work, the infinite set of DSE's closes upon itself for all considered approximations. With Eq. (3.24)-Eq. (3.27) the fermion DSE results in a closed system of non-linear integral equations for 6 unknown static functions on the Brioullin zone ($M_{\sigma,\boldsymbol{k}}, Z_{\sigma,\boldsymbol{k}}, \phi_{\sigma,\boldsymbol{k}}$).

As explained above, the number of equations can be halved by fixing the system to one phase (CDW or SDW) beforehand, whereas the system can make its choice by doubling the degrees of freedom at the expense of a much higher numerical effort. We have tested both methods for various truncation schemes but never found a stable phase of coexistence and therefore no deviation from the solutions that were extracted from the first method was found (see also Sec. 3.5).

Unfortunately, the determination of initial values for all renormalization functions and especially for those of $M_{\uparrow,\boldsymbol{k}}$ and $M_{\downarrow,\boldsymbol{k}}$ causes a preference for either the CDW or SDW state. Maybe this problem can be solved by the introduction of randomly distributed initial values on the momentum lattice, but this has not been pursued within this work. In the following we therefore focus on the solution of the restricted system as discussed in Sec. 3.3.

Generally, also the renormalization functions $M_{\sigma,\boldsymbol{k}}$ and $Z_{\sigma,\boldsymbol{k}}$ are complex valued functions, but in simple truncation schemes they remain real valued. This is of

special importance regarding calculations at finite temperature T and finite chemical potential μ. However, the system of coupled equations which need to be solved throughout this work is mostly similar to the form of the basic system of equations from Eq. (3.24)-Eq. (3.27). This kind of equations are solved by a fixed point iteration [71].

Iteration Procedure

The iteration is typically started with the bare counterparts of the corresponding renormalization functions, $\phi_{\sigma,\boldsymbol{k}} = \varphi_{\boldsymbol{k}}$ and $Z_{\sigma,\boldsymbol{k}} = 1$, and a constant value for the mass renormalization function, $M_{\sigma,\boldsymbol{k}} = I$, which is usually chosen to be $I = 1$ or $I = 10$. Since we are mainly interested in the bifurcation point of our theory where one solution bifurcates away from the other, we commonly have to deal with more than one possible solution. In general the solution should not depend on the choice of I, but we might find the trivial solution instead of an existing non-trivial, therefore the starting value should not be too small. Another exception is the case of a first-order transition, where the solution of the system of equations depends on I due to the effect of hysteresis, as discussed in Chap. 5.

The frequency integrals can either be solved analytically or are approximated by a discrete sum within the formalism of Matsubara sums in Euclidean space-time (see App. D.1). Additionally the sum over all discrete momentum modes of the Brioullin zone can be executed on the momentum lattice as introduced in the last chapter. All involved renormalization functions are updated after each iteration step until a certain relative precision p is achieved to which the considered functions do not change anymore. This stop criterion can be expressed as

$$\left| \frac{\mathcal{F}^{\mathrm{old}}(k_n^0, \boldsymbol{k}_{ij}) - \mathcal{F}^{\mathrm{new}}(k_n^0, \boldsymbol{k}_{ij})}{\mathcal{F}^{\mathrm{old}}(k_n^0, \boldsymbol{k}_{ij})} \right| < p \,, \tag{3.40}$$

where n denotes the frequency index containing N_t lattice points, and i and j refer to the indices on the momentum lattice. Furthermore, $\mathcal{F}^{\mathrm{new}}$ indicates the solution from the actual iteration step and $\mathcal{F}^{\mathrm{old}}$ that of the previous one. If this condition is fulfilled for each renormalization function, for the real and the imaginary part, as well as for every lattice point in frequency-momentum space, the system is assumed to be converged.

The precision p is usually fixed to 10^{-5} and provides insight up to which relative order the function should not change any more in the following iterations. The error estimated on the basis of this convergence precision is absolutely negligible in comparison to finite volume effects for instance. In order to minimize these effects caused by finite lattice sizes N^2 and N_t, which is probably the main numerical source of errors, the lattice sizes have to be as large as possible. Although N^2 is directly connected to the spatial size of the considered graphene sheet, a real graphene sheet e.g. with the size of $1\,\mathrm{mm}^2$ would correspond to a number of unit cells in one direction of the order of $N \sim 10^7$. This explains why huge lattice sizes are of general interest.

The iteration procedure was therefore accelerated with several techniques. One simple approach is to start the iteration for a certain coupling value with the already obtained result for a little higher coupling parameter. In practice this procedure

saves a lot of iteration steps. Especially in the regime near the critical coupling it can be quite difficult to obtain a converged solution from the iteration method, this certainly depends on the considered truncation scheme. In some cases it can also be useful to not completely update all renormalization functions in every iteration step, but to perform the next iteration step on the basis of a weighted average, determined by a factor λ,

$$\mathcal{F}^{\text{new}}(k_n^0, \boldsymbol{k}_{ij}) = \lambda\, \mathcal{F}^{\text{new}}(k_n^0, \boldsymbol{k}_{ij}) + (1-\lambda)\, \mathcal{F}^{\text{old}}(k_n^0, \boldsymbol{k}_{ij})\,, \tag{3.41}$$

of the new and the old values for the considered renormalization function. The application of such techniques is additionally specified for the individual calculation.

Parallelization with OpenCL

In order to achieve a maximized code performance we take advantage of the possibilities of parallel programming and we exploit a couple of numerical properties. In this context, code parallelization was realized by using OpenCL (Open Computing Language) [72, 73] which enables a programmer to utilize various kind of devices, such as *Central Processing Units* (CPU's), *Graphics Processing Units* (GPU's), *Field-Programmable Gate Arrays* (FPGA'S) or other hardware accelerators within one heterogeneous system [74]. The *Application Programming Interface* (API) OpenCL gives access to a wide range of hardware, the calculations within this work, however, were either made on GPU's or on CPU cluster systems which provides a valuable flexibility and the opportunity of real runtime optimization. In the sense of parallel programming a lot of computer time is saved by executing code parts concurrently, called *General Purpose Computation on Graphics Processing Unit* (GPGPU).

In order to even gain more flexibility, the existing source code can be executed in double as well as single precision by making use of template classes, anyhow all results shown in this work were calculated in double precision.

Convolution Method

In order to save even more computation time, another technique has proven itself to be a very effective instrument. From a mathematical point of view, the integral parts of Eq. (3.24)-Eq. (3.27) have the form of a convolution and even the Hartree term for the CDW state can simply be transformed to comply with the representation of a convolution (Eq. (3.31)).

Considering the two-dimensional sum in momentum space, N^2 complex multiplication steps have to be executed due to a matrix vector multiplication. In terms of the convolution theorem, the sum can rather be calculated by doing two *Fast Fourier Transforms* (FFT) of the interaction matrix and the associated part of the fermion propagator separately, performing a point multiplication for the same argument in position space and a back-transform into momentum space afterwards.

The FFT, in comparison to the trivial matrix vector multiplication, merely needs $N \cdot \log_2(N)$ operations [75, 76]. A usual discrete Fourier transform (DFT) would require N^2 steps likewise. The same applies to calculations including the Matsubara sum for $N^2 \to N^2 \cdot N_t$. In order to verify the FFT method, all integral equations that matches the form of Eq. (3.24)-Eq. (3.27) are solved with both procedures, all

final results presented in this work were obtained by using the FFT method due to large lattice sizes. This numerical advantage provides the possibility of reaching sufficient large lattice sizes to reduce occurring finite volume effects and even give access to quantities like critical exponents. Eventually, the limiting factor is not given by runtime restrictions but rather by memory aspects.

The FFT is implemented by making use of recent software libraries, namely the clFFT or the FFTW for CPU routines [77]. In current software libraries the fast Fourier transform can usually be calculated for an arbitrary number of lattice points N in one dimension, but due to prime factorization for powers of $2, 3$ and 5, the algorithm is optimized. Within the clFFT library only those kind of lattice sizes $N = 2^k \cdot 3^m \cdot 5^n$ with $\{k, m, n\} \in \mathbb{N}_0$ are allowed, which gives reason to the sometimes extraordinary choice of N or N_t similarly.

4

Aspects of Mean Field Approximations

In this chapter we want to investigate the semimetal-insulator phase transition on the hexagonal lattice within several mean field approaches. These kind of approximations represent the most simple but probably also most important access.

First, the critical exponent of the order parameter β will be derived within a simple ansatz neglecting the band-structure renormalization. Then the idea of *Finite Size Scaling* (FSS) will be introduced and applied in order to obtain the critical exponent ν corresponding to the correlation length. Subsequently the effects of a renormalized band structure will be included within a so-called Hartree-Fock approximation and the phase diagram will be represented within the coupling plane (U-V-plane) for the CDW and the SDW state. Finally, the formalism of nPI effective action will be introduced in order to analytically deduce the location of the first-order phase transition between an SDW and CDW formation.

4.1 Mean-Field Approximation and Critical Exponents

In the first step we are interested in the behavior of the electron system at zero temperature ($T = 0$) and zero chemical potential $\mu_\uparrow = \mu_\downarrow = 0$, i.e. for a half filled hexagonal lattice. In App. D.2 we have convinced ourselves that the assumption of $\mu_\uparrow = \mu_\downarrow = 0$ for the effective chemical potential (also containing terms from the interaction Hamiltonian, see Eq. (3.7)) really provide the description of a neutral graphene sheet with a preserved number of fermions.

For zero chemical potential Eq. (3.27) immediately entails that the wavefunction renormalizations remain trivial,

$$Z_{\uparrow,\boldsymbol{k}} = Z_{\downarrow,\boldsymbol{k}} = 1\,, \tag{4.1}$$

due to the symmetric frequency integral over an anti-symmetric integrand. Moreover

we also assume the wave-function renormalizations to be bare,

$$\phi_{\uparrow,\boldsymbol{k}} = \phi_{\downarrow,\boldsymbol{k}} = \varphi_{\boldsymbol{k}}\,, \tag{4.2}$$

i.e. we can neglect renormalization effects on the band structure, which of course includes the renormalization of the Fermi velocity with a more descriptive meaning.

The photon propagator from Eq. (3.35) within the Hubbard approximation furthermore is applied to Eq. (3.27), leading to a kind of mean field approximation with actually very interesting and surprising outcomes. In the following we set the explicitly symmetry breaking mass term to zero ($m_{\mathrm{sdw}} = m_{\mathrm{cdw}} = 0$) which equates to a calculation in the chiral limit. The resulting mass renormalization functions is then given by

$$\mathcal{M} = \tilde{v}\ \frac{1}{N^2}\sum_{\boldsymbol{k}}\ \frac{\mathcal{M}}{2\sqrt{\mathcal{M}^2 + \kappa^2|\varphi_{\boldsymbol{k}}|^2}}\,, \tag{4.3}$$

or in terms of a continuous integral,

$$\mathcal{M} = \tilde{v}\ \mathcal{A}\mathcal{Z}\int_{\mathcal{B}\mathcal{Z}'}\frac{d^2k}{(2\pi)^2}\ \frac{\mathcal{M}}{2\sqrt{\mathcal{M}^2 + \kappa^2|\varphi_{\boldsymbol{k}}|^2}}\,, \tag{4.4}$$

with $\tilde{v} = (2\,V^{AB}_{\boldsymbol{q}=0} - V^{AA}_{\boldsymbol{q}=0}) = 6\,V - U$ for the CDW case and $\tilde{v} = U$ for the SDW case respectively. Moreover, the sum is rewritten as a continuous integral in momentum space (for $N \to \infty$, see App. B.1) since the critical exponents that we are interested in are determined via quantities defined in the infinite volume limit. As this equation only depends on the absolute value of the structure function, it can be solved on the small Brioullin-zone (Fig. 2.2) which is denoted by $\mathcal{B}\mathcal{Z}'$ and contains two independent Dirac points. Here the mass renormalization function in mean-field approximation is denoted by $\mathcal{M}$ and does not depend on the momentum variable, due to the momentum independent interaction. The generated mass gap is thus constant over the whole Brioullin zone ($\mathcal{M} = \text{const.}$) and therefore also agrees with the mass function at the Dirac points serving as order parameter for the considered phase transition.

Although we are not yet interested in a classical temperature driven phase transition, we can translate all general principles to the considered semimetal-insulator phase transition where the strength of the interaction now serves as control parameter and the mass term $\mathcal{M}$ identifies the order parameter. For this kind of approximation we expect to find a phase transition of second-order as usual for such mean field calculations in two dimensions [78]. Of special interest in this context are the critical exponents, which describe the phase transition, i.e. the behavior near the corresponding singularity, in corresponding power laws. In general one distinguishes between order parameters which describe singularities resulting from non-analycities of the free energy ($\alpha, \beta, \gamma, \delta$, related by thermodynamic scaling laws), and those resulting from non-analycities of the correlation function (ν, η), which are related to the others via so called hyperscaling relations [79, 80].

In the following we are merely interested in the critical exponent of the order parameter β and the critical exponent ν of the correlation length ξ,

$$\mathcal{M} \propto |t|^{\beta}\,, \qquad \text{and} \qquad \xi \propto |t|^{-\nu}\,, \tag{4.5}$$

with the reduced parameter $t = (\tilde{v} - \tilde{v}_c)/\tilde{v}_c$. Generally, the critical exponents are determined by the corresponding universality class that is characterized by a few basic quantities, just like the dimensionality of a system, its symmetry and the range of interaction.

For now, we want to focus on the critical behavior of the mass renormalization in this simple model. An usual procedure to find the critical point where the non-trivial solutions arise (here always a pair consisting of $\mathcal{M}$ and $-\mathcal{M}$) in addition to the trivial solution and bifurcate away from each other, is to expand Eq. (4.3) in powers of $\mathcal{M}$. This idea can not be straightforwardly performed here, due to the singularity at the Dirac points $\varphi_{K^\pm} = 0$ for a zero mass value $\mathcal{M} = 0$ at the bifurcation point, or rather in the unbroken symmetry regime.

However, the singularity is removable and can be handled by exploiting the relativistic behavior of the structure function around the Dirac points with the expansion from Eq. (2.33). In order to remove the singularity, the integral from Eq. (4.3) is considered at $K^\pm$ and a small sphere around the Dirac points with radius Λ,

$$\begin{aligned}\int_0^\Lambda \frac{q\,dq}{(2\pi)} \frac{1}{\sqrt{\mathcal{M}^2 + v_f^2 q^2}} &= \frac{1}{v_f^2\,(2\pi)} \left[\sqrt{\mathcal{M}^2 + v_f^2\,q^2}\right]_0^\Lambda \\ &= \frac{1}{v_f^2\,(2\pi)} \left[v_f \Lambda \sqrt{1 + {}^{\mathcal{M}^2}/_{v_f^2 \Lambda^2}} - |\mathcal{M}|\right]. \end{aligned} \tag{4.6}$$

Note that the linear term in $\mathcal{M}$ results from the singular behavior around the Dirac points, and is completely independent of the radius Λ. To account for the number of singularities, the linear contribution enters with a factor of two. The integral from Eq. (4.4) can thus be split as follows,

$$1 = \tilde{v} \int_{\mathcal{BZ}'} \frac{d^2q}{(2\pi)^2}\, \frac{1}{2\sqrt{\mathcal{M}^2 + |\varphi_{\boldsymbol{q}}|^2}} \tag{4.7}$$

$$= \tilde{v} \int_{\mathcal{BZ}'\setminus K^\pm} \frac{d^2q}{(2\pi)^2}\, \frac{1}{2\sqrt{\mathcal{M}^2 + |\varphi_{\boldsymbol{q}}|^2}} - \tilde{v} \frac{|\mathcal{M}|}{v_f^2\,(2\pi)}, \tag{4.8}$$

where $\mathcal{BZ}'\setminus K^\pm$ denotes the Brioullin zone without the singular Dirac points. Now the required expansion around the bifurcation point $\mathcal{M} = 0$ can be performed,

$$1 = \tilde{v} \left[\int_{\mathcal{BZ}'\setminus K^\pm} \frac{d^2q}{(2\pi)^2} \frac{1}{2\,|\varphi_{\boldsymbol{q}}|} - \frac{|\mathcal{M}|}{v_f^2\,(2\pi)} - \frac{1}{4} \int_{\mathcal{BZ}'\setminus K^\pm} \frac{d^2q}{(2\pi)^2}\, \frac{\mathcal{M}^2}{|\varphi_{\boldsymbol{p}}|^3} \right], \tag{4.9}$$

the critical coupling parameter $\tilde{v}_c$ can now be identified by the inverse of the zeroth order contribution,

$$\frac{1}{\tilde{v}_c} = \int_{\mathcal{BZ}'\setminus K^\pm} \frac{d^2q}{(2\pi)^2}\, \frac{1}{2\,|\varphi_{\boldsymbol{p}}|}. \tag{4.10}$$

Dropping the second-order term yields

$$\frac{\tilde{v} - \tilde{v}_c}{\tilde{v}_c} \left(1 - \frac{|\mathcal{M}|\,\tilde{v}_c}{2\pi\,v_f^2}\right) = \frac{|\mathcal{M}|\,\tilde{v}_c}{2\pi\,v_f^2}, \tag{4.11}$$

so in leading order one finds

$$|\mathcal{M}| \sim \frac{\tilde{v} - \tilde{v}_c}{\tilde{v}_c}. \tag{4.12}$$

For the critical exponent of the semimetal-insulator transition we then obtain

$$\beta = 1\,, \tag{4.13}$$

in mean-field approximation (Eq. (4.5)).

Consequently, in contrary to a common mean-field critical exponent of $\beta = 0.5$ in two dimensions [78], that would of course also come from the second-order contribution in our calculation, we find a dissenting critical exponent due to the relativistic behavior of the band structure, directly resulting from the hexagonal lattice itself.

The basic equation from Eq. (4.3) was numerically solved by a fixed point iteration. The obtained values for the mean-field mass $\mathcal{M}$, here denoted by M_K as the standard order parameter, and different coupling values $\tilde{v}$ is shown in Fig. 4.1. Here the volume dependence is demonstrated for a huge number of lattice sizes in the range of $N = 30$ to $N = 3000$. In order to resolve the high accuracy from this large lattice sizes, the precision for the iteration process (Eq. (3.40)) was set to $p = 10^{-8}$.

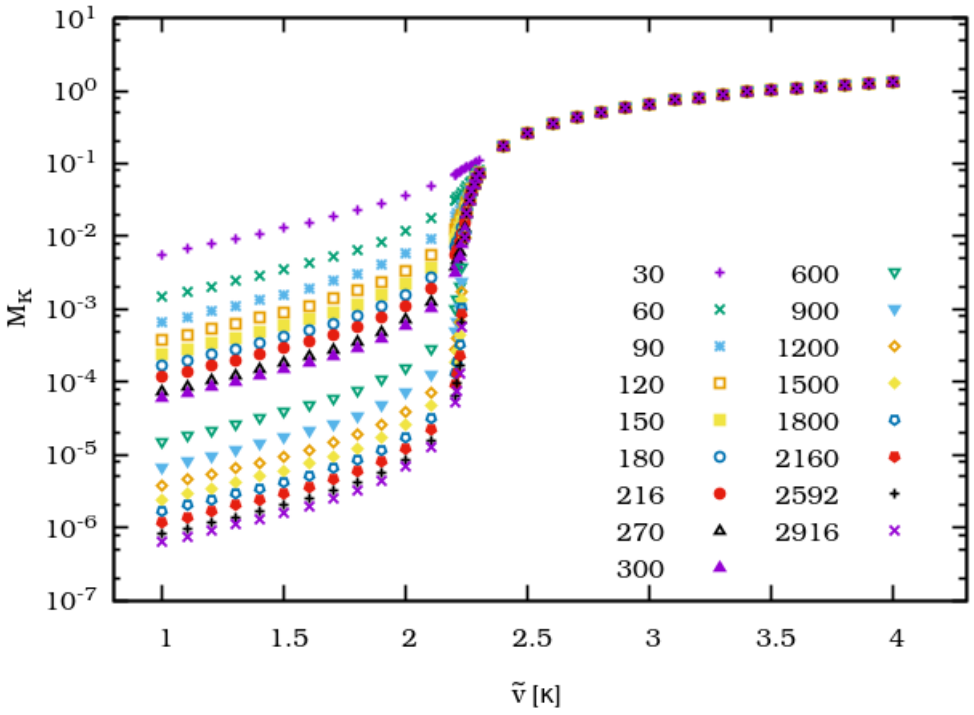

Figure 4.1: The mass renormalization, which has a constant value in momentum space, is plotted for different coupling values $\tilde{v}$ and different lattice sizes between $N = 30$ and $N = 3000$.

With the procedure from the next section the critical coupling was precisely fixed to

$$\tilde{v}_c = 2.231\ \kappa\,. \tag{4.14}$$

This value can even be extracted analytically with the help of the second of Watson's three triple integrals [81],

$$I_2 = \frac{3\,\Gamma^6(1/3)}{2^{14/3}\,\pi^4} = 0.448220394\ldots\,, \tag{4.15}$$

with $\Gamma(z)$ being the gamma function. The critical coupling is exactly determined by its inverse value [82] and nicely demonstrates the high precision of the previous FSS considerations,

$$\tilde{v}_c = I_2^{-1}\ \kappa \approx 2.2310453\ \kappa\,. \tag{4.16}$$

4.2 Finite Systems

In order to extract critical exponents out of our numerical results, we additionally have to think about the impact of finite lattices within our considerations. The partition function, connecting statistical mechanics to thermodynamics and of course quantum field theory (the latter is particularly discussed in App. E), is shortened given by

$$Z = e^{-F/T} = \mathrm{tr}\, e^{-H/T}, \tag{4.17}$$

with the temperature T, the Hamilton function H and tr denoting the trace over all degrees of freedom in the system described by H. A closer look on the partition function immediately reveals that a non-analyticity of the free energy, as described by the power laws from above (Eq. (4.5)), can not arise from a finite sum over exponentials of $-H/T$. The non-analytic behavior is only possible in relation to the thermodynamic limit, where the volume V and the number of particles N (or rather the degrees of freedom) go to infinity, while the ratio remains constant, $N/V \to \infty$. From that point of view it seems to be quite clear that critical exponents are generally hard to extract from numerical results. However, with the following procedure it is at least optimized and systematic.

4.2.1 Finite-Size Scaling

For finite systems one can extract so called finite-size scaling (FSS) laws, with the help of renormalization group approaches [78]. These FSS laws generalize the original scaling laws to finite lattice sizes and make critical exponents accessible in a systematic way. As a standard rule one can keep in mind to replace the reduced order parameter t by the length N of the system and multiply the exponent with $-1/\nu$ to obtain FSS laws out of the scaling laws defined in the thermodynamic limit.

The scaling behavior should also be valid if the size of the system N is much larger than the characteristic length scale given by the correlation length ξ. The idea then is that only these two quantities are important length scales for the macroscopic behavior of the system. For an infinite volume we have $\xi \sim |t|^{-\nu}$, so for $N \gg \xi$ we also expect $M \sim |t|^{\beta} \sim \xi^{-\beta/\nu}$ and for $N \ll \xi$, where N represents the limiting length scale one would expect $M \sim N^{-\beta/\nu}$. This motivates the ansatz [80, 83]

$$M = \xi^{-\beta/\nu}\, g(N/\xi)\,, \qquad \text{with} \quad g(x) = \begin{cases} \sim x^{-\beta/\nu}\,, & x \to 0\,, \\ \text{const.}\,, & |x| \gg 1\,, \end{cases} \tag{4.18}$$

or in a more conventional way,

$$M = N^{-\beta/\nu}\,\tilde{g}(t\,N^{1/\nu}), \qquad \text{with} \quad \tilde{g}(x) = x^{\beta}\cdot f(x^{\nu}) = \begin{cases} \text{const.}\,, & x \to 0\,, \\ \sim N^{\beta/\nu}\,t^{\beta}\,, & |x| \gg 1\,. \end{cases} \tag{4.19}$$

In order to primarily extract the critical coupling and the scaling exponent β/ν, we apply the so called crossing method [54, 84]. This method is based on the idea that for all finite sizes N the calculated curves for the order parameter scaled by $N^{\beta/\nu}$ and plotted against the reduced control parameter, should intersect at the critical point, where the correlation length diverges ($x \to 0$).

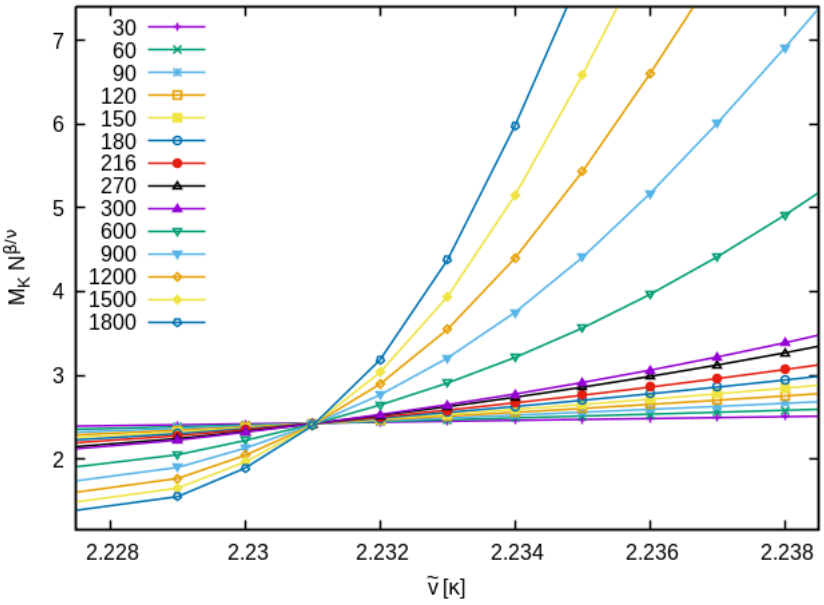

Figure 4.2: The on-site coupling in units of κ is plotted against the scaled order parameter, the critical coupling is extracted by means of the intersection point of all curves for lattice sizes $N = 30 - 1800$.

So the quotient β/ν, that exponentially scales the volume, was fixed to obtain the smallest crossing region for all volumes. For the mean-field approximation described above, we obtain a nice coincidence (see Fig. 4.2) of intersection points for $\beta/\nu = 1.0$ and found the critical coupling to be $\tilde{v}_c = 2.231\,\kappa$ as already mentioned. Consequently, within the mean-field approximation we found $\tilde{v}_c = U_c = 2.231\,\kappa$ in case of a SDW state. For the CDW case we deduce a linear dependence $V_c = (U_c + 2.231\,\kappa)/6$ in the Hubbard space spanned by U and V.

By replacing the abscissa values by the reduced order parameter scaled with $N^{1/\nu}$ all points should fall on one curve for the right choice of critical exponents (see Eq. (4.19)). An optimal data collapse (see Fig. 4.3) for this wide volume spectrum was reached for $\nu = 1$, therefore we found $\beta = \nu = 1$ what of course confirms the analytically obtained value of $\beta = 1$. The findings of this consideration or in nice accordance to previous studies of Ref. [20, 21, 55] and Ref. [20, 23] were the Hartree-Fock exponent $\beta = 1$ is validated numerically.

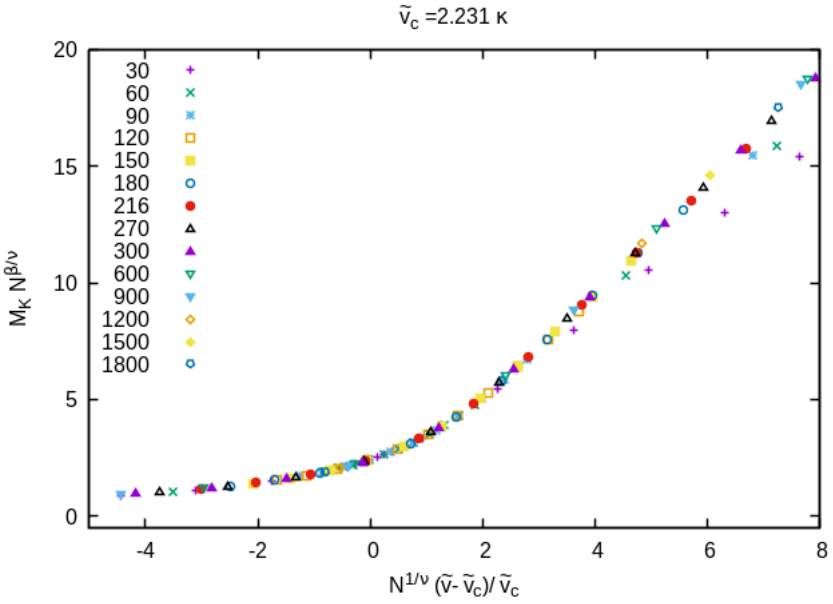

Figure 4.3: The scaled order parameter $M_K\, N^{\beta/\nu}$ is shown as a function of the reduced control parameter which is scaled by $N^{1/\nu}$. An almost perfect data collapse near the critical point was obtained for $\beta = \nu = 1$.

4.3 Hartree-Fock Approximation

In a next step, the renormalization of the band structure is taken into account within the so called Hartree-Fock approximation for the case of zero temperature and zero chemical potential ($T = \mu = 0$). The coupled system of equations, Eq. (3.30) and Eq. (3.31), is solved while the wave-function renormalization still remains trivial for zero chemical potential ($Z_{\boldsymbol{k}} = 1$). Of course, all renormalization functions are now momentum dependent.

In Fig. 4.4 the order parameter M_K, indicating a band gap opening for $M_K \neq 0$, is plotted against the on-site coupling U for an exemplary fixed nearest-neighbor interaction of $V = 0.7\ \kappa$. The number of lattice points is $N = 3000$ for the following results. The emergence of both kinds of phase transitions (CDW and SDW) can be observed for certain coupling regimes. For a dominant on-site repulsion, the SDW phase is realized whereas the CDW state is favored for a comparatively strong nearest neighbor interaction. In between there is a regime were the order parameter is zero for both phases, representing the semimetal phase (SM). Furthermore, the fit to a general power law is shown to motivate the expectation of a standard second-order phase transition.

The critical coupling pairs (U_c/V_c) were determined for both phases, the CDW and SDW case, first for fixed values of the on-site coupling U and second for fixed values of the nearest-neighbor coupling V. Here the critical value is estimated by the middle of the bin in which the order parameter reaches zero. The error is simply approximated by the discretization of the coupling parameter which was

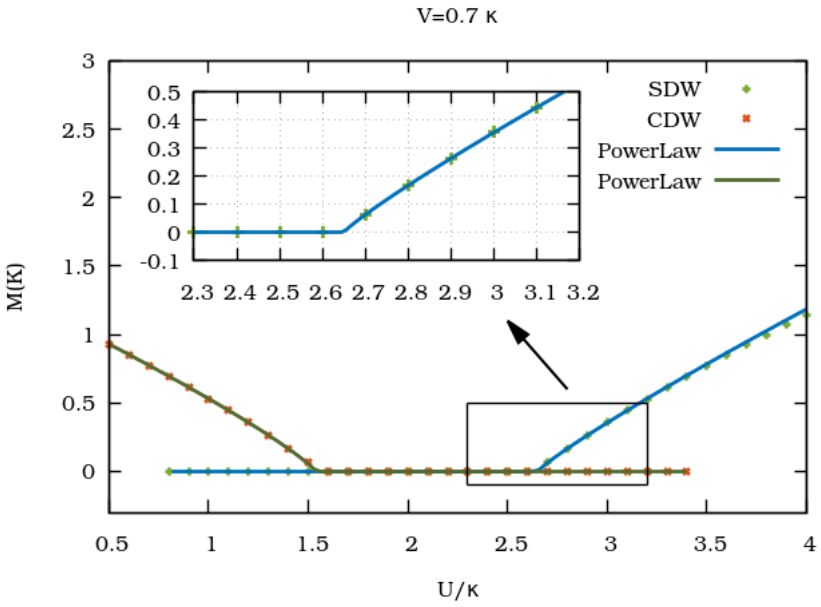

Figure 4.4: The mass renormalization function at the Dirac point K, representing the order parameter, in units of the hopping parameter κ is plotted against the on-site repulsion U also given in units of κ. The nearest neighbor interaction is fixed to $V = 0.7\,\kappa$ in this example.

used for the calculation. In the presented results, this discretization was chosen to be $\Delta U = \Delta V = 0.1\,\kappa$. For the results represented in Fig. 4.4 we would extract a critical coupling pair of $(U_c, V_c) = (2.65 \pm 0.05, 0.7 \pm 0.1)$ for the SDW case.

By representing the critical coupling pairs for both competing phases in the U-V-plane, the corresponding phase diagram is obtained and is illustrated in Fig. 4.5.

On the right hand side of the transition illustrated by blue points, an SDW state becomes possible, above the violet line a CDW state is possible and in the low coupling area indicated by SM we find the semimetal phase. The real phase transitions for which one state becomes energetically preferred over another are indicated by solid lines. The red lines are found to be second order phase transitions whereas the black line ($V = U/3$) represents the discrete transition from a CDW to an SDW state and is analytically calculated by the consideration of the free energy in the next section, Sec. 4.4. Due to the discrete redistribution of charge carriers involved within the transition between this competing phases, we expect a first-order phase transition here. The black dot therefore represents a tricrital point (TP) of the phase diagram, where three phases coexist. Here two second-order transitions convert to one first-order transition separating the two considered possibilities for an insulating phase (CDW, SDW) on the hexagonal lattice and determining the end of the semimetal phase. The violet and blue points above the tricritical point represent the spinodal lines. Here the associated phase transition becomes possible and both states are minima of the free energy, but the competing phase is still energetically preferred until the black solid line is reached.

Additionally, the results from the mean field consideration of the last chapter

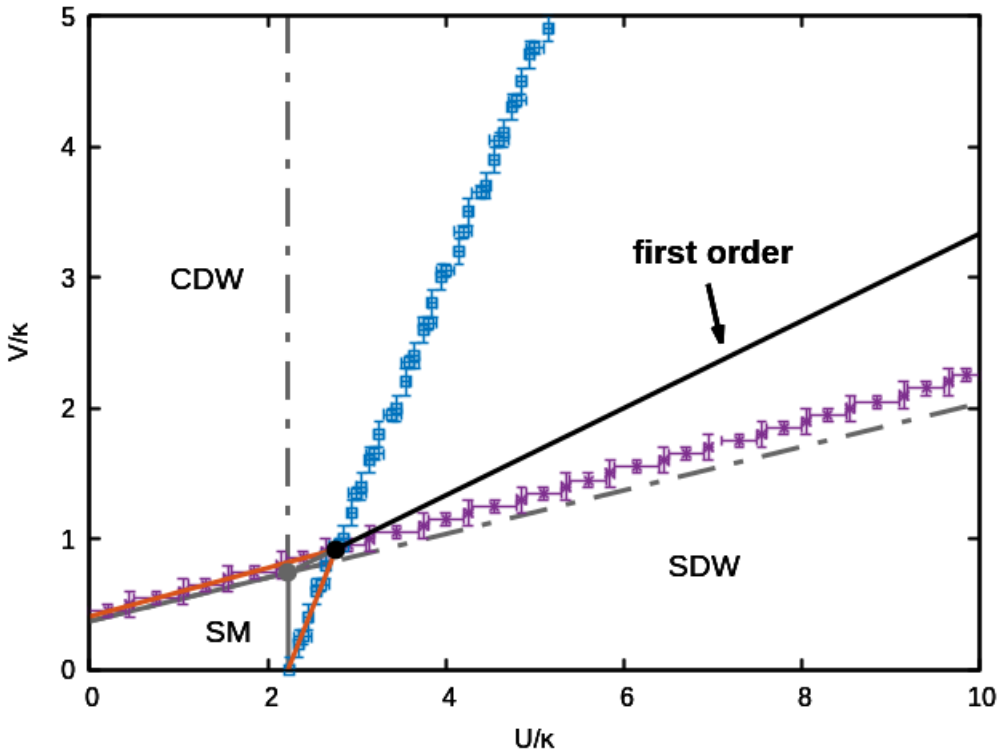

Figure 4.5: The extracted critical coupling values (U_c/V_c) are represented in the U-V-plane, in blue for the SDW constellation and in violet for the CDW constellation. Above the black tricritical point, the blue and violet lines illustrate the spinodal line of the corresponding phase transition, while the black line identifies the first-order transition between SDW and CDW state. The gray lines illustrate the analytic result from the mean field considerations of the last section.

are shown for comparison in gray. The TP is illustrated as a gray dot and the spinodals are dashed. Together with the first-order transition ($V = U/3$), this phase diagram is an exact analytical result of mean field theory. The inclusion of renormalization effects on the band structure are therefore rather small, especially for the CDW case, as one can conclude from Fig. 4.5. For the SDW case the band-structure renormalization and likewise the renormalized Fermi velocity increase with increasing nearest-neighbor interaction which causes a higher critical on-site coupling. For the phase diagram in Fig. 4.5 we found excellent agreement with the phase diagram by Araki and Semenoff [55] from 2012 calculated by using variational techniques and with Ref. [48] using the approach of functional renormalization group. Note that the calculation for $V = 0$ is identical with the before discussed results within the mean field approximation since the band structure is only dressed by at least nearest-neighbor interactions.

We additionally investigate the phase transition of the CDW case for $U = 0$ with the FSS procedure from above and find also very nice results for $\beta = \nu = 1$, see Fig. 4.6. So one can conclude that the influence of the renormalization of the

structure function is not strong enough to change the critical exponents crucially. The critical nearest-neighbor coupling was determined by the crossing method and found to be $V_c = 0.412$ within the Hartree-Fock approximation.

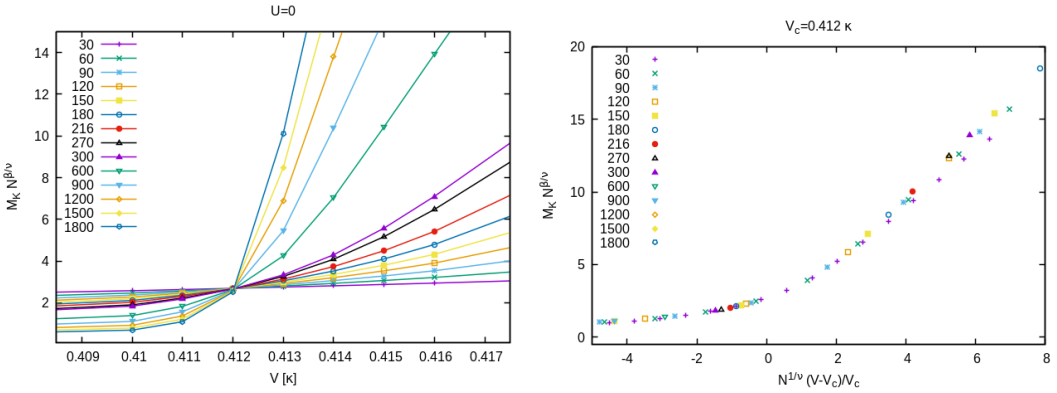

Figure 4.6: On the left hand side the scaled order parameter is represented in dependence of the nearest-neighbor coupling for various lattice sizes $N = 30 - 1800$ in the CDW state. On the right hand side an excellent data collapse is shown for $\beta = \nu = 1$.

By further investigations of the critical exponents in the whole U-V-plane we ultimately have a good evidence to deduce a second-order phase transition with $\beta = \nu = 1$ for both the CDW and SDW transition within the considered approximation.

4.4 Free Energy and nPI Effective Action

In this section the free energy of the electronic many-body system, especially concerning the difference for SDW and CDW configurations, will be investigated.

Finally, we will be able to analytically localize the first-order transition between CDW and SDW state to the $V = 1/3\,U$-line as depicted in Fig. 4.5. This result is still valid for the case of higher truncation schemes including a dressed vertex function as well as a dressed photon propagator and is therefore exact for $\mu = 0$.

The effective action Γ in QFT provides an analog to the Gibbs free energy in thermodynamics [70, 85], where the most stable state is given by the absolute minimum of the free energy. Generally, the effective action can be gained from the generating functional $Z[J, R]$ for all correlation functions, building the equivalent to the partition function of thermodynamics in Euclidean spacetime. Then, the generating functional for connected Green functions $W[J, R]$ can be extracted by the linked-cluster theorem. Eventually they are connected via the exponential, which effectively sums up all kind of combinations of the connected Feynman diagrams to produce the set of general correlation functions, generated by $Z[J, R]$,

$$\begin{aligned} Z[J,R] =& \exp(\mathrm{i}\, W[J,R]) \\ =& \int \mathcal{D}\Phi\, \exp\left(i\Big[S[\Phi] + \int_x J_a(x)\Phi_a(x) + \frac{1}{2}\int_{xy} R_{ab}(x,y)\Phi_a(x)\Phi_b(y)\Big]\right). \end{aligned} \tag{4.20}$$

Similar generating functionals $\mathcal{Z}[j]$ and $\mathcal{W}[j]$ are introduced in App. E.1, where the complete set of Dyson-Schwinger equations is deduced from the path integral formalism in Euclidean spacetime, therefore the calligraphic letters should remind the reader to use associated Euclidean conventions. For simplicity $\Phi_a(x)$ is meant to represent an arbitrary set of bosonic fields, the formalism can be straightforwardly generalized to fermionic Grassman valued fields as it was done in App. E.1 by the introduction of left and right derivatives.

Beside the standard source term, denoted by the source $J_a(x)$, a second source term has been introduced in Eq. (4.20) which is quadratic in the field variables (compare also to Eq. (E.22)). This source term can be interpreted as a spacetime dependent mass term and plays the crucial role in the derivation of the so-called 2PI effective action in comparison to the 1PI theory.

In the following, the idea of the nPI formalism should be briefly introduced with the aim of unifying the 2PI formalism and the already elaborated approach of DSE's, here we roughly follow the conventions from Ref. [86]. For a deeper understanding we want to refer to the original publications in condensed matter physics, Ref. [87–89] and the extension to relativistic QFT in Ref. [90]. For a broad overview, we recommend Ref. [86] and Ref. [91]. With the relations

$$\frac{\delta W[J,R]}{\delta J_a(x)} = \langle \Phi_a(x) \rangle_{[J,R]} = \Phi_a^c(x)\,, \tag{4.21}$$

and

$$\frac{\delta W[J,R]}{\delta R_{ab}(x,y)} = \langle \Phi_a(x)\Phi_b(y) \rangle_{[J,R]} = \frac{1}{2}(\Phi_a^c(x)\Phi_b^c(y) + D_{ab}(x,y))\,, \tag{4.22}$$

with $\Phi_a^c(x)$ being the macroscopic or classical field and $D_{ab}(x,y)$ the connected two-point function, the 2PI effective action is derived as follows.

First, in order to obtain the one-particle irreducible effective action one has to perform a Legendre transformation with respect to the source $J_a(x)$, performing another Legendre transform with respect to the source $R_{ab}(x)$ the two-particle irreducible (2PI) effective action is obtained. Hence, the effective action is not a functional only depending on the classical field variables any more, but it also directly depends on the connected two-point function,

$$\begin{aligned}
\Gamma[\Phi, D] &= W[J,R] - \int_x \frac{\delta W[J,R]}{\delta J_a(x)} J_a(x) - \int_{xy} \frac{\delta W[J,R]}{\delta R_{ab}(x,y)} R_{ab}(x,y) \\
&= W[J,R] - \int_x \Phi_a^c(x) J_a(x) - \frac{1}{2}\int_{xy} \Phi_a^c(x)\Phi_b^c(y) R_{ab}(x,y) - \frac{1}{2}\int_{xy} D_{ab}(x,y) R_{ab}(x,y) \\
&= W[J,R] - \int_x \Phi_a^c(x) J_a(x) - \frac{1}{2}\int_{xy} \Phi_a^c(x)\Phi_b^c(y) R_{ab}(x,y) - \frac{1}{2}\mathrm{Tr}[DR]\,.
\end{aligned} \tag{4.23}$$

The fundamental idea is to rewrite higher order field dependencies within explicit functional dependencies on proper n-point functions. Thus the presented 2PI effective action $\Gamma[\Phi, G]$ can be generalized to the n-particle irreducible (nPI) effective action $\Gamma[\Phi, G, V_3, V_4 \ldots, V_n]$ with an analog procedure. Here V_3 denotes the proper

three-vertex, V_4 the proper four-vertex and so forth. In order to fulfill the so called stationary conditions due to functional minimization of the effective energy [86],

$$\frac{\delta\Gamma[\Phi^c, D, V_3, V_4 \ldots, V_n]}{\delta\Phi^c} = 0\,, \quad \frac{\delta\Gamma[\Phi^c, D, V_3, V_4 \ldots, V_n]}{\delta D} = 0\,, \tag{4.24}$$

$$\frac{\delta\Gamma[\Phi^c, D, V_3, V_4 \ldots, V_n]}{\delta V_3} = 0\,, \quad \ldots\,, \tag{4.25}$$

the equations of motion for all proper n-point functions $\Phi^c, D, V_3, V_4 \ldots, V_n$ are obtained. Of course, the effective action has to be truncated in a certain manner, but the formalism itself provides a highly systematic procedure to solve problems of non-perturbative and even far-from equilibrium dynamics.

For the theory that should be investigated in this work, a loop expansion seems to be the most suitable approach. In this context, another great advantage of the 2PI formalism is the existence of a certain equivalence scheme, what means that for a certain degree in the loop expansion there exists a certain $n_{\max}$ for the corresponding nPI effective action which completely determines the dynamics of the system up to the considered approximation level (characterized by n). This hierarchy can be specified by

$$\Gamma^{1\text{loop}}[\Phi^c] = \Gamma^{1\text{loop}}[\Phi^c, D] = \Gamma^{1\text{loop}}[\Phi^c, D, V_3] = \ldots\,, \tag{4.26}$$

$$\Gamma^{2\text{loop}}[\Phi^c] \neq \Gamma^{2\text{loop}}[\Phi^c, D] = \Gamma^{2\text{loop}}[\Phi^c, D, V_3] = \ldots\,, \tag{4.27}$$

$$\Gamma^{3\text{loop}}[\Phi^c] \neq \Gamma^{3\textit{loop}}[\Phi^c, D] \neq \Gamma^{3\text{loop}}[\Phi^c, D, V_3] = \Gamma^{3\text{loop}}[\Phi^c, D, V_3, V_4] = \ldots\,, \tag{4.28}$$

which is explicitly shown in Ref. [86]. Regarding our previous truncation scheme we will concentrate on the 2-loop expansion of the 2PI effective action in the following, Eq. (4.27) of course tells us that the 3-vertex V_3 remains bare within this consideration and we only have to deal with classical vertex functions. Afterwards we will also have a look on higher loop contributions within the 3PI effective action in order to understand the next higher truncation approach.

The connection to the DSE's considered until now is given by the stationary condition for the connected Green function, which should indeed generate the DSE's. For higher n-point functions the DSE's and their equations of motion from nPI formalism do not have to coincide since the nPI formalism often provides a symmetrized version of DSE's what might be an advantage. Considering the QED_{2+1}-like theory on the hexagonal lattice, they are at least equal up to 2-loop order in which we are mainly interested in (see Ref. [86]). Starting again from Eq. (4.23), the stationary conditions

$$\frac{\delta\Gamma[\Phi^c, D]}{\Phi^c_a(x)} = -J_a(x) - \int_y R_{ab}(x,y)\Phi^c_b(y)\,, \quad \frac{\delta\Gamma[\Phi^c, D]}{D_{ab}(x,y)} = -R_{ab}(x,y)\,, \tag{4.29}$$

provide the equations of motion for Φ^c and $D_{ab}(x,y)$ for zero source terms, $J = R = 0$. Conveniently the 1-loop contribution is separated from the rest term denoted by Γ_2 as first introduced in Ref. [90],

$$\Gamma[\Phi^c, D] = S[\Phi^c] + \frac{\mathrm{i}}{2}\mathrm{Tr}\ln D^{-1} + \frac{\mathrm{i}}{2}\mathrm{Tr}D_0^{-1}D + \Gamma_2[\Phi^c, D] + \text{const.}\,, \tag{4.30}$$

where $S[\Phi^c]$ is the classical action or the zeroth order that usually vanishes in case of fermion fields. The third term results from the $-\frac{1}{2}\mathrm{Tr}[DR]$ contribution with $D^{-1} = D_0^{-1} - \mathrm{i}\,R$ within the 1-loop approximation.

In order to address the theory of interest, as described in the last chapters we additionally introduce fermion fields and use the notation established in App. B.1 in momentum space from now on. One main difference for the fermion effective action already appears in the 1-loop contribution with the evaluation of the corresponding Gaussian integrals (see App. A.2), which are given by

$$-\,\mathrm{i}\,\ln\int\mathcal{D}\phi\;\exp(iS_0^b)=-\mathrm{i}\,\ln(\det D_0^{-1})^{-\frac{1}{2}}=\frac{\mathrm{i}}{2}\mathrm{Tr}\ln D_0^{-1}\,, \tag{4.31}$$

and

$$-\,\mathrm{i}\,\ln\int\mathcal{D}\bar{\psi}\mathcal{D}\psi\;\exp(iS_0^f)=-\mathrm{i}\,\ln(\det G_0^{-1})=-\mathrm{i}\,\mathrm{Tr}\ln G_0^{-1}\,, \tag{4.32}$$

with the bare propagators D_0 and G_0 respectively, and the associated action in momentum space,

$$S_0^f=\sum\!\!\!\!\!\!\int_p\bar{\psi}(x)\,\mathrm{i}\,G_0^{-1}(p)\psi(p)\,,\qquad\text{and}\qquad S_0^b=\sum\!\!\!\!\!\!\int_p\Phi(-p)\,\mathrm{i}\,D_0^{-1}(p)\Phi(p)\,. \tag{4.33}$$

So in total, for a system containing bosons and fermions one obtains

$$\Gamma[\Phi^c,D,G]=S[\Phi^c]+\underbrace{\frac{\mathrm{i}}{2}\mathrm{Tr}\ln D^{-1}+\frac{\mathrm{i}}{2}\mathrm{Tr}D_0^{-1}D-\mathrm{i}\,\mathrm{Tr}\ln G^{-1}-\mathrm{i}\,\mathrm{Tr}G_0^{-1}G}_{1-loop\ contributions}+\Gamma_2[\Phi^c,G,D]\,, \tag{4.34}$$

where a constant term was omitted and the trace includes the sum over all frequency momentum variables as well as the trace in sublattice space usually denoted by small letters 'tr'. The stationary condition for G with

$$\frac{\delta(-\mathrm{i}\,\mathrm{Tr}\,G_0^{-1}G)}{\delta G}=-\mathrm{i}\,G_0^{-1}\,, \tag{4.35}$$

and

$$\frac{\delta(-\mathrm{i}\,\mathrm{Tr}\ln G^{-1})}{\delta G}=\frac{\mathrm{i}}{\det(G)}\begin{pmatrix}G^{BB}&-G^{BA}\\-G^{AB}&G^{AA}\end{pmatrix}=\mathrm{i}\,G^{-1} \tag{4.36}$$

then entails the fermionic DSE,

$$\frac{\delta\Gamma}{\delta G}=\mathrm{i}\,G^{-1}-\mathrm{i}\,G_0^{-1}+\frac{\delta\Gamma_2}{\delta G}=0\qquad\Longleftrightarrow\qquad G^{-1}=G_0^{-1}+\mathrm{i}\,\frac{\delta\Gamma_2}{\delta G}\,, \tag{4.37}$$

which provides the fermionic self-energy Σ as given in Eq. (3.16),

$$\frac{\delta\Gamma_2}{\delta G}=-\mathrm{i}\,\Sigma\qquad\Longleftrightarrow\qquad G^{-1}=G_0^{-1}+\Sigma. \tag{4.38}$$

In complete analogy, the equation of motion for the photon propagator is obtained to be

$$\frac{\delta\Gamma}{\delta D}=-\frac{\mathrm{i}}{2}D^{-1}+\frac{\mathrm{i}}{2}D_0^{-1}+\frac{\delta\Gamma_2}{\delta D}=0\qquad\Longleftrightarrow\qquad D^{-1}=D_0^{-1}-2\mathrm{i}\,\frac{\delta\Gamma_2}{\delta D}\,, \tag{4.39}$$

where the original DSE from Eq. (5.4) can be recovered with

$$\frac{\delta\Gamma_2}{\delta D}=\frac{\mathrm{i}}{2}\Pi\qquad\Longleftrightarrow\qquad D^{-1}=D_0^{-1}+\Pi\,. \tag{4.40}$$

To get the interesting point concerning the established theory of competing order on the hexagonal lattice, two more thoughts are necessary. First, one has to check that the effective action except the contribution from Γ_2 only depends on M_σ^2 or at least $m_\sigma \cdot M_\sigma$, which means that the difference of the Gibbs free energy for the SDW and CDW case merely results from higher loop contributions contained in Γ_2. This point can be easily verified for the 1-loop contribution, concerning the classical action the field expectation values of the Hubbard fields have to be calculated (which enter the classical action quadratically), done in App. E.2. Indeed, it turns out that the deviation in the free energy for the CDW and SDW state can only result from Γ_2. The second point is that the DSE's should not be derived from the 2PI effective action but vise versa, for that the 2-loop contribution of Γ_2 is reversely engineered from the known DSE's, discussed in the following section.

4.4.1 2PI Effective Action

From the fermion DSE, Eq. (3.16), the following 2-loop contribution could be deduced,

$$\Gamma_2[D,G] = -\frac{\mathrm{i}}{2}\left[\sum_{s,s',\sigma}\oint\!\!\!\!\!\!\sum_{k,q} G^{ss'}_{F,\sigma}(q)\, D^{ss'}(k)\,(-1)^{|s-s'|}\, G^{s's}_{F,\sigma}(k+q)\right. \tag{4.41}$$

$$\left. -\sum_{s,s'}(-1)^{|s-s'|}\, D^{0,ss'}(p=0)\sum_{\sigma,\sigma'}\oint\!\!\!\!\!\!\sum_{k} G^{s's'}_{F,\sigma}(k)\oint\!\!\!\!\!\!\sum_{q} G^{ss}_{F,\sigma'}(q)\right]. \tag{4.42}$$

This can also be compared to the fermion (Eq. (E.79)) and photon (Eq. (5.5)) DSE's derived in App. E. Diagrammatically, the 2-loop contribution for the 2PI effective action is shown in Fig. 4.7, where all possible sublattice combinations (sum over s, s') and spin contributions (σ, σ') have to be taken into account. Here we have already introduced a dressed photon propagator, which will be the topic of the next chapter.

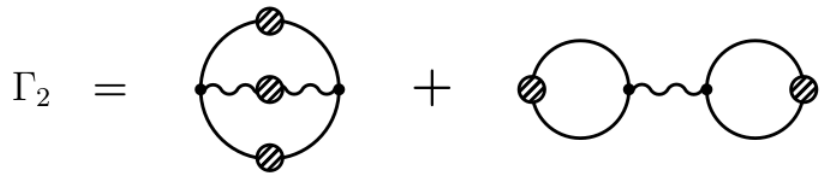

Figure 4.7: Shown is a diagrammatic representation of the two loop contribution to the 2PI effective action. The shaded dots represent dressed propagators, while the vertices remain undressed within the two loop approach.

The first contribution from Eq. (4.42) is exactly equal for the CDW and SDW case if $D^{AA}(k) = D^{BB}(k)$, what is certainly true for the mean field and Hartree-Fock approximation. The fermionic self-energy can be obtained by the derivative of Γ_2 with respect to the particular fermion propagator. In terms of Feynman diagrams this is realized by cutting the corresponding fermion line, as illustrated in Fig. 4.8.

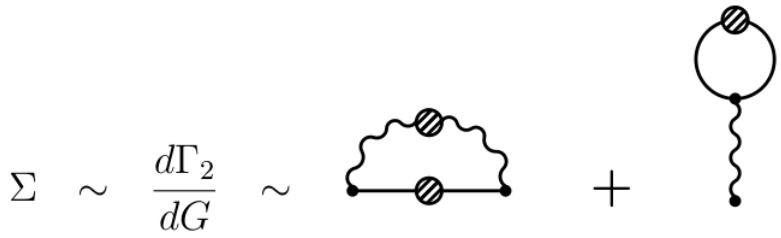

Figure 4.8: The fermion self energy, obtained by cutting one fermion line of Γ_2, is shown diagrammatically.

Similarly, the photon self-energy can be extracted and is illustrated in Fig. 4.9. The Hartree term indeed do not contribute to the photon self-energy since the derivative of Γ_2 has to be performed with respect to the dressed Green function. Moreover, disconnected diagrams do not contribute to the self-energy anyway.

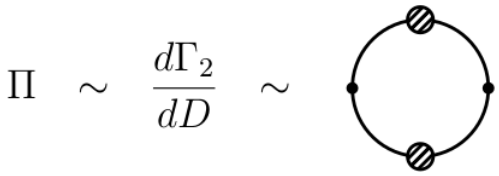

Figure 4.9: The vacuum polarization function is depicted as Feynman graph.

The fact that only the bare photon propagator enters the Hartree-term is considered in the next chapter in detail.

Furthermore, by using the symmetry requirements from Sec. 3.3 for the renormalization functions of the different spin states ($M_\uparrow = M_\downarrow$ for CDW and $M_\uparrow = -M_\downarrow$ for SDW), the effective action in 2-loop approximation can be formally calculated for both phases. Thereby, the difference is found to be

$$\begin{aligned}\Delta_2 &= \Gamma_2^{\mathrm{SDW}}[D,G] - \Gamma_2^{\mathrm{CDW}}[D,G] \qquad (4.43)\\ &= \mathrm{i}\,(D^{0,AA}_{p=0} - D^{0,AB}_{p=0}) \sum\!\!\!\!\!\!\int_k \frac{\mathrm{i}\,M_{\mathrm{cdw},k}}{(k^0\,Z_k)^2 - \Omega^2_{\mathrm{cdw},k} + \mathrm{i}\,\epsilon} \sum\!\!\!\!\!\!\int_q \frac{\mathrm{i}\,M_{\mathrm{cdw},q}}{(k^0\,Z_q)^2 - \Omega^2_{\mathrm{cdw},q} + \mathrm{i}\,\epsilon}\,, \qquad (4.44)\end{aligned}$$

for $\mu_\uparrow = \mu_\downarrow = 0$. Here the symmetry of the potential for zero frequency and zero momentum transfer,

$$D^{0,AA}_{p=0} = D^{0,BB}_{p=0} \qquad \text{and} \qquad D^{0,AB}_{p=0} = D^{0,BA}_{p=0}\,, \qquad (4.45)$$

was additionally used. With the bare photon interaction within the extended Hubbard model from Eq. (3.35) one finds

$$\Delta_2^{\mathrm{Hubbard}} = -\,(U - 3V) \sum\!\!\!\!\!\!\int_k \frac{\mathrm{i}\,M_{\mathrm{cdw},k}}{(k^0\,Z_k)^2 - \Omega^2_{\mathrm{cdw},k} + \mathrm{i}\,\epsilon} \sum\!\!\!\!\!\!\int_q \frac{\mathrm{i}\,M_{\mathrm{cdw},q}}{(q^0\,Z_k)^2 - \Omega^2_{\mathrm{cdw},q} + \mathrm{i}\,\epsilon}\,, \qquad (4.46)$$

what means that the expected first-order transition between the SDW and the CDW state in the coupling plane spanned by U and V can be analytically determined to the line $V = 1/3\,U$. This is also valid in the case of a screened or frequency-dependent photon propagator, as long as $D^{AA}(k) = D^{BB}(k)$ or equivalently $\Pi^{AA}(k) = \Pi^{BB}(k)$, as will be shown in the next chapter.

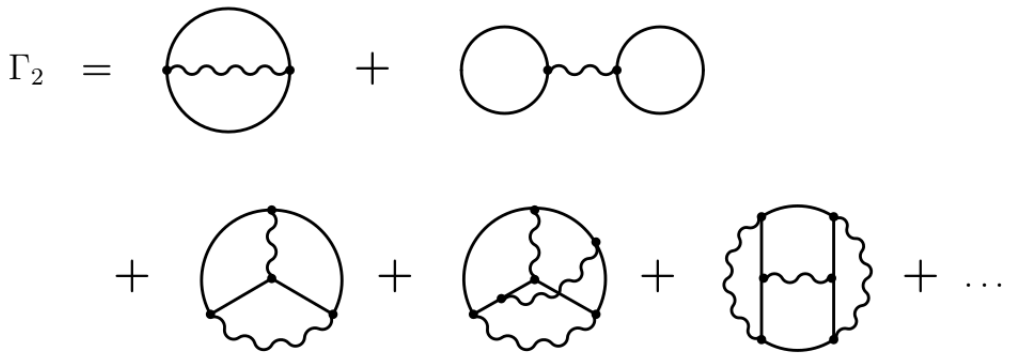

Figure 4.10: Higher loop contributions to the effective action are shown. Due to a better visibility dressed propagator and vertices are not indicated.

Higher contributions to the effective action, such as 3-loop and 4-loop, representing the 3PI structure [92], are illustrated in Fig. 4.10. Diagrammatically, it can be easily reconstructed that these contributions are catched by a vertex dressing as illustrated in Fig. 4.11.

Figure 4.11: The DSE for the vertex function is diagrammatically represented and can be deduced from the higher loop contributions of the effective action as given in Fig. 4.10.

The inclusion of such a vertex dressing would make the considered theory (only involving 3-vertices V_3) exact due to the hierarchy scheme from Eq. (4.28).

5

The Static Approximation

An important effect with high influence on the behavior of fermionic many particle systems, especially well-known in solid state physics, is the screening effect within charge distributions. In this chapter the screening of electrons from the π-bands itself will be taken into account via appropriate Dyson-Schwinger equations for the photon propagator. To be more precise, only the zeroth component of the photon field is taken into account since electromagnetic retardation effects are suppressed by a factor of about ~ 300, resulting from the ratio of Fermi velocity and the speed of light.

5.1 Dyson-Schwinger Equations

In order to neatly derive the set of DSE's for the described strongly coupled electronic system, the more descriptive formulation of second quantization is completely transferred into the path integral formulation in Euclidean spacetime as pointed out in App. E.1. Since the interaction matrix from Eq. (3.35) is negative definite for the regime

$$V > U/3 \,, \tag{5.1}$$

lattice calculations become extremely complicated [54] or even impossible. This is one good reason to establish DSE's also for this region. To make sure that we obtain valid DSE's in this region with an existing and well-defined generating functional for the corresponding Green functions, the interaction is separated into two parts,

$$\mathcal{H}_{tp} = \underbrace{\frac{1}{2} \sum_{x,y,\sigma,\sigma'} : c^\dagger_{x,\sigma} c_{x,\sigma} \, V^+_{xy} \, c^\dagger_{y,\sigma'} c_{y,\sigma'} :}_{\geq 0} \underbrace{- \frac{1}{2} \sum_{x,y,\sigma,\sigma'} : c^\dagger_{x,\sigma} c_{x,\sigma} \, (-V^-_{xy}) \, c^\dagger_{y,\sigma'} c_{y,\sigma'} :}_{\geq 0} , \tag{5.2}$$

with V^+ and V^- indicating the positive semidefinite and negative semidefinite part, respectively. The related bosonic fields which were introduced by a Hubbard-Stratonovich transformation (HST, see App. A.2), which is different for the positive and negative semidefinite part respectively, join the effective action with different signs. Consequently, the DSE's might be different as well.

For this reason, the corresponding DSE's were concretely derived in App. E and they were found to really be the same, independent of starting with a positive or negative semidefinite interaction matrix. They hence can again be summarized within one interaction matrix, $V = V^- + V^+$, without hesitation and the problem of singularities known from lattice calculations is shown to be nonexistent in the applied Dyson-Schwinger formalism.

The corresponding propagator of the required bosonic field from the HST is simply identified with the photon propagator D of the established theory where its bare counterpart is determined by the interaction potential V via Eq. (3.35). The fermionic DSE's (Eq. (E.79)) were proven to be quite similar to the equations obtained from the Heisenberg formalism (compare to Eq. (3.16)),

$$G^{-1}_{F,\sigma}(k) = G^0_{F,\sigma}(k)^{-1} + \frac{1}{N^2}\int \frac{dq^0}{2\pi} \sum_{\boldsymbol{q},u,u'} D^{u'u}(q)\, \Gamma^0[q, k+q]\, \Gamma^u\, G_{F,\sigma}(k+q)\, \gamma^0 \Gamma^{u'}$$
$$- \frac{1}{N^2}\int \frac{dq^0}{2\pi} \sum_{\boldsymbol{q},u,u',\sigma'} (-1)^{|u-u'|}\, \mathrm{tr}\left(D^{0,uu'}(q=0)\, \Gamma^u\, G_{F,\sigma'}(q)\, \Gamma^u\right) \Gamma^{u'}\,, \quad (5.3)$$

with the difference that also a dressed photon propagator D and vertex function is considered. Additionally we deal with three vectors in Minskowski spacetime as introduced in App. B.1 from now on. Here we have also introduced the notation of the vertex function Γ^0 which is not completely equivalent to the proper three-point function from Eq. (E.46) due to some prefactors. For simplicity, Γ^0 labels the part of the fermion-photon vertex that is given by γ^0 for the tree level (tl) vertex $\Gamma^0_{tl}[q, q+p] = \gamma^0$ (see App. E).

In Fig. 5.1 the Fermion DSE's are illustrated in terms of Feynman diagrams where we have an additional sum over the sublattice index s and the spin degree of freedom denoted by σ'.

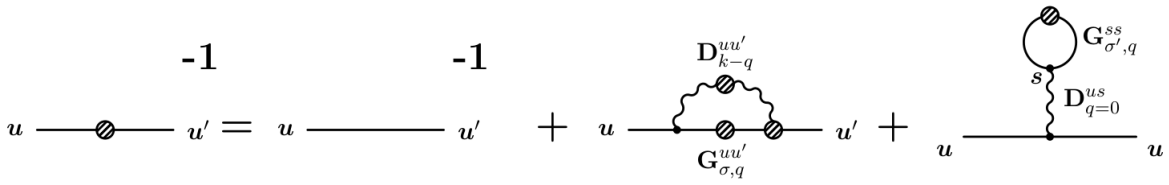

Figure 5.1: The Fermion DSE from Eq. (5.3) as derived in App. E is illustrated by Feynman diagrams. Here u, u' and s denote sublattice indices, while σ and σ' label the spin index, a sum over s and σ' is implicitly included.

In this context it is important to note that the Hartree-term still enters the DSE with the bare photon propagator D^0 and the bare photon-fermion vertex (see App. E.2). This might be counterintuitive, but expresses the fact that the original background field is not dynamically adjusted to the dressed photon field what

would lead to an overestimation of the influence of the Hartree-term. The associated self energy for the photon field can be represented by the following Feynman graph (Fig. 5.2) and is also derived in App. E.2.

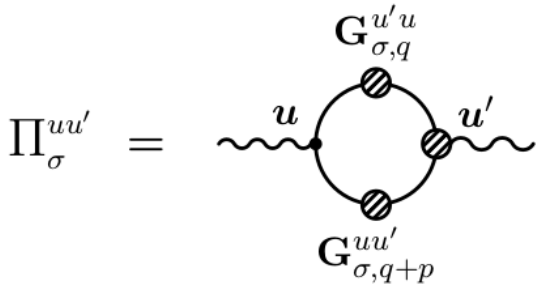

Figure 5.2: The photon self-energy as given in Eq. (5.5) is diagrammatically depicted with sublattice indices u and u' and is determined by certain combinations of the fermion propagator.

Here u and u' again denote sublattice indices and the total self-energy is of course given by the sum over all fermion flavors indicated by σ. The self-energy is equivalently represented by a matrix in sublattice space.

In this context, one has to pay attention to the single sublattice entries of the self-energy matrix which do not result from a matrix multiplication of the fermion propagators, but rather from the multiplication of single particular entries as illustrated in Fig. 5.2. The associated DSE for the propagator of the introduced interaction $D^0(p) = \mathrm{i}\, V(p)$ takes the insertion of this vacuum polarization in infinite succession into account, illustrated in Fig. 5.3.

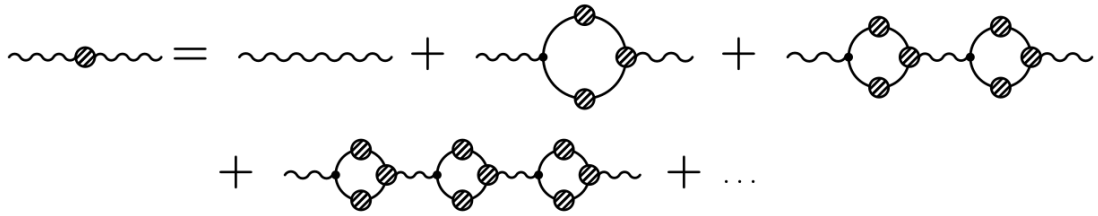

Figure 5.3: The DSE for the photon propagator, which effectively takes one-loop screening effects of the π-electrons into account is shown with a dressed fermion propagator as well as a dressed fermion-photon vertex.

Analytically one finds a geometric series in sublattice space,

$$D(k) = D^0(k) - D^0(k)\Pi(k)D^0(k) + \cdots = D^0(k)\left(\mathbb{1} + \Pi(k)D^0(k)\right)^{-1}, \qquad (5.4)$$

so the fermion DSE can be rewritten in its common form as

$$D^{uu'}(k)^{-1} = D^{0,uu'}(k)^{-1} \underbrace{-\frac{1}{N^2}\int \frac{dq^0}{2\pi} \sum_{\boldsymbol{q},\sigma} \operatorname{tr}\left(G_{F,\sigma}(q)\,\Gamma^0[q,k+q]\,\Gamma^u\,G_{F,\sigma}(k+q)\gamma^0\Gamma^{u'}\right)}_{\Pi(k)} . \tag{5.5}$$

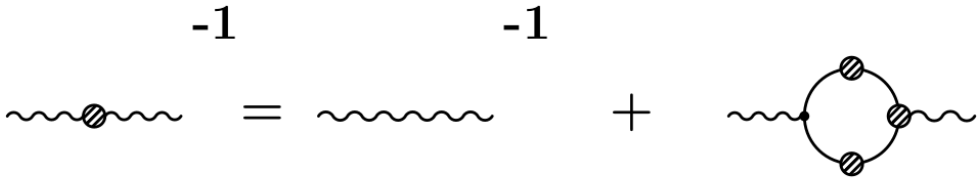

Figure 5.4: The photon DSE is represented diagrammatically, with the self-energy particularly depicted in Fig. 5.2. The shaded dots again indicated dressed propagators and vertices.

In terms of Feynman diagrams, the photon DSE is illustrated in Fig. 5.4. This kind of dressing for the photon propagator considers the mutual screening of the π-band electrons of the hexagonal lattice of graphene. It does not take the screening effects from inner electron shells into account, which could have an additional influence for the investigation of graphene.

In solid state physics this particle-hole polarization function with $\Gamma^0 = \gamma^0$ and $G_F = G_F^0$ follows from a quantum mechanical consideration within a random-phase approximation (RPA) [93] and is commonly called the *Lindhard function* of the considered electronic many particle system [60, 94, 95]. In analogy to that we also refer to $\Pi(k)$ as Lindhard function in the following.

5.2 Static Lindhard Screening

In this section, the screening effects as introduced in the last chapter will now be taken into account within a static approximation. In the framework of this common ansatz, only the zero frequency contribution of the Lindhard function is considered,

$$\chi(\boldsymbol{k}) = \Pi(k^0 = 0, \boldsymbol{k})\,, \tag{5.6}$$

and the interaction therefore remains frequency independent, which ensures a trivial wave-function renormalization for zero chemical potential,

$$Z_\sigma(k) = 1\,. \tag{5.7}$$

In order to complete the set of DSE's, we would have to consider another DSE for the fermion-photon vertex to close the obtained set of Dyson-Schwinger equations (see Fig. 4.11). But the Ward-Takahashi identity still determines the vertex function to its tree level counterpart, $\Gamma^0 = \gamma^0$, for zero chemical potential in the static

approximation. With the tree level vertex, the renormalization functions from the ansatz of Eq. (3.18) read

$$\begin{aligned} M_\sigma(k) =& m_\sigma + \frac{1}{2\,N^2}\int \frac{dq^0}{2\pi}\sum_{\boldsymbol{q}}\Bigg[-\mathrm{i}\,(D_q^{AA}+D_q^{BB})\frac{\mathrm{i}\,M_{\sigma,k+q}}{(q^0+\mu^\sigma)^2 Z_{\sigma,k+q}^2-\Omega_{\sigma,k+q}^2} \\ & -2\,\mathrm{i}\,(D_{q=0}^{0,AB}-D_{q=0}^{0,AA})\sum_{\sigma'}\frac{\mathrm{i}\,M_{\sigma',q}}{(q^0+\mu^{\sigma'})^2 Z_{\sigma',q}^2-\Omega_{\sigma',q}^2}\Bigg]\,, \end{aligned} \tag{5.8}$$

$$\Phi_\sigma(k) = \varphi_{\boldsymbol{k}} + \frac{1}{N^2}\int\frac{dq^0}{2\pi}\sum_{\boldsymbol{q}}(-\mathrm{i}\,D_q^{BA})\frac{\mathrm{i}\,\Phi_{\sigma,k+q}}{(q^0+\mu^\sigma)^2 Z_{\sigma,k+q}^2-\Omega_{\sigma,k+q}^2}\,, \tag{5.9}$$

$$\Phi_\sigma^*(k) = \varphi_{\boldsymbol{k}}^* + \frac{1}{N^2}\int\frac{dq^0}{2\pi}\sum_{\boldsymbol{q}}(-\mathrm{i}\,D_q^{AB})\frac{\mathrm{i}\,\Phi_{\sigma,k+q}^*}{(q^0+\mu^\sigma)^2 Z_{\sigma,k+q}^2-\Omega_{\sigma,k+q}^2}\,, \tag{5.10}$$

with $D_{q=0}^{0,AB} = D_{q=0}^{0,BA}$ and $D_{q=0}^{0,AA} = D_{q=0}^{0,BB}$ for the bare instantaneous interaction.

For the static approximation, i.e. for the assumption of a frequency-independent photon propagator within the presented truncation scheme, one finds $D^{AA} = D^{BB}$ as well. Consequently, the equations for M can be further simplified and the frequency integral can be evaluated analytically (see App. D.1), what finally results in the following equations for arbitrary temperature $\beta = 1/T$ and chemical potential μ_σ,

$$\begin{aligned} M_{\sigma,\boldsymbol{k}} =& m_\sigma + \frac{1}{N^2}\sum_{\boldsymbol{q}}(-\mathrm{i}\,D_{\boldsymbol{q}}^{AA})\frac{M_{\sigma,\boldsymbol{k}+\boldsymbol{q}}}{4\,\Omega_{\sigma,\boldsymbol{k}+\boldsymbol{q}}}\Big[\tanh\Big(\frac{\Omega_{\sigma,\boldsymbol{k}+\boldsymbol{q}}-\mu^\sigma}{2}\beta\Big)+\tanh\Big(\frac{\Omega_{\sigma,\boldsymbol{k}+\boldsymbol{q}}+\mu^\sigma}{2}\beta\Big)\Big] \\ & -\frac{\mathrm{i}\,(D_{q=0}^{AB}-D_{q=0}^{AA})}{N^2}\sum_{\boldsymbol{p},\sigma'}\frac{M_{\sigma',\boldsymbol{p}}}{4\,\Omega_{\sigma',\boldsymbol{p}}\,Z_{\sigma',\boldsymbol{p}}^2}\Big[\tanh\Big(\frac{\Omega_{\sigma',\boldsymbol{p}}-\mu^\sigma}{2}\beta\Big)+\tanh\Big(\frac{\Omega_{\sigma',\boldsymbol{p}}+\mu^\sigma}{2}\beta\Big)\Big], \\ \phi_{\sigma,\boldsymbol{k}} =& \phi_{\sigma,\boldsymbol{k}} + \frac{1}{N^2}\sum_{\boldsymbol{q}}(-\mathrm{i}\,D_{\boldsymbol{q}}^{BA})\frac{\phi_{\sigma,\boldsymbol{k}+\boldsymbol{q}}}{4\,\Omega_{\sigma,\boldsymbol{k}+\boldsymbol{q}}}\Big[\tanh\Big(\frac{\Omega_{\sigma,\boldsymbol{k}+\boldsymbol{q}}-\mu^\sigma}{2}\beta\Big)+\tanh\Big(\frac{\Omega_{\sigma,\boldsymbol{k}+\boldsymbol{q}}+\mu^\sigma}{2}\beta\Big)\Big], \\ \phi_{\sigma,\boldsymbol{k}}^* =& \phi_{\sigma,\boldsymbol{k}}^* + \frac{1}{N^2}\sum_{\boldsymbol{q}}(-\mathrm{i}\,D_{\boldsymbol{q}}^{AB})\frac{\phi_{\sigma,\boldsymbol{k}+\boldsymbol{q}}^*}{4\,\Omega_{\sigma,\boldsymbol{k}+\boldsymbol{q}}}\Big[\tanh\Big(\frac{\Omega_{\sigma,\boldsymbol{k}+\boldsymbol{q}}-\mu^\sigma}{2}\beta\Big)+\tanh\Big(\frac{\Omega_{\sigma,\boldsymbol{k}+\boldsymbol{q}}+\mu^\sigma}{2}\beta\Big)\Big]. \end{aligned} \tag{5.11}$$

Here the bold symbols again denote discrete vectors in momentum space and the μ-dependence is just kept for completeness.

On the basis of frequency independent renormalization functions, the frequency integral of the vacuum polarization can also be evaluated analytically in the imaginary-time formalism by using Eq. (D.13). The sum over the Matsubara frequencies $q_0 = i(2n+1)\pi T$ with fermionic boundary conditions in the polarization loop is therefore evaluated for discrete bosonic frequencies $\omega = i2\pi mT$ (with integer m, n). After an analytic back-continuation to real frequencies ω, where we have introduced retarded boundary conditions (indicated by R), the sublattice components of the Lindhard susceptibility for the honeycomb lattice are finally given by

$$\begin{aligned} \Pi^{AA,R}(\omega,\boldsymbol{p}) =& \frac{\mathrm{i}}{4\,N^2}\sum_{\sigma,\boldsymbol{q}}\sum_{s,s'=\pm}(1+sM_{\sigma,\boldsymbol{q}}/\Omega_{\sigma,\boldsymbol{q}})(1+s'M_{\sigma,\boldsymbol{q}+\boldsymbol{p}}/\Omega_{\sigma,\boldsymbol{q}+\boldsymbol{p}}) \\ & \times\frac{\rho_f(\beta(s'\Omega_{\sigma,\boldsymbol{q}+\boldsymbol{p}}-\mu^\sigma))-\rho_f(\beta(s\Omega_{\sigma,\boldsymbol{q}}-\mu^\sigma))}{-s\Omega_{\sigma,\boldsymbol{q}}+s'\Omega_{\sigma,\boldsymbol{q}+\boldsymbol{p}}-\omega-\mathrm{i}\,\epsilon}, \end{aligned} \tag{5.12}$$

$$\Pi^{BB,R}(\omega,\boldsymbol{p}) = \frac{\mathrm{i}}{4\,N^2}\sum_{\sigma,\boldsymbol{q}}\sum_{s,s'=\pm}(1-sM_{\sigma,\boldsymbol{q}}/\Omega_{\sigma,\boldsymbol{q}})(1-s'M_{\sigma,\boldsymbol{q}+\boldsymbol{p}}/\Omega_{\sigma,\boldsymbol{q}+\boldsymbol{p}}) \times \frac{\rho_f(\beta(s'\Omega_{\sigma,\boldsymbol{q}+\boldsymbol{p}}-\mu^\sigma))-\rho_f(\beta(s\Omega_{\sigma,\boldsymbol{q}}-\mu^\sigma))}{-s\Omega_{\sigma,\boldsymbol{q}}+s'\Omega_{\sigma,\boldsymbol{q}+\boldsymbol{p}}-\omega-\mathrm{i}\,\epsilon}, \tag{5.13}$$

$$\Pi^{AB,R}(\omega,\boldsymbol{p}) = \frac{\mathrm{i}}{4\,N^2}\sum_{\sigma,\boldsymbol{q}}\sum_{s,s'=\pm}\frac{\kappa^2\phi^*_{\sigma,\boldsymbol{q}}\phi_{\sigma,\boldsymbol{p}+\boldsymbol{q}}}{\Omega_{\sigma,\boldsymbol{q}}\Omega_{\sigma,\boldsymbol{p}+\boldsymbol{q}}}(s\cdot s') \frac{\rho_f(\beta(s'\Omega_{\sigma,\boldsymbol{q}+\boldsymbol{p}}-\mu^\sigma))-\rho_f(\beta(s\Omega_{\sigma,\boldsymbol{q}}-\mu^\sigma))}{-s\Omega_{\sigma,\boldsymbol{q}}+s'\Omega_{\sigma,\boldsymbol{q}+\boldsymbol{p}}-\omega-\mathrm{i}\,\epsilon}, \tag{5.14}$$

$$\Pi^{BA,R}(\omega,\boldsymbol{p}) = \frac{\mathrm{i}}{4\,N^2}\sum_{\sigma,\boldsymbol{q}}\sum_{s,s'=\pm}\frac{\kappa^2\phi_{\sigma,\boldsymbol{q}}\phi^*_{\sigma,\boldsymbol{p}+\boldsymbol{q}}}{\Omega_{\sigma,\boldsymbol{q}}\Omega_{\sigma,\boldsymbol{p}+\boldsymbol{q}}}(s\cdot s') \frac{\rho_f(\beta(s'\Omega_{\sigma,\boldsymbol{q}+\boldsymbol{p}}-\mu^\sigma))-\rho_f(\beta(s\Omega_{\sigma,\boldsymbol{q}}-\mu^\sigma))}{-s\Omega_{\sigma,\boldsymbol{q}}+s'\Omega_{\sigma,\boldsymbol{q}+\boldsymbol{p}}-\omega-\mathrm{i}\,\epsilon}, \tag{5.15}$$

with the Fermi-Dirac distribution $\rho_f(x) = 1/(e^x+1)$. The classical density-density correlation for the honeycomb lattice, namely the Lindhard function, can be inferred by taking the sum of all sublattice contributions and replacing the dressed renormalization functions by its bare values with $m_\sigma = 0$ (indicated by the index 0),

$$\Pi^R_0(\omega,\boldsymbol{p}) = \sum_{uu'}\Pi_0^{uu',R}(\omega,\boldsymbol{p})\,, \tag{5.16}$$

which exactly agrees with the results from T. Stauber (2010) in Ref. [96] (see also Ref. [97]). The contributions with $s = s'$ are related to intraband transitions $\Pi^R_{0,+}(\omega,\boldsymbol{p})$, i.e. excitations of fermionic particles and holes within the same energy band, whereas contributions with $s = -s'$ analogically involve interband transitions $\Pi^R_{0,-}(\omega,\boldsymbol{p})$ between both bands. This can be easily retraced from the partial fraction expansion of the fermion propagator (note the imaginary frequency argument),

$$G_{F,\sigma}(\mathrm{i}\,\omega,\boldsymbol{p}) = \frac{1}{2}\sum_{s=\pm}\frac{\gamma_0+(M_{\sigma,\boldsymbol{p}}+\kappa\,\phi_{\sigma,\boldsymbol{p}}\gamma^+ + \kappa\,\phi^*_{\sigma,\boldsymbol{p}}\gamma^-)s/\Omega_{\sigma,\boldsymbol{p}}}{(\omega-\mathrm{i}\,\mu_\sigma)+\mathrm{i}\,s\,\Omega_{\sigma,\boldsymbol{p}}}\,, \tag{5.17}$$

where s identifies the two different energy bands.

The imaginary part of Π^R_0 vanishes in the static limit as long as the spatial momentum is nonzero. Then, the usual Thomas-Fermi susceptibility is in turn defined as the subsequent long-wavelength limit $\chi_{tf} = \lim_{\boldsymbol{p}\to 0}\chi(\vec{p})$, and the order of limits is of course important here.

In the long-wavelength limit, on the other hand, it is easy to see that only interband transitions survive and that these are given by the density of states per 'volume' (area of sample) at the Fermi 'surface' (contour) [96],

$$\begin{aligned}\chi_{tf} &= \lim_{\boldsymbol{p}\to 0}\Pi^R_0(\omega=0,\boldsymbol{p}) = \lim_{\boldsymbol{p}\to 0}\mathrm{Re}\,\Pi^R_{0,+}(\omega=0,\boldsymbol{p}) \\ &= \int_{\mathrm{BZ}}\frac{d^2q}{(2\pi)^2}\,\delta(\varepsilon_{\boldsymbol{q}}-|\mu|) = \rho(\mu)\,.\end{aligned} \tag{5.18}$$

The density of states was first derived for transverse vibrations of a hexagonal lattice by Hobson and Nierenberg in 1953 [12]. They found logarithmic divergences near the saddles of the energy bands, i.e., the van Hove singularities, as well as the zeros now identified with the Dirac points.

In a first approach we are interested in the semimetal-insulator transition for zero temperature, $T = 0$, and zero chemical potential, $\mu_\sigma = 0$. Static Lindhard screening χ is furthermore described by the zeroth frequency contribution of the retarded vacuum polarization

$$\chi^{uu'}(\boldsymbol{p}) = \Pi^{uu',R}(\omega = 0, \boldsymbol{p})\,, \tag{5.19}$$

where u and u' denote sublattice indices. In summary, for zero temperature and zero chemical potential ($T = \mu_\sigma = 0$) the coupled DSE's reduce to the following equations

$$M_{\sigma,\boldsymbol{k}} = m_\sigma + \frac{1}{N^2}\left(\sum_{\boldsymbol{q}}(-\mathrm{i}\, D_{\boldsymbol{q}}^{AA})\frac{M_{\sigma,\boldsymbol{k}+\boldsymbol{q}}}{2\Omega_{\sigma,\boldsymbol{k}+\boldsymbol{q}}} - \mathrm{i}\,(D_0^{AB} - D_0^{AA})\sum_{\boldsymbol{p},\sigma'}\frac{M_{\sigma',\boldsymbol{p}}}{2\Omega_{\sigma',\boldsymbol{p}}}\right), \tag{5.20}$$

$$\phi_{\sigma,\boldsymbol{k}} = \varphi_{\sigma,\boldsymbol{k}} + \frac{1}{N^2}\sum_{\boldsymbol{q}}(-\mathrm{i}\, D_{\boldsymbol{q}}^{BA})\frac{\phi_{\sigma,\boldsymbol{k}+\boldsymbol{q}}}{2\,\Omega_{\sigma,\boldsymbol{k}+\boldsymbol{q}}}, \tag{5.21}$$

$$\phi^*_{\sigma,\boldsymbol{k}} = \varphi^*_{\sigma,\boldsymbol{k}} + \frac{1}{N^2}\sum_{\boldsymbol{q}}(-\mathrm{i}\, D_{\boldsymbol{q}}^{AB})\frac{\phi^*_{\sigma,\boldsymbol{k}+\boldsymbol{q}}}{2\,\Omega_{\sigma,\boldsymbol{k}+\boldsymbol{q}}}, \tag{5.22}$$

$$Z_{\sigma,\boldsymbol{k}} = 1, \tag{5.23}$$

$$\chi_{\boldsymbol{p}}^{AA} = \frac{1}{2\,N^2}\sum_{\sigma,\boldsymbol{q}}\left(1 - \frac{M_{\sigma,\boldsymbol{q}}M_{\sigma,\boldsymbol{q}+\boldsymbol{p}}}{\Omega_{\sigma,\boldsymbol{q}}\Omega_{\sigma,\boldsymbol{q}+\boldsymbol{p}}}\right)\,\frac{1}{\Omega_{\sigma,\boldsymbol{q}} + \Omega_{\sigma,\boldsymbol{q}+\boldsymbol{p}}} = \chi_{\boldsymbol{p}}^{BB}, \tag{5.24}$$

$$\chi_{\boldsymbol{p}}^{AB} = -\frac{1}{2\,N^2}\sum_{\sigma,\boldsymbol{q}}\frac{\Phi^*_{\sigma,\boldsymbol{q}}\,\Phi_{\sigma,\boldsymbol{q}+\boldsymbol{p}}}{\Omega_{\sigma,\boldsymbol{q}}\,\Omega_{\sigma,\boldsymbol{q}+\boldsymbol{p}}}\,\frac{1}{\Omega_{\sigma,\boldsymbol{q}} + \Omega_{\sigma,\boldsymbol{q}+\boldsymbol{p}}} = \chi_{\boldsymbol{p}}^{BA*}, \tag{5.25}$$

which build a closed set of non-linear integral equations. In order to obtain the photon propagator and not its inverse as required by the fermionic DSE's, the photon DSE is inverted in two-dimensional sublattice space. With the established symmetries of the bare interaction matrix from Eq. (3.10)-Eq. (3.12),

$$V_{\boldsymbol{p}}^{AA} = V_{\boldsymbol{p}}^{BB} = V_{-\boldsymbol{p}}^{AA} \in \mathbb{R}\,, \qquad \text{and} \qquad V_{\boldsymbol{p}}^{AB} = V_{\boldsymbol{p}}^{BA*} = V_{-\boldsymbol{p}}^{BA}\,, \tag{5.26}$$

the inverse matrix is given by

$$(\mathbb{1} + \chi_{\boldsymbol{p}}\, D_{\boldsymbol{p}}^0)^{-1} = \frac{1}{|x|^2 - |y|^2}\begin{pmatrix} x^* & -y \\ -y^* & x \end{pmatrix}, \tag{5.27}$$

with

$$x = 1 + \chi_{\boldsymbol{p}}^{AA} D_{\boldsymbol{p}}^{0,AA} + \chi_{\boldsymbol{p}}^{AB} D_{\boldsymbol{p}}^{0,BA}, \tag{5.28}$$

$$y = \chi_{\boldsymbol{p}}^{AA} D_{\boldsymbol{p}}^{0,AB} + \chi_{\boldsymbol{p}}^{AB} D_{\boldsymbol{p}}^{0,AA}. \tag{5.29}$$

So the screened propagator can be written as

$$D_{\boldsymbol{p}}^{uu'} = \frac{1}{|x|^2 - |y|^2}\begin{pmatrix} D_{\boldsymbol{p}}^{0,AA}x^* - D_{\boldsymbol{p}}^{0,AB}y^* & D_{\boldsymbol{p}}^{0,AB}x - D_{\boldsymbol{p}}^{0,AA}y \\ D_{\boldsymbol{p}}^{0,BA}x^* - D_{\boldsymbol{p}}^{0,BB}y^* & D_{\boldsymbol{p}}^{0,BB}x - D_{\boldsymbol{p}}^{0,BA}y \end{pmatrix}, \tag{5.30}$$

with $u, u' \in \{A, B\}$. Considering $D^{uu'}$, it is easy to see that the symmetries from Eq. (5.26) are still valid for the screened potential with $D^{uu'}(\boldsymbol{p}) = \mathrm{i}\, V_{sc}^{uu'}(\boldsymbol{p})$ as specified before.

As argued in the beginning of this chapter, the instantaneous interaction as well as the neglect of retardation effects are justified by the difference of the Fermi velocity and the speed of light by a few orders of magnitude ($\sim 1/300$). A priori there is no argument that the assumption of a static Lindhard approximation results in realistic predictions for the critical coupling of the semimetal insulator phase transition. The particular advantage is that the infinite tower of Dyson-Schwinger equations closes upon itself in the fully instantaneous approximation. The idea is to compare the obtained results with already existing quantum Monte Carlo algorithms [23, 84] for $\mu = 0$ in the low temperature regime for the SDW state, where a good accordance should verify the static approximation and legitimate the same truncation scheme for the CDW calculation as well as calculations for finite chemical potential and arbitrary temperature, which can not be gained from lattice calculations.

5.2.1 Zero Temperature and Zero Chemical Potential

In analogy to the procedure from Sec. 3.3, a restricted renormalization functions to one of the competing phases, either SDW or CDW, are introduced. The resulting system of coupled integral equations was subsequently solved for both phases with the same methods as described in Sec. 3.5, where the new vacuum polarization and from that the screened potential is additionally calculated in every iteration step.

A huge numerical disadvantage in the static approximation comes from the fact that the frequency independent Lindhard susceptibility $\chi_{\boldsymbol{p}}$ can not be represented as a convolution. The numerical effort therefore again effectively increases with N^2 and can not be reduced to $N \log N$ by exploiting the convolution theorem. This is why calculations within this truncation become comparatively slow for huge lattices in momentum space.

At first, the SDW results will be investigated on the basis of the solution for $V = 0$, i.e. without nearest-neighbor interaction. In contrast to the previous findings and also to results from lattice calculations (see [84]) the SDW semimetal-insulator transition is found to be a first-order phase transition and exhibits the typical hysteresis behavior which is shown in Fig. 5.5 for $V = 0$. Obviously the location of the phase transition decisively depends on the starting values I for the iteration procedure which is chosen to be $I = 10$ for results represented in blue and $I = 0.01$ for those in green. This is equivalent to the effect of magnetic hysteresis, where the position of the phase transition depends on whether one starts from the symmetric phase or from the symmetry broken phase. We deliberately choose comparatively high or rather lower starting values to make sure to obtain a lower and an upper boundary value for the considered transition. All datapoints in Fig. 5.5 are solutions of the considered DSE's, i.e. minima of the free energy. For some coupling strengths we found two solutions due to the first-order transition, where the energetically preferred solution can be identified by the absolute minimum of the free energy. Consequently, the corresponding free energy has to be calculated numerically as described in Sec. 4.4 in order to decide where the real phase transition consisting of energetically preferred states is located.

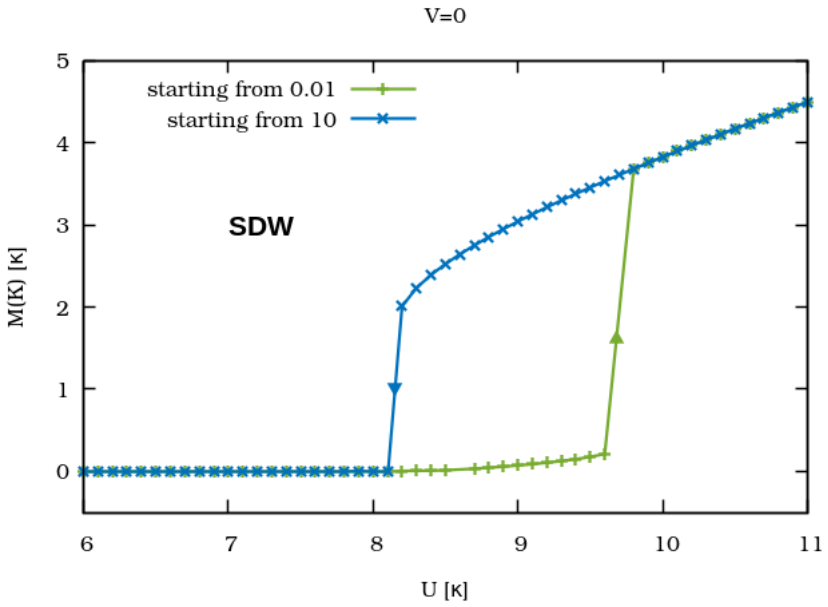

Figure 5.5: The mass renormalization function at the Dirac point $M(K)$ is plotted against the strength of the on-site repulsion U, both in units of the hopping parameter κ. Depending on the initial value for the iteration method with which the system of DSE's is solved, different solutions are found. This behavior represents the classical hysteresis effect commonly known from magnetism.

Nevertheless, we found an upper and lower boundary where the associated transition definitely lies in between, what is absolutely sufficient for the following consideration. Eventually, the critical on-site coupling within the static truncation framework is roughly located between $U = 8\,\kappa$ and $U = 10\,\kappa$, which is not compatible to lattice results [23, 25, 54, 84], that estimates the critical on-site coupling to be slightly below $U_c = 4\,\kappa$ for the low temperature regime. The results in Fig. 5.5 were obtained from calculations with lattice size $N = 300$.

Next, we want to focus on equivalent results for the CDW state, namely for the case of zero on-site repulsion $U = 0$. Here, we still found a second-order phase transition as illustrated in Fig. 5.6. For the regime of $U = 0 - 0.6\,\kappa$ we could not obtain reliable results in the vicinity of the phase transition in the chiral limit $m = 0$, which means that we did not find a solution that converged with a precision of 10^{-4} within 10000 iterations. In general the phenomena of critical slowing down, typically known from lattice calculations, is here reflected by the increasing number of necessary iteration steps for coupling strengths approaching the critical value. Here the attraction area from both solutions, the symmetry broken and the trivial solution respectively, are close together.

Numerically there are several ways to work around, one possibility is to introduce small nonzero explicitly symmetry breaking mass terms and extrapolate them to zero. The result of this procedure is shown in Fig. 5.6, where additionally a power law fit was applied in order to locate the critical coupling which was determined

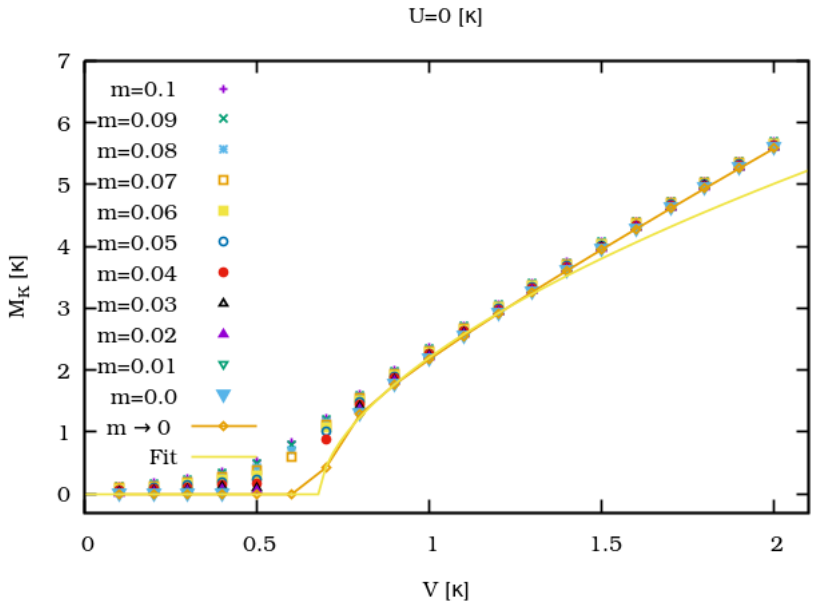

Figure 5.6: Shown are solutions of the mass renormalization function at the Dirac point to the considered system of DSE's for different values of explicit masses m. The obtained solutions are extrapolated to a zero mass solution $m \to 0$ which is subsequently fitted to a power law in order to extract the critical coupling.

to be $V = 0.68\ \kappa$. Since the extrapolated values (indicated by $m \to 0$ in Fig. 5.6) exactly agree with those for $m = 0$ away from the critical coupling, the extrapolation method seems to work quite well. For the regime of $U > 0.6\,\kappa$ we can again calculate with zero explicit mass terms and omit the extrapolation procedure. This is why we apply the method of FSS as described in Sec. 4.2.1 for $U = 1\,\kappa$ in order to extract the critical exponents. We obtain a compact crossing point for different lattice sizes $N = 54 - 180$ with $\beta/\nu = 1$, illustrated in Fig. 5.7. The critical nearest-neighbor coupling is determined to be $V_c = 0.6727\,\kappa \approx 0.673\,\kappa$, for which we also find very nice data collapse for $\beta = \nu = 1$ (Fig. 5.8). So for the CDW case the critical exponents do not change in comparison to the extracted exponents of the Hartee-Fock approximation from Sec. 4.3. Furthermore, in comparison to the unscreened Hartree-Fock approximation we observe an increase of the critical coupling for $U = 0$ from $V_c = 0.412\,\kappa$ to $V_c = 0.68\,\kappa$. Therefore the coupling strength is effectively suppressed because of electronic screening effects, which requires an enhanced critical coupling to induce the considered semimetal insulator phase transition.

The corresponding phase diagram where the extracted critical coupling pairs are plotted in the U-V plane is depicted in Fig. 5.9, for the second-order CDW (violet) as well as for the first-order SDW (blue) transition. The errorbars are again estimated by the discretization in the U-V-plane and do not include the errors caused by finite volume effects. The critical couplings are determined with the same procedure as already described for the Hartree-Fock consideration of Sec. 4.3 for a fixed lattice size of $N = 120$. The unscreened results obtained within the Hartree-Fock

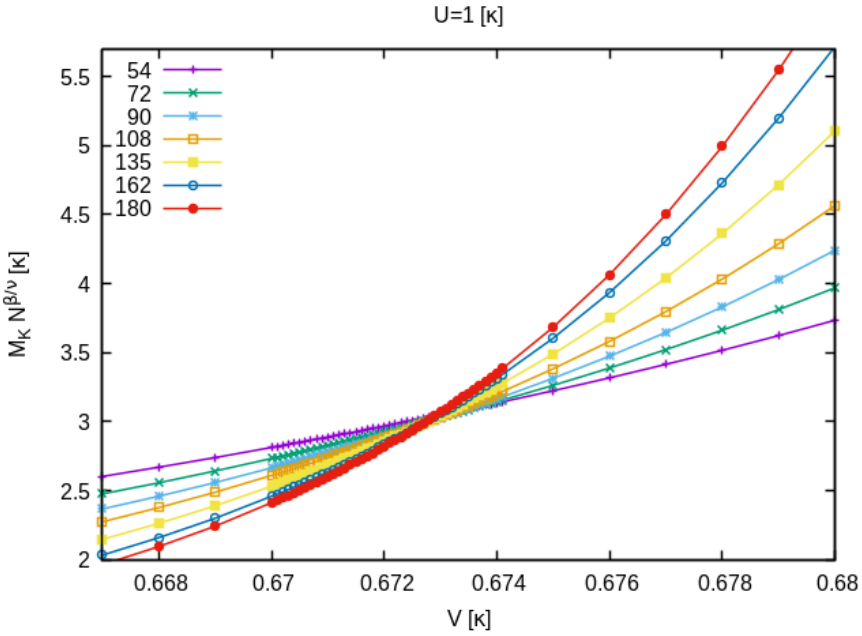

Figure 5.7: The scaled order parameter for $\beta/\nu = 1$ is shown as a function of the nearest neighbour coupling for different lattice sizes $N = 54 - 180$ in the CDW case.

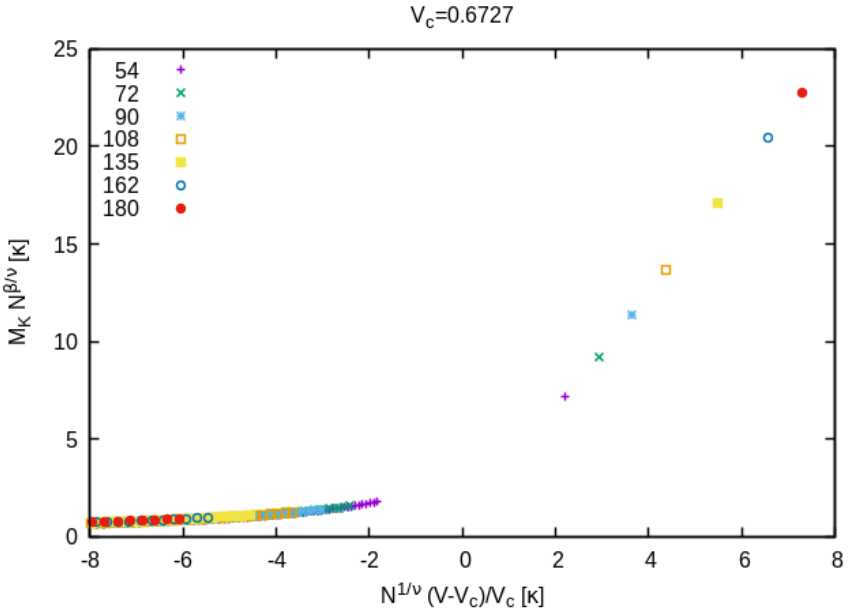

Figure 5.8: The scaled order parameter is represented as a function of the scaled reduced coupling as established in Sec. 4.2.1 in order to show a nice data collapse for $\beta = \nu = 1$.

approximation is illustrated in orange in order to compare both approaches. The function $V = 1/3\,U$ is represented as solid black line and still provides the first-order transition between the CDW and the SDW state, whereas the dashed gray lines indicate the spinodals in qualitative analogy to the Hartree-Fock phase diagram from Fig. 4.5. The shaded area represents the regime of coexistence and the white dot locates the tricritical point at about $(U_{tc}/V_{tc}) = (9\,\kappa/3\,\kappa)$.

For an increasing nearest-neighbor interaction, the hysteresis effect of the first-order SDW transition decreases and both first-order transitions seem to merge and coincide for $N \to \infty$ with the second-order CDW transition at the tricritical point. Above the tricritical point, $V = 1/3\ U$ still identifies the first-order CDW-SDW-transition that has not changed in comparison to the Hartree-Fock approximation and is also exactly valid for a frequency dependent consideration.

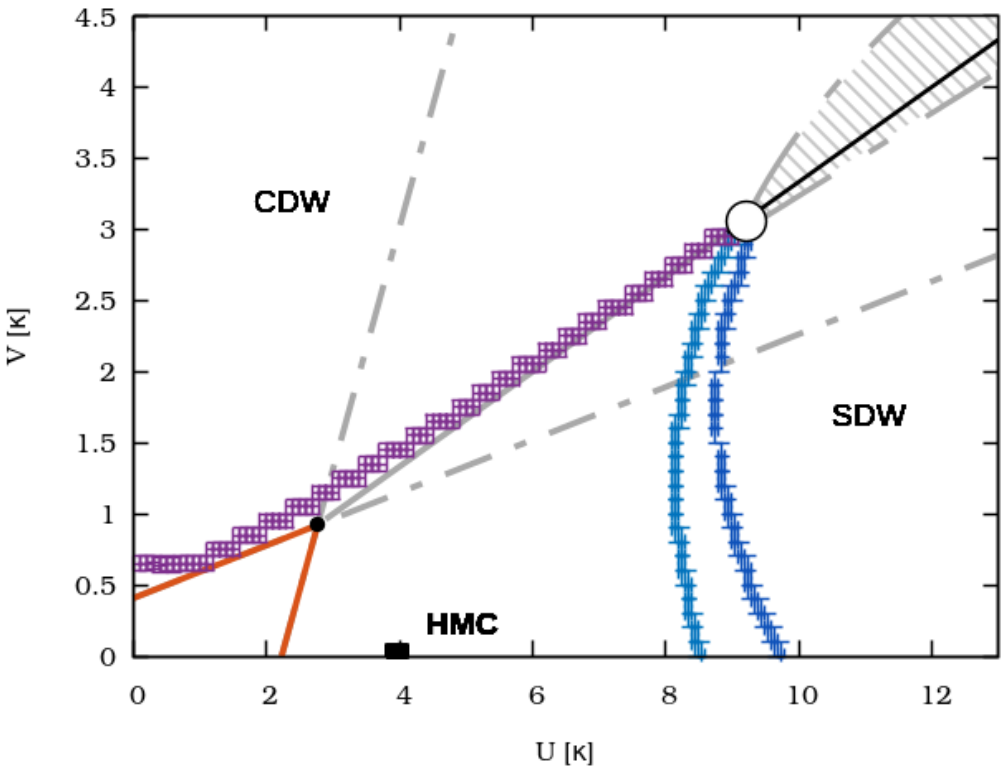

Figure 5.9: The phase diagram for the static screened Lindhard interaction for $N = 120$ is represented. The second-order CDW transition is shown in violet, and the first-order SDW transition is indicated in blue. For comparison the mean field results from the last chapter are shown with orange colored lines. The 1/3-line, separating the CDW and SDW state beyond the tricritical point, is shown by a solid line in black or gray, for the static and mean field approximation respectively. Furthermore the spinodals are marked by dashed gray lines.

Generally, one can observe an increase of the critical couplings due to the inclusion of screening effects. For the SDW calculation a huge increase of the critical line in

the U - V plane has been found. For comparison, the associated Hybrid-Monte-Carlo results (HMC) [20–23, 25, 54, 84] are indicated by a black rectangle. Unfortunately the HMC results are definitely located between the Hartree-Fock and the screened result. Consequently the static approximation seems to highly overestimate the influence of screening effects for the SDW state, but we always obtain a lower and an upper limit regarding the Hartree-Fock calculation and the statically screened interaction.

For the CDW case, where the results from the static approximation and those from the Hartree-Fock consideration are much closer together, we obtain a more significant result. Following the interpretation for the SDW case, one would expect the Hartree-Fock calculation and the statically screened approximation to give a lower and an upper boundary again, which provides only a small area for the CDW transition. For $U = 0$ - $0.6\,\kappa$, the critical nearest-neighbor coupling seems to remain almost constant, all in all the CDW transition for the static approximation is quite similar to the results obtained from the Hartree-Fock ansatz.

5.2.2 Finite Temperature and Chemical Potential

Additionally we have solved the static DSE's from Eq. (5.11) for finite temperatures and finite chemical potential in order to estimate their qualitative influence on the phase transition. Here we were especially interested in the temperature dependence to investigate whether we can come closer to the critical coupling results from lattice calculations by approaching comparable finite temperatures. Therefore, limits of $\mu \to 0$ and $T \to 0$ in Eq. (5.12) - Eq. (5.15) were examined separately, where the limit $\Omega_{\boldsymbol{q}+\boldsymbol{p}} \to \Omega_{\boldsymbol{q}}$, providing singularities, have to be evaluated analytically and the concerned momentum contributions has to be treated separately within the discrete momentum sum. Unfortunately, the overall outcome of this consideration was a further increase of the critical couplings for both finite temperature and chemical potential, as one would naively expect.

Finally we have to conclude that the static approximation for the SDW case neither provide quantitative nor qualitative suitable results. In contrary, the results concerning the CDW states seems to be more promising.

Additionally it should be briefly mentioned that the DSE's for a complete Fierz transformed version of the interaction, given in Eq. (E.11) and Eq. (E.12), have been also derived in App. E. The resulting photon DSE's are listed in Eq. (E.62)-Eq. (E.63) which are included in the fermion DSE's from Eq. (E.75) and Eq. (E.76). A similar mean field ansatz as represented in Sec. 4.1 for the SDW state would yield the same critical on-site coupling with a factor of three half $U_c = \frac{3}{2}\,\tilde{v}_c$ (Eq. (4.16)) which was found in Ref. [82]. This approximation seems to result in a critical on-site coupling which is much closer to the abovementioned lattice results than the approximation schemes which have been considered until now. Hence it might be worthwhile to investigate this set of DSE's more precisely and could be content the content in following studies. Of course both approaches (see Eq. (E.12)) should give identical solutions in the full theory, but with certain truncations on the level of DSE's different results can be obtained. In this work we still focus on solving the set of DSE's as discussed in Sec. 5.2.

6

Frequency Dependent Solution

Since the static approach could not be validated in order to describe the SDW semimetal-insulator transition on the hexagonal lattice as extensively examined in the last chapter, the static ansatz will now be rejected and the frequency dependence will be analyzed in this chapter.

The first step is to let all Dyson-Schwinger equations be frequency-dependent and allow for non-trivial wavefunction renormalizations and non-trivial vertex dressings to generate a closed system of coupled differential equations again. A dressed vertex function is subsequently introduced by a Ball Chiu Ansatz including only the zeroth component of the photon propagator as before. In Sec. 6.3 it will then be shown that the inclusion of a non-trivial wavefunction renormalization has almost no effect and therefore $Z_k = 1$ is a very good approximation. With regard to the achievement of higher lattice sizes the wavefunction renormalization will then be reset to its bare value and the semimetal insulator transition will be studied in detail.

6.1 Ball-Chiu Vertex Ansatz

In order to obtain a system of DSE's that closes upon itself to provide an internally conclusive approximation, we again start from the more general DSE's of Eq. (5.3) and Eq. (5.5). The neglect of electromagnetic retardation effects and the validity of an instantaneous bare interaction should still be warranted by the huge difference of the Fermi velocity and the speed of light. The screening effects, on the other hand, can strongly depend on the frequency as it seems to be the case for the SDW phase. These results are in qualitative accordance with the calculations of Ref. [51,52] where retardations effects were included within a low-energy approach. In Ref. [51, 52] it was also shown that comparable calculations for a Coulomb interaction in the low-energy approximation were rather unsensitive to the form of the vertex function, why

they only take the first term of the noncovariant Ball-Chiu (1BC) vertex into account [52]. We therefore assume to find reasonable results in the same approximation which further simplifies to the zeroth component of 1BC by the neglect of retardation effects. The tree-level vertex is therefore replaced by a part of the classical Ball Chiu vertex ansatz, where we again only have to take the zeroth component of the photon field into account. The idea of this vertex function is to primarily fulfill the corresponding Ward identities of the corresponding theory [98, 99]. In the simplest truncation, this simply results in the inclusion of the wavefunction renormalization within the vertex function as follows,

$$\Gamma^0_\sigma[q, q+p] = \gamma_0 \, \frac{Z_\sigma(q) + Z_\sigma(q+p)}{2} = \gamma_0 \, \widetilde{Z}_\sigma[q, q+p] \,, \tag{6.1}$$

fulfilling the corresponding Ward-Takahashi identity. Here, we effectively symmetrize both contributing vertices within a loop diagram.

Note that the explicit frequency dependence of the vacuum polarization function is of course given by Eq. (5.12)-Eq. (5.15). Without any symmetry assumption for the potential we obtain a more general expression for the associated frequency dependent screened interaction with frequency dependent polarization function Π_p in sublattice space,

$$(\mathbb{1} + \Pi_p \, D^0_{\boldsymbol{p}}) = \begin{pmatrix} a & b \\ c & d \end{pmatrix} , \tag{6.2}$$

with

$$a = 1 + \Pi_p^{AA} \, D_{\boldsymbol{p}}^{0,AA} + \Pi_p^{AB} \, D_{\boldsymbol{p}}^{0,BA} \,, \tag{6.3}$$

$$b = \Pi_p^{AA} \, D_{\boldsymbol{p}}^{0,AB} + \Pi_p^{AB} \, D_{\boldsymbol{p}}^{0,BB} \,, \tag{6.4}$$

$$d = 1 + \Pi_p^{BB} \, D_{\boldsymbol{p}}^{0,BB} + \Pi_p^{BA} \, D_{\boldsymbol{p}}^{0,AB} \,, \tag{6.5}$$

$$c = \Pi_p^{BA} \, D_{\boldsymbol{p}}^{0,AA} + \Pi_p^{BB} \, D_{\boldsymbol{p}}^{0,BA} \,. \tag{6.6}$$

For the inverse matrix one finds

$$(\mathbb{1} + \Pi_p \, D^0_{\boldsymbol{p}})^{-1} = \frac{1}{ad - bc} \begin{pmatrix} d & -b \\ -c & a \end{pmatrix} , \tag{6.7}$$

and consequently

$$D_p^{uu'} = \frac{1}{ad - bc} \begin{pmatrix} D_{\boldsymbol{p}}^{0,AA} + \Pi_p^{BB} \, \widetilde{v}_{\boldsymbol{p}} & D_{\boldsymbol{p}}^{0,AB} - \Pi_p^{AB} \, \widetilde{v}_{\boldsymbol{p}} \\ D_{\boldsymbol{p}}^{0,BA} - \Pi_p^{BA} \, \widetilde{v}_{\boldsymbol{p}} & D_{\boldsymbol{p}}^{0,BB} + \Pi_p^{AA} \, \widetilde{v}_{\boldsymbol{p}} \end{pmatrix} , \tag{6.8}$$

with $\widetilde{v}_{\boldsymbol{p}} = (V_{\boldsymbol{p}}^{AA} V_{\boldsymbol{p}}^{BB} - V_{\boldsymbol{p}}^{AB} V_{\boldsymbol{p}}^{BA})$. Since $\widetilde{v}_{\boldsymbol{p}} \in \mathbb{R}$ (see Eq. (5.26)), the symmetry properties of Π_p can be directly transferred to the screened photon propagator or rather the screened interaction $D_p^{uu'} = \mathrm{i} \, V_{sc,p}^{uu'}$. The bare photon propagator still depends only on the spatial momentum, indicated by a bold vector notation. In this context we have to examine whether $D_q^{AA} = D_q^{AA}$ is still valid in order to simplify the DSE's analogically to the procedure from Sec. 5.2. From the explicitly frequency-dependent Lindhard function, Eq. (5.12)-Eq. (5.15), the following symmetries can be extracted in Minkowski spacetime,

$$(\mathrm{i} \, \Pi^{AA}(\omega, \boldsymbol{p}))^* = \mathrm{i} \, \Pi^{AA}(\omega, -\boldsymbol{p}) = \mathrm{i} \, \Pi^{AA}(\omega, \boldsymbol{p}), \tag{6.9}$$

$$(\mathrm{i}\,\Pi^{BB}(\omega,\boldsymbol{p}))^* = \mathrm{i}\,\Pi^{BB}(\omega,-\boldsymbol{p}) = \mathrm{i}\,\Pi^{BB}(\omega,\boldsymbol{p}), \tag{6.10}$$

$$(\mathrm{i}\,\Pi^{AB}(\omega,\boldsymbol{p}))^* = \mathrm{i}\,\Pi^{AB}(\omega,-\boldsymbol{p}) = \mathrm{i}\,\Pi^{BA}(\omega,\boldsymbol{p}), \tag{6.11}$$

where the renormalization functions are assumed to transform like

$$M_{\sigma,-p} = M_{\sigma,p}\,, \quad \phi_{\sigma,-p} = \phi^*_{\sigma,p}\,, \qquad \text{and} \qquad Z_{\sigma,-p} = Z_{\sigma,p}\,, \tag{6.12}$$

due to their bare counterparts and the corresponding symmetry for the self-energy part. Moreover it can be shown that

$$\Pi^{AA}(\omega,\boldsymbol{p}) = \Pi^{BB}(\omega,\boldsymbol{p})\,, \tag{6.13}$$

for the SDW case, where unequal contributions cancel because of the sum over different spin states with $M_{\uparrow,p} = -M_{\downarrow,p}$. This symmetry is still valid for the CDW constellation, but only for the case of $\mu = 0$. However, these symmetries are assumed to be still valid in terms of frequency dependent fermion propagators, since the DSE's do not change structurally. For the screened interaction ($V^{-1}_{sc,p} = V^{-1}_p + \mathrm{i}\,\Pi_p$) the symmetry of the polarization loop immediately entail

$$(-\mathrm{i}\;D^{AA}(\omega,\boldsymbol{p}))^* = -\mathrm{i}\;D^{AA}(\omega,-\boldsymbol{p}) = -\mathrm{i}\;D^{AA}(\omega,\boldsymbol{p})\,, \tag{6.14}$$

$$(-\mathrm{i}\;D^{BB}(\omega,\boldsymbol{p}))^* = -\mathrm{i}\;D^{BB}(\omega,-\boldsymbol{p}) = -\mathrm{i}\;D^{BB}(\omega,\boldsymbol{p})\,, \tag{6.15}$$

$$(-\mathrm{i}\;D^{AB}(\omega,\boldsymbol{p}))^* = -\mathrm{i}\;D^{AB}(\omega,-\boldsymbol{p}) = -\mathrm{i}\;D^{BA}(\omega,\boldsymbol{p})\,, \tag{6.16}$$

and $D^{AA}_p = D^{BB}_p$ for the SDW case and the CDW case with $\mu = 0$.

In order to solve the obtained equations numerically, a Wick rotation to Euclidean spacetime has been performed and the standard fermionic or bosonic Matsubara frequencies were introduced (see App. B),

$$q^0 = \mathrm{i}\,q^0_{E,n} = \mathrm{i}\,(2n+1)\pi/\beta\,, \qquad p^0 = \mathrm{i}\,p^0_{E,m} = \mathrm{i}\,2\pi\,m/\beta\,, \tag{6.17}$$

here β again denotes the inverse temperature. The frequency-momentum vector is then represented by $q_n = (\mathrm{i}\,q^0_{E,n}, \boldsymbol{q})$, where n denotes the index of the introduced time lattice with N_t being the number of lattice sites in time direction and $\delta = \beta/N_t$ the associated lattice discretization. Numerically, we perform the sum from $n = -N_t/2$ to $n = N_t/2-1$ in order to obtain a real periodic function. The final set of equations is specified in the following,

$$\Pi^{AA}(p_m) = -\frac{\mathrm{i}}{\beta\,N^2}\sum_{\sigma,n,\boldsymbol{q}} G^{AA}_{F,\sigma}(q_n)\;\widetilde{Z}_\sigma[q_n, q_n+p_m]\;G^{AA}_{F,\sigma}(q_n+p_m)\,, \tag{6.18}$$

$$\Pi^{AB}(p_m) = \frac{\mathrm{i}}{\beta\,N^2}\sum_{\sigma,n,\boldsymbol{q}} G^{BA}_{F,\sigma}(q_n)\;\widetilde{Z}_\sigma[q_n, q_n+p_m]\;G^{AB}_{F,\sigma}(q_n+p_m)\,, \tag{6.19}$$

$$\Pi^{BA}(p_m) = \frac{\mathrm{i}}{\beta\,N^2}\sum_{\sigma,n,\boldsymbol{q}} G^{AB}_{F,\sigma}(q_n)\;\widetilde{Z}_\sigma[q_n, q_n+p_m]\;G^{BA}_{F,\sigma}(q_n+p_m)\,, \tag{6.20}$$

$$\Pi^{BB}(p_m) = -\frac{\mathrm{i}}{\beta\,N^2}\sum_{\sigma,n,\boldsymbol{q}} G^{BB}_{F,\sigma}(q_n)\;\widetilde{Z}_\sigma[q_n, q_n+p_m]\;G^{BB}_{F,\sigma}(q_n+p_m)\,, \tag{6.21}$$

$$M_\sigma(k_v) = m_\sigma + \frac{\mathrm{i}}{\beta N^2}\sum_{n,\boldsymbol{q}}\Bigg[(-\mathrm{i}\,D^{AA}_{q_n-k_v})\frac{\mathrm{i}\;M_{\sigma,q_n}}{(\mathrm{i}\,q^0_{E,n}+\mu^\sigma)^2 Z^2_{\sigma,q_n}-\Omega^2_{\sigma,q_n}}\,\widetilde{Z}_\sigma[q_n,k_v] \\ -\mathrm{i}\,(D^{0,AB}_{q_n=0}-D^{0,AA}_{q_n=0})\sum_{\sigma'}\frac{\mathrm{i}\;M_{\sigma',q_n}}{(\mathrm{i}\,q^0_{E,n}+\mu^{\sigma'})^2 Z^2_{\sigma',q_n}-\Omega^2_{\sigma',q_n}}\Bigg]\,, \tag{6.22}$$

$$Z_\sigma(k_v) = 1 - \frac{\mathrm{i}}{\beta N^2\,(\mathrm{i}\,k^0_{E,v}+\mu^\sigma)}\sum_{n,\boldsymbol{q}}\Bigg[(-\mathrm{i}\,D^{AA}_{q_n-k_v})\frac{\mathrm{i}\;(\mathrm{i}\,q^0_{E,n}+\mu^\sigma)\,Z_{\sigma,q_n}}{(\mathrm{i}\,q^0_{E,n}+\mu^\sigma)^2 Z^2_{\sigma,q_n}-\Omega^2_{\sigma,q_n}}\,\widetilde{Z}_\sigma[q_n,k_v] \tag{6.23}$$

$$+\mathrm{i}\,(D^{0,AB}_{q_n=0}+D^{0,AA}_{q_n=0})\sum_{\sigma}\frac{\mathrm{i}\;(\mathrm{i}\,q^0_{E,n}+\mu^{\sigma'})\,Z_{\sigma',q_n}}{(\mathrm{i}\,q^0_{E,n}+\mu^{\sigma'})^2 Z^2_{\sigma',q_n}-\Omega^2_{\sigma',q_n}}\Bigg]\,, \tag{6.24}$$

$$\phi_\sigma(k_v) = \varphi_{\boldsymbol{k}} + \frac{\mathrm{i}}{\beta N^2}\sum_{n,\boldsymbol{q}}(-\mathrm{i}\,D^{BA}_{q_n-k_v})\frac{\mathrm{i}\;\phi_{\sigma,q_n}}{(\mathrm{i}\,q^0_{E,n}+\mu^\sigma)^2 Z^2_{\sigma,q_n}-\Omega^2_{\sigma,q_n}}\,\widetilde{Z}_\sigma[q_n,k_v]\,, \tag{6.25}$$

$$\phi^*_\sigma(k_v) = \varphi^*_{\boldsymbol{k}} + \frac{\mathrm{i}}{\beta N^2}\sum_{n,\boldsymbol{q}}(-\mathrm{i}\,D^{AB}_{q_n-k_v})\frac{\mathrm{i}\;\phi^*_{\sigma,q_n}}{(\mathrm{i}\,q^0_{E,n}+\mu^\sigma)^2 Z^2_{\sigma,q_n}-\Omega^2_{\sigma,q_n}}\,\widetilde{Z}_\sigma[q_n,k_v]\,. \tag{6.26}$$

6.2 Order Parameter

Before we continue with the examination of the numerical results, the order parameter should be reviewed again. The order parameter for the semimetal-insulator phase transition is still given by the singularities of the fermion propagator at the Dirac point, providing the quasi-particle energies. The renormalized band-structure here remains zero $|\Phi(\omega,K)| = 0$ for all frequencies. Consequently, the following equation has to be solved for ω in Minkowski spacetime,

$$\omega = -\mu \pm \sqrt{M^2(\omega,\boldsymbol{q})/Z^2(\omega,\boldsymbol{q})}\,, \tag{6.27}$$

with M being either the CDW or the SDW mass renormalization function. On the Euclidean lattice with discretized frequencies, this equation formally cannot be solved, since there is no singularity in euclidean spacetime. Another difficulty that comes with the consideration of a fermionic system instead of a bosonic is the nonexistence of real zero modes, whereas the right hand side of Eq. (6.27) surely reaches zero within the numerical accuracy.

The best and simplest approximation to determine an order parameter for this strongly correlated electron system, without an extraction from the exponential decay of the imaginary time propagator [84], is to evaluate the fermionic renormalization functions for the minimal Matsubara frequency given by

$$q^0_{E,min} = \pi/\beta\,. \tag{6.28}$$

Therefore the order parameter is fixed to $\sqrt{M^2_\sigma(q^0_{E,min},K)/Z^2_\sigma(q^0_{E,min},K)}$. As long as the chemical potential is set to zero, the wave-function renormalization as well as the mass renormalization function are found to be real, so that

$$\sqrt{M^2(q^0_{E,min},K)/Z^2(q^0_{E,min},K)} = \Big|\,\mathrm{Re}[M(q^0_{E,min},K)]/\,\mathrm{Re}[Z(q^0_{E,min},K)]\Big|\,. \tag{6.29}$$

6.3 Inclusion of Effects from Wave Function Renormalization

In a first step, we want to discuss the numerical results obtained by solving the set of DSE's, given in Sec. 6.1, for the SDW case. For simplicity, the nearest neighbor interaction V is again omitted and the calculations have been computed with a fixed spatial lattice size $N = 90$ and $N_t = 1000$ lattice sites in imaginary time direction. For $\mu = 0$ the resulting dispersion relation, given by the dressed analog of Eq. (2.32), is plotted in Fig. 6.1 for different on-site interactions along the high symmetry points, introduced in Fig. 2.5. The temperature is chosen to be $\beta = 20\,\kappa^{-1}$ which is nicely resolved by $N_t = 1000$ lattice points, as will be shown in the next section.

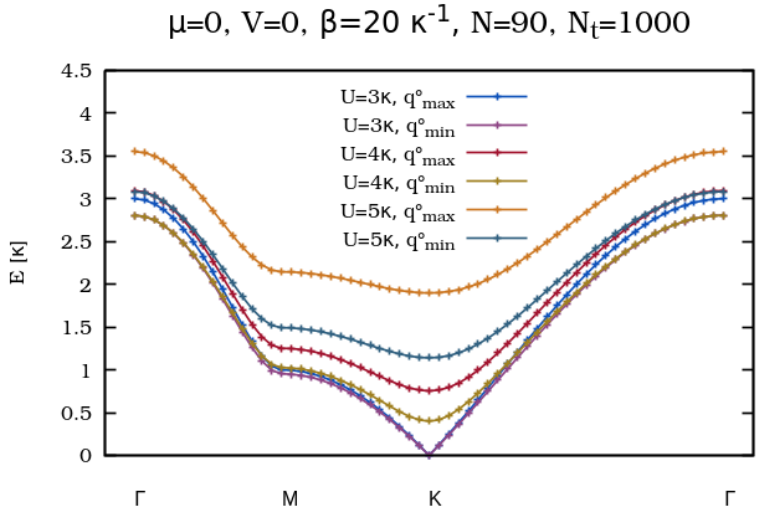

Figure 6.1: Shown is the dressed dispersion relation for different on-site interactions $U = 3{-}4\,\kappa$. Here the results are plotted for the minimal and the maximal Matsubara frequency, while all other contributions usually lie in between them.

Since the mass renormalization function as well as the wavefunction renormalization remain real-valued, one also ends up with a real energy function E in units of the hopping parameter κ. For comparison, the energy function is shown for both, the minimal Matsubara frequency q^0_{min} as well as the maximal Matsubara frequency q^0_{max}. From the gap opening the critical on-site coupling can be clearly determined to lie between $U = 3\,\kappa$ and $U = 4\,\kappa$. In the symmetric phase the band structure is almost equal in the vicinity of the Dirac points for all Matsubara frequencies. With an increasing band gap, the energy dispersion relation for the minimal and maximal Matsubara frequency becomes more and more separated. This confirms the assumption that one could principally choose every Matsubara frequency to provide the order parameter for the considered phase transition (see also Fig. 6.16).

In Fig. 6.2 the single contributions to the energy dispersion of Fig. 6.1, namely the set of fermionic renormalization functions, are depicted in the symmetry-broken

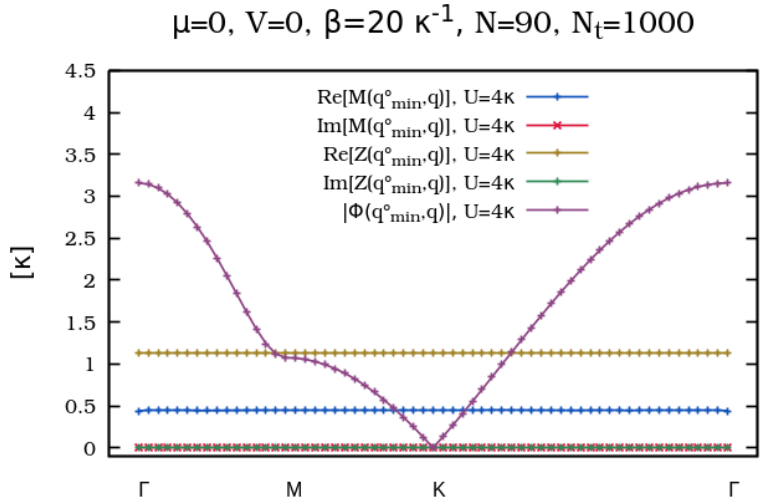

Figure 6.2: The real and imaginary part of the fermionic renormalization functions is represented along the high symmetry points of the Brioullin zone for the minimal Matsubara frequency denoted by q^0_{min}.

phase for $U = 4\,\kappa$. The mass renormalization function as well as the wavefunction renormalization are almost constant and real. Here the minimal Matsubara contributions are plotted, providing the maximal values for the real part of Z_k which is found to be slightly above its bare value $Z_k = 1$.

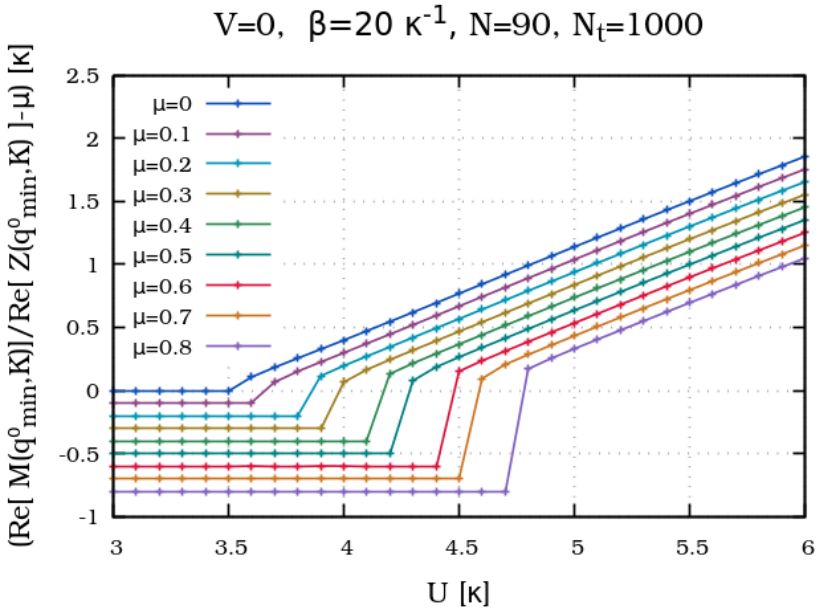

Figure 6.3: The semimetal to antiferromagnetic insulator transition is shown for different values of μ for a fixed temperature $\beta = 20\,\kappa^{-1}$.

Since the truncation scheme for the considered DSE's should also be valid for $\mu \neq 0$ in the SDW case, the behavior of the wavefunction renormalization was also investigated for small chemical potentials greater than zero. In Fig. 6.3 the obtained order parameter (Eq. (6.29)) shifted by μ is plotted against the on-site coupling. With increasing chemical potential the critical coupling increases as well due to the raised charge carrier density, while a first-order transition emerges. This results are shown for a starting value of $I = 10$ in the iteration procedure, for a better overview the corresponding counterparts for low starting values, exhibiting the hysteresis effect of the first-order transition, are omitted.

Here it should be mentioned that for $\mu > 1\,\kappa$ it is hard to obtain a converged solution in the vicinity of the phase transition. In order to overcome these issues, some numerical methods as described in Sec. 3.5 could help. For now the considered area of the chemical potential is absolutely sufficient. The main point that should be considered here is the influence of the chemical potential on the wavefunction renormalization which is shown in Fig. 6.4. The real an imaginary part of the wavefunction renormalization is illustrated for a fixed on-site coupling in the symmetry-broken phase for both, maximal and minimal Matsubara frequency as upper and lower boundaries. Shown is the comparison between the wavefunction renormalization for $\mu = 0$ and $\mu = 0.5\,\kappa$ which do not decisively differ in magnitude.

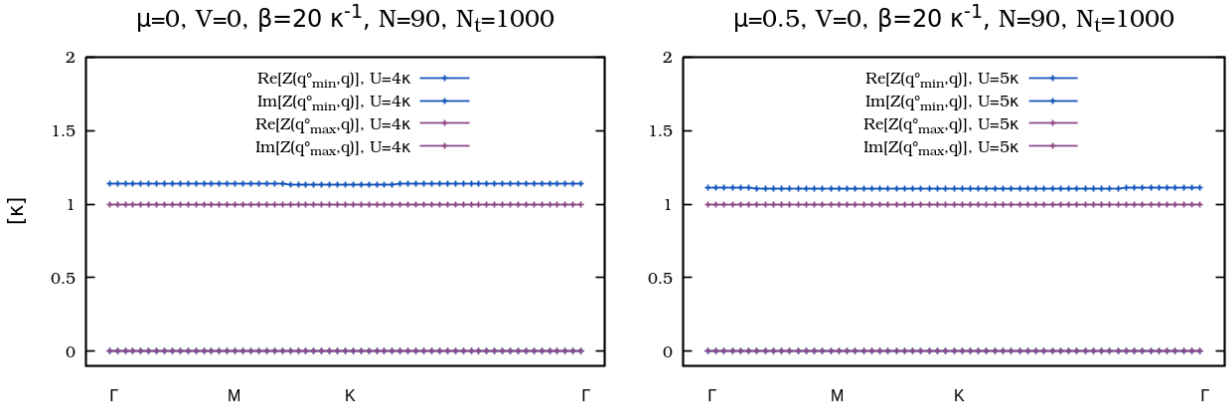

Figure 6.4: On the left hand side the wavefunction renormalization is illustrated for zero chemical potential, while the right hand side represents comparable results for $\mu = 0.5\,\kappa$.

Finally, in Fig. 6.5 the comparison between calculations with non-trivial and trivial wavefunction renormalization is represented (indicated by $Z = 1$). Obviously the dynamic inclusion of the wave function renormalization do neither change the critical coupling nor the behavior of the order parameter intensively.

Additionally the influence of the wavefunction renormalization on the CDW solution was investigated for $\mu = 0$. In Fig. 6.6 the computed renormalization functions are illustrated individually within the symmetric phase $V = 0.2\,\kappa$ as well as in the symmetry-broken phase $V = 0.8\,\kappa$. In analogy to the corresponding SDW calcula-

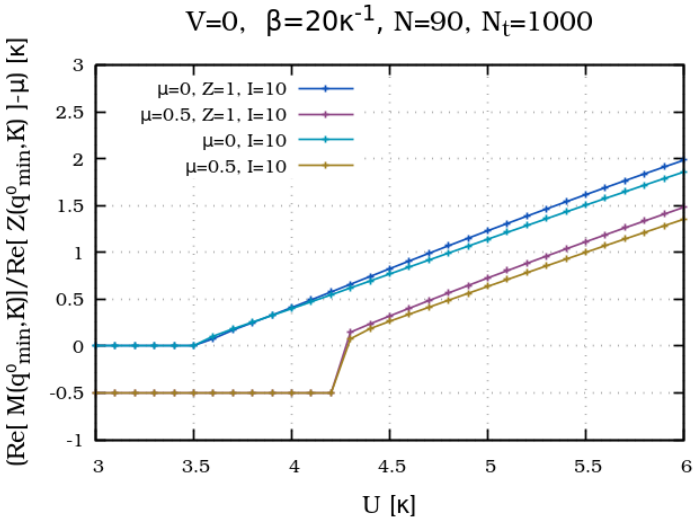

Figure 6.5: Shown are the resulting order parameters for various on-site couplings for a fixed temperature and a fixed lattice size. For comparison the results with non-trivial wavefunction renormalization as well as those for a trivial wavefunction renormalization, denoted by $Z = 1$, are illustrated. The specified parameter $I = 10$ refers to the initial value of the iteration procedure in order to indicate the upper boundary concerning the first-order transition.

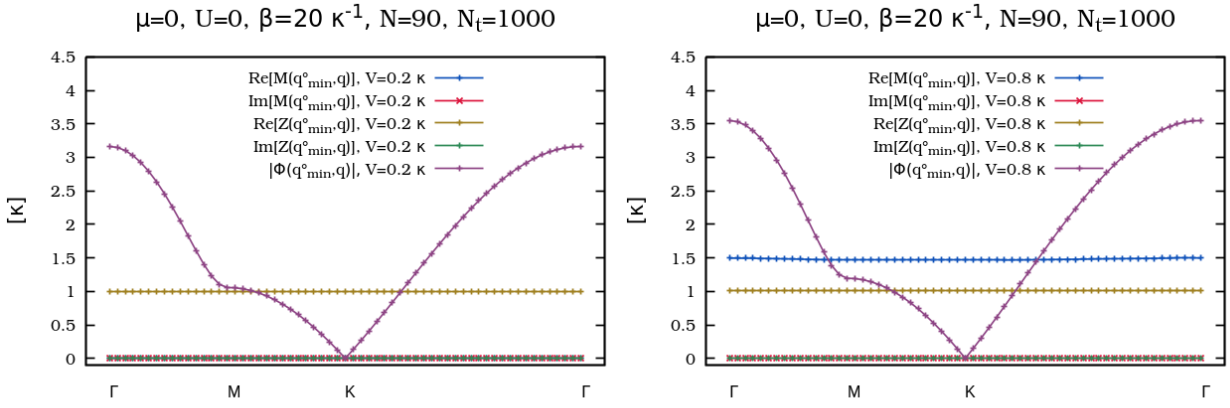

Figure 6.6: The solution for the single renormalization functions for different nearest neighbor interactions is shown with $U = 0$. On the left hand the system is in the symmetric phase with a zero mass renormalization function. The real part of the wavefunction renormalization obviously do not visually differ from one. The structure function is slightly dressed which can be seen from the somewhat raised values at the Γ points as well as at the M point.

tion the temperature is set to $\beta = 20\,\kappa^{-1}$, while the on-site coupling is now fixed to zero. As it can be observed in Fig. 6.6 the influence from the wavefunction renormalization is even lower as in the SDW case. The wavefunction renormalization remains bare in a very good approximation.

Consequently we really found $Z_k = 1$ to be an excellent approximation for the values that we are interested in. Indeed, it turned out that this is even valid within the whole U-V-plane for both, the SDW as well as the CDW phase. The wavefunction renormalization is therefore again set to its trivial value in the following calculations. This naturally saves run time as well as memory requirements and enables the calculation for even higher lattice sizes characterized by $N^2 \cdot N_t$.

6.4 Results with Trivial Wave Function Renormalizations

In the first part, the final results for the semimetal to insulator transition will be shown within the whole U-V plane for a fixed temperature $\beta = 20\,\kappa^{-1}$. In the next subsections the critical exponents and the temperature dependence of the critical on-site coupling for the SDW state will be investigated. Finally we will present the outcomes of the finite μ consideration for the SDW case as well.

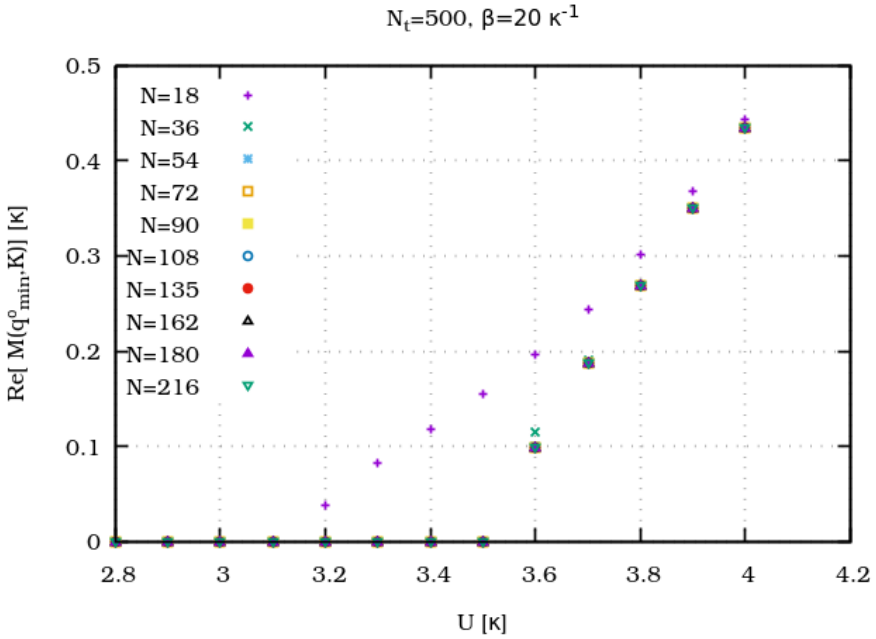

Figure 6.7: The dependence of the order parameter (Eq. (6.29)) from the spatial lattice size, characterized by N, is represented for a fixed inverse temperature $\beta = 20\ \kappa^{-1}$ and a fixed number of lattice points in imaginary time direction $N_t = 500$.

6.4.1 Finite Volume Effects and Phase Transition

In a first step, the numerical results for the spin density wave constellation will now be discussed in detail, subsequently corresponding results for the CDW state are represented. In the following the temperature is set to $\beta = 20\ \kappa^{-1}$ and the chemical potential is fixed to $\mu = 0$ in order to compare with recent results from Ref. [54] for the whole U-V coupling plane and especially with Ref. [84] and Ref. [23] for the case of vanishing nearest neighbor potential $V = 0$.

With the current numerical setup we are able to reach huge lattice sizes in comparison to calculations on the basis of Monte Carlo methods. Since the lattice size in real space determined by N^2 reflects the real size of the graphene sheet, we expect equal results for equal lattice sizes here. However, correction terms due to the finite lattice in the imaginary time formalism might differ. Therefore we should make sure to reach the limit $N_t \to \infty$ and preferably $N \to \infty$ likewise.

In Fig. 6.7 the order parameter in dependence of the on site coupling U for zero nearest-neighbor coupling $V = 0$ is shown for a fixed time lattice $N_t = 500$ for different lattice sizes in momentum space $N = 18 - 216$.

As one can see in Fig. 6.7 we found almost no volume effects for lattice sizes greater or equal to $N = 54$ for this setup. In contrary, lattice sizes of $N = 18$ are shown to be way too small in order to estimate the phase transition. As a good tradeoff, in order to minimize finite volume effects concerning the spatial lattice and similarly choose a possibly small N to allow for larger time lattice sizes N_t, we fix the number of unit cells to $N = 90$ in the following.

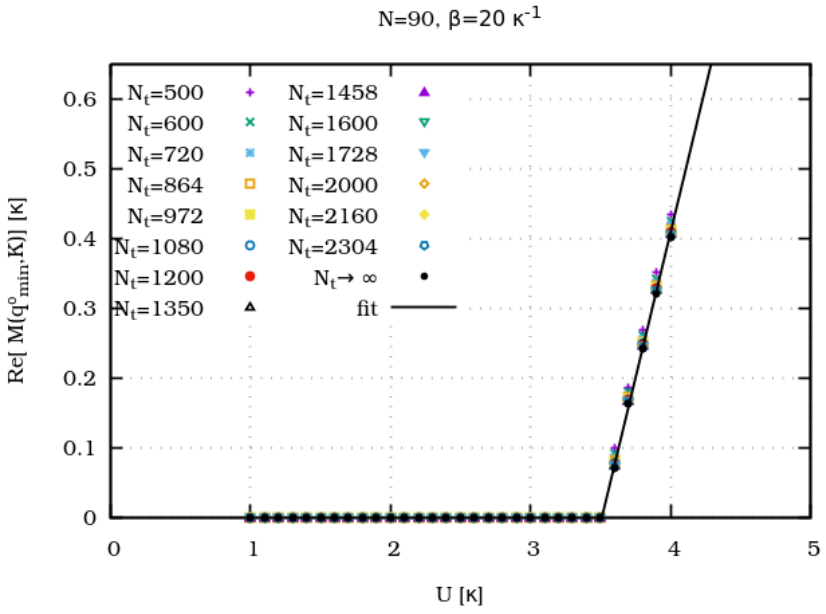

Figure 6.8: Here the order parameter (Eq. (6.29)) for different lattice sizes in imaginary time direction N_t is shown for a fixed spatial lattice with $N = 90$ and a fixed inverse temperature of $\beta = 20\ \kappa^{-1}$. The obtained values were extrapolated to $N_t \to \infty$ as shown in Fig. 6.9 and fitted to a polynomial function of first-order.

In Fig. 6.8 an analogical consideration is represented for various lattice sizes in time direction between $N_t = 500$ and $N_t = 2300$.

Here the results for different lattice sizes N_t were additionally extrapolated to $N_t \to \infty$ by a polynomial least-square fit of second degree,

$$f(x) = a\,(1/N_t)^2 + b\,(1/N_t) + c\,.$$

Such a fit is exemplary shown in Fig. 6.9 for $U = 3.8\ \kappa$, where the extracted order parameter is plotted against the inverse lattice size $1/N_t$. The value for $N_t \to \infty$ is then finally determined by the parameter c, for a fitted intercept smaller than zero the order parameter was accordingly set to zero.

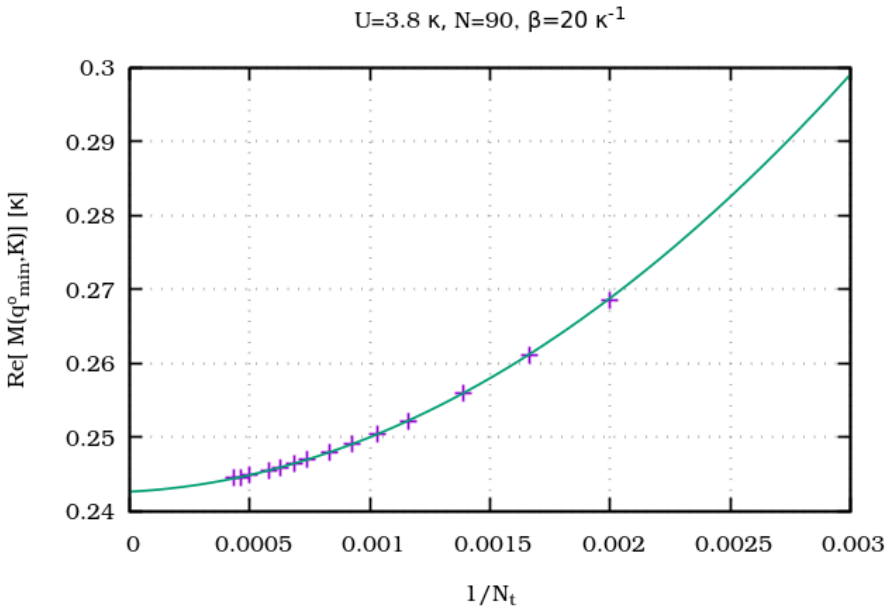

Figure 6.9: The polynomial fit of second degree to the order parameter is illustrated in dependence of the inverse number of lattice points in imaginary time direction $1/N_t$. Exemplary, an on-site coupling of $U = 3.8\ \kappa$ was chosen.

These values extrapolated to $N \to \infty$ are represented as black dots in Fig. 6.8 where they were additionally fitted to a straight line. The interception with the x-axis consequently determines the critical coupling for $V = 0$ to be

$$U_c = 3.51\ \kappa\,. \tag{6.30}$$

This is in rough accordance to the results from Ref. [84] and Ref. [23] were a critical coupling between $U_c \sim 3.7 - 3.8\ \kappa$ was found. The deviation could still be caused by the vertex approximation of the applied Dyson-Schwinger framework, but also finite volume and temperature effects are not excluded. As it was shown in the last section, a Ball Chiu vertex ansatz would not change the result, a vertex dressing as discussed in Sec. 4.4 should therefore be taken into account. However, the achieved accordance with the results from Quantum Monte Carlo algorithms

within the frequency dependent ansatz is more than satisfactory for the considered SDW case and really overcomes the observed overestimation of the critical on-site coupling as obtained in the last chapter with the static approach of the screening function.

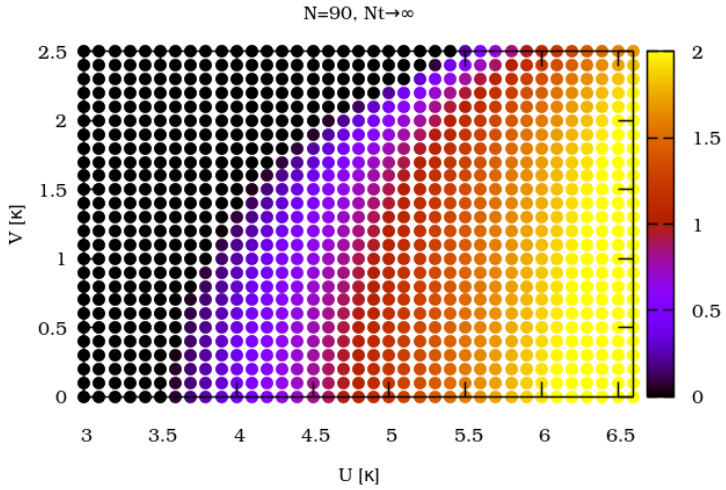

Figure 6.10: The semimetal to antiferromagnetic insulator transition is shown as contour plot for $\beta = 20\ \kappa^{-1}$ within the U-V coupling plane for a spatial lattice size fixed to $N = 90$.

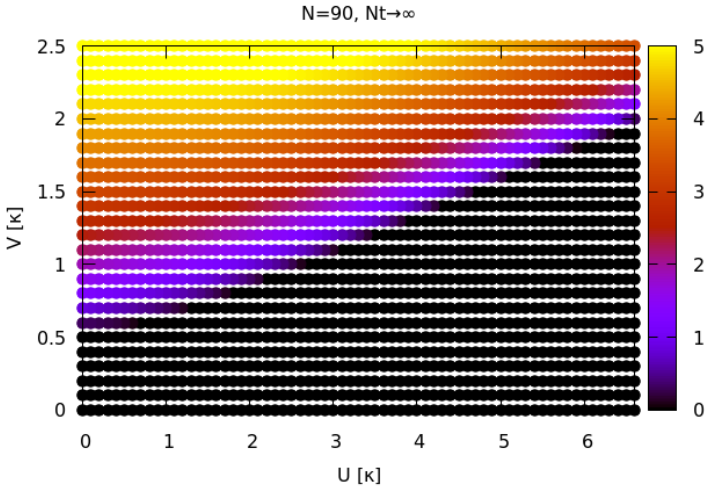

Figure 6.11: The order parameter is plotted in the U-V coupling plane for the case of a CDW configuration. Analogically to Fig. 6.11, the calculations were made for $\beta = 20\ \kappa^{-1}$ for a fixed spatial lattice size $N = 90$, whereas the imaginary time lattice has been extrapolated to $N_t \to \infty$ for lattice sizes between $N_t = 100 - 1000$.

As one can conclude from Fig. 6.8 and Fig. 6.9 the calculation for such large lattices in imaginary time direction is not necessary for the considered temperature regime. An analog evaluation for time lattices between $N_t = 100$ and $N_t = 1000$ was therefore applied to the whole coupling regime characterized by U and V. The received phase diagram, where the order parameter as given in Eq. (6.29) is represented in dependence of the control parameters U and V, is shown in Fig. 6.10.

This results finally show up a very nice qualitative as well as quantitative accordance with the outcomes from Ref. [54]. The great advantage of the Dyson-Schwinger framework is the accessibility of the coupling regime beyond $V = 1/3\ U$ since the theory exhibits no sign problem here. Apart from that, the numerical setup established in Sec. 3.5 enables the calculation for very large lattice sizes.

In order to eventually access the phase transition with regard to both phases, the SDW as well as the SDW phase, an anolog consideration was made for the numerical system fixed to the CDW case. The result is represented in Fig. 6.11. In contrary to the SDW state the phase transition concerning the CDW state seems to be in nice quantitative and qualitative agreement with the results obtained in the static approximation.

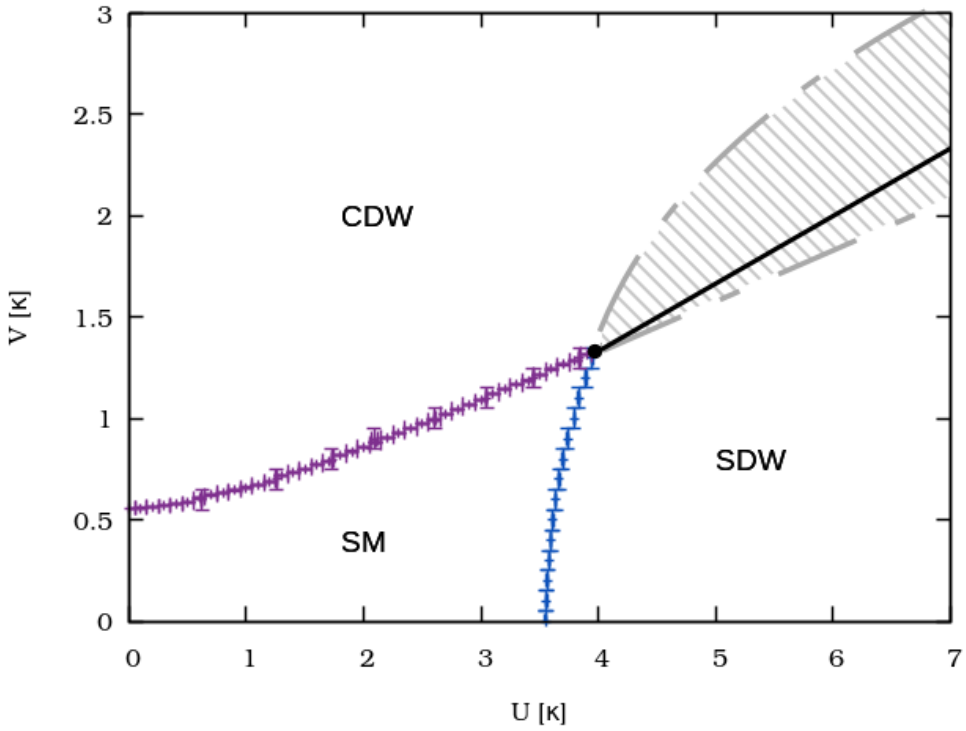

Figure 6.12: The resulting phase diagram is plotted on the extended Hubbard plane. The critical coupling pairs as well as the indicated errorbars were obtained with the same techniques as already pointed out in Sec. 4.3.

All in all, the considered screening effects from the $\pi-$bands itself seem to be of much higher influence regarding the SDW case. In complete analogy to Fig. 5.9 the presented phase transitions are summarized in Fig. 6.12 where the individual areas of the SDW, CDW and SM phase are sketched. The regime of coexistence is shaded

in gray and limited by the spinodal lines as before. The first-order line, $V = 1/3\,U$, separating CDW and SDW constellations is still valid as shown in Sec. 4.4.

6.4.2 Critical Exponents

As next step, the critical exponents will be investigated with the help of the established finite size method from Sec. 4.2.1 in the SDW case. Until now we could not extract critical exponents which deviate from the analytical finding of Sec. 4.1 within a mean field approximation which determines the critical exponent of the order parameter to $\beta = 1$ and were in nice accordance to the results from Ref. [20,23].

As extensively discussed in Chap. 4 the critical exponents characterize the system to belong to a certain universality class which is only specified by a few macroscopic properties. One of these properties is the range of the interaction, for the Hubbard model there are several studies suggesting a chiral Heisenberg Gross-Neveu model in three spacetime dimensions to be the adequate model [30,84,100,101] and indeed these expectations has been validated [84,102–104]. In order to extract the critical exponents we observe some difficulties concerning the approximation of the order parameter by the mass renormalization function at the Dirac point evaluated at the smallest Matsubara frequency. As mentioned above for $M(q_n^0, K) \neq 0$ it is not decisively relevant which Matsubara contribution is chosen to be the order parameter. As shown in Fig. 6.16, the mass renormalization function at the Dirac point provides an order parameter independent of the frequency variable, because the be-

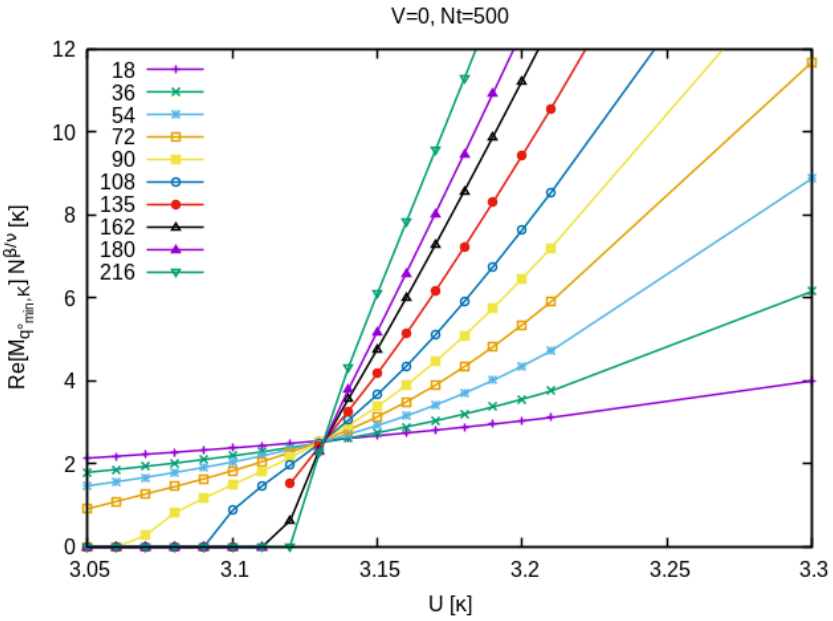

Figure 6.13: The scaled order parameter is represented for varying on-site couplings. An optimal intersection point was found for $\beta/\nu = 0.96$ at $U_c = 3.131\,\kappa$. Concerning the red data points illustrating the results for $N = 135$, we did not find a convergent solution for $U = 3.11\,\kappa$ within a maximal number of 10^4 iterations.

havior coincides for all Matusbara modes in the vicinity of the critical coupling. For the extraction of the critical coupling, the choice of the minimal Matsubara mode is therefore more appropriate.

Regarding the determination of the critical exponents the situation is slightly different. In order to make reliable results the FSS method should be applied, for that the volume dependence of the order parameter is needed for coupling values which are larger than the critical coupling, as well as for the coupling regime below the critical value. For a numerically obtained mass renormalization function that equals, or is approximately zero, Eq. (6.29) cannot be fulfilled for $\mu = 0$ due to the fermionic character and the related nonexistence of a zero Matsubara mode.

For the investigation of the critical exponents a simple solution to this problem is provided by considering higher temperatures. Higher temperatures at least provide very small minimal Matsubara modes and the finite volume behavior for control parameters slightly below the critical coupling can be resolved.

This phenomena is depicted in Fig. 6.13, where the scaled order parameter is plotted against the on-site coupling in order to determine the critical coupling value in terms of the intersection point for all volumes. The finite volume behavior exactly corresponds to what one would expect for a second-order phase transition for the shown lattice sizes between $N = 18$ and $N = 54$. For larger lattice sizes one can again observe the problem that the order parameter immediately drops to zero. By minimizing the crossing section for varying critical exponents β/ν with the eye, an optimal intersection point was found for

$$\beta/\nu = 0.96\,. \tag{6.31}$$

This optical method works also quite well for the achievement of an optimized data collapse by systematically extending the coupling regime around zero, as illustrated in Fig. 6.14. Due to the abovementioned unusual behavior for lattice sizes larger than $N = 54$, only the values for $N = 72$ have been added exemplary in Fig. 6.14. Finally, a nice data collapse could be obtained for

$$\nu = 1.1\,, \tag{6.32}$$

leading to $\beta = 1.056$, which is still in markedly good agreement with the finding of $\beta = 1$ from Sec. 4.1. This result justifies the choice of a polynomial fitting procedure of first degree, as already presented in Fig. 6.8.

In the following the critical exponents of the continuous chiral Heisenberg Gross-Neveu model in three spacetime dimensions obtained from either renormalization group approaches in certain expansion schemes or from related Monte-Carlo simulations of discrete Hubbard systems are shown (Tab. 6.1). The table is taken from the summary of Ref. [54] and was originally given in Ref. [132]. The entries of the table where $1/\nu$ and ν is denoted have been evaluated independently. As one can see the obtained results are in really nice accordance to the critical exponents listed in the table, providing a good evidence for the considered model to lie in the Heisenberg Gross-Neveu universality class.

This situation can change by taking the long-range tail of the interaction into account, especially if the screening effects from the inner σ-orbitals are included. These screening effects are mostly important for the short-distance interactions, were the long-range tail can again be dominant in the vicinity of the phase transition. The

	$1/\nu$	β/ν	ν
ϵ expansion [2,2] Padé [105]	0.6426	0.99925	
ϵ expansion [3,1] Padé [105]	0.6447	0.97815	1.2352
Functional RG [106]	0.795	1.016	1.26
Large N [132]	0.8458	1.09245	1.1823
Monte-Carlo [102]		0.74(2)	1.02(1)
Monte-Carlo [104]		0.85(8)	0.84(4)

Table 6.1: For comparison, the critical exponents of the Heisenberg Gross-Neveu model are shown for different expansion schemes as well as the results from Monte-Carlo calculations, taken from Ref. [54].

dominance of the long-range interaction would suggest a conformal phase transition of infinite order [136] in contrary to the Gross-Neveu universality class. In Ref. [40] they found numerical evidence for such a behavior, the inclusion of the long-range interaction would therefore be an interesting extension to the present model.

For the consideration of the critical exponents, the finite size effects regarding the imaginary time lattice are expected to be not relevant, this effect should rather be important concerning dynamical critical exponents. In order to extract a reliable

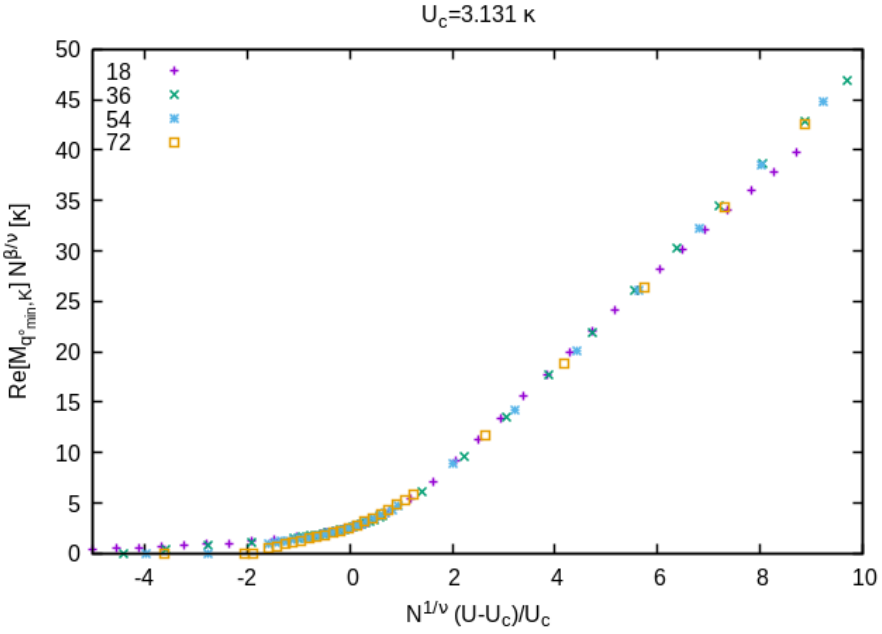

Figure 6.14: Shown is a nice data collapse for the scaled order parameter in dependence of an appropriate scaled reduced control parameter. Due to the described fermionic character of the many body system, data points from lattice sizes equal or greater than $N = 72$ drop out of the data collapse to zero on the left hand side of the critical coupling.

critical coupling for $\beta = 100\ \kappa^{-1}$, these effects again have to be taken into account and they are of course enhanced caused by the highly decreased temperature. In the following we will therefore study the temperature dependence of the critical coupling.

6.4.3 Temperature Dependence

In order to extract the critical coupling, the same procedure as pointed out for $\beta = 20\ \kappa^{-1}$ was undertaken for $\beta = 100\ \kappa^{-1}$ (see Fig. 6.15) and the critical coupling was fixed to about $U_c = 3.45\ \kappa$ by the fit to a straight line. The values slightly differ from zero below the critical coupling, again exhibits finite volume effects from the spatial lattice, which can be nicely compensated by the polynomial fit of first degree which is justified by the findings of the last section ($\beta \approx 1$).

With this approach we were able to determine the critical coupling for temperatures between $\beta = 10\ \kappa^{-1}$ and $\beta = 200\ \kappa^{-1}$ at most. For smaller temperatures the procedure is of course much simpler, here the choice of $N = 90$ and $N_t = 1000$ reveals a good tradeoff between the lattice size in momentum space and the number of lattice points in imaginary time direction with almost no finite volume effects. For inverse temperatures below $\beta = 10\ \kappa^{-1}$ we thus omit the finite size extrapolation

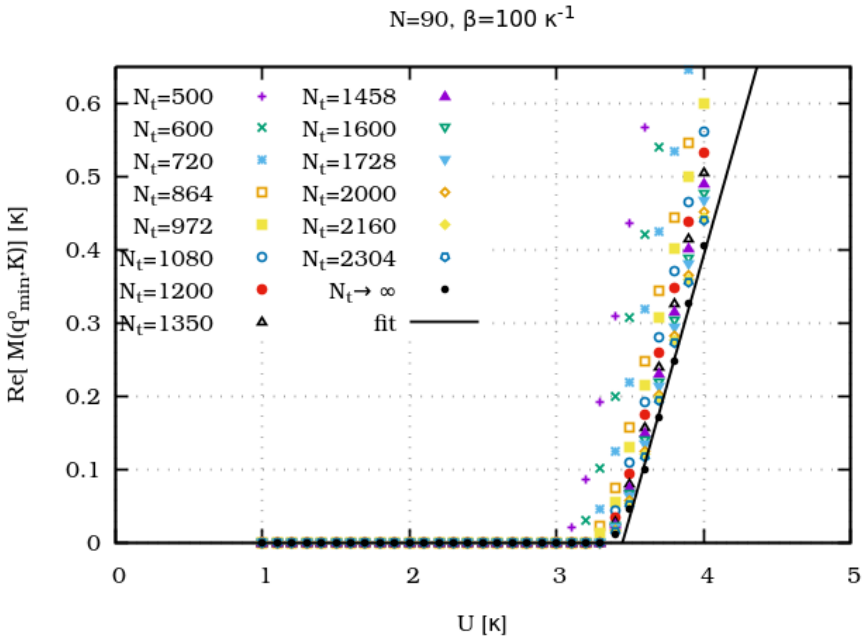

Figure 6.15: The real part of the mass renormalization function at the Dirac point for the minimal Matsubara contribution is plotted against the on-site coupling for various time lattice sizes N_t for a fixed finite temperature of $\beta = 100\,\kappa^{-1}$. As explained in relation with Fig. 6.8 a polynomial fit of second order was used to extrapolate to $N_t \to \infty$. Afterwards the extrapolated values were fitted to a straight line in order to extract the critical on-site coupling.

and determine the critical coupling with the same procedure as in Sec. 4.3, where the error is similarly estimated by the discretization in direction of the on-site coupling. In Fig. 6.16 the order parameter is represented for varying on-site couplings for high temperatures $\beta = 0.3 - 1\,\kappa^{-1}$ for both, the minimal as well as the maximal Matsubara frequency. Here the coincidence for both frequencies in the vicinity of the semimetal insulator transition can be nicely observed. Moreover, the critical on-site coupling increases with increasing temperature, due to higher kinetic energies a stronger on-site coupling is necessary to keep the system into an antiferromagnetic ordered insulator phase.

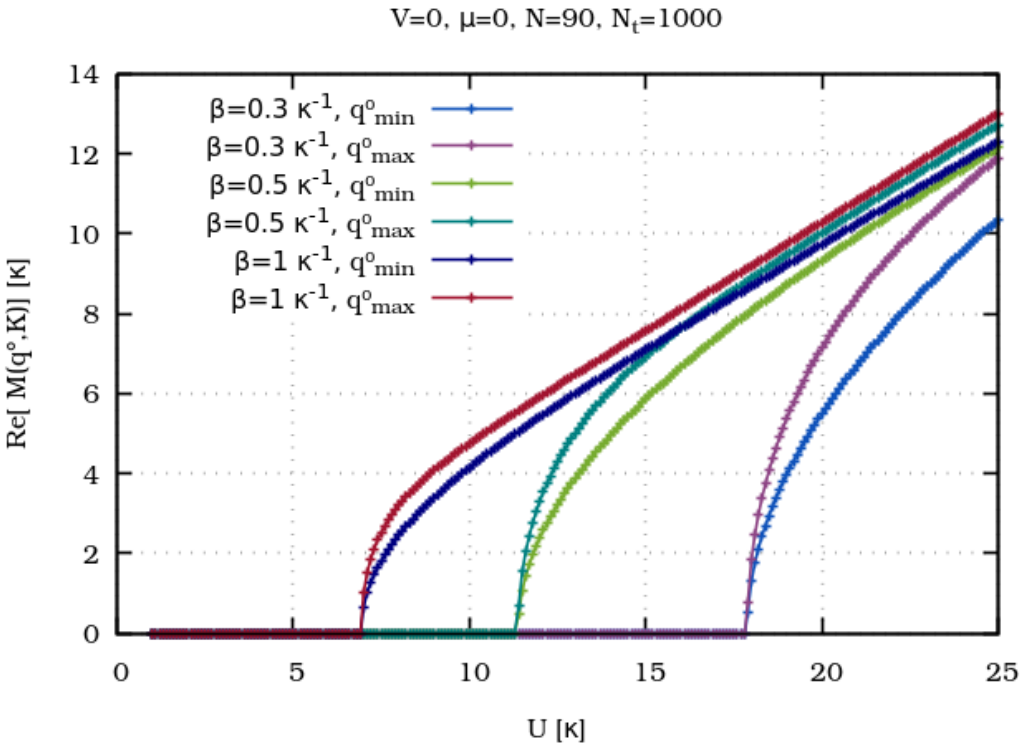

Figure 6.16: The semimetal to insulator transition for the SDW case is illustrated for different temperatures in the high temperature regime. Here we found to be in good accordance with the infinite volume limit $N \to \infty$, $N_t \to \infty$ for $N = 90$ and $N_t = 1000$ lattice points. For comparison the results for the minimal and maximal Matsubara frequency are depicted which are in nice agreement near the critical point.

The final results for the SDW case are shown in Fig. 6.17 where the obtained critical on-site potential is represented for different temperatures in units of the hopping parameter κ. These data points were fitted to a power function and show excellent accordance with the following fit parameters, given by

$$f(x) = 0.35 \cdot (x - 3.43)^{0.84}\,. \tag{6.33}$$

In the high-temperature regime the critical coupling increases fast for an increasing temperature. In order to obtain a critical on-site coupling for $T \to 0$, quite

small temperatures have to be reached, for instance even for $\beta = 20\,\kappa^{-1}$ the critical coupling still drifts to lower values for lower temperatures. Therefore really high lattice sizes N_t in imaginary time direction are necessary which can be provided by using the framework of DSE's as demonstrated in this section.

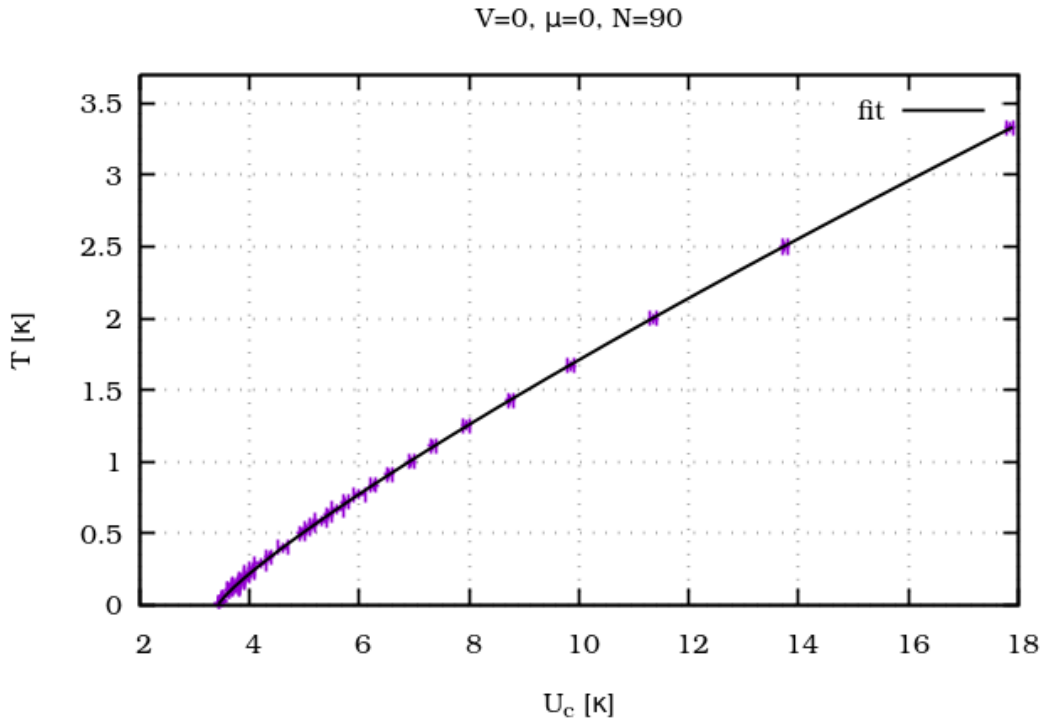

Figure 6.17: The extracted critical on-site coupling is represented for different temperatures in units of the hopping parameter κ. The data points have been fitted to a power function given by Eq. (6.33).

As one can see the extracted critical coupling $U_c \simeq 3.43\,\kappa$ in the applied calculation for $T \to 0$ is merely a bit larger than the on-site coupling of graphene $U_0 \simeq 3.32\,\kappa$ given in Sec. D.2. In the next section we therefore want to discuss the possibility of an infinite chemical potential concerning the charge carrier density as discussed in App. D.2 with $\mu = \mu_\uparrow = \mu_\downarrow$. Experimentally, this could be realized by chemical modification in terms of doping or different substrate possibilities or e.g. by applying a gate voltage.

6.4.4 Phase Diagram

As last step, the μ dependence of SDW state should be investigated. In order to study the μ dependence concerning the CDW phase one has to include effects from $\Pi_k^{AA} \neq \Pi_k^{BB}$ for the vacuum polarization which should not be taken into account within this work. In Sec. 6.3 it was argued that the wavefunction renormalization function even do not decisively influence the antiferromagnetic semimetal insulator transition, at least for small chemical potentials. Within the truncation scheme

keeping $Z_k = 1$, the calculations for $\mu \neq 0$ are of course numerically less expensive. The order parameter shifted by μ, what eventually equates to the single quasi-particle energies at the Dirac point, is illustrated in Fig. 6.18 for different values of μ. Even higher chemical potentials are easily accessible with the applied numerics. For small chemical potentials we found a good agreement with the solution for the included non-ttrivial wavefunction renormalizations (see Fig. 6.5). Above the critical couplings the mass renormalization functions without μ shift all fall onto one line due to the Silverblaze property.

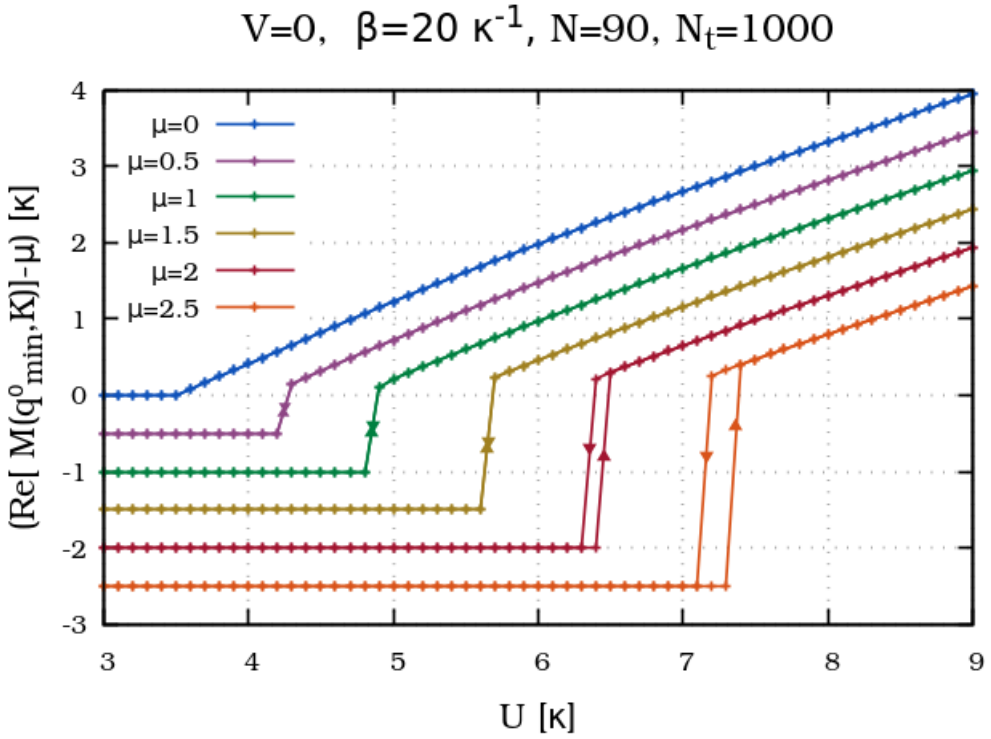

Figure 6.18: The μ dependence for the antiferromagnetic semimetal insulator transition is illustrated within the truncation scheme for $Z_k = 1$.

In the following we want to consider a system which merely exhibits a fixed on-site potential $U = 5\,\kappa$. The coupling is fixed to a value slightly above the critical coupling, exemplary we choose $U = 5\,\kappa$ and $V = 0$ but it could have been fixed to any other coupling pair of the U-V plane. For this system the real phase diagram illustrating the μ-T-dependence of the phase transition was calculated.

As we found a first-order transition for $\mu \neq 0$ as illustrated in Fig. 6.18, the starting point of the iteration was determined to find an upper and lower boundary for the phase transition. In Fig. 6.19 the results are shown for a fixed lattice size, $N = 90$ and $N_t = 1000$. On the left hand side the initial value for the iteration was set to $I = 0.1$ whereas the results for a initial value of $I = 10$ are demonstrated on the right hand side. For small chemical potentials and low temperatures the system persists in an insulating phase realized by an SDW configuration.

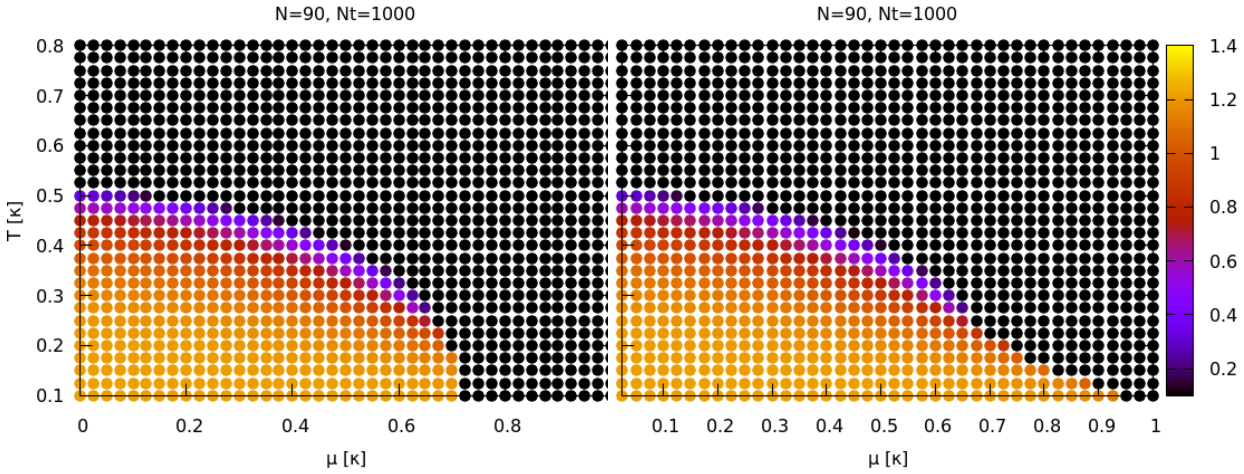

Figure 6.19: An electron system with zero nearest neighbor interaction and a fixed on-site coupling $U = 5\,\kappa$ is investigated. On the left hand side the T-μ phase diagram is shown for a fixed lattice $N = 90$ and $N_t = 1000$ and an initial iteration value of $I = 0.1$. On the right hand side the corresponding results are illustrated for an initial iteration value of $I = 10$. From that the lower and upper boundary of the first-order transition can be determined.

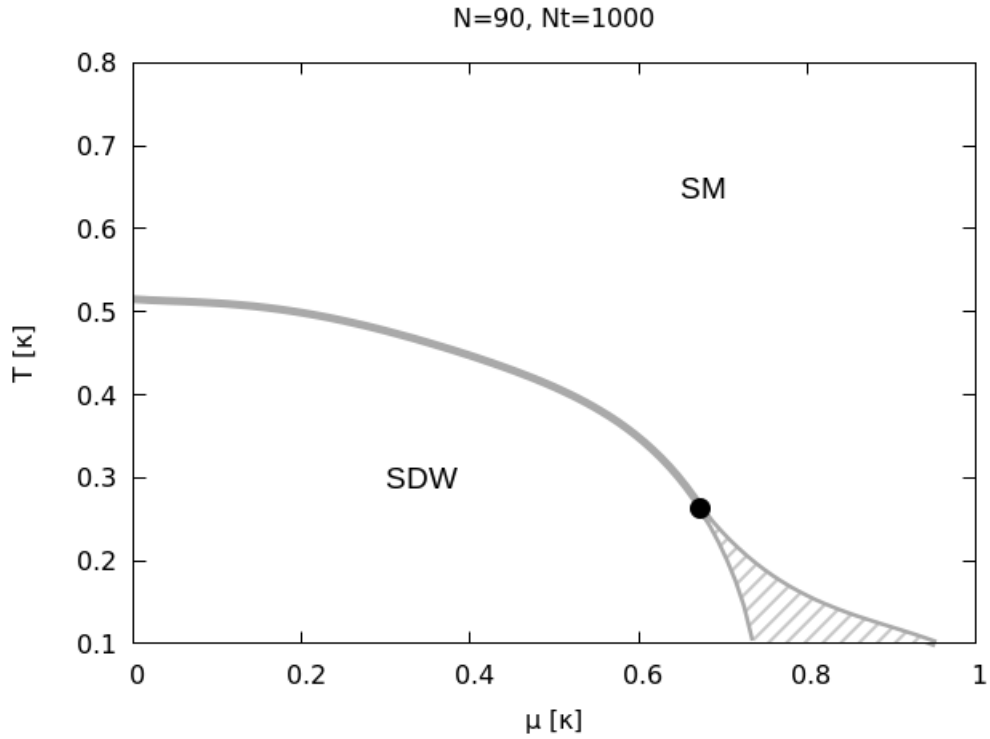

Figure 6.20: The obtained phase diagram from Fig. 6.19 is summarized in order to locate the end point of the first-order transition for the electron system exhibiting a fixed on-site coupling $U = 5\,\kappa$.

The phase diagram resulting from Fig. 6.19 is summarized in Fig. 6.20 where the endpoint of the first-order phase transition is identified by about

$$(\mu, T) = (0.6725, 0.2625)\,\kappa \tag{6.34}$$

within the presented accuracy. This diagram provides an qualitative impression of possible modifications on the location of the phase transition for a strongly correlated electron system with a fixed coupling strength on the hexagonal lattice. Larger chemical potentials as well as higher temperatures at some point pushes the considered electron system into the semimetal phase. Here a quantitative more realistic and also the comparison to such CDW results would be interesting.

7

Summary and Outlook

In this thesis the semimetal to insulator transition of the hexagonal lattice was investigated in regard to a possible SDW or CDW insulating phase [27, 29–31]. Motivated by the strongly coupled electrons of graphene, a tight binding model was applied, the kinetic energy is therefore approximated by nearest neighbor hopping contributions. These contributions are determined by the hopping parameter κ which describes the probability of an electron to hop from one lattice site to an adjacent one [11, 16] and is experimentally fixed to about $\kappa = 2.8\,\mathrm{eV}$. The hopping parameter consequently sets the natural energy unit for the considered theory.

In particular, the realization of two competing phases in the insulator regime, the CDW and SDW configuration, were studied in Sec. 3.3. These configurations represent different vacuum alignments within the same symmetry-breaking pattern, the involved symmetry is an analog of chiral symmetry in QED_{2+1} concerning the sublattice-valley symmetry of the hexagonal lattice as pointed out in Sec. 2.3. This sublattice-valley symmetry can either be broken by an imbalance of the charge carrier distribution or of the spin distribution (CDW or SDW state) which can both cause a dynamical gap leading to an insulator phase of the fermionic many body system.

The fermionic interaction was modeled within a Coulomb interaction neglecting electromagnetic retardation effects due to the small ratio between Fermi velocity and speed of light, $v_f/c \sim 1/300$. Additionally, we followed the approach of an extended Hubbard model in Sec. 3.4, where the long-range tail of the interaction is omitted and only the on-site potential U as well as the nearest neighbor interaction V have been taken into account. In recent studies it was shown that the long-range tail is expected to have only marginal influence on the semimetal insulator transition [24, 25]. Furthermore, the extended Hubbard model provides an optimal framework in order to study the competing order within these insulating phases. This is because a dominating on-site or nearest neighbor potential is directly related

to the preference of an SDW or CDW state, respectively. The coupling strengths U and V of the interaction determine the second important energy scale of the theory and are also specified in units of κ. The kinetic energy and the interaction accordingly are of the same magnitude which defines the coupling parameter to be $\alpha = 2.2$, and makes perturbative methods unfeasible.

According to this we make use of the Dyson-Schwinger framework, representing an effective and successful non-perturbative approach in QED [63, 65, 66, 107, 108] as well as QCD [109, 110] phenomena. In comparison to Quantum Monte Carlo procedures we are not faced with the sign problem and can therefore reach coupling regions beyond $V = U/3$ where the CDW phase becomes interesting. Moreover, the Dyson-Schwinger formalism provides access to huge lattice sizes which is important in order to reduce finite volume effects and extract critical exponents.

The Dyson-Schwinger equations have been derived twofold. In App. C the fermion DSE was deduced from the Heisenberg equation within a Hartree-Fock approximation by means of second quantization, whereas we had to switch to the path integral formalism (App. E) in order to obtain the full set of DSE's also including a dressed photon propagator. The main difference between the CDW and SDW state was proven to be a nonzero Hartree contribution concerning the CDW phase (see Eq. (3.16) or Fig. 3.1). In the first part of this work the interaction is assumed to be static and the temperature as well as the chemical potential was set to zero. In this context, the static approximation ensures the frequency independence of the fermionic renormalization functions and consequently all frequency dependencies could be integrated out analytically. Furthermore, the Ward identity within the static approach requires a bare vertex function and provides a closed set of Dyson-Schwinger equations.

In Chap. 4 several approaches within a mean field theory were discussed. In the first step only the mass renormalization was considered where the critical coupling was found to be analytically accessible [82]. Then bifurcation theory was applied in order to extract the critical exponent of the order parameter $\beta = 1$ also analytically. In a next step, in Sec. 4.3, the renormalization effects on the band structure involving Fermi velocity renormalization was included. The resulting phase transition for the competing electron configurations was represented in Fig. 4.5 where we have also sketched the $V = U/3$-line locating the first-order transition between the SDW state and the CDW state. This $V = U/3$-line was found analytically in Sec. 4.4 by means of the 2PI effective action and turned out to be even valid in the exact theory for $\mu = 0$.

In Chap. 5 the previous model was then extended towards a static approximation considering the screening effects from the π-band electrons itself. In this context the Dyson-Schwinger equation for the photon propagator was dynamically included where the vacuum polarization is approximated by its zero frequency contribution. Except to the static approximation the setup is similar to several studies employing Quantum Monte Carlo techniques for the SDW case [20–24], hence the assumption of a static screening should ideally be validated against these lattice results. Unfortunately, the static approximation was proven to highly overestimate the screening effects and hence the critical on-site coupling at least in the SDW case. For the CDW case the deviation from the Hartree-Fock approximation is much smaller and therefore the results seem to be much more reliable.

However, in order to find an appropriate approximation, the fully frequency dependent photon propagator was taken into account in Chap. 6. Based on the frequency dependent interaction, the fermionic renormalization functions become frequency dependent too, which requires a dressed vertex function. Due to fulfill the Ward Takahashi identity, a kind of simplified Ball Chiu vertex ansatz was chosen to account for vertex corrections. This likewise asks for a dressed wavefunction renormalization which is thus dynamically included. The numerical results within this truncation scheme supply clear evidence that the contained wavefunction renormalization do not have a considerable influence on the quantities of interest, not for the SDW case and even less regarding the CDW case. For this reason the wavefunction renormalization is again fixed to its bare value in order to reach even larger lattice sizes and in order to save run time.

The obtained critical coupling values for the SDW case are then found to be in satisfying accordance with comparable lattice results [20–23, 31, 40, 54] why we assume to end up with an appropriate truncation scheme. The obtained phase diagram representing the semimetal to insulator transition regarding the SDW as well as the CDW case is shown in Fig. 6.12. In general, the results for the CDW configuration seem to be much more stable throughout the applied approximations which suggests that it is dominantly affected by the Hartree term of the self-energy.

With a finally reasonable truncation scheme at hand, we additionally investigated the critical exponents of the theory which were found to be in nice agreement with the critical exponents that were expected within a Gross-Neveu universality class [30, 84, 100, 101]. Moreover, we could not find a deviation from $\beta = 1$ for the critical exponent of the order parameter within our numerical accuracy. Apart from that we investigated the temperature dependence of the critical on-site coupling as well as the influence from a finite chemical potential μ. The T-μ phase diagram for an exemplary on-site coupling of $U = 5\,\kappa$ and zero nearest neighbor interaction was calculated and is represented in Fig. 6.20.

On the basis of the established truncation scheme there are several further interesting scenarios that can be investigated by only small modifications of the existing numerical setup. For instance, the extension to possible deviations between the interactions on the different sublattices, $V^{AA} \neq V^{BB}$, would make the semimetal insulator transition accessible for the CDW case at finite μ. Also a similar finite-size scaling and the investigation of the temperature dependence of the critical coupling for the CDW phase would be interesting and is already in progress. Furthermore, the numerical realization of real competing phases within one system would be reasonable in order to even find possible stable mixed states. This ansatz has already been implemented numerically but with the choice of the initial iteration value one likewise determines a preference of the system towards either an SDW or an CDW realization. This problem might be solved by randomly distributed positive and negative initial values and could be part of a future project. Also the possibility of an external magnetic field [111, 112] could be studied in order to push graphene into the insulating phase. Another interesting model is motivated by the introduction of an arbitrary number of fermion flavors N_f regarding many flavor QED_{2+1} [113] or for instance also the so-called t-V model where the CDW case for $N_f = 1$ and zero on-site coupling is considered. Furthermore the inclusion of the long-range interaction [69, 114] or an improved Hubbard model [115] could provide a next step, here we

would not expect remarkable changes in the location of the semimetal insulator transition. In this context also the inclusion of screening effects from inner σ-electrons can be interesting (see [69]) since it mainly affects the short-range interaction and could lead to a dominant long-range interaction in the vicinity of the phase transition which would manifest itself in a conformal phase transition as suggested in Ref. [40].

Beyond these simple extensions, the investigation of other hexagonal structures with different structure functions as introduced in Chap. 1 or also allotropes of graphene (see Chap. 2) such as bilayer graphene would be exciting.

A

Notation and Relations

A.1 Basis of the Hexagonal Lattice

In the following the characteristic quantities for two possible lattice representations for the hexagonal lattice are listed.

Representation 1

Basis vectors in position space:

$$\boldsymbol{a}_1 = a \begin{pmatrix} 0 \\ 1 \end{pmatrix}, \qquad \boldsymbol{a}_2 = \frac{a}{2} \begin{pmatrix} \sqrt{3} \\ -1 \end{pmatrix}. \tag{A.1}$$

Basis vectors in momentum space:

$$\boldsymbol{b}_1 = \frac{2\pi}{3a} \begin{pmatrix} \sqrt{3} \\ 3 \end{pmatrix}, \qquad \boldsymbol{b}_2 = \frac{4\pi}{3a} \begin{pmatrix} \sqrt{3} \\ 0 \end{pmatrix}. \tag{A.2}$$

Unit cell area in position space: $\mathcal{A}_c = |\boldsymbol{a}_1 \times \boldsymbol{a}_2| = \sqrt{3}\, a^2/2$.

Area of the Brillouin zone: $\mathcal{BZ} = |\boldsymbol{b}_1 \times \boldsymbol{b}_2| = 8\pi^2/\sqrt{3}\, a^2$.

Nearest neighbour vectors:

$$\boldsymbol{\delta}_1 = \boldsymbol{a}_1, \qquad \boldsymbol{\delta}_2 = \boldsymbol{a}_2, \qquad \boldsymbol{\delta}_3 = -(\boldsymbol{a}_1 + \boldsymbol{a}_2). \tag{A.3}$$

The discrete position vector and the associated vector on the discrete momentum lattice within the Brioullin zone is given by

$$\boldsymbol{k}_{mn} = \frac{1}{N}(m\,\boldsymbol{b}_1 + n\,\boldsymbol{b}_2), \qquad \boldsymbol{r}_{ij} = i\,\boldsymbol{a}_1 + j\,\boldsymbol{a}_2, \tag{A.4}$$

the structure function therefore reads

$$\varphi_{mn} = \sum_{n=1}^{3} e^{\mathrm{i}\,\boldsymbol{k}\boldsymbol{\delta}_n} = e^{\frac{2\pi\mathrm{i}}{3N}m} + e^{\frac{2\pi\mathrm{i}}{3N}n} + e^{\frac{-2\pi\mathrm{i}}{3N}(m+n)} \tag{A.5}$$

and fulfills several symmetry transformations and in particular all boundary conditions,

$$\varphi_{mn} = \varphi_{m+Nn+N}\,, \qquad \varphi_{mn} = \varphi^*_{N-mN-n}\,, \qquad \varphi_{mn} = \varphi_{nm}\,, \tag{A.6}$$

(see Eq. (A.13)) and

$$\varphi_{mn} = \varphi_{m+Nn}\,, \qquad \varphi_{mn} = \varphi_{mn+N}\,. \tag{A.7}$$

Representation 2

Basis vectors in position space:

$$\boldsymbol{a}_1 = \frac{a}{2}\begin{pmatrix}\sqrt{3}\\ 3\end{pmatrix}, \qquad \boldsymbol{a}_2 = \frac{a}{2}\begin{pmatrix}\sqrt{3}\\ -3\end{pmatrix}. \tag{A.8}$$

Basis vectors in momentum space:

$$\boldsymbol{b}_1 = \frac{2\pi}{3a}\begin{pmatrix}\sqrt{3}\\ 1\end{pmatrix}, \qquad \boldsymbol{b}_2 = \frac{2\pi}{3a}\begin{pmatrix}\sqrt{3}\\ -1\end{pmatrix}. \tag{A.9}$$

Unit cell area in position space: $\mathcal{AZ} = |\boldsymbol{a}_1 \times \boldsymbol{a}_2| = \frac{3\sqrt{3}a^2}{2}$.

Area of the Brillouin zone: $\mathcal{BZ} = |\boldsymbol{b}_1 \times \boldsymbol{b}_2| = \frac{8\pi^2}{3\sqrt{3}a^2}$.

Nearest neighbour vectors:

$$\boldsymbol{\delta}_1 = \frac{\boldsymbol{a}_1 - \boldsymbol{a}_2}{3}\,, \qquad \boldsymbol{\delta}_2 = \frac{\boldsymbol{a}_1 + 2\boldsymbol{a}_2}{3}\,, \qquad \boldsymbol{\delta}_3 = -\frac{2\boldsymbol{a}_1 + \boldsymbol{a}_2}{3}\,. \tag{A.10}$$

The position and momentum space vectors are discretized as in Eq. (A.4) and the corresponding structure function is given by

$$\varphi_{mn} = \sum_{n=1}^{3} e^{\mathrm{i}\,\boldsymbol{k}\boldsymbol{\delta}_n} = e^{\frac{2\pi\mathrm{i}}{3N}(m-n)} + e^{\frac{2\pi\mathrm{i}}{3N}(m+2n)} + e^{\frac{-2\pi\mathrm{i}}{3N}(2m+n)}\,, \tag{A.11}$$

which also fulfills (compare with Eq. (A.6) and Eq. (A.7))

$$\varphi_{mn} = \varphi_{m+Nn+N}, \qquad \varphi_{mn} = \varphi^*_{N-mN-n}, \qquad \varphi_{mn} = \varphi^*_{nm}\,, \tag{A.12}$$

but not the boundary conditions given by

$$\varphi_{mn} \neq \varphi_{m+Nn}\,, \qquad \varphi_{mn} \neq \varphi_{mn+N}\,. \tag{A.13}$$

Note that this basis is sufficient for considerations which only depend on the absolute value $|\varphi_{mn}|$ since the absolute value again complies with the boundary conditions of Eq. (A.13). Nevertheless, in order to generalize φ to a renormalization function within the Dyson-Schwinger formalism one needs to distinguish between φ and φ^* and therefore one has to use the basis representation 1, discussed above.

A.2 Mathematical Relations

Dirac Matrices

The following Dirac matrices are introduced in the two-dimensional sublattice space

$$\gamma_0 = \sigma_3, \qquad \gamma_i = \sigma_3\ \sigma_i\,, \tag{A.14}$$

with $i = 1, 2$, satisfying the Clifford algebra $\{\gamma_\mu, \gamma_\nu\} = 2g_{\mu\nu}$ with $g_{\mu\nu} = \mathrm{diag}(1, -1, -1)$ for $\mu, \nu \in \{0, 1, 2\}$. The matrices σ_i label the standard Pauli matrices given by

$$\sigma_0 = \begin{pmatrix} 1 & 0 \\ 0 & 1 \end{pmatrix}, \qquad \sigma_1 = \begin{pmatrix} 0 & 1 \\ 1 & 0 \end{pmatrix}, \qquad \sigma_2 = \begin{pmatrix} 0 & -\mathrm{i} \\ \mathrm{i} & 0 \end{pmatrix}, \qquad \sigma_3 = \begin{pmatrix} 1 & 0 \\ 0 & -1 \end{pmatrix}. \tag{A.15}$$

Gaussian Integrals

The n-dimensional form of the Gaussian integral, with J and ϕ denoting n-dimensional fields and A being an $n \times n$ matrix, is given by

$$\int \frac{\mathcal{D}\phi}{(2\pi)^{\frac{n}{2}}}\, e^{-\frac{1}{2}\phi_i A_{ij} \phi_j + \phi_i J_i} = [\det A]^{-\frac{1}{2}}\, e^{\frac{1}{2} J_i A^{-1}_{ij} J_j}\,, \tag{A.16}$$

where the product of field integrations is commonly abbreviated by

$$\mathcal{D}\phi = \prod_{m=1}^{n} \phi_m\,. \tag{A.17}$$

For the integration over fermionic complex fields the behavior of the complex Grassmann valued variables has to be taken into account (see e.g. Ref. [85, 116]) wherefore one obtains

$$\int \mathcal{D}\eta^* \mathcal{D}\eta\, e^{-\eta_i^* A_{ij} \eta_j + \xi_i^* \eta_i + \xi_i \eta_i^*} = [\det A]\, e^{\xi_i^* A^{-1}_{ij} \xi_j} \tag{A.18}$$

as fermionic version of the Gaussian integral. Note that in the bosonic case the inverse of the determinant appears. The determinant in the numerator results from a coordinate transformation for Grassmann valued variables [116].

Hubbard-Stratonovich Transformation

The transformation introduced by Strotonovich and Hubbard [117] makes use of the above presented Gaussian integrals to construct a quantum field theory in which the interaction is permitted by bosonic gauge fields. These gauge fields are introduced by the transformation of a Gaussian integral, where exponents of quadratic powers in the fermionic density fields are converted into an integral over an auxilary bosonic field (that plays the role of a gauge field) that is now linearly coupled to the fermionic density [70, 116],

$$e^{\frac{\delta}{2}\rho_i V_{ij}\rho_j} = [\det((\delta\, V)^{-1})]^{\frac{1}{2}} \int \frac{\mathcal{D}\sigma}{(2\pi)^{n/2}}\; e^{-\frac{\delta}{2}\sigma_i V_{ij}^{-1}\sigma_j + \delta\,\sigma_i\rho_i}\,, \tag{A.19}$$

where n represents the dimension of the field vector and V is an $n \times n$ matrix. For a negative sign in the exponent, a complex coupled field is needed [116]

$$e^{-\frac{\delta}{2}\rho_i V_{ij}\rho_j} = [\det((\delta\, V)^{-1})]^{\frac{1}{2}} \int \frac{\mathcal{D}\sigma}{(2\pi)^{n/2}}\; e^{-\frac{\delta}{2}\sigma_i V_{ij}^{-1}\sigma_j - \mathrm{i}\,\delta\,\sigma_i\rho_i}\,. \tag{A.20}$$

B

Minkowski and Euclidean Spacetime

B.1 Three-Vector Notation and Fourier Transform

Minkowski spacetime

For the Minkowskian spacetime we define the common vector notation with real-time variable $t = x^0$ and the corresponding Minkowskian action and Lagrangian, denoted by $\mathcal{S}_M$ and $\mathcal{L}_M$ respectively,

$$x \equiv (t, \boldsymbol{x})\,, \qquad \mathcal{S}_M = \int\!\!\!\!\!\!\diagup_x \mathcal{L}_M \quad \text{with} \quad \int\!\!\!\!\!\!\diagup_x \equiv \sum_{\boldsymbol{x}} \int dx^0\,, \tag{B.1}$$

where $\mathbf{x}$ is a two-dimensional vector of the discrete honeycomb lattice generally given by

$$\boldsymbol{x} = i\,\boldsymbol{a}_1 + j\,\boldsymbol{a}_2\,, \tag{B.2}$$

explicitly described in App. A.1. The spatial sum means the sum over the lattice indices i and j and still contains the sum over the sublattices A and B as well as the sum over unoccupied sites for the finer triangular lattice (App. A.1). However, the summands are often restricted to one sublattice as described by (see also Eq. (2.15))

$$\xi_a(x) = \begin{cases} \xi(t,\boldsymbol{x})\,, & \boldsymbol{x} \text{ on sublattice } A, \\ 0\,, & \text{otherwise,} \end{cases} \quad \text{and} \quad \xi_b(x) = \begin{cases} \xi(t,\boldsymbol{x})\,, & \boldsymbol{x} \text{ on sublattice } B, \\ 0\,, & \text{otherwise.} \end{cases} \tag{B.3}$$

For the transition to a continuous spatial integral, of course the area of the unit cell $\mathcal{A}_c$ has to be taken into account

$$\mathcal{A}_c \sum_{\boldsymbol{x}} = \mathcal{A}_c \sum_{i,j} \quad \longrightarrow \quad \int d^2x \tag{B.4}$$

The corresponding frequency-momentum space description results by a Fourier transform

$$f(x) = \sum\!\!\!\!\!\!\int_k \tilde{f}(k)\; e^{-\mathrm{i}\,kx} \quad \text{with} \quad k \equiv (k^0, \boldsymbol{k}) \quad \text{and} \quad \sum\!\!\!\!\!\!\int_k \equiv \frac{1}{N^2} \sum_{\boldsymbol{k}} \int \frac{dk^0}{2\pi}\,, \tag{B.5}$$

with the common Minkowski metric as defined in App. A.2, the inner product is given by

$$k \cdot x = k^0 x^0 - \boldsymbol{k}\,\boldsymbol{x}\,. \tag{B.6}$$

Here the lattice decomposition from above accordingly demands for a discretization of momentum space

$$\boldsymbol{k} = \frac{1}{N}(m\,\boldsymbol{b}_1 + n\,\boldsymbol{b}_2)\,, \tag{B.7}$$

with normalized basis vectors $\boldsymbol{a}_i \cdot \boldsymbol{b}_j = 2\pi\delta_{ij}$. The sum over $\boldsymbol{k}$ therefore means the sum over momentum space indices m and n, providing an usual discrete Fourier transform between spatial and momentum space variables. A transition to a continuous description can be realized by

$$\frac{\mathcal{BZ}}{N^2\,(2\pi)^2} \sum_{\boldsymbol{k}} = \frac{\mathcal{BZ}}{N^2\,(2\pi)^2} \sum_{m,n} \quad \longrightarrow \quad \int \frac{d^2k}{(2\pi)^2}\,, \tag{B.8}$$

with $\mathcal{BZ}$ being the surface area of the Brioullin zone as defined in App. A.1 and $\mathcal{A}_c \cdot \mathcal{BZ} = (2\pi)^2$.

Euclidean spacetime

For Euclidean spacetime we take an analog notation with the three-vector

$$x_E \equiv (x_E^0, \boldsymbol{x}) \quad \text{and} \quad S_E = \sum\!\!\!\!\!\!\int_{x_E} L_E \quad \text{with} \quad \sum\!\!\!\!\!\!\int_{x_E} \equiv \sum_{\boldsymbol{x}} \int dx_E^0\,, \tag{B.9}$$

where S_E is the Euclidean action with the corresponding Euclidean Lagrangian L_E. The Euclidean time x_E^0 is denoted by τ as usual.

Fourier analysis then results with standard Matsubara frequencies k_n as follows

$$f(x_E) = \sum\!\!\!\!\!\!\int_{k_E} \tilde{f}(k_E)\; e^{\mathrm{i}\,k_E\,x_E} \quad \text{with} \quad k_E \equiv (k_E^0, \boldsymbol{k}) \quad \text{and} \quad \sum\!\!\!\!\!\!\int_{k_E} \equiv \frac{1}{N^2} \sum_{\boldsymbol{k}} \int \frac{d\omega}{2\pi}\,, \tag{B.10}$$

where the Euclidean scalar product can be identified by

$$k_E \cdot x_E = \omega\tau + \boldsymbol{k}\,\boldsymbol{x}\,, \tag{B.11}$$

with $\boldsymbol{k}$ and $\boldsymbol{x}$ as explained above and the Euclidean frequency is denoted by ω.

The transition from Minkowski to Euclidean spacetime is related to some ambiguous analytical continuation. The direct formal continuation is carried out by a Wick rotation, which is here defined by $t \to \mathrm{i}\,\tau$ and $k^0 \to \mathrm{i}\,\omega$. For finite temperature, the frequency integral from Eq. (B.9) is finite as well,

$$\int dx_E^0 \to \int_0^\beta dx_E^0\,,$$

with the inverse temperature $\beta = 1/T$, leading to discrete periodic functions in frequency space characterized by the standard Matsubara frequencies $\omega_n = (2n + 1)\pi/\beta$ for antiperiodic and $\omega_n = 2\pi n/\beta$ for periodic boundary conditions, i.e. for a fermionic and bosonic behavior respectively. Consequently the continuous frequency integral is rewritten in terms of a discrete Matsubara sum for finite temperature considerations [118]

$$\int \frac{d\omega}{2\pi} \to \frac{1}{\beta} \sum_n \qquad \text{and} \qquad \int\!\!\!\!\!\!\sum_{k_E} \to \frac{1}{\beta N^2} \sum_{\boldsymbol{k},n} . \tag{B.12}$$

Conventions of propagators in different time formalisms

In the following we want to investigate the transition between the Euclidean propagator marked with a subscript E and the corresponding Feynman propagator G_F. In general the action in Minkowski space $\mathcal{S}_M$ should satisfy the following equation

$$\mathcal{Z} = \int \mathcal{D}\Phi_\alpha \; e^{-S_E[\Phi_\alpha]} = \int \mathcal{D}\Phi_\alpha \; e^{i\,\mathcal{S}_M[\Phi_\alpha]} , \tag{B.13}$$

where α labels arbitrary quantum fields. For simplicity we consider the bare fermionic action which was obtained directly from path integral formalism (see App. E) and is given by

$$S_E^0 = \sum_\sigma \int\!\!\!\!\!\!\sum_{x_E} \int\!\!\!\!\!\!\sum_{x'_E} \bar{\psi}(x_E) \; G^0_{E,\sigma}(x_E - x'_E)^{-1} \; \psi(x'_E) , \tag{B.14}$$

where σ indicates the spin index and the Euclidean propagator in position space is given by

$$G^0_{E,\sigma}(x_E - x'_E)^{-1} = \begin{pmatrix} (\partial_\tau - \mu_\sigma + m_\sigma)\,\delta(x_E - x'_E) & -\kappa \sum_{l=0}^{2} \delta_{\boldsymbol{x}+\boldsymbol{\Delta}\,l,\boldsymbol{x}'}\,\delta_{\tau\tau'} \\ \kappa \sum_{l=0}^{2} \delta_{\boldsymbol{x}+\Delta\,l,\boldsymbol{x}'}\,\delta_{\tau\tau'} & (-\partial_\tau + \mu_\sigma + m_\sigma)\,\delta(x_E - x'_E) \end{pmatrix} . \tag{B.15}$$

In momentum space we obtain

$$S_E^0 = \sum_\sigma \int\!\!\!\!\!\!\sum_{k_E} \bar{\psi}(k_E)\, G^0_{E,\sigma}(k_E)^{-1}\, \psi(k_E) \tag{B.16}$$

with

$$G^0_{E,\sigma}(k_E)^{-1} = \begin{pmatrix} -\mathrm{i}\; k_E^0 - \mu_\sigma + m_\sigma & -\kappa\,\varphi_{\boldsymbol{k}} \\ \kappa\,\varphi^*_{\boldsymbol{k}} & \mathrm{i}\; k_E^0 + \mu_\sigma + m_\sigma \end{pmatrix} . \tag{B.17}$$

This can be related to the Minkowskian notation where the action is given by

$$\mathcal{S}_M^0 = \sum_\sigma \int\!\!\!\!\!\!\sum_{k} \bar{\psi}(k)\,\mathrm{i}\; G^0_{F,\sigma}(k)^{-1}\, \psi(k) , \tag{B.18}$$

so the associated Green functions are connected via

$$G^0_E(k_E)^{-1} = -\mathrm{i}\, G_F(k^0 = \mathrm{i}\, k_E^0)^{-1} , \tag{B.19}$$

with the bare inverse fermion propagator in momentum space

$$G^0_{F,\sigma}(k)^{-1} = \mathrm{i} \begin{pmatrix} -k^0 - \mu_\sigma + m_\sigma & -\kappa\, \varphi_{\boldsymbol{k}} \\ \kappa\, \varphi^*_{\boldsymbol{k}} & k^0 + \mu_\sigma + m_\sigma \end{pmatrix} \tag{B.20}$$

The corresponding propagator is found to be

$$G^0_{F,\sigma}(k) = \frac{\mathrm{i}}{(k^0 + \mu_\sigma)^2 - (m_\sigma^2 + \kappa^2 |\varphi_{\boldsymbol{k}}|^2) + \mathrm{i}\,\epsilon} \begin{pmatrix} k^0 + \mu_\sigma + m_\sigma & \varphi_{\boldsymbol{k}} \kappa \\ -\varphi^*_{\boldsymbol{k}} \kappa & -k^0 - \mu_\sigma + m_\sigma \end{pmatrix}. \tag{B.21}$$

For completeness we also want to specify the Feynman propagator in position space

$$G^0_{F,\sigma}(x - x')^{-1} = \mathrm{i} \begin{pmatrix} (-\mathrm{i}\, \partial_t - \mu_\sigma + m_\sigma)\, \delta(x - x') & -\kappa \sum_{l=0}^{2} \delta_{\boldsymbol{x} + \boldsymbol{\Delta}\, l, \boldsymbol{x}'}\, \delta_{tt'} \\ \kappa \sum_{l=0}^{2} \delta_{\boldsymbol{x} + \Delta\, l, \boldsymbol{x}'}\, \delta_{tt'} & (\mathrm{i}\, \partial_t + \mu_\sigma + m_\sigma)\, \delta(x - x') \end{pmatrix}. \tag{B.22}$$

C

The Fermionic DSE's from the Heisenberg Equations

C.1 The Free Propagator

At first, the free fermion propagator should be derived from the Heisenberg equations for the non-interacting Hamiltonian $\mathcal{H}_0$ from Eq. (2.28). With the time ordered propagator for fermionic fields

$$\langle T(c_{i,\boldsymbol{k},\sigma}(t)c^\dagger_{j,\boldsymbol{k},\sigma}(0))\rangle = \begin{cases} \langle c_{i,\boldsymbol{k},\sigma}(t)c^\dagger_{j,\boldsymbol{k},\sigma}(0)\rangle & t \geq 0 \\ -\langle c^\dagger_{j,\boldsymbol{k},\sigma}(0)c_{i,\boldsymbol{k},\sigma}(t)\rangle & t < 0 \end{cases} \tag{C.1}$$

$$= \Theta(t)\ \langle c_{i,\boldsymbol{k},\sigma}(t)c^\dagger_{j,\boldsymbol{k},\sigma}(0)\rangle - \Theta(-t)\ \langle c^\dagger_{j,\boldsymbol{k},\sigma}(0)c_{i,\boldsymbol{k},\sigma}(t)\rangle\,, \tag{C.2}$$

where i and j denote sublattice indices, with $i, j \in \{0, 1\}$ for the A and B lattice respectively.

The time differenciated propagator then is given by

$$\frac{d}{dt}G^{ij}_{F,\sigma}(t,\boldsymbol{k}) = \frac{3}{N^2}(-1)^j \left(\Theta(t)\ \langle \dot{c}_{i,\boldsymbol{k},\sigma}(t)c^\dagger_{j,\boldsymbol{k},\sigma}(0)\rangle - \Theta(-t)\ \langle c^\dagger_{j,\boldsymbol{k},\sigma}(0)\dot{c}_{i,\boldsymbol{k},\sigma}(t)\rangle\right) \tag{C.3}$$

$$+ \frac{3}{N^2}(-1)^j\,\delta(t)\ \langle [c_{i,\boldsymbol{k},\sigma}(t), c^\dagger_{j,\boldsymbol{k},\sigma}(0)]_+\rangle \tag{C.4}$$

$$= \frac{3}{N^2}(-1)^j\,\langle T(\dot{c}_{i,\boldsymbol{k},\sigma}(t)c^\dagger_{j,\boldsymbol{k},\sigma}(0))\rangle + (-1)^j\,\delta(t)\,\delta_{ij} \tag{C.5}$$

with the anti-commutator relations from Eq. (2.22). The time dependence of the operator can be derived from the Heisenberg equation ($\hbar = 1$)

$$\mathrm{i}\,\frac{\partial}{\partial t}c_{i,\boldsymbol{k},\sigma}(t) = -[\mathcal{H}_0, c_{i,\boldsymbol{k},\sigma}(t)]_-\,, \tag{C.6}$$

where the minus sign now refers to the commutator instead of the anti-commutator indicated by a plus sign. For the commutator one finds

$$[\mathcal{H}_0, c_{i,\boldsymbol{k},\sigma}]_- = \frac{\kappa}{N^2} \sum_{\boldsymbol{k}',\sigma'} \left([a^\dagger_{\boldsymbol{k}',\sigma'}, c_{i,\boldsymbol{k},\sigma}]_+ \; \phi_{\boldsymbol{k}'} \, b_{\boldsymbol{k}',\sigma'} + [b^\dagger_{\boldsymbol{k}',\sigma'}, c_{i,\boldsymbol{k},\sigma}]_+ \; \phi^*_{\boldsymbol{k}'} \, a_{\boldsymbol{k}',\sigma'} \right) \tag{C.7}$$

$$+ \mu_\sigma \, c_{i,\boldsymbol{k},\sigma} + (-1)^i \; m_\sigma \, c_{i,\boldsymbol{k},\sigma} \, . \tag{C.8}$$

With the symmetry transformations from Chap. 2

$$\phi_{\boldsymbol{k}+l\Delta} = e^{\frac{2\pi \mathrm{i}}{3} l} \phi_{\boldsymbol{k}} \, , \qquad b_{\boldsymbol{k}+l\Delta} = e^{-\frac{2\pi \mathrm{i}}{3} l} b_{\boldsymbol{k}} \, , \tag{C.9}$$

and

$$\phi^*_{\boldsymbol{k}+l\Delta} = e^{-\frac{2\pi \mathrm{i}}{3} l} \phi^*_{\boldsymbol{k}} \, , \qquad a_{\boldsymbol{k}+l\Delta} = a_{\boldsymbol{k}} \, , \tag{C.10}$$

the following equations were found

$$\mathrm{i} \, \dot{a}_{\boldsymbol{k},\sigma}(t) = -\kappa \phi_{\boldsymbol{k}} b_{\boldsymbol{k},\sigma}(t) - \mu_\sigma a_{\boldsymbol{k},\sigma}(t) + m_\sigma a_{\boldsymbol{k},\sigma}(t) \, , \tag{C.11}$$

$$\mathrm{i} \, \dot{b}_{\boldsymbol{k},\sigma}(t) = -\kappa \phi^*_{\boldsymbol{k}} a_{\boldsymbol{k},\sigma}(t) - \mu_\sigma b_{\boldsymbol{k},\sigma}(t) - m_\sigma b_{\boldsymbol{k},\sigma}(t) \, . \tag{C.12}$$

By multiplying with the appropriate creation operator at $t = 0$, the matrix equation for the free fermion propagator can be obtained

$$\frac{d}{dt} G^0_{F,\sigma}(t, \boldsymbol{k}) = \underbrace{-\mathrm{i} \begin{pmatrix} -\mu_\sigma + m_\sigma & -\phi_{\boldsymbol{k}} \kappa \\ -\phi^*_{\boldsymbol{k}} \kappa & -\mu_\sigma - m_\sigma \end{pmatrix}}_{M_0} G^0_{F,\sigma}(t, \boldsymbol{k}) + \delta(t) \; \gamma^0 \, . \tag{C.13}$$

Fourier transforming this expression into frequency space yields

$$\int dt \, \frac{dG^0_{F,\sigma}(t, \boldsymbol{k})}{dt} \, e^{\mathrm{i} \, k^0 t} = -\mathrm{i} \, k^0 G^0_{F,\sigma}(k^0, \boldsymbol{k}) \, . \tag{C.14}$$

By Fourier transforming Eq. (C.13), the free fermion propagator is given by

$$G^0_{F,\sigma}(k^0, \boldsymbol{k})^{-1} = -\mathrm{i} \begin{pmatrix} k^0 + \mu_\sigma - m_\sigma & \phi_{\boldsymbol{k}} \kappa \\ -\phi^*_{\boldsymbol{k}} \kappa & -k^0 - \mu_\sigma - m_\sigma \end{pmatrix} , \tag{C.15}$$

and its associated inverse matrix with appropriate Feynman boundary conditions

$$G^0_{F,\sigma}(k^0, \boldsymbol{k}) = \frac{\mathrm{i}}{(k^0 + \mu_\sigma)^2 - (m_\sigma^2 + \kappa^2 |\phi_{\boldsymbol{k}}|^2) + \mathrm{i} \, \epsilon} \begin{pmatrix} k^0 + \mu_\sigma + m_\sigma & \phi_{\boldsymbol{k}} \kappa \\ -\phi^*_{\boldsymbol{k}} \kappa & -k^0 - \mu_\sigma + m_\sigma \end{pmatrix} . \tag{C.16}$$

C.2 The Interacting Propagator

Exactly the same procedure should now be repeated for the interacting theory. The Coulomb interaction on the honeycomb lattice in momentum space is given in Eq. (3.14) and can be separated into its sublattice contributions via

$$\mathcal{H}_{\mathcal{C}}{}^{ij} = \frac{1}{2N^6} \sum_{\boldsymbol{k},\boldsymbol{p},\boldsymbol{q},\sigma,\sigma'} V^{ij}_{\boldsymbol{q}} \; c^\dagger_{i,\boldsymbol{p}+\boldsymbol{q},\sigma}(t) \, c^\dagger_{j,\boldsymbol{k}-\boldsymbol{q},\sigma'}(t) \, c_{j,\boldsymbol{k},\sigma'}(t) \, c_{i,\boldsymbol{p},\sigma}(t) \, , \tag{C.17}$$

where the time index is again supressed in the following. The corresponding commutator is finally given by

$$[\mathcal{H}\mathcal{C}^{ij}, c_{v,\boldsymbol{k}',s}]_- = \frac{1}{2N^4}\sum_{\boldsymbol{p},\boldsymbol{q},\sigma} V_{\boldsymbol{q}}^{ij}\ (\delta_{vj}\, c^\dagger_{i,\boldsymbol{p}+\boldsymbol{q},\sigma}\, c_{v,\boldsymbol{k}'+\boldsymbol{q},s}\, c_{i,\boldsymbol{p},\sigma} - \delta_{iv}\, c^\dagger_{j,\boldsymbol{p}-\boldsymbol{q},\sigma}\, c_{j,\boldsymbol{p},\sigma}\, c_{v,\boldsymbol{k}'-\boldsymbol{q},s})\,, \tag{C.18}$$

the two terms can be further summarized by a shift of the momentum sum with $\boldsymbol{q} \to -\boldsymbol{q}$.

Following the procedure from the last section, the Heisenberg equation now is used to obtain the time dependence of the annihilation operator. Additionally, time ordered products of annihilation and creation operators, which arise in combinations of four, were factorized by possible combinations of corresponding nonzero expectation values of two operators [68]. Exemplary, for sublattice A we found

$$\begin{aligned}
\langle T(a^\dagger_{\boldsymbol{p}+\boldsymbol{q},\sigma'} a_{\boldsymbol{k}+\boldsymbol{q},\sigma} a_{\boldsymbol{p},\sigma'} a^\dagger_{\boldsymbol{k},\sigma}(0))\rangle =& \sum_{l=0}^{2} \delta_{\boldsymbol{p},\boldsymbol{k}+l\Delta}\delta_{\sigma\sigma'}\langle T(a^\dagger_{\boldsymbol{p}+\boldsymbol{q},\sigma'} a_{\boldsymbol{k}+\boldsymbol{q},\sigma})\rangle\langle T(a_{\boldsymbol{p},\sigma'} a^\dagger_{\boldsymbol{k},\sigma}(0))\rangle \\
&- \sum_{l=0}^{2} \delta_{\boldsymbol{q}+l\Delta,0}\langle T(a^\dagger_{\boldsymbol{p}+\boldsymbol{q},\sigma'} a_{\boldsymbol{p},\sigma'})\rangle\langle T(a_{\boldsymbol{k}+\boldsymbol{q},\sigma} a^\dagger_{\boldsymbol{k},\sigma}(0))\rangle \\
=& 3\,(\delta_{\boldsymbol{p}\boldsymbol{k}}\delta_{\sigma\sigma'}\langle T(a^\dagger_{\boldsymbol{p}+\boldsymbol{q},\sigma'} a_{\boldsymbol{k}+\boldsymbol{q},\sigma})\rangle\langle T(a_{\boldsymbol{p},\sigma'} a^\dagger_{\boldsymbol{k},\sigma}(0))\rangle \\
&- \delta_{\boldsymbol{q}0}\langle T(a^\dagger_{\boldsymbol{p}+\boldsymbol{q},\sigma'} a_{\boldsymbol{p},\sigma'})\rangle\langle T(a_{\boldsymbol{k}+\boldsymbol{q},\sigma} a^\dagger_{\boldsymbol{k},\sigma}(0))\rangle) \\
=& N^2\,(\delta_{\boldsymbol{p}\boldsymbol{k}}\delta_{\sigma\sigma'}\langle T(a^\dagger_{\boldsymbol{p}+\boldsymbol{q},\sigma'} a_{\boldsymbol{k}+\boldsymbol{q},\sigma})\rangle - \delta_{\boldsymbol{q}0}\langle T(a^\dagger_{\boldsymbol{p}+\boldsymbol{q},\sigma'} a_{\boldsymbol{p},\sigma'})\rangle)\, G_F^{AA}(t,\boldsymbol{k})\,.
\end{aligned} \tag{C.19}$$

The equation of motion can therefore be written as

$$\frac{dG_{F,\sigma}(t,\boldsymbol{k})}{dt} - \delta(t)\gamma^0 = (M^0 + M)\ G_{F,\sigma}(t,\boldsymbol{k})\,, \tag{C.20}$$

with M^0 from Eq. (C.13) and the following components of M

$$\begin{aligned}
M^{AA} &= \frac{3\,\mathrm{i}}{N^4}\left(\sum_{\boldsymbol{q}} \tilde{V}^{AA}_{\boldsymbol{q}}\langle T(a^\dagger_{\boldsymbol{k}+\boldsymbol{q},\sigma} a_{\boldsymbol{k}+\boldsymbol{q},\sigma})\rangle - \tilde{V}^{AA}_{\boldsymbol{q}=0}\sum_{\boldsymbol{p},\sigma'}\langle T(a^\dagger_{\boldsymbol{p},\sigma'} a_{\boldsymbol{p},\sigma'})\rangle - \tilde{V}^{BA}_{\boldsymbol{q}=0}\sum_{\boldsymbol{p},\sigma'}\langle T(b^\dagger_{\boldsymbol{p},\sigma'} b_{\boldsymbol{p},\sigma'})\rangle\right)\,, \\
M^{AB} &= \frac{3\,\mathrm{i}}{N^4}\sum_{\boldsymbol{q}} \tilde{V}^{BA}_{\boldsymbol{q}}\langle T(b^\dagger_{\boldsymbol{k}+\boldsymbol{q},\sigma} a_{\boldsymbol{k}+\boldsymbol{q},\sigma})\rangle\,, \\
M^{BA} &= \frac{3\,\mathrm{i}}{N^4}\sum_{\boldsymbol{q}} \tilde{V}^{AB}_{\boldsymbol{q}}\langle T(a^\dagger_{\boldsymbol{k}+\boldsymbol{q},\sigma} b_{\boldsymbol{k}+\boldsymbol{q},\sigma})\rangle\,, \\
M^{BB} &= \frac{3\,\mathrm{i}}{N^4}\left(\sum_{\boldsymbol{q}} \tilde{V}^{BB}_{\boldsymbol{q}}\langle T(b^\dagger_{\boldsymbol{k}+\boldsymbol{q},\sigma} b_{\boldsymbol{k}+\boldsymbol{q},\sigma})\rangle - \tilde{V}^{BB}_{\boldsymbol{q}=0}\sum_{\boldsymbol{p},\sigma'}\langle T(b^\dagger_{\boldsymbol{p},\sigma'} b_{\boldsymbol{p},\sigma'})\rangle - \tilde{V}^{AB}_{\boldsymbol{q}=0}\sum_{\boldsymbol{p},\sigma'}\langle T(a^\dagger_{\boldsymbol{p},\sigma'} a_{\boldsymbol{p},\sigma'})\,.\rangle\right)
\end{aligned}$$

The tilde here indicates a symmetrized version of the interaction terms given by

$$\tilde{V}^{AA}_{\boldsymbol{q}} = \frac{1}{2}(V^{AA}_{\boldsymbol{q}} + V^{AA}_{-\boldsymbol{q}})\,, \qquad \tilde{V}^{BB}_{\boldsymbol{q}} = \frac{1}{2}(V^{BB}_{\boldsymbol{q}} + V^{BB}_{-\boldsymbol{q}})\,, \tag{C.21}$$

$$\tilde{V}^{AB}_{\boldsymbol{q}} = \frac{1}{2}(V^{AB}_{\boldsymbol{q}} + V^{BA}_{-\boldsymbol{q}})\,, \qquad \tilde{V}^{BA}_{\boldsymbol{q}} = \frac{1}{2}(V^{BA}_{\boldsymbol{q}} + V^{AB}_{-\boldsymbol{q}})\,. \tag{C.22}$$

In principal we have $V^{AA}_{-\boldsymbol{q}} = V^{AA}_{\boldsymbol{q}} = V^{BB}_{\boldsymbol{q}}$ and $V^{AB}_{-\boldsymbol{q}} = V^{AB\,*}_{\boldsymbol{q}} = V^{BA}_{\boldsymbol{q}}$, so that the sublattice matrices $\tilde{V}_{\boldsymbol{q}}$ and $V_{\boldsymbol{q}}$ coincide ($V^{AB}_{\boldsymbol{q}=0} = V^{BA}_{\boldsymbol{q}=0} \in \mathbb{R}$). This point has to be reconsidered for the case of a frequency-dependent potential, which can be simply introduced by an extension of the momentum variable within the presented formalism. For now, the interaction is assumed to be frequency independent, and so is the self-energy (see Eq. (C.26) in the following).

Performing a Fourier transform of Eq. (C.20) yields

$$-\left(M^0 + \mathrm{i}\,k^0 + M\right) G_{F,\sigma}(k^0, \boldsymbol{k}) = \gamma^0 \,. \tag{C.23}$$

So we end up with the Dyson-Schwinger equation for the interacting fermion propagator

$$G_{F,\sigma}(k^0, \boldsymbol{k})^{-1} = G^0_{F,\sigma}(k^0, \boldsymbol{k})^{-1} + \Sigma_\sigma(\boldsymbol{k}) \,, \tag{C.24}$$

where the self-energy Σ can be identified by $-\gamma^0 M$, and is finally given by

$$\begin{aligned}
\Sigma^{AA}_\sigma(\boldsymbol{k}) &= +\frac{\mathrm{i}}{N^2} \int \frac{dq^0}{2\pi} \left(\sum_{\boldsymbol{q}} V^{AA}_{\boldsymbol{q}} G^{AA}_{F,\sigma}(q^0, \boldsymbol{k}+\boldsymbol{q}) - V^{AA}_{\boldsymbol{q}=0} \sum_{\boldsymbol{p},\sigma'} G^{AA}_{F,\sigma'}(q^0, \boldsymbol{p}) + V^{BA}_{\boldsymbol{q}=0} \sum_{\boldsymbol{p},\sigma'} G^{BB}_{F,\sigma'}(q^0, \boldsymbol{p}) \right) , \\
\Sigma^{AB}_\sigma(\boldsymbol{k}) &= -\frac{\mathrm{i}}{N^2} \int \frac{dq^0}{2\pi} \sum_{\boldsymbol{q}} V^{BA}_{\boldsymbol{q}} G^{AB}_{F,\sigma}(q^0, \boldsymbol{k}+\boldsymbol{q}) \,, \\
\Sigma^{BA}_\sigma(\boldsymbol{k}) &= -\frac{\mathrm{i}}{N^2} \int \frac{dq^0}{2\pi} \sum_{\boldsymbol{q}} V^{AB}_{\boldsymbol{q}} G^{BA}_{F,\sigma}(q^0, \boldsymbol{k}+\boldsymbol{q}) \,, \\
\Sigma^{BB}_\sigma(\boldsymbol{k}) &= +\frac{\mathrm{i}}{N^2} \int \frac{dq^0}{2\pi} \left(\sum_{\boldsymbol{q}} V^{BB}_{\boldsymbol{q}} G^{BB}_{F,\sigma}(q^0, \boldsymbol{k}+\boldsymbol{q}) - V^{BB}_{\boldsymbol{q}=0} \sum_{\boldsymbol{p},\sigma'} G^{BB}_{F,\sigma'}(q^0, \boldsymbol{p}) + V^{AB}_{\boldsymbol{q}=0} \sum_{\boldsymbol{p},\sigma'} G^{AA}_{F,\sigma'}(q^0, \boldsymbol{p}) \right) .
\end{aligned} \tag{C.25}$$

In a more convenient way the self-energy can be represented in sublattice space as

$$\Sigma_\sigma(\boldsymbol{k}) = \frac{1}{N^2} \int \frac{dq^0}{2\pi} \sum_{\boldsymbol{q},u,u'} D^{u'u}_0(\boldsymbol{q})\, \gamma^0 \Gamma^u\, G_{F,\sigma}(q^0, \boldsymbol{k}+\boldsymbol{q})\, \gamma^0 \Gamma^{u'} \tag{C.26}$$

$$- \frac{1}{N^2} \int \frac{dq^0}{2\pi} \sum_{\boldsymbol{q},u',u,\sigma'} (-1)^{|u-u'|}\, \mathrm{tr}\left(D^{uu'}_0(\boldsymbol{q}=0)\, \Gamma^u\, G_{F,\sigma'}(q^0, \boldsymbol{q})\, \Gamma^u \right) \Gamma^{u'} , \tag{C.27}$$

where the trace has to be taken in sublattice space and also u and u' represent sublattice indices, either refering to the A ($u = 0$) or B ($u = 1$) lattice. Furthermore, we introduce explicit sublattice projectors Γ^u (Eq. (3.15)) to come closer to the well known form of DSE's within a standard QED approach. Additionally we identify the bare photon propagator with the presumed interaction via

$$D^{uu'}_0(\boldsymbol{q}) = \mathrm{i}\, V^{uu'}(\boldsymbol{q}) \,. \tag{C.28}$$

D

Frequency Integrals and Matsubara Sums

D.1 Matsubara Sums

In the static approximation the explicitly frequency dependent parts of the DSE's can be evaluated analytically. For that we mainly have to handle two kind of integrals,

$$I_{1,\sigma}(\boldsymbol{k}) = \int \frac{dq^0}{2\pi} \frac{\mathrm{i}}{(q^0+\mu)^2 - \Omega_{\sigma,\boldsymbol{k}}^2}\,, \tag{D.1}$$

and

$$I_{2,\sigma}(\boldsymbol{k}) = \int \frac{dq^0}{2\pi} \frac{\mathrm{i}\ (q^0+\mu) Z_{\sigma,\boldsymbol{k}}}{(q^0+\mu)^2 Z_{\sigma,\boldsymbol{k}}^2 - \Omega_{\sigma,\boldsymbol{k}}^2}\,, \tag{D.2}$$

which were solved within the Matsubara sum formalism for finite temperature and by using the residue theorem with modified integration contours as elaborated in Ref. [119] and Ref. [120]. So finally we found

$$I_{1,\sigma}(\boldsymbol{k}) = \frac{1}{\beta Z_{\sigma,\boldsymbol{k}}^2} \sum_{n\in\mathbb{Z}} \frac{1}{\omega_n + \mathrm{i}\,(\Omega_{\sigma,\boldsymbol{k}}/Z_{\sigma,\boldsymbol{k}} - \mu)} \frac{1}{\omega_n - \mathrm{i}\,(\Omega_{\sigma,\boldsymbol{k}}/Z_{\sigma,\boldsymbol{k}} + \mu)} \tag{D.3}$$

$$= \frac{1}{4\,\Omega_{\sigma,\boldsymbol{k}}\,Z_{\sigma,\boldsymbol{k}}} \Big[\tanh\Big(\frac{\Omega_{\sigma,\boldsymbol{k}}/Z_{\sigma,\boldsymbol{k}} - \mu}{2}\beta\Big) + \tanh\Big(\frac{\Omega_{\sigma,\boldsymbol{k}}/Z_{\sigma,\boldsymbol{k}} + \mu}{2}\beta\Big)\Big] \tag{D.4}$$

$$\xrightarrow{\mu\to 0} \frac{1}{2\,\Omega_{\sigma,\boldsymbol{k}}\,Z_{\sigma,\boldsymbol{k}}} \tanh\Big(\frac{\Omega_{\sigma,\boldsymbol{k}}/Z_{\sigma,\boldsymbol{k}}}{2}\beta\Big) \tag{D.5}$$

$$\xrightarrow{\beta\to\infty} \frac{1}{2\,\Omega_{\sigma,\boldsymbol{k}}\,Z_{\sigma,\boldsymbol{k}}}\ \Theta\big(\Omega_{\sigma,\boldsymbol{k}}/Z_{\sigma,\boldsymbol{k}} - |\mu|\big) \tag{D.6}$$

$$\xrightarrow{\mu\to 0,\,\beta\to\infty} \frac{1}{2\,\Omega_{\sigma,\boldsymbol{k}}\,Z_{\sigma,\boldsymbol{k}}}\,, \tag{D.7}$$

and

$$I_{2,\sigma}(\boldsymbol{k}) = \frac{1}{4\,Z_{\sigma,\boldsymbol{k}}}\Big[\tanh\Big(\frac{\Omega_{\sigma,\boldsymbol{k}}/Z_{\sigma,\boldsymbol{k}}-\mu}{2}\beta\Big) - \tanh\Big(\frac{\Omega_{\sigma,\boldsymbol{k}}/Z_{\sigma,\boldsymbol{k}}+\mu}{2}\beta\Big)\Big] \tag{D.8}$$

$$\xrightarrow{\mu\to 0} 0 \tag{D.9}$$

$$\xrightarrow{\beta\to\infty} -\operatorname{sgn}(\mu)\;\frac{1}{2\,Z_{\sigma,\boldsymbol{k}}}\;\Theta\big(|\mu| - \Omega_{\sigma,\boldsymbol{k}}/Z_{\sigma,\boldsymbol{k}}\big) \tag{D.10}$$

$$\xrightarrow{\mu\to 0,\,\beta\to\infty} 0\,, \tag{D.11}$$

with $q^0 \to \mathrm{i}\,\omega_n$ and $\omega_n = \frac{(2n+1)\pi}{\beta}$ for fermionic boundary conditions. Regarding the second integral, it can be helpful to introduce a regularization term which is equal to the case of $\mu = 0$, in order to apply the residue theorem

$$I_{2,\sigma}(\boldsymbol{k}) = \int \frac{dq^0}{2\pi}\frac{\mathrm{i}\;(q^0+\mu)Z_{\sigma,\boldsymbol{k}}}{(q^0+\mu)^2 Z_{\sigma,\boldsymbol{k}}^2 - \Omega_{\sigma,\boldsymbol{k}}^2} - \underbrace{\int \frac{dq^0}{2\pi}\frac{\mathrm{i}\;q^0 Z_{\sigma,\boldsymbol{k}}}{(q^0\,Z_{\sigma,\boldsymbol{k}})^2 - \Omega_{\sigma,\boldsymbol{k}}^2}}_{=0}\,. \tag{D.12}$$

From the evaluation of Eq. (D.3) one can additionally extract

$$\sum_n \frac{1}{n+1/2+\mathrm{i}\,x}\;\frac{1}{n+1/2+\mathrm{i}\,y} = \frac{\pi}{x-y}\left[\tanh(\pi x) - \tanh(\pi y)\right] \tag{D.13}$$

which is a usefule relation in order to evaluate Matsubara sums and is also exploited to determine the frequency integrals that occur in the vacuum polarization function in Sec. 5.2.

D.2 Fermion Number Conservation

With the frequency integrals at hand, the free energy for the non-interacting theory and thus especially the number of fermions per unit cell can be easily extracted. The fermionic contribution to the free energy in the non-interacting theory is given by $\Omega_f(T,\mu) = -T\,\ln\mathcal{Z}_0$ [118, 121, 122] with

$$\mathcal{Z}_0 = \int \mathcal{D}\bar{\psi}\,\mathcal{D}\psi\;e^{-S_E^0}\,, \qquad \text{and} \qquad S_E^0[\bar{\psi},\psi] \quad \text{from Eq. (B.16)}\,, \tag{D.14}$$

where σ labels the spin index. By evaluating the gaussian integral (see Sec. A.2), the free energy per unit cell is found to be

$$\Omega_f(T,\mu)/N^2 = -\frac{T}{N^2}\sum_\sigma \mathrm{Tr}\big[\ln((k_0+\mu_\sigma)^2 - \varepsilon_{\boldsymbol{k},\sigma}^2)/T^2)\big] \tag{D.15}$$

Here the trace is given by the sum over all Matsubara frequencies and momentum modes within the Briouillin zone $\mathrm{Tr} \to \sum_{\boldsymbol{k},n}$ with $k_0 = i\,\omega_n$ as usual. With

$$[\varepsilon_{\boldsymbol{k},\sigma}^2 + (k_0 + \mathrm{i}\;\mu_\sigma)^2][\varepsilon_{\boldsymbol{k},\sigma}^2 + (-k_0 + \mathrm{i}\;\mu_\sigma)^2] = [k_0^2 + (\varepsilon_{\boldsymbol{k},\sigma} - \mu_\sigma)^2][k_0^2 + (\varepsilon_{\boldsymbol{k},\sigma} + \mu_\sigma)^2]\,, \tag{D.16}$$

and

$$\sum_n \ln\left((\omega_n^2 + \tilde{\varepsilon}_{\boldsymbol{k},\sigma})/T^2\right) = \int_1^{\tilde{\varepsilon}_{\boldsymbol{k},\sigma}^2/T^2} dx^2 \sum_n \frac{1}{(\omega_n/T)^2 + x^2} + \sum_n \ln(1 + (\omega_n/T)^2)\,, \tag{D.17}$$

where the Matsubara sum of the first term has already been calculated in Eq. (D.4), the Matsubara sum within the free ernergy can be evaluated. The second term has been dropped, due to the fact that it neither depends on the chemical potential nor on the temperature (with fermionic frequencies $\omega_n = (2n+1)\,\pi\,T$), what effectively regularizes the integral and determines the vacuum energy to be zero. So we finally find

$$\Omega_f(T,\mu)/N^2 = -\frac{T}{N^2}\sum_{\boldsymbol{k},\sigma} \ln\,\cosh(\beta(\varepsilon_{\boldsymbol{k},\sigma}-\mu_\sigma)/2) + \ln\,\cosh(\beta(\varepsilon_{\boldsymbol{k},\sigma}+\mu_\sigma)/2) \tag{D.18}$$

$$\overset{T\to\infty}{=} -\frac{T}{N^2}\sum_{\boldsymbol{k},\sigma}(\varepsilon_{\boldsymbol{k},\sigma}\,\Theta(\varepsilon_{\boldsymbol{k},\sigma}-|\mu_\sigma|) + |\mu_\sigma|\,\Theta(|\mu_\sigma|-\varepsilon_{\boldsymbol{k},\sigma})), \tag{D.19}$$

from what the fermion number per unit cell can be simply extracted and is given by

$$n_\sigma = \frac{1}{N^2}\frac{d\,\Omega_f}{d\mu_\sigma} = \mathrm{sign}(\mu_\sigma)\sum_{\boldsymbol{k},\sigma}\frac{1}{N^2}\Theta(|\mu_\sigma|-\varepsilon_{\boldsymbol{k},\sigma}) \tag{D.20}$$

$$= \mathrm{sign}(\mu_\sigma)\int_0^{|\mu|} d\varepsilon\;\rho(\varepsilon)\,, \tag{D.21}$$

with $\rho(\epsilon)$ being the density of states [16], originally calulated in Ref. [12] in 1953. Consequently for $\mu \to \pm\infty$ one finds plus or minus one quasiparticle per unit cell and per spin degree of freedom, here negative values refer to hole states of the energy band. However, important to note here is that the neutrality point for electron states and holes, so for graphene at half-filling, is found for $\mu_\uparrow = \mu_\downarrow = 0$ for two fermion flavors.

E

Dyson-Schwinger Equations

E.1 Path Integral Formalism

In the following the formalism of second quantization is translated to the path integral formalism of a quantum field theory by the introduction of coherent fermionic states via

$$|\psi\rangle = e^{-\sum_i \psi_i \, c_i^\dagger} \, |0\rangle \qquad \text{and} \qquad \langle\psi| = \langle 0| \, e^{-\sum_i c_i \, \psi_i^*} \,, \tag{E.1}$$

with the fermionic creation and annihilation operators $c_i^\dagger$ and c_i for the quasiparticles in coordinate space as already introduced in Sec. 2.1. These states composed by Grassmann numbers and the corresponding creation/annihilation operator build a basis of Eigenstates of the respective operator

$$c_i \, |\psi\rangle = -\psi_i \, |\psi\rangle \qquad \text{and} \qquad \langle\psi| \, c_i^\dagger = \langle\psi| \, (-\psi_i^*) \,. \tag{E.2}$$

For a detailed description and derivation of the basic principles we recommend Ref. [116] or Ref. [123]. Note that in the considered theory the vacuum state indicated by $|0\rangle$ or $\langle 0|$ refers to the many-particle state of the half-filled hexagonal lattice.

Starting from the Hamiltonian in second quantization, the partition function that leads to the generating functional for correlation functions in Euclidean space-time is given by

$$\mathcal{Z} = \operatorname{tr} e^{-\beta H} = \int \prod_x d\xi_x^* \, d\xi_x \, d\eta_x^* \, d\eta_x \; e^{-\sum_x (\xi_x^* \xi_x + \eta_x^* \eta_x)} \, \langle -\xi, \, -\eta| \, e^{-\beta H} \, |\xi, \, \eta\rangle \;, \tag{E.3}$$

for convenience we drop the subscript E (as introduces in App. B) for Euclidean space-time variables throughout the whole chapter. The fermionic many-particle

state $|\xi,\,\eta\rangle$ is characterized by two complex Grassmann valued fields η and ξ. In order to distinguish between spin-up and spin-down fermions we introduce the notation

$$\xi_x = \psi_{x,\uparrow} \qquad \text{and} \qquad \eta_x = \psi_{x,\downarrow}\,. \tag{E.4}$$

For any normal ordered function $\mathcal{F}(c^\dagger_{x,\uparrow},\, c_{x,\uparrow}, c^\dagger_{x,\downarrow}, c_{x,\downarrow})$ the matrix element is then given by [116]

$$\langle \xi,\,\eta|\,\mathcal{F}(c^\dagger_{x,\uparrow},\, c_{x,\uparrow}, c^\dagger_{x,\downarrow}, c_{x,\downarrow})\,|\widetilde{\xi},\,\widetilde{\eta}\rangle = \mathcal{F}(\xi^*_x, \widetilde{\xi}_x, \eta^*_x, \widetilde{\eta}_x)\; e^{\sum_x \xi^*_x\widetilde{\xi}_x + \eta^*_x\widetilde{\eta}_x}\,. \tag{E.5}$$

With the Trotter-Theorem [70] the partition function from Eq. (E.3) is factorized via

$$e^{-\beta H} \approx e^{-\delta H} e^{-\delta H} \dots\; e^{-\delta H}\,, \tag{E.6}$$

with $\delta = \frac{\beta}{N_t}$ and a complete set of states building the unity

$$\int \prod_x \; d\xi^*_x\, d\xi_x\, d\eta^*_x\, d\eta_x\; e^{-\sum_x (\xi^*_x\xi_x + \eta^*_x\eta_x)}\;\; |\xi,\,\eta\rangle\,\langle\xi,\,\eta| = \mathbb{1}\,, \tag{E.7}$$

is inserted between all exponentials. With antiperiodic boundary conditions

$$\langle -\xi,\,-\eta| = \langle -\xi_{x,0},\,-\eta_{x,0}| = \langle \xi_{x,N_t},\,\eta_{x,N_t}|\;, \tag{E.8}$$

and a new integration variable for each insertion which is labeled by a second index t, one obtains

$$\begin{aligned}\mathcal{Z} = \int \prod_{t=0}^{N_t-1} \prod_x \; d\xi^*_{x,t}\, d\xi_{x,t}\, d\eta^*_{x,t}\, d\eta_{x,t}\; e^{-\sum_{x,t}(\xi^*_{x,t+1}\xi_{x,t+1} + \eta^*_{x,t+1}\eta_{x,t+1})}\;\langle \xi_{x,N_t},\,\eta_{x,N_t}|\,e^{-\delta H}\,|\xi_{x,N_t-1},\,\eta_{x,N_t-1}\rangle \\ \times\,\langle \xi_{x,N_t-1},\,\eta_{x,N_t-1}|\,e^{-\delta H}\,|\xi_{x,N_t-2},\,\eta_{x,N_t-2}\rangle \dots \langle \xi_{x,1},\,\eta_{x,1}|\,e^{-\delta H}\,|\xi_{x,0},\,\eta_{x,0}\rangle\,.\end{aligned}$$

In the next step the expectation values have to be evaluated for the Hamiltonian of interest, here given by the free Hamiltonian from Eq. (2.25)

$$\mathcal{H}_0 = -\kappa \sum_{\langle \boldsymbol{i},\boldsymbol{j}\rangle,\sigma} (c^\dagger_{\boldsymbol{i},\sigma} c_{\boldsymbol{j},\sigma} + c^\dagger_{\boldsymbol{j},\sigma} c_{\boldsymbol{i},\sigma}) + \sum_{\boldsymbol{i}_s,s,\sigma} (-1)^s m_\sigma\, c^\dagger_{\boldsymbol{i}_s,\sigma} c_{\boldsymbol{i}_s,\sigma} - \sum_{\boldsymbol{i},\sigma} \mu_\sigma\, c^\dagger_{\boldsymbol{i},\sigma} c_{\boldsymbol{i},\sigma}\,, \tag{E.9}$$

plus the two-particle interaction, as already introduced in Eq. (5.2),

$$\mathcal{H}_{tp} = \frac{1}{2} \underbrace{\sum_{\boldsymbol{i},\boldsymbol{j},\sigma,\sigma'} :c^\dagger_{\boldsymbol{i},\sigma} c_{\boldsymbol{i},\sigma} (\lambda\mathbb{1} + \widetilde{V}^+_{\boldsymbol{ij}})\; c^\dagger_{\boldsymbol{j},\sigma'} c_{\boldsymbol{j},\sigma'}:}_{\geq 0} - \frac{1}{2} \underbrace{\sum_{\boldsymbol{i},\boldsymbol{j},\sigma,\sigma'} :c^\dagger_{\boldsymbol{i},\sigma} c_{\boldsymbol{i},\sigma}\; (\lambda\mathbb{1} - \widetilde{V}^-_{\boldsymbol{ij}})\; c^\dagger_{\boldsymbol{j},\sigma'} c_{\boldsymbol{j},\sigma'}:}_{\geq 0} + \mathcal{H}_{os}\,. \tag{E.10}$$

Here the on-site interaction $\mathcal{H}_{os}$ is additionally separated from the interaction matrix with $\widetilde{V}^+_{\boldsymbol{ii}} = \widetilde{V}^-_{\boldsymbol{ii}} = 0$ and we formally introduce an arbitrary term proportional to $\lambda \in \mathbb{R}$, to ensure the invertibility of $(\lambda\mathbb{1} + \widetilde{V}^+_{xy})$ and $(\lambda\mathbb{1} - \widetilde{V}^-_{xy})$. Note that contributions proportional to the particle number operator has been absorbed in the chemical potential (see Eq. (3.7)).

In order to take a closer look on the predominant on-site interaction, we use a kind of complete Fierz transformation

$$(c^\dagger_{\boldsymbol{i}}\, c_{\boldsymbol{i}} - 1)(c^\dagger_{\boldsymbol{i}}\, c_{\boldsymbol{i}} - 1) = -\frac{1}{3}(c^\dagger_{\boldsymbol{i}}\,\vec{\sigma}\, c_{\boldsymbol{i}})(c^\dagger_{\boldsymbol{i}}\,\vec{\sigma}\, c_{\boldsymbol{i}})\,, \tag{E.11}$$

to gain another representation of the on-site contribution which directly couples to the order parameter of an SDW state.

The spin index notation here is replaced by a two dimensional vector notation with $c_{\boldsymbol{i}} = (c_{\boldsymbol{i},\uparrow}, c_{\boldsymbol{i},\downarrow})$ and analogically for the creation operator, $\vec{\sigma}$ is refering to the Pauli matrices σ^l in spin space were the matrix product should be understood as follows: $\vec{\sigma}_{\alpha\beta}\vec{\sigma}_{\gamma\delta} = \sum_{m=1}^{3} \sigma^m_{\alpha\beta} \cdot \sigma^m_{\gamma\delta}$. In order to keep track of both possibilities in the derivation of DSE's an artificial parameter α was inserted which equals to $\alpha = 1$ for the theory investigated in the main part of this work,

$$\mathcal{H}_{os} = \alpha \frac{U}{2} \sum_{\boldsymbol{i}} : (c^\dagger_{\boldsymbol{i}} c_{\boldsymbol{i}})^2 : -(1-\alpha)\frac{U}{6} \sum_{\boldsymbol{i}} : (c^\dagger_{\boldsymbol{i}}\, \vec{\sigma}\, c_{\boldsymbol{i}})\,(c^\dagger_{\boldsymbol{i}}\, \vec{\sigma}\, c_{\boldsymbol{i}}) : . \tag{E.12}$$

Next, the required expectation values within the partition function are evaluated with the use of Eq. (E.5) and contributions which are quadratic in the density operator were linearized by a Hubbard-Stratonovich transformation (HST) (App. A.2). As an example, the HST for the long-range contribution is considered in the following, where the bosonic fields σ^+ and σ^- have been introduced. These fields therefore couple to the positive or negative semidefinite part of the interaction,

$$\exp\left[-\frac{\delta}{2}\sum_{x,y,t,t'} (\xi^*_{x,t+1}\xi_{x,t} + \eta^*_{x,t+1}\eta_{x,t})\,(\lambda\mathbb{1} + \widetilde{V}^+_{xy})\,(\xi^*_{y,t'+1}\xi_{y,t'} + \eta^*_{y,t'+1}\eta_{y,t'})\right. \tag{E.13}$$

$$\left. +\frac{\delta}{2}\sum_{x,y,t,t'} (\xi^*_{x,t+1}\xi_{x,t} + \eta^*_{x,t+1}\eta_{x,t})\,(\lambda\mathbb{1} - \widetilde{V}^-_{xy})\,(\xi^*_{y,t'+1}\xi_{y,t'} + \eta^*_{y,t'+1}\eta_{y,t'})\right] =$$

$$\times \sqrt{\det\left[(\lambda\mathbb{1} + \delta\widetilde{V}^+_{xy})^{-1}\right]}\sqrt{\det\left[(\lambda\mathbb{1} - \delta\widetilde{V}^-_{xy})^{-1}\right]} \int \frac{\mathcal{D}\sigma^+}{(2\pi)^{D/2}} \int \frac{\mathcal{D}\sigma^-}{(2\pi)^{D/2}} \tag{E.14}$$

$$\times \exp\left[-\frac{\delta}{2}\sum_{x,y,t,t'} \sigma^+_{x,t}\,(\lambda\mathbb{1} + \widetilde{V}^+)^{-1}_{xy}\sigma^+_{y,t'} - \mathrm{i}\,\delta\sum_{x,t}\sigma^+_{x,t}\,(\xi^*_{x,t+1}\xi_{x,t} + \eta^*_{x,t+1}\eta_{x,t})\right]$$

$$\times \exp\left[-\frac{\delta}{2}\sum_{x,y,t,t'} \sigma^-_{x,t}\,(\lambda\mathbb{1} - \widetilde{V}^-)^{-1}_{xy}\sigma^-_{y,t'} + \delta\sum_{x,t}\sigma^-_{x,t}\,(\xi^*_{x,t+1}\xi_{x,t} + \eta^*_{x,t+1}\eta_{x,t})\right].$$

Here the product of integrals over all fields in Euclidean space-time is abbreviated by

$$\mathcal{D}\xi = \prod_{t=0}^{N_t-1}\prod_{x} d\xi_{x,t}. \tag{E.15}$$

With the view of a compact notation we additionally absorb the prefactors in the integral measures ($D = N^2 \cdot N_t$). Furthermore we analogically introduce the Hubbard-fields Φ and $\vec{\rho}$ which couple to the on-site interaction and its Fierz transformed version (Eq. (E.12)).

In the next step we introduce the fermionic fields in sublattice space, this representation simply divides the summation from above over all lattice points x (with all fermionic fields being zero on unoccupied lattice points due to Eq. (2.15)) into a summation over all lattice points of the corresponding sublattice (either A or B), labeled by an index i,

$$\bar{\xi}_i = \bar{\xi}_i(t) = \begin{pmatrix}\xi^*_{x_a}(t)\\ \xi^*_{x_b}(t)\end{pmatrix}^{\mathsf{T}} \cdot \gamma^0 \qquad \text{and} \qquad \xi_i = \xi_i(t) = \begin{pmatrix}\xi_{x_a}(t)\\ \xi_{x_b}(t)\end{pmatrix}, \tag{E.16}$$

for the bosonic fields we use

$$\Phi_i^{\mathsf{T}} = \Phi_i^{\mathsf{T}}(t) = \begin{pmatrix} \Phi_{x_a}(t) \\ \Phi_{x_b}(t) \end{pmatrix}^{\mathsf{T}}, \qquad \text{and} \qquad \Phi_i = \Phi_i(t) = \begin{pmatrix} \Phi_{x_a}(t) \\ \Phi_{x_b}(t) \end{pmatrix}, \tag{E.17}$$

with the gamma matrices in sublattice space, given in App. A.2. With a transition to a continuous time integral with $\delta \to 0$ and $N_t \to \infty$ for a fixed value of β (note also the continuous time argument in Eq. (E.17) and Eq. (E.16)) we obtain the partition function of the form

$$\begin{aligned} \mathcal{Z} &= \int \mathcal{D}\bar{\xi}\mathcal{D}\xi \; \mathcal{D}\bar{\eta}\mathcal{D}\eta \, \mathcal{D}\phi \, \mathcal{D}\vec{\rho} \, \mathcal{D}\sigma^+\mathcal{D}\sigma^- \; \exp\left[- \int_{\tau=0}^{\beta=\delta\cdot N_t} d\tau \sum_i \mathcal{L}_i[\bar{\xi}, \xi, \bar{\eta}, \eta, \phi, \vec{\rho}, \sigma^+, \sigma^-] \right] \\ &= \int \mathcal{D}\bar{\xi}\mathcal{D}\xi \; \mathcal{D}\bar{\eta}\mathcal{D}\eta\mathcal{D}\phi\mathcal{D}\rho\mathcal{D}\sigma^+\mathcal{D}\sigma^- \;\; e^{-S_E[\bar{\xi},\xi,\bar{\eta},\eta,\phi,\vec{\rho},\sigma^+,\sigma^-]} . \end{aligned} \tag{E.18}$$

In order to cover the sum over A and B sublattices within a matrix notation, the sublattice projectors Γ^A and Γ^B already defined in Eq. (3.15) are used to obtain the following Lagrangian,

$$\begin{aligned} \mathcal{L}_i = \Big[& \Big(\bar{\xi}_i \, \gamma^0 \partial_t \, \xi_i + \bar{\eta}_i \, \gamma^0 \partial_t \, \eta_i \Big) - \kappa \sum_{l=0}^{2} \bar{\xi}_i \, \gamma^1 \, \xi_{i+\Delta_l} + m_\uparrow \, \bar{\xi}_i \, \xi_i - \mu_\uparrow \, \bar{\xi}_i \gamma^0 \xi_i - \kappa \sum_{l=0}^{2} \bar{\eta}_i \, \gamma^1 \, \eta_{i+\Delta_l} \\ & + m_\downarrow \, \bar{\eta}_i \, \eta_i - \mu_\downarrow \, \bar{\eta}_i \gamma^0 \eta_i + \frac{1}{2\alpha \, U} \, \Phi_i^2 + \mathrm{i} \sum_s \left(\Phi_i^s + \sigma_i^{+s} + \mathrm{i} \, \sigma_i^{-s} \right) \left(\bar{\xi}_i \gamma^0 \, \Gamma^s \, \xi_i + \bar{\eta}_i \gamma^0 \, \Gamma^s \, \eta_i \right) \\ & + \frac{3}{2(1-\alpha)U} \, \vec{\rho}_i^{\,2} - \sum_s \rho_{1,i}^s \, \left(\bar{\eta}_i \gamma^0 \, \Gamma^s \, \xi_i + \bar{\xi}_i \gamma^0 \, \Gamma^s \, \eta_i \right) - \sum_s \mathrm{i} \, \rho_{2,i}^s \, \left(\bar{\eta}_i \gamma^0 \, \Gamma^s \, \xi_i - \bar{\xi}_i \gamma^0 \, \Gamma^s \, \eta_i \right) \\ & - \sum_s \rho_{3,i}^s \, \left(\bar{\xi}_i \gamma^0 \, \Gamma^s \, \xi_i - \bar{\eta}_i \gamma^0 \, \Gamma^s \, \eta_i \right) + \frac{1}{2} \sigma_i^{+\mathsf{T}} [(\lambda \mathbb{1} + V^+)_{ij}^{-1}] \sigma_j^+ + \frac{1}{2} \sigma_i^{-\mathsf{T}} [(\lambda \mathbb{1} - V^-)_{ij}^{-1}] \sigma_j^- \Big] , \end{aligned} \tag{E.19}$$

where $s = 0, 1$ denotes the sublattice index, corresponding to the A or B lattice, respectively, and $\vec{\rho} = (\rho_1, \rho_2, \rho_3)$. The first terms can exactly be identified by the Euclidean propagator from Eq. (B.15) and the Euclidean action is eventually given by

$$S_E[\bar{\xi}, \xi, \bar{\eta}, \eta, \Phi, \vec{\rho}, \sigma^+, \sigma^-] = \sum\!\!\!\!\!\!\int_{\tilde{x},\tilde{y}} \bar{\xi}_{\tilde{x}} \, G^0_{E,\uparrow}(\tilde{x}, \tilde{y})^{-1} \, \xi_{\tilde{y}} + \sum\!\!\!\!\!\!\int_{\tilde{x},\tilde{y}} \bar{\eta}_{\tilde{x}} \, G^0_{E,\downarrow}(\tilde{x}, \tilde{y})^{-1} \, \eta_{\tilde{y}} \tag{E.20}$$

$$\begin{aligned} & + \sum\!\!\!\!\!\!\int_{\tilde{x}} \frac{1}{2\alpha \, U} \, \Phi_{\tilde{x}}^2 + \mathrm{i} \sum_s \sum\!\!\!\!\!\!\int_{\tilde{x}} \left(\Phi_{\tilde{x}}^s + \sigma_{\tilde{x}}^{+s} + \mathrm{i} \, \sigma_{\tilde{x}}^{-s} \right) \left(\bar{\xi}_{\tilde{x}} \gamma^0 \, \Gamma^s \, \xi_{\tilde{x}} + \bar{\eta}_{\tilde{x}} \gamma^0 \, \Gamma^s \, \eta_{\tilde{x}} \right) \\ & + \sum\!\!\!\!\!\!\int_{\tilde{x}} \frac{3}{2(1-\alpha)U} \, \vec{\rho}_{\tilde{x}}^{\,2} - \sum_s \sum\!\!\!\!\!\!\int_{\tilde{x}} \rho_{1,\tilde{x}}^s \, \left(\bar{\eta}_{i\tilde{x}} \gamma^0 \, \Gamma^s \, \xi_{\tilde{x}} + \bar{\xi}_{\tilde{x}} \gamma^0 \, \Gamma^s \, \eta_{\tilde{x}} \right) \\ & - \mathrm{i} \sum_s \sum\!\!\!\!\!\!\int_{\tilde{x}} \rho_{2,\tilde{x}}^s \, \left(\bar{\eta}_{\tilde{x}} \gamma^0 \, \Gamma^s \, \xi_{\tilde{x}} - \bar{\xi}_{\tilde{x}} \gamma^0 \, \Gamma^s \, \eta_{\tilde{x}} \right) - \sum_s \sum\!\!\!\!\!\!\int_{\tilde{x}} \rho_{3,\tilde{x}}^s \, \left(\bar{\xi}_{\tilde{x}} \gamma^0 \, \Gamma^s \, \xi_{\tilde{x}} - \bar{\eta}_{\tilde{x}} \gamma^0 \, \Gamma^s \, \eta_{\tilde{x}} \right) \\ & + \frac{1}{2} \sum\!\!\!\!\!\!\int_{\tilde{x},\tilde{y}} \sigma_{\tilde{x}}^{+\mathsf{T}} [(\lambda \mathbb{1} + V^+)_{\tilde{x}\tilde{y}}^{-1}] \sigma_{\tilde{y}}^+ + \frac{1}{2} \sum\!\!\!\!\!\!\int_{\tilde{x},\tilde{y}} \sigma_{\tilde{x}}^{-\mathsf{T}} [(\lambda \mathbb{1} - V^-)_{\tilde{x}\tilde{y}}^{-1}] \sigma_{\tilde{y}}^- \Big] , \end{aligned} \tag{E.21}$$

with the generating functional

$$\mathcal{Z}[j] = \int \mathcal{D}\phi \, \exp\left[-S_E[\phi] + \int d^3x \, j_\alpha(x)\phi_\alpha(x)\right] , \tag{E.22}$$

$\phi = \{\xi, \bar{\xi}, \eta, \bar{\eta}, \Phi, \vec{\rho}, \sigma^+, \sigma^-\}$ and $j = \{\bar{\psi}^\uparrow, \psi^\uparrow, \bar{\psi}^\downarrow, \psi^\downarrow, h_1, \vec{h}_2, j^+, j^-\}$ should abbreviate the entirety of all fields and sources. The generating functional for connected n-point function is then given by (see Ref. [85, 124, 125] for a general introduction)

$$\mathcal{W}[j] = \ln \mathcal{Z}[j] , \tag{E.23}$$

which accounts for the correctly normalized expectation values in presence of all sources within the resulting n-point functions. If all sources are set to zero, $\mathcal{W}[0] = 0$ is retained from $\mathcal{Z}[0] = 1$.

The full propagator $\langle\phi_1(x)\phi_1(y)\rangle$ resulting from the functional derivative of $\mathcal{Z}[j]$ is easily connected to the associated counterpart of $\mathcal{Z}[j]$, the so called connected Green function $G(x-y)$,

$$\begin{aligned} G_{\alpha\beta}(x-y) = \langle\phi_\alpha(x)\phi_\beta(y)\rangle_{conn.} &= \frac{\delta^2\mathcal{W}[j]}{\delta j_\alpha(x)\delta j_\beta(y)}\Big|_{j=0} = \langle\phi_\alpha(x)\phi_\beta(y)\rangle - \langle\phi_\alpha(x)\rangle\langle\phi_\beta(y)\rangle \\ &= \frac{\delta^2\mathcal{Z}[j]}{\delta j_\alpha(x)\delta j_\beta(y)}\Big|_{j=0} - \phi^c_\alpha(x)\phi^c_\beta(y) . \end{aligned} \tag{E.24}$$

Here the derivatives are defined as right- and left-derivatives, respectively,

$$\frac{\delta}{\delta\bar{\xi}(x)} =: \text{left derivative} , \qquad \text{and} \qquad \frac{\delta}{\delta\xi(x)} =: \text{right derivative} . \tag{E.25}$$

The conventions in Euclidean space-time follow them from Ref. [110].

With a Legendre transformation with respect to the sources $j_\alpha(x) = \delta\Gamma[\phi^c]/\delta\phi^c_\alpha(x)$,

$$\Gamma[\phi^c] = -\mathcal{W}[j] + \int d^3x \, \phi^c_\alpha(x) j_\alpha(x) , \tag{E.26}$$

the generating functional for 1PI n-point functions $\Gamma[\phi^c]$ depending on the corresponding field expectation values with nonzero sources $\phi^c_\alpha(x) = \delta\mathcal{W}[j]/\delta j_\alpha(x) = \langle\phi_\alpha\rangle_j$ is obtained. The complete set of classical field variables is given by

$$\phi^c = \{\xi^c, \bar{\xi}^c, \eta^c, \bar{\eta}^c, \Phi^c, \vec{\rho}^c, \sigma^{+c}, \sigma^{-c}\} .$$

The DSE's result from performing a total derivative on an integral equation which surely vanishes [110], from Eq. (E.22) one immediately finds

$$\begin{aligned} 0 = -\frac{\delta}{\delta\phi_\beta(y)} \int \mathcal{D}\phi e^{-S[\phi]+\int dx j_\alpha(x)\phi_\alpha(x)} &= \int \mathcal{D}\phi \, e^{-S[\phi]+\int dx j_\alpha(x)\phi_\alpha(x)} \big(\frac{\delta}{\delta\phi_\beta(y)} S[\phi] - j_\beta(y)\big) \\ =: \Big\langle \big(\frac{\delta}{\delta\phi_\beta(y)} S[\phi] - j_\beta(y)\big)\Big\rangle_j . \end{aligned} \tag{E.27}$$

By replacing all field dependencies within the expectation value by the derivative with respect to the corresponding source, $\mathcal{Z}[j]$ can be separated as a factor,

$$\Big(- \frac{\delta S}{\delta\phi_\beta(y)}\left[\frac{\delta}{\delta j}\right] + j_\beta(y)\Big)\mathcal{Z}[j] = 0 , \tag{E.28}$$

in terms of the generating functional for connected Green functions this can be rewritten as

$$-\frac{\delta S}{\delta\phi_\beta(y)}\left[\frac{\delta\mathcal{W}}{\delta j}+\frac{\delta}{\delta j}\right]+j_\beta(y)=0\,, \tag{E.29}$$

where the additional derivative with respect to j in the replacement for the field dependency take account for the product rule. Finally, for the 1PI generating functional we obtain

$$\frac{\delta\Gamma[\phi]}{\delta\phi^c_\beta(y)}-\frac{\delta S}{\delta\phi^c_\beta(y)}\left[\phi^c+\frac{\delta^2\mathcal{W}}{\delta j\delta j}\frac{\delta}{\delta\phi^c}\right]=0\,, \tag{E.30}$$

where the field component $\phi_\alpha(x)$ more precisely has to be replaced by

$$\phi_\alpha(x)\longrightarrow\phi^c_\alpha(x)+\int_z\sum_\gamma\frac{\delta^2\mathcal{W}}{\delta j_\gamma(z)\delta j_\alpha(x)}\frac{\delta}{\delta\phi^c_\gamma(z)}\,, \tag{E.31}$$

for instance. These equations build the starting point for the derivation of DSE's for full, connected or proper n-point functions, respectively.

In the following we will take the Ansatz from Eq. (E.28) as a starting point and use the relations of App. E.4 to obtain the DSE's for 1PI Green functions. Although starting from Eq. (E.30) and use Eq. (E.98) would probably be less laborious, following Eq. (E.28) and elaborate the 1PI part afterwards clearly contribute to a better understanding.

Performing an additional derivative on Eq. (E.28) with respect to a source entails

$$\frac{\delta}{\delta j_\gamma(z)}\int\mathcal{D}\phi\;e^{-S[\phi]+\int dx j_\alpha(x)\phi_\alpha(x)}\big(\frac{\delta}{\delta\phi_\beta(y)}S[\phi]-j_\beta(y)\big) \tag{E.32}$$

$$=\int\mathcal{D}\phi\;e^{-S[\phi]+\int dx j_\alpha(x)\phi_\alpha(x)}\big(\phi_\gamma(z)\frac{\delta}{\delta\phi_\beta(y)}S[\phi]-\phi_\gamma(z)j_\beta(y)-\delta_{\beta\gamma}\delta(y-x)\big)\,, \tag{E.33}$$

from that the DSE directly follows,

$$\Big\langle\frac{\delta S[\phi]}{\delta\phi_\beta(y)}\phi_\gamma(z)\Big\rangle_{j=0}=\delta_{\beta\gamma}\,\delta(y-x)\,, \tag{E.34}$$

with all sources set to zero.

E.2 Boson DSE

First of all the DSE for the long-range field σ^+ should be derived exemplary. The derivative of the Euclidean action Eq. (E.21) yields

$$\frac{\delta S[\phi]}{\delta\sigma^{+,\tilde{s}}(x)}=\sum_{s'}\sum\!\!\!\!\!\!\int_{\tilde{y}}G^{0,\tilde{s}s'}_{\sigma^+\sigma^+}(x,\tilde{y})^{-1}\sigma^{+,s'}_{\tilde{y}}+\mathrm{i}\,\bar{\xi}_x\gamma^0\Gamma^{\tilde{s}}\xi_x+\mathrm{i}\,\bar{\eta}_x\gamma^0\Gamma^{\tilde{s}}\eta_x\,, \tag{E.35}$$

with

$$G^{0,\tilde{s}s'}_{\sigma^+\sigma^+}(x,\tilde{y})^{-1}=\frac{1}{2}\big((\lambda\mathbb{1}+\widetilde{V}^+)^{-1,\tilde{s}s'}_{x\tilde{y}}+(\lambda\mathbb{1}+\widetilde{V}^+)^{-1,s'\tilde{s}}_{\tilde{y}x}\big)\,, \tag{E.36}$$

where $\tilde{s}$ and s' again are sublattice indices. This can be simplified by the general relation for the components of the interaction matrix in sublattice space. For the interaction matrix between different sublattices $\widetilde{V}^{AB} = (\widetilde{V}_{ij}^{AB})$ the transposition effectively changes the sublattices, so that the following applies $\widetilde{V}_{ij}^{AB} = (\widetilde{V}_{ij}^{BA})^{\mathsf{T}} = \widetilde{V}_{ji}^{BA}$ and of course $\widetilde{V}_{ij}^{AA} = \widetilde{V}_{ji}^{AA}$ and $\widetilde{V}_{ij}^{BB} = \widetilde{V}_{ji}^{BB}$. So also the 2×2 dimensional inverse interaction matrix from Eq. (E.36) reduces to

$$G^{0,\tilde{s}s'}_{\sigma^+\sigma^+}(x,\tilde{y})^{-1} = (\lambda \mathbb{1} + \widetilde{V}^+)^{-1,\tilde{s}s'}_{x\tilde{y}}. \tag{E.37}$$

Furthermore one obtains

$$\begin{aligned}\Big\langle \frac{\delta S[\phi]}{\delta \sigma^{+,\tilde{s}}(x)}\, \sigma^{+,s}(y)\Big\rangle =& \sum_{s'} \oint\!\!\!\!\!\!\int_{\tilde{y}} G^{0,\tilde{s}s'}_{\sigma^+\sigma^+}(x,\tilde{y})^{-1}\, \langle \sigma^{+,s'}_{\tilde{y}} \sigma^{+,s}_{y}\rangle + \mathrm{i}\,(-1)^{\tilde{s}} \langle \bar{\xi}^{\tilde{s}}_x \xi^{\tilde{s}}_x \sigma^{+,s}_y\rangle + \mathrm{i}\,(-1)^{\tilde{s}} \langle \bar{\eta}^{\tilde{s}}_x \eta^{\tilde{s}}_x \sigma^{+,s}_y\rangle \\ =& \delta(x-y)\delta_{\tilde{s}s}\,, \end{aligned} \tag{E.38}$$

and

$$\begin{aligned}\delta(x-y)\,\delta_{\tilde{s}s} =& \sum_{s'} \oint\!\!\!\!\!\!\int_{\tilde{y}} G^{0,\tilde{s}s'}_{\sigma^+\sigma^+}(x,\tilde{y})^{-1}\, \langle \sigma^{+,s'}_{\tilde{y}} \sigma^{+,s}_{y}\rangle_{conn.} + \sum_{s'} \oint\!\!\!\!\!\!\int_{\tilde{y}} G^{0,\tilde{s}s'}_{\sigma^+\sigma^+}(x,\tilde{y})^{-1}\, \langle \sigma^{+,s'}_{\tilde{y}}\rangle \langle \sigma^{+,s}_{y}\rangle \\ &+ \mathrm{i}\,(-1)^{\tilde{s}}\, \langle \sigma^{+,s}_y\rangle (G^{\tilde{s}\bar{\tilde{s}}}_{\xi\bar{\xi}}(0) + G^{\tilde{s}\bar{\tilde{s}}}_{\eta\bar{\eta}}(0)) \\ &+ \mathrm{i}\,(-1)^{\tilde{s}} \sum_{s'} \oint\!\!\!\!\!\!\int_{x',y',z'} G^{s'\bar{s}}_{\xi\bar{\xi}}(z'-x)\, G^{\tilde{s}s'}_{\xi\bar{\xi}}(x-y') \Gamma^{\xi^{s'}\bar{\xi}^{s'}\sigma^{+,s'}}(z',y',x') G^{s's}_{\sigma^+\sigma^+}(x'-y) \\ &+ \mathrm{i}\,(-1)^{\tilde{s}} \sum_{s'} \oint\!\!\!\!\!\!\int_{x',y',z'} G^{s'\bar{s}}_{\eta\bar{\eta}}(z'-x)\, G^{\tilde{s}s'}_{\eta\bar{\eta}}(x-y') \Gamma^{\eta^{s'}\bar{\eta}^{s'}\sigma^{+,s'}}(z',y',x') G^{s's}_{\sigma^+\sigma^+}(x'-y)\,, \end{aligned} \tag{E.39}$$

by making use of App. E.4 and especially of Eq. (E.97).

Taking the sum over $\sum_s \oint\!\!\!\!\!\!\int_y$ and multiplying with $G^{ss''}_{\sigma^+\sigma^+}(y-z)^{-1}$ gives

$$\begin{aligned} G^{\tilde{s}s''}_{\sigma^+\sigma^+}(x-z)^{-1} =& G^{0,\tilde{s}s''}_{\sigma^+\sigma^+}(x,z)^{-1} + \Delta^{\tilde{s}s''}_{\sigma+\sigma+}(x-z) \\ &+ \mathrm{i}\,(-1)^{\tilde{s}} \oint\!\!\!\!\!\!\int_{z',y'} G^{s''\bar{\tilde{s}}}_{\xi\bar{\xi}}(z'-x)\, G^{\tilde{s}s''}_{\xi\bar{\xi}}(x-y') \Gamma^{\xi^{s''}\bar{\xi}^{s''}\sigma^{+,s''}}(z',y',z) \\ &+ \mathrm{i}\,(-1)^{\tilde{s}} \oint\!\!\!\!\!\!\int_{z',y'} G^{s''\bar{\tilde{s}}}_{\eta\bar{\eta}}(z'-x)\, G^{\tilde{s}s''}_{\eta\bar{\eta}}(x-y') \Gamma^{\eta^{s''}\bar{\eta}^{s''}\sigma^{+,s''}}(z',y',z)\,, \end{aligned} \tag{E.40}$$

with

$$\Delta^{\tilde{s}s''}_{\sigma+\sigma+}(x-z) = \Big(\sum_{s'} \oint\!\!\!\!\!\!\int_{\tilde{y}} G^{0,\tilde{s}s'}_{\sigma^+\sigma^+}(x,\tilde{y})^{-1}\, \langle \sigma^{+,s'}_{\tilde{y}}\rangle + \mathrm{i}\,(-1)^{\tilde{s}} (G^{\tilde{s}\bar{\tilde{s}}}_{\xi\bar{\xi}}(0) + G^{\tilde{s}\bar{\tilde{s}}}_{\eta\bar{\eta}}(0))\Big) \tag{E.41}$$

$$\times \sum_{s} \oint\!\!\!\!\!\!\int_{y} \langle \sigma^{+,s}_y\rangle\, G^{ss''}_{\sigma^+\sigma^+}(y-z)^{-1}\,. \tag{E.42}$$

Moreover, Eq. (E.27) for zero source terms

$$\langle \frac{\delta S_E[\phi]}{\delta \sigma^{+s}(x)}\rangle_{j=0} \stackrel{!}{=} 0\,, \tag{E.43}$$

immediately entails

$$\langle \sigma^{+s}_y\rangle = -\mathrm{i} \sum_{\tilde{s}} \oint\!\!\!\!\!\!\int_x G^{0,s\tilde{s}}_{\sigma^+\sigma^+}(x,y)\,(-1)^s (G^{\tilde{s}\bar{\tilde{s}}}_{\xi\bar{\xi}}(0) + G^{\tilde{s}\bar{\tilde{s}}}_{\bar{\eta}\eta}(0))\,, \tag{E.44}$$

and consequently $\Delta^{\tilde{s}s''}_{\sigma^+\sigma^+}(x-z)=0$. In a first approach we will assume the fully dressed vertex function to be at tree level (indicated by a subscript tl), which is given by

$$\Gamma^{\xi^s\bar{\xi}^s\sigma^{+s}}_{tl}(z',y',z)=\Gamma^{\eta^s\bar{\eta}^s\sigma^{+s}}_{tl}(z',y',z)=\frac{\delta^3 S_E[\phi=const.]}{\delta\sigma^{+s}(z')\delta\xi^s(y')\delta\bar{\xi}^s(z)} \tag{E.45}$$

$$=\mathrm{i}\,\delta(z-y')\delta(z-z')\,(-1)^s\,. \tag{E.46}$$

With the help of the tree level vertex and the sublattice projectors, Eq. (E.41) can be written as

$$\begin{aligned}G^{ss'}_{\sigma^+\sigma^+}(x-z)^{-1}=&G^{0,ss'}_{\sigma^+\sigma^+}(x-z)^{-1}+\mathrm{i}\sum\!\!\!\!\!\!\int_{z',y'}\mathrm{tr}\left(G_{\xi\bar{\xi}}(z'-x)\gamma^0\Gamma^s\,G_{\xi\bar{\xi}}(x-y')\Gamma^{s'}\right)\Gamma^{\xi^{s'}\bar{\xi}^{s'}\sigma^{+,s'}}(z',y',z)\\&+\mathrm{i}\sum\!\!\!\!\!\!\int_{z',y'}\mathrm{tr}\left(G_{\eta\bar{\eta}}(z'-x)\gamma^0\Gamma^s\,G_{\eta\bar{\eta}}(x-y')\Gamma^{s'}\right)\Gamma^{\eta^{s'}\bar{\eta}^{s'}\sigma^{+,s'}}(z',y',z)\\=&G^{0,ss'}_{\sigma^+\sigma^+}(x,z)^{-1}-\mathrm{tr}\left(G_{\xi\bar{\xi}}(z-x)\gamma^0\Gamma^s\,G_{\xi\bar{\xi}}(x-z)\gamma^0\Gamma^{s'}\right)\\&-\mathrm{tr}\left(G_{\eta\bar{\eta}}(z-x)\gamma^0\Gamma^s\,G_{\eta\bar{\eta}}(x-z)\gamma^0\Gamma^{s'}\right).\end{aligned} \tag{E.47}$$

Analogically for the σ^- one obtains

$$\begin{aligned}G^{ss'}_{\sigma^-\sigma^-}(x-z)^{-1}=&G^{0,ss'}_{\sigma^-\sigma^-}(x-z)^{-1}+\mathrm{tr}\left(G_{\xi\bar{\xi}}(z-x)\gamma^0\Gamma^s\,G_{\xi\bar{\xi}}(x-z)\gamma^0\Gamma^{s'}\right)\\&+\mathrm{tr}\left(G_{\eta\bar{\eta}}(z-x)\gamma^0\Gamma^s\,G_{\eta\bar{\eta}}(x-z)\gamma^0\Gamma^{s'}\right),\end{aligned} \tag{E.48}$$

with

$$G^{0,ss'}_{\sigma^-\sigma^-}(x-z)^{-1}=(\lambda\mathbb{1}-\widetilde{V}^-)^{-1,ss'}_{xz}\,, \tag{E.49}$$

and

$$\langle\sigma^{-s}_y\rangle=\sum_{\tilde{s}}\sum\!\!\!\!\!\!\int_x G^{0,s\tilde{s}}_{\sigma^-\sigma^-}(x,y)\,\langle\xi_x\gamma^0\Gamma^{\tilde{s}}\bar{\xi}_x+\bar{\eta}_x\gamma^0\Gamma^{\tilde{s}}\eta_x\rangle \tag{E.50}$$

$$=\sum_{\tilde{s}}\sum\!\!\!\!\!\!\int_x G^{0,s\tilde{s}}_{\sigma^-\sigma^-}(x,y)\,(-1)^s(G^{\tilde{s}\tilde{s}}_{\bar{\xi}\xi}(0)+G^{\tilde{s}\tilde{s}}_{\bar{\eta}\eta}(0))\,. \tag{E.51}$$

These equations are actually of the same form, except the global minus sign which can be absorbed in the dressed and bare bosonic propagators, respectively. For the Hubbard field Φ the same procedure similary results in

$$\begin{aligned}G^{ss'}_{\Phi\Phi}(x-z)^{-1}=&\frac{1}{\alpha\,U}\,\delta(x-z)\delta_{ss'}-\mathrm{tr}\left(G_{\xi\bar{\xi}}(z-x)\gamma^0\Gamma^s\,G_{\xi\bar{\xi}}(x-z)\gamma^0\Gamma^{s'}\right)\\&-\mathrm{tr}\left(G_{\eta\bar{\eta}}(z-x)\gamma^0\Gamma^s\,G_{\eta\bar{\eta}}(x-z)\gamma^0\Gamma^{s'}\right),\end{aligned} \tag{E.52}$$

with the associated field expectation value

$$\langle\Phi^s_x\rangle=-\mathrm{i}\,\alpha\,U\,(-1)^s(G^{ss}_{\bar{\xi}\xi}(0)+G^{ss}_{\bar{\eta}\eta}(0)). \tag{E.53}$$

These contributions can again be summarized in one DSE were we additionally define a factor of i within the bosonic propagator in order to match the conventions from Eq. (3.35)

$$D=\mathrm{i}\,(G_{\Phi\Phi}+G_{\sigma^+\sigma^+}-G_{\sigma^-\sigma^-})\,. \tag{E.54}$$

So with the bare contribution

$$D^0(x,y) = \mathrm{i}\,(U\,\delta(x-y) + \widetilde{V}^+_{x,y} - \widetilde{V}^-_{x,y})\,, \tag{E.55}$$

the combined DSE reads

$$\begin{aligned} D^{ss'}(x-z)^{-1} =& D^{0,ss'}(x-z)^{-1} + \mathrm{i}\,\mathrm{tr}\,(G_{\xi\bar{\xi}}(z-x)\gamma^0\Gamma^s\,G_{\xi\bar{\xi}}(x-z)\gamma^0\Gamma^{s'}) \\ &+ \mathrm{i}\,\mathrm{tr}\,(G_{\eta\bar{\eta}}(z-x)\gamma^0\Gamma^s\,G_{\eta\bar{\eta}}(x-z)\gamma^0\Gamma^{s'})\,. \end{aligned} \tag{E.56}$$

Doing a Fourier transform into frequency-momentum space

$$\begin{aligned} D^{ss'}(p_E)^{-1} =& D^{0,ss'}(p_E)^{-1} + \mathrm{i}\sum\!\!\!\!\!\!\int_{k_E} \mathrm{tr}\,(G_{\xi\bar{\xi}}(p_E)\gamma^0\Gamma^s\,G_{\xi\bar{\xi}}(p_E+k_E)\gamma^0\Gamma^{s'}) \\ &+ \mathrm{i}\sum\!\!\!\!\!\!\int_{k_E} \mathrm{tr}\,(G_{\eta\bar{\eta}}(p_E)\gamma^0\Gamma^s\,G_{\eta\bar{\eta}}(p_E+k_E)\gamma^0\Gamma^{s'})\,, \end{aligned} \tag{E.57}$$

and performing a Wick rotation (App. B) to Minkowskian space-time with the Feynman propagator from Eq. (B.21), finally yields

$$D^{ss'}(p)^{-1} = D^{0,ss'}(p)^{-1} - (-1)^{|s-s'|}\sum_\sigma \int\!\!\!\!\!\!\int_k G^{s's}_{F,\sigma}(k)\,G^{ss'}_{F,\sigma}(p+k) \tag{E.58}$$

$$= D^{0,ss'}(p)^{-1} \underbrace{-\sum_\sigma \int\!\!\!\!\!\!\int_k \mathrm{tr}\,(G_{F,\sigma}(k)\gamma^0\Gamma^s\,G_{F,\sigma}(p+k)\gamma^0\Gamma^{s'})}_{\Pi^{uu'}}\,. \tag{E.59}$$

The second ansatz for the vector field $\vec{\rho}$, where a complete Fierz transformation was used, yields

$$\begin{aligned} G^{ss'}_{\vec{\rho}\vec{\rho}}(x-z)^{-1} =& \frac{3}{(1-\alpha)\,U}\,\delta(x-z)\delta_{ss'} \\ &- (-1)^s \int\!\!\!\!\!\!\int_{z',y'} G^{s's}_{\Psi\bar{\Psi}}(z'-x)\;\vec{\sigma}\;G^{ss'}_{\Psi\bar{\Psi}}(x-y')\Gamma^{\Psi^{s'}\bar{\Psi}^{s'}\rho^{s'}}(z',y',z)\,, \end{aligned} \tag{E.60}$$

with the shorthand notation $G_{\vec{\rho}\vec{\rho}} = (G_{\rho_1\rho_1}, G_{\rho_2\rho_2}, G_{\rho_3\rho_3})$ and the fermionic Green function in spin space $G_{\Psi\bar{\Psi}} = (G_{\eta\bar{\eta}}, G_{\xi\bar{\xi}})$. The corresponding expectation values of the Hubbard fields are given by

$$\langle\rho^s_{3,x}\rangle = \frac{(1-\alpha)\,U}{3}(-1)^s(G^{ss}_{\bar{\xi}\xi}(0) + G^{ss}_{\bar{\eta}\eta}(0))\,, \qquad \text{and} \qquad \langle\rho^s_{1,x}\rangle = \langle\rho^s_{2,x}\rangle = 0. \tag{E.61}$$

By making use of the tree level vertex again the following DSE's for the three Hubbard-fields were found

$$\begin{aligned} G^{ss'}_{\rho_1\rho_1}(x-z)^{-1} =& G^{ss'}_{\rho_2\rho_2}(x-z)^{-1} \\ =& \frac{3}{(1-\alpha)\,U}\,\delta(x-z)\delta_{ss'} + \mathrm{tr}\,(G_{\eta\bar{\eta}}(z-x)\gamma^0\Gamma^s\,G_{\xi\bar{\xi}}(x-z)\gamma^0\Gamma^{s'}) \\ &+ \mathrm{tr}\,(G_{\xi\bar{\xi}}(z-x)\gamma^0\Gamma^s\,G_{\eta\bar{\eta}}(x-z)\gamma^0\Gamma^{s'})\,, \end{aligned} \tag{E.62}$$

and

$$G^{ss'}_{\rho_3\rho_3}(x-z)^{-1} = \frac{3}{(1-\alpha)\,U}\,\delta(x-z)\delta_{ss'} + \mathrm{tr}\left(G_{\xi\bar{\xi}}(z-x)\gamma^0\Gamma^s\,G_{\xi\bar{\xi}}(x-z)\gamma^0\Gamma^{s'}\right) + \mathrm{tr}\left(G_{\eta\bar{\eta}}(z-x)\gamma^0\Gamma^s\,G_{\eta\bar{\eta}}(x-z)\gamma^0\Gamma^{s'}\right). \tag{E.63}$$

E.3 Fermion DSE

In the following the fermion DSE for the spin-up field ξ_x is derived from the Euclidean action (Eq. (E.21)). Following the manner from the last section one finds

$$\frac{\delta S_E[\phi]}{\delta\bar{\xi}(x)} = \sum\!\!\!\!\!\!\int_{\tilde{y}} G^0_{E,\uparrow}(x,\tilde{y})^{-1}\;\xi_{\tilde{y}} + \mathrm{i}\sum_s \underbrace{\left(\Phi^s_x + \sigma^{+s}_x + \mathrm{i}\,(\sigma^{-s}_x + \rho^s_{3,x})\right)}_{=:\tilde{\Phi}^s_x}\gamma^0\,\Gamma^s\,\xi_x \tag{E.64}$$

$$-\sum_s \underbrace{(\rho^s_{1,x} - \mathrm{i}\,\rho^s_{2,x})}_{=:\tilde{\rho}}\;\gamma^0\Gamma^s\,\eta_x\,, \tag{E.65}$$

and consequently

$$\left\langle\frac{\delta S_E[\phi]}{\delta\bar{\xi}(x)}\,\bar{\xi}(y)\right\rangle = \sum\!\!\!\!\!\!\int_{\tilde{y}} G^0_{E,\uparrow}(x,\tilde{y})^{-1}\,\langle\xi_{\tilde{y}}\bar{\xi}_y\rangle + \sum\!\!\!\!\!\!\int_{z,\tilde{z}}\sum_s \underbrace{\mathrm{i}\;\delta(x-z)\delta(x-\tilde{z})\gamma^0\,\Gamma^s}_{\text{bare vertex for }\Phi}\langle\tilde{\Phi}^s_{\tilde{z}}\,\xi_z\bar{\xi}_y\rangle$$

$$-\sum_s\;\gamma^0\Gamma^s\,\langle\tilde{\rho}^s_x\eta_x\bar{\xi}_y\rangle \tag{E.66}$$

$$= \delta(x-y)\,. \tag{E.67}$$

Since $G^0_{E,\uparrow}(\tilde{x},x)^{-1}$ does not depend on any field variable, it can be separated from the expectation value. The sum over the 3-point functions for each sublattice can be understood as

$$\sum_s\gamma^0\,\Gamma^s\langle\tilde{\Phi}^s_{\tilde{z}}\,\xi_z\bar{\xi}_y\rangle = \begin{pmatrix}\langle\tilde{\Phi}^a_{\tilde{z}}\,\xi^a_z\,\bar{\xi}^a_y\rangle & \langle\tilde{\Phi}^a_{\tilde{z}}\,\xi^a_z\,\bar{\xi}^b_y\rangle\\ -\langle\tilde{\Phi}^b_{\tilde{z}}\,\xi^b_z\,\bar{\xi}^a_y\rangle & -\langle\tilde{\Phi}^b_{\tilde{z}}\,\xi^b_z\,\bar{\xi}^b_y\rangle\end{pmatrix}. \tag{E.68}$$

The appearing 3-point functions can be rewritten with Eq. (E.88). Here one has to take care of the non-zero expectation values of the bosonic fields, even for vanishing sources. The fermionic expectation values of course still vanish $\langle\xi_x\rangle = \langle\bar{\xi}_x\rangle = 0$. So finally the 3-point function can be written in terms of connected Green functions (see App. E.4)

$$\sum_s\gamma^0\,\Gamma^s\langle\tilde{\Phi}^s_{\tilde{z}}\,\xi_z\bar{\xi}_y\rangle = \sum_s\gamma^0\,\Gamma^s\langle\tilde{\Phi}^s_{\tilde{z}}\,\xi_z\bar{\xi}_y\rangle_{conn.} + \sum_s\gamma^0\,\Gamma^s\langle\tilde{\Phi}^s_{\tilde{z}}\rangle\,G_{\xi\bar{\xi}}(z-y)$$

$$= \sum\!\!\!\!\!\!\int_{z',y',x'}\sum_{s,s'} G^{ss'}_{\tilde{\Phi}\tilde{\Phi}}(z'-\tilde{z})\gamma^0\Gamma^{s'}\,G_{\xi\bar{\xi}}(z-y')\Gamma^{\tilde{\Phi}^s\bar{\xi}^s\xi^s}(z',y',x')\Gamma^s\;G_{\xi\bar{\xi}}(x'-y)$$

$$+\sum_s\gamma^0\,\Gamma^s\langle\tilde{\Phi}^s_{\tilde{z}}\rangle\,G_{\xi\bar{\xi}}(z-y)\,, \tag{E.69}$$

with

$$G_{\tilde{\Phi}\tilde{\Phi}}(\tilde{z}-y') = G_{\Phi\Phi}(\tilde{z}-y') + G_{\sigma^+\sigma^+}(\tilde{z}-y') + \mathrm{i}\,G_{\sigma^-\sigma^-}(\tilde{z}-y') + \mathrm{i}\,G_{\rho_3\rho_3}(\tilde{z}-y')\,, \tag{E.70}$$

as matrices in sublattice space and the corresponding vertex function abbreviated by $\Gamma^{\tilde{\Phi}^s\xi^s\bar{\xi}^s}$, with the appropriate field $\tilde{\Phi} = \{\Phi, \sigma^+, \sigma^-, \rho_3\}$ for each term. The expectation value is composed by

$$\langle\tilde{\Phi}_{\tilde{z}}\rangle = \langle\Phi_{\tilde{z}}\rangle + \langle\sigma^+_{\tilde{z}}\rangle + \mathrm{i}\,\langle\sigma^-_{\tilde{z}}\rangle + \mathrm{i}\,\langle\rho_{3,\tilde{z}}\rangle\,. \tag{E.71}$$

Accordingly one obtains

$$\begin{aligned}\delta(x-y) =& \sum\!\!\!\!\!\!\int_{\tilde{y}} G^0_{E,\uparrow}(x,\tilde{y})^{-1}\,\langle\xi_{\tilde{y}}\bar{\xi}_y\rangle + \mathrm{i}\sum_s \gamma^0\,\Gamma^s\langle\tilde{\Phi}^s_x\rangle\,G_{\xi\bar{\xi}}(x-y) \\ &+ \mathrm{i}\sum\!\!\!\!\!\!\int_{z',y',x'}\sum_{s,s'} G^{ss'}_{\tilde{\Phi}\tilde{\Phi}}(z'-x)\gamma^0\Gamma^{s'}\,G_{\xi\bar{\xi}}(x-y')\Gamma^{\tilde{\Phi}^s\bar{\xi}^s\xi^s}(z',y',x')\Gamma^s\;G_{\xi\bar{\xi}}(x'-y) \\ &- \sum\!\!\!\!\!\!\int_{z',y',x'}\sum_{s,s'} G^{ss'}_{\tilde{\rho}\tilde{\rho}}(z'-x)\gamma^0\Gamma^{s'}\,G_{\eta\bar{\eta}}(x-y')\Gamma^{\tilde{\rho}^s\bar{\eta}^s\xi^s}(z',y',x')\Gamma^s\;G_{\xi\bar{\xi}}(x'-y)\,,\end{aligned} \tag{E.72}$$

with analogical abbreviations for $\tilde{\rho}$, e.g. $G_{\tilde{\rho}\tilde{\rho}}(\tilde{z}-y') = G_{\rho_1\rho_1}(\tilde{z}-y') - \mathrm{i}\,G_{\rho_2\rho_2}(\tilde{z}-y')$. Multiplying Eq. (E.73) with $G^{-1}_{\xi\bar{\xi}}(y-z)$, where $G^{-1}_{\xi\bar{\xi}}$ denotes the inverse matrix of the propagator in 2×2 sublattice space, and integrating over y ($\langle\xi_x\bar{\xi}_y\rangle = \langle\xi_x\bar{\xi}_y\rangle_{conn.} = G_{\xi\bar{\xi}}(x-y)$) gives

$$\begin{aligned}G_{\xi\bar{\xi}}(x-z)^{-1} =& G^0_{E,\uparrow}(x,z)^{-1} + \mathrm{i}\sum_s \gamma^0\,\Gamma^s\langle\tilde{\Phi}^s_x\rangle\,\delta(x-z) \\ &+ \mathrm{i}\sum\!\!\!\!\!\!\int_{z',y}\sum_{s,s'} G^{ss'}_{\tilde{\Phi}\tilde{\Phi}}(z'-x)\gamma^0\Gamma^{s'}\,G_{\xi\bar{\xi}}(x-y')\Gamma^{\tilde{\Phi}^s\bar{\xi}^s\xi^s}(z',y',z)\Gamma^s \\ &- \sum\!\!\!\!\!\!\int_{z',y}\sum_{s,s'} G^{ss'}_{\tilde{\rho}\tilde{\rho}}(z'-x)\gamma^0\Gamma^{s'}\,G_{\eta\bar{\eta}}(x-y')\Gamma^{\tilde{\rho}^s\bar{\eta}^s\xi^s}(z',y',z)\Gamma^s\,.\end{aligned} \tag{E.73}$$

By using again the tree-level vertex, the full fermion DSE reads

$$\begin{aligned}G_{\xi\bar{\xi}}(x-z)^{-1} =& G^0_{E,\uparrow}(x-z)^{-1} + \mathrm{i}\sum_s \gamma^0\,\Gamma^s(\langle\Phi^s_x\rangle + \langle\sigma^{+,s}_x\rangle + \mathrm{i}\,\langle\sigma^{-,s}_x\rangle + \mathrm{i}\,\langle\rho^s_{3,x}\rangle)\,\delta(x-z) \\ &- \sum_{s,s'}\Big[G^{ss'}_{\Phi\Phi}(z-x) + G^{ss'}_{\sigma^+\sigma^+}(z-x) - G^{ss'}_{\sigma^-\sigma^-}(z-x)\Big]\gamma^0\Gamma^{s'}\,G_{\xi\bar{\xi}}(x-z)\gamma^0\Gamma^s \\ &+ \sum_{s,s'} G^{ss'}_{\rho_3\rho_3}(z-x)\gamma^0\Gamma^{s'}\,G_{\xi\bar{\xi}}(x-z)\gamma^0\Gamma^s \\ &+ \sum_{s,s'}\Big[G^{ss'}_{\rho_1\rho_1}(z-x) + G^{ss'}_{\rho_2\rho_2}(z-x)\Big]\gamma^0\Gamma^{s'}\,G_{\eta\bar{\eta}}(x-z)\gamma^0\Gamma^s\,.\end{aligned} \tag{E.74}$$

For the spin-down propagator $G_{\eta\bar{\eta}}(x-z)$ we obtain exactly the same result except a minus sign as a prefactor of $\langle\rho_z\rangle$,

$$\begin{aligned}G_{\eta\bar{\eta}}(x-z)^{-1} =& G^0_{E,\downarrow}(x-z)^{-1} + \mathrm{i}\sum_s \gamma^0\,\Gamma^s(\langle\Phi^s_x\rangle + \langle\sigma^{+,s}_x\rangle + \mathrm{i}\,\langle\sigma^{-,s}_x\rangle - \mathrm{i}\,\langle\rho^s_{3,x}\rangle)\,\delta(x-z) \\ &- \sum_{s,s'}\Big[G^{ss'}_{\Phi\Phi}(z-x) + G^{ss'}_{\sigma^+\sigma^+}(z-x) - G^{ss'}_{\sigma^-\sigma^-}(z-x)\Big]\gamma^0\Gamma^{s'}\,G_{\eta\bar{\eta}}(x-z)\gamma^0\Gamma^s \\ &+ \sum_{s,s'} G^{ss'}_{\rho_3\rho_3}(z-x)\gamma^0\Gamma^{s'}\,G_{\eta\bar{\eta}}(x-z)\gamma^0\Gamma^s \\ &+ \sum_{s,s'}\Big[G^{ss'}_{\rho_1\rho_1}(z-x) + G^{ss'}_{\rho_2\rho_2}(z-x)\Big]\gamma^0\Gamma^{s'}\,G_{\xi\bar{\xi}}(x-z)\gamma^0\Gamma^s\,.\end{aligned} \tag{E.75}$$

Based on the calculations for the bosonic DSE's, the related vacuum expectation values were found to be

$$(\langle\Phi_x^s\rangle + \langle\sigma_x^{+,s}\rangle + \mathrm{i}\,\langle\sigma_x^{-,s}\rangle \pm \mathrm{i}\,\langle\rho_x^s\rangle) = -\mathrm{i}\sum_{s'}\Big[\alpha\,U\,\delta_{ss'} \mp (1-\alpha)\,U\,\delta_{ss'} \tag{E.76}$$
$$+ \oint\!\!\!\!\!\!\int_y G^{0,ss'}_{\sigma^+\sigma^+}(y,x) - \oint\!\!\!\!\!\!\int_y G^{0,ss'}_{\sigma^-\sigma^-}(y,x)\Big]\ \times(-1)^{s'}(G^{s's'}_{\xi\bar{\xi}}(0) + G^{s's'}_{\eta\bar{\eta}}(0)))\,.$$

In the following the contributions from the $\vec{\rho}$ field should be omitted to end up in the final representation of DSE's solved in this work. With the combined photon propagator from Eq. (E.55) the fermion DSE's can be summarized as

$$G_{E,\sigma}(x-z)^{-1} = G^0_{E,\sigma}(x-z)^{-1} - \mathrm{i}\sum_{s,s'}(-1)^{|s-s'|}\oint\!\!\!\!\!\!\int_y D^{0,ss'}(y-x)\sum_\sigma G^{s's'}_{E,\sigma}(0)\ \delta(x-z)$$
$$+\,\mathrm{i}\sum_{s,s'} D^{ss'}(z-x)\,\gamma^0\Gamma^{s'}\,G_{\eta\bar{\eta}}(x-z)\gamma^0\Gamma^s\,.$$

By a Fourier transform into momentum space as described in App. B one obtains

$$G_{E,\sigma}(p_E)^{-1} = G^0_{E,\uparrow}(p_E)^{-1} - \mathrm{i}\sum_{s,s',\sigma}(-1)^{|s-s'|}\,D^{0,ss'}(p_E=0)\sum_\sigma\oint\!\!\!\!\!\!\int_{k_E} G^{s's'}_{E,\sigma}(k_E) \tag{E.77}$$
$$+\,\mathrm{i}\sum_{s,s'}\int_{k_E} D^{ss'}(k_E)\,\gamma^0\Gamma^{s'}\,G_{E,\sigma}(k_E+p_E)\gamma^0\Gamma^s\,. \tag{E.78}$$

Eventually a Wick-rotation to Minkoswkian space-time was performed and the Feynman propagator was inserted via Eq. (B.21) as described in App. B to finally obtain the fermionic DSE

$$G_{F,\sigma}(p)^{-1} = G^0_{F,\sigma}(p)^{-1} + \sum_{s,s'}\oint\!\!\!\!\!\!\int_k D^{ss'}(k)\,\gamma^0\Gamma^{s'}\,G_{F,\sigma}(k+p)\gamma^0\Gamma^s \tag{E.79}$$
$$-\sum_{s,s'}(-1)^{|s-s'|}\,D^{0,ss'}(p=0)\sum_\sigma\oint\!\!\!\!\!\!\int_k G^{s's'}_{F,\sigma}(k)\,.$$

E.4 Full, Connected and 1PI n-point Correlators

For the 1-point function or the field expectation value respectively one simply finds

$$\langle\phi_\alpha(x)\rangle_j = \frac{\delta\,\mathcal{Z}[j]}{\delta j_\alpha(x)} = e^{\mathcal{W}[j]}\,\frac{\delta\,\mathcal{W}[j]}{\delta j_\alpha(x)} = e^{\mathcal{W}[j]}\,\langle\phi_\alpha(x)\rangle_{conn.,\,j}\,, \tag{E.80}$$

turning off all sources then yields

$$\langle\phi_\alpha(x)\rangle = \langle\phi_\alpha(x)\rangle_{conn.}\,, \tag{E.81}$$

with the same procedure for the 2-point function we get

$$\langle \phi_\alpha(x)\phi_\beta(y)\rangle_{[j]} = \frac{\delta^2\,\mathcal{Z}[j]}{\delta j_\alpha(x)\delta j_\beta(y)} \tag{E.82}$$

$$= e^{\mathcal{W}[j]}\left[\frac{\delta\,\mathcal{W}[j]}{\delta j_\alpha(x)}\frac{\delta\,\mathcal{W}[j]}{\delta j_\beta(y)} + \frac{\delta^2\,\mathcal{W}[j]}{\delta j_\alpha(x)\delta j_\beta(y)}\right], \tag{E.83}$$

so we have

$$\langle \phi_\alpha(x)\phi_\beta(y)\rangle = \langle \phi_\alpha(x)\phi_\beta(y)\rangle_{conn.} + \langle \phi_\alpha(x)\rangle\langle \phi_\beta(y)\rangle\,. \tag{E.84}$$

An analog consideration for the 3-point function leads to

$$\langle \phi_\alpha(x)\phi_\beta(y)\phi_\beta(y)\rangle_{[j]} = \frac{\delta^3\mathcal{Z}[j]}{\delta j_\alpha(x)\delta j_\beta(y)\delta j_\gamma(z)} \tag{E.85}$$

$$= e^{\mathcal{W}[j]}\left[\frac{\delta\,\mathcal{W}[j]}{\delta j_\alpha(x)}\frac{\delta\,\mathcal{W}[j]}{\delta j_\beta(y)}\frac{\delta\,\mathcal{W}[j]}{\delta j_\gamma(z)} + \frac{\delta\,\mathcal{W}[j]}{\delta j_\beta(y)}\frac{\delta^2\,\mathcal{W}[j]}{\delta j_\gamma(z)\delta j_\alpha(x)} + \frac{\delta\,\mathcal{W}[j]}{\delta j_\alpha(x)}\frac{\delta^2\,\mathcal{W}[j]}{\delta j_\gamma(z)\delta j_\beta(y)}\right.$$
$$\left. + \frac{\delta\,\mathcal{W}[j]}{\delta j_\gamma(z)}\frac{\delta^2\,\mathcal{W}[j]}{\delta j_\alpha(x)\delta j_\beta(y)} + \frac{\delta^3\mathcal{W}[j]}{\delta j_\alpha(x)\delta j_\beta(y)\delta j_\gamma(z)}\right], \tag{E.86}$$

and hence

$$\langle \phi_\alpha(x)\phi_\beta(y)\phi_\gamma(z)\rangle = \langle \phi_\alpha(x)\phi_\beta(y)\phi_\gamma(z)\rangle_{conn.} + \langle \phi_\alpha(x)\rangle\langle \phi_\beta(y)\rangle\langle \phi_\gamma(z)\rangle \tag{E.87}$$

$$+ \langle \phi_\alpha(x)\rangle G_{\gamma\beta}(z-y) + \langle \phi_\beta(y)\rangle G_{\gamma\alpha}(z-x) + \langle \phi_\gamma(z)\rangle G_{\alpha\beta}(x-y)\,. \tag{E.88}$$

With the identity

$$\sum\!\!\!\!\!\!\int_y \sum_\beta \frac{\delta^2\mathcal{W}[j]}{\delta j_\alpha(x)\delta j_\beta(y)}\frac{\delta^2\Gamma[\phi^c]}{\delta\phi^c_\beta(y)\delta\phi^c_\delta(z)} = \sum\!\!\!\!\!\!\int_y \sum_\beta \frac{\delta\phi^c_\alpha(x)}{\delta j_\beta(y)}\frac{\delta j_\beta(y)}{\delta\phi^c_\delta(z)} = \delta_{\alpha\delta}\,\delta(x-z)\,, \tag{E.89}$$

where greek indices denote the field index, the functional inverse of the propagator is obtained by additionally setting all sources to zero

$$G^{-1}_{\alpha\beta}(x-y) = \frac{\delta^2\Gamma[\phi^c]}{\delta\phi^c_\beta(y)\delta\phi^c_\alpha(x)}\Big|_{j=0}. \tag{E.90}$$

Performing an additional further derivative on the first relation (Eq. (E.89)) with respect to another source term,

$$\frac{\delta}{\delta j_\gamma(z)} = \sum\!\!\!\!\!\!\int_{z'} \sum_\mu \frac{\delta\phi^c_\mu(z')}{\delta j_\gamma(z)}\frac{\delta}{\delta\phi^c_\mu(z')} = \sum\!\!\!\!\!\!\int_{z'} dz' \sum_\mu \frac{\delta^2\mathcal{W}[j]}{\delta j_\mu(z')\delta j_\gamma(z)}\frac{\delta}{\delta\phi^c_\mu(z')}\,, \tag{E.91}$$

yields

$$\sum\!\!\!\!\!\!\int_{y'}\sum_{\beta'}\frac{\delta^3\mathcal{W}[j]}{\delta j_\gamma(z)\delta j_\alpha(x)\delta j_{\beta'}(y')}\frac{\delta^2\Gamma[\phi^c]}{\delta\phi^c_{\beta'}(y')\delta\phi^c_\delta(x')} \tag{E.92}$$

$$= \sum\!\!\!\!\!\!\int_{z'}\sum\!\!\!\!\!\!\int_{y'}\sum_{\mu,\beta'}\frac{\delta^2\mathcal{W}[j]}{\delta j_\mu(z')\delta j_\gamma(z)}\frac{\delta^2\mathcal{W}[j]}{\delta j_\alpha(x)\delta j_{\beta'}(y')}\frac{\delta^3\Gamma[\phi^c]}{\delta\phi^c_\mu(z')\delta\phi^c_{\beta'}(y')\delta\phi^c_\delta(x')}\,. \tag{E.93}$$

Multiplying this expression by $\frac{\delta^2\mathcal{W}[j]}{\delta j_\delta(x')\delta j_\beta(y)}$, integrating over x' and taking the sum over δ (relabeling $\beta' \to \nu$) results in

$$\not\int_{y'} \sum_{\beta'} \frac{\delta^3\mathcal{W}[j]}{\delta j_\gamma(z)\delta j_\alpha(x)\delta j_{\beta'}(y')} \not\int_{x'} \sum_{\delta} \frac{\delta^2\Gamma[\phi^c]}{\delta\phi^c_{\beta'}(y')\delta\phi^c_\delta(x')} \frac{\delta^2\mathcal{W}[j]}{\delta j_\delta(x')\delta j_\beta(y)} \tag{E.94}$$

$$= \frac{\delta^3\mathcal{W}[j]}{\delta j_\gamma(z)\delta j_\alpha(x)\delta j_\beta(y)} \tag{E.95}$$

$$= \not\int_{z',y',x'} \sum_{\mu,\nu,\delta} \frac{\delta^2\mathcal{W}[j]}{\delta j_\mu(z')\delta j_\gamma(z)} \frac{\delta^2\mathcal{W}[j]}{\delta j_\alpha(x)\delta j_\nu(y')} \frac{\delta^3\Gamma[\phi^c]}{\delta\phi^c_\mu(z')\delta\phi^c_\nu(y')\delta\phi^c_\delta(x')} \frac{\delta^2\mathcal{W}[j]}{\delta j_\delta(x')\delta j_\beta(y)}\,, \tag{E.96}$$

which can be rewritten as

$$\langle\phi_\gamma(z)\phi_\alpha(x)\phi_\beta(y)\rangle_{conn.} = \not\int_{z',y',x'} \sum_{\mu,\nu,\delta} G_{\mu\gamma}(z'-z)\, G_{\alpha\nu}(x-y')\Gamma^{\mu\nu\delta}(z',y',x')G_{\delta\beta}(x'-y)\,. \tag{E.97}$$

Additionally, the following expression can be extracted

$$\frac{\delta}{\delta\phi^c_\epsilon(z'')} \frac{\delta^2\mathcal{W}[j]}{\delta j_\alpha(x)\delta j_\beta(y)} = \not\int_{z} \sum_{\gamma} \frac{\delta j_\gamma(z)}{\delta\phi^c_\epsilon(z'')} \frac{\delta}{\delta j_\gamma(z)} \frac{\delta^2\mathcal{W}[j]}{\delta j_\alpha(x)\delta j_\beta(y)} \tag{E.98}$$

$$= \not\int_{z} \sum_{\gamma} \frac{\delta\Gamma[\phi^c]}{\delta\phi^c_\gamma(z)\delta\phi^c_\epsilon(z'')} \frac{\delta^3\mathcal{W}[j]}{\delta j_\gamma(z)\delta j_\alpha(x)\delta j_\beta(y)}$$

$$= \not\int_{z',y',x'} \sum_{\mu,\nu,\delta} \delta_{\mu\epsilon}\delta(z'-z'') \frac{\delta^2\mathcal{W}[j]}{\delta j_\alpha(x)\delta j_\nu(y')} \frac{\delta^3\Gamma[\phi^c]}{\delta\phi^c_\mu(z')\delta\phi^c_\nu(y')\delta\phi^c_\delta(x')} \frac{\delta^2\mathcal{W}[j]}{\delta j_\delta(x')\delta j_\beta(y)}$$

$$= \not\int_{y',x'} \sum_{\nu,\delta} \frac{\delta^2\mathcal{W}[j]}{\delta j_\alpha(x)\delta j_\nu(y')} \frac{\delta^3\Gamma[\phi^c]}{\delta\phi^c_\epsilon(z'')\delta\phi^c_\nu(y')\delta\phi^c_\delta(x')} \frac{\delta^2\mathcal{W}[j]}{\delta j_\delta(x')\delta j_\beta(y)}.$$

Bibliography

[1] K. S. Novoselov, A. K. Geim, S. V. Morozov, D. Jiang, Y. Zhang, S. V. Dubonos et al., *Electric field effect in atomically thin carbon films*, *Science* **306** (2004) 666 [http://www.sciencemag.org/content/306/5696/666.full.pdf].

[2] L. D. Landau, *On the theory of phase transitions*, *Zh. Eksp. Teor. Fiz.* **7** (1937) 19.

[3] L. Landau, E. Lifshits, E. Lifshits and L. Pitaevski, *Statistical physics*, no. Bd. 1 in Pergamon international library of science, technology, engineering, and social studies. Pergamon Press, 1980.

[4] J. C. Meyer, A. K. Geim, M. I. Katsnelson, K. S. Novoselov, T. J. Booth and S. Roth, *The structure of suspended graphene sheets*, *Nature* **446** (2007) 60.

[5] N. D. Mermin, *Crystalline order in two dimensions*, *Phys. Rev.* **176** (1968) 250.

[6] N. D. Mermin and H. Wagner, *Absence of ferromagnetism or antiferromagnetism in one- or two-dimensional isotropic heisenberg models*, *Phys. Rev. Lett.* **17** (1966) 1133.

[7] A. K. Geim and K. S. Novoselov, *The rise of graphene*, *Nature Materials* **6** (2007) 183.

[8] V. P. Gusynin, S. G. Sharapov and J. P. Carbotte, *Ac conductivity of graphene: From tight-binding model to 2 + 1-dimensional quantum electrodynamics*, *International Journal of Modern Physics B* **21** (2007) 4611 [http://www.worldscientific.com/doi/pdf/10.1142/S0217979207038022].

[9] V. N. Kotov, B. Uchoa, V. M. Pereira, F. Guinea and A. H. Castro Neto, *Electron-electron interactions in graphene: Current status and perspectives*, *Rev. Mod. Phys.* **84** (2012) 1067.

[10] M. I. Katsnelson, *Graphene: Carbon in Two Dimensions*. Cambridge University Press, 2012, 10.1017/CBO9781139031080.

[11] P. R. Wallace, *The band theory of graphite*, *Phys. Rev.* **71** (1947) 622.

[12] J. P. Hobson and W. A. Nierenberg, *The statistics of a two-dimensional, hexagonal net*, *Phys. Rev.* **89** (1953) 662.

[13] G. W. Semenoff, *Condensed-matter simulation of a three-dimensional anomaly*, *Phys. Rev. Lett.* **53** (1984) 2449.

[14] K. S. Novoselov, A. K. Geim, S. V. Morozov, D. Jiang, M. I. Katsnelson, I. V. Grigorieva et al., *Two-dimensional gas of massless dirac fermions in graphene*, *Nature* **438** (2005) 197.

[15] M. Katsnelson and K. Novoselov, *Graphene: New bridge between condensed matter physics and quantum electrodynamics*, *Solid State Communications* **143** (2007) 3 .

[16] A. H. Castro Neto, F. Guinea, N. M. R. Peres, K. S. Novoselov and A. K. Geim, *The electronic properties of graphene*, *Rev. Mod. Phys.* **81** (2009) 109.

[17] N. M. R. Peres, F. Guinea and A. H. Castro Neto, *Electronic properties of disordered two-dimensional carbon*, *Physical Review B* **73** (2006) .

[18] D. C. Elias, R. V. Gorbachev, A. S. Mayorov, S. V. Morozov, A. A. Zhukov, P. Blake et al., *Dirac cones reshaped by interaction effects in suspended graphene*, *Nature Physics* **7** (2011) 701.

[19] A. S. Mayorov, D. C. Elias, I. S. Mukhin, S. V. Morozov, L. A. Ponomarenko, K. S. Novoselov et al., *How close can one approach the dirac point in graphene experimentally?*, *Nano Letters* **12** (2012) 4629 [`https://doi.org/10.1021/nl301922d`].

[20] S. Sorella and E. Tosatti, *Semi-metal-insulator transition of the hubbard model in the honeycomb lattice*, *Europhysics Letters (EPL)* **19** (1992) 699.

[21] L. M. Martelo, M. Dzierzawa, L. Siffert and D. Baeriswyl, *Mott-hubbard transition and antiferromagnetism on the honeycomb lattice*, *Zeitschrift für Physik B Condensed Matter* **103** (1996) 335.

[22] T. Paiva, R. T. Scalettar, W. Zheng, R. R. P. Singh and J. Oitmaa, *Ground-state and finite-temperature signatures of quantum phase transitions in the half-filled hubbard model on a honeycomb lattice*, *Phys. Rev. B* **72** (2005) 085123.

[23] S. Sorella, Y. Otsuka and S. Yunoki, *Absence of a spin liquid phase in the hubbard model on the honeycomb lattice*, *Scientific Reports* **2** (2012) 992.

[24] M. V. Ulybyshev, P. V. Buividovich, M. I. Katsnelson and M. I. Polikarpov, *Monte carlo study of the semimetal-insulator phase transition in monolayer graphene with a realistic interelectron interaction potential*, *Physical Review Letters* **111** (2013) .

[25] D. Smith and L. von Smekal, *Monte carlo simulation of the tight-binding model of graphene with partially screened coulomb interactions*, *Phys. Rev. B* **89** (2014) 195429.

[26] C. L. Kane and E. J. Mele, *Quantum spin hall effect in graphene*, *Phys. Rev. Lett.* **95** (2005) 226801.

[27] S. Raghu, X.-L. Qi, C. Honerkamp and S.-C. Zhang, *Topological mott insulators*, *Physical Review Letters* **100** (2008) .

[28] V. P. Gusynin, V. A. Miransky, S. G. Sharapov and I. A. Shovkovy, *Excitonic gap, phase transition, and quantum hall effect in graphene*, *Phys. Rev. B* **74** (2006) 195429.

[29] C. Honerkamp, *Density waves and cooper pairing on the honeycomb lattice*, *Phys. Rev. Lett.* **100** (2008) 146404.

[30] I. F. Herbut, *Interactions and phase transitions on graphene's honeycomb lattice*, *Phys. Rev. Lett.* **97** (2006) 146401.

[31] P. Buividovich, D. Smith, M. Ulybyshev and L. von Smekal, *Competing order in the fermionic hubbard model on the hexagonal graphene lattice*, 2016.

[32] Z. Y. Meng, T. C. Lang, S. Wessel, F. F. Assaad and A. Muramatsu, *Quantum spin liquid emerging in two-dimensional correlated dirac fermions*, *Nature* **464** (2010) 847–851.

[33] M. Hermele, *Su(2) gauge theory of the hubbard model and application to the honeycomb lattice*, *Phys. Rev. B* **76** (2007) 035125.

[34] P. A. Lee, N. Nagaosa and X.-G. Wen, *Doping a mott insulator: Physics of high temperature superconductivity*, 2004.

[35] B. Uchoa and A. H. Castro Neto, *Superconducting states of pure and doped graphene*, *Physical Review Letters* **98** (2007) .

[36] A. Giuliani and V. Mastropietro, *The two-dimensional hubbard model on the honeycomb lattice*, *Communications in Mathematical Physics* **293** (2009) 301–346.

[37] Y. Cao, V. Fatemi, S. Fang, K. Watanabe, T. Taniguchi, E. Kaxiras et al., *Unconventional superconductivity in magic-angle graphene superlattices*, *Nature* **556** (2018) 43.

[38] J. C. Slonczewski and P. R. Weiss, *Band structure of graphite*, *Phys. Rev.* **109** (1958) 272.

[39] J. E. Drut and T. A. Lähde, *Is graphene in vacuum an insulator?*, *Phys. Rev. Lett.* **102** (2009) 026802.

[40] P. Buividovich, D. Smith, M. Ulybyshev and L. von Smekal, *Numerical evidence of conformal phase transition in graphene with long-range interactions*, *Phys. Rev. B* **99** (2019) 205434.

[41] A. K. Geim and I. V. Grigorieva, *Van der waals heterostructures*, *Nature* **499** (2013) 419.

[42] F. Withers, O. Del Pozo-Zamudio, A. Mishchenko, A. P. Rooney, A. Gholinia, K. Watanabe et al., *Light-emitting diodes by band-structure engineering in van der waals heterostructures*, *Nature Materials* **14** (2015) 301.

[43] N. Mounet, M. Gibertini, P. Schwaller, D. Campi, A. Merkys, A. Marrazzo et al., *Two-dimensional materials from high-throughput computational exfoliation of experimentally known compounds*, *Nature Nanotechnology* **13** (2018) 246.

[44] S. Haastrup, M. Strange, M. Pandey, T. Deilmann, P. S. Schmidt, N. F. Hinsche et al., *The computational 2d materials database: high-throughput modeling and discovery of atomically thin crystals*, *2D Materials* **5** (2018) 042002.

[45] J. González, F. Guinea and M. Vozmediano, *Non-fermi liquid behavior of electrons in the half-filled honeycomb lattice (a renormalization group approach)*, *Nuclear Physics B* **424** (1994) 595 .

[46] J. González, *Renormalization group approach to chiral symmetry breaking in graphene*, *Physical Review B* **82** (2010) .

[47] L. Classen, M. Scherer and C. Honerkamp, *Instabilities on graphene's honeycomb lattice with electron-phonon interactions*, *Physical Review B* **90** (2014) .

[48] L. Classen, I. F. Herbut, L. Janssen and M. M. Scherer, *Competition of density waves and quantum multicritical behavior in dirac materials from functional renormalization*, *Physical Review B* **93** (2016) .

[49] C. Popovici, C. S. Fischer and L. von Smekal, *Effects of electron-electron interactions in suspended graphene*, *Proceedings of Science* **(Confinement X)** (2013) 269.

[50] C. Popovici, C. S. Fischer and L. von Smekal, *Fermi velocity renormalization and dynamical gap generation in graphene*, *Phys. Rev. B* **88** (2013) 205429.

[51] M. Carrington, C. Fischer, L. Von Smekal and M. Thoma, *Dynamical gap generation in graphene with frequency dependent renormalization effects*, *Physical Review B* **94** (2016) .

[52] M. E. Carrington, C. S. Fischer, L. von Smekal and M. H. Thoma, *Role of frequency dependence in dynamical gap generation in graphene*, *Phys. Rev.* **B97** (2018) 115411 [1711.01962].

[53] M. E. Carrington, *Effect of a chern-simons term on dynamical gap generation in graphene*, *Physical Review B* **99** (2019) .

[54] P. Buividovich, D. Smith, M. Ulybyshev and L. von Smekal, *Hybrid monte carlo study of competing order in the extended fermionic hubbard model on the hexagonal lattice*, *Phys. Rev. B* **98** (2018) 235129.

[55] Y. Araki and G. W. Semenoff, *Spin versus charge-density-wave order in graphenelike systems*, *Phys. Rev. B* **86** (2012) 121402.

[56] L. Classen, I. F. Herbut, L. Janssen and M. M. Scherer, *Mott multicriticality of dirac electrons in graphene*, *Physical Review B* **92** (2015) .

[57] M. Körner, D. Smith, P. Buividovich, M. Ulybyshev and L. von Smekal, *Hybrid monte carlo study of monolayer graphene with partially screened coulomb interactions at finite spin density*, *Phys. Rev. B* **96** (2017) 195408.

[58] J. González, F. Guinea and M. Vozmediano, *The electronic spectrum of fullerenes from the dirac equation*, *Nuclear Physics B* **406** (1993) 771 .

[59] K. Kleeberg, *Instantaneous coulomb interactions of fermions on graphene's honeycomb lattice*, Master's thesis, Justus-Liebig-Universität Giessen, 2015.

[60] N. Ashcroft and N. Mermin, *Solid State Physics*. Cengage Learning, 2011.

[61] W. Nolting, *Grundkurs Theoretische Physik 7*, Grundkurs Theoretische Physik. Springer, 2005.

[62] T. W. Appelquist, M. Bowick, D. Karabali and L. C. R. Wijewardhana, *Spontaneous chiral-symmetry breaking in three-dimensional qed*, *Phys. Rev.* **D 33** (1986) .

[63] T. W. Appelquist and R. D. Pisarski, *High-temperature yang-mills theories and three-dimensional quantum chromodynamics*, *Phys. Rev.* **D 23** (1980) .

[64] D. Curtis, M. Pennington and D. Walsh, *Dynamical mass generation in qed3 and the 1/n expansion*, *Physics Letters* **B 295** (1992) .

[65] T. Appelquist, J. Terning and L. C. R. Wijewardhana, *(2+1)-dimensional qed and a novel phase transition*, *Physical Review Letters* **75** (1995) 2081–2084.

[66] T. Goecke, C. S. Fischer and R. Williams, *Finite-volume effects and dynamical chiral symmetry breaking inqed3*, *Physical Review B* **79** (2009) .

[67] G. W. Semenoff, *Chiral symmetry breaking in graphene*, *Physica Scripta* **T146** (2012) 014016.

[68] F. Schwabl, *Quantenmechanik für Fortgeschrittene (QM II)*, Springer-Lehrbuch. Springer-Verlag, 2008.

[69] T. O. Wehling, E. Şaşıoğlu, C. Friedrich, A. I. Lichtenstein, M. I. Katsnelson and S. Blügel, *Strength of effective coulomb interactions in graphene and graphite*, *Phys. Rev. Lett.* **106** (2011) 236805.

[70] M. E. Peskin and D. V. Schroeder, *An introduction to Quantum Field Theory*. Westview Press, 1995.

[71] W. H. Press, S. A. Teukolsky, W. T. Vetterling and B. P. Flannery, *Numerical Recipes-The Art of scientific Computing*. Cambridge University Press, 2007.

[72] A. Munshi, B. Gaster, T. G. Mattson, J. Fung and D. Ginsburg, *OpenCL Programming Guide*. Addison-Wesley Professional, 1st ed., 2011.

[73] M. Scarpino, *OpenCL in Action: How to Accelerate Graphics and Computation*. Manning, 2012.

[74] B. Gaster, L. Howes, D. R. Kaeli, P. Mistry and D. Schaa, *Heterogeneous Computing with OpenCL*. Morgan Kaufmann Publishers Inc., San Francisco, CA, USA, 1st ed., 2011.

[75] G. Bärwolff, *Numerik für Ingenieure, Physiker und Informatiker: für Bachelor und Diplom*, Für Bachelor und Diplom. Spektrum Akademischer Verlag, 2006.

[76] H. Schwarz and N. Köckler, *Numerische Mathematik*, Vieweg Studium. Vieweg+Teubner Verlag, 2009.

[77] M. Frigo and S. G. Johnson, *The design and implementation of fftw3*, *Proceedings of the IEEE* **93** (2005) 216.

[78] H. Nishimori and G. Ortiz, *Elements of Phase Transitions and Critical Phenomena*, Oxford Graduate Texts. OUP Oxford, 2011.

[79] I. Herbut, *A Modern Approach to Critical Phenomena*. Cambridge University Press, 2007.

[80] J. Zinn-Justin, *Phase Transitions and Renormalization Group*, Oxford Graduate Texts. OUP Oxford, 2007.

[81] G. N. WATSON, *THREE TRIPLE INTEGRALS*, *The Quarterly Journal of Mathematics* **os-10** (1939) 266 [http://oup.prod.sis.lan/qjmath/article-pdf/os-10/1/266/4363160/os-10-1-266.pdf].

[82] L. V. Smekal.

[83] M. E. Fisher and M. N. Barber, *Scaling theory for finite-size effects in the critical region*, *Phys. Rev. Lett.* **28** (1972) 1516.

[84] F. F. Assaad and I. F. Herbut, *Pinning the order: The nature of quantum criticality in the hubbard model on honeycomb lattice*, *Phys. Rev. X* **3** (2013) 031010.

[85] L. Ryder, *Quantum Field Theory*. Cambridge University Press, 1996.

[86] J. Berges, *Introduction to nonequilibrium quantum field theory*, *AIP Conf. Proc.* **739** (2004) 3 [hep-ph/0409233].

[87] G. Baym, *Self-consistent approximations in many-body systems*, *Phys. Rev.* **127** (1962) 1391.

[88] J. M. Luttinger and J. C. Ward, *Ground-state energy of a many-fermion system. ii*, *Phys. Rev.* **118** (1960) 1417.

[89] G. Baym and L. P. Kadanoff, *Conservation laws and correlation functions*, *Phys. Rev.* **124** (1961) 287.

[90] J. M. Cornwall, R. Jackiw and E. Tomboulis, *Effective action for composite operators*, *Phys. Rev. D* **10** (1974) 2428.

[91] J. Berges, S. Borsanyi, U. Reinosa and J. Serreau, *Nonperturbative renormalization for 2PI effective action techniques*, *Annals Phys.* **320** (2005) 344 [hep-ph/0503240].

[92] W.-J. Fu, *Hubbard Model in the Two-particle Irreducible Effective Action Formalism*, 1209.6018.

[93] M. Gell-Mann and K. A. Brueckner, *Correlation energy of an electron gas at high density*, *Phys. Rev.* **106** (1957) 364.

[94] G. Czycholl, *Theoretische Festkörperphysik Band 1: Grundlagen: Phononen und Elektronen in Kristallen*. Springer Berlin Heidelberg, 2015.

[95] G. Czycholl, *Theoretische Festkörperphysik Band 2: Anwendungen: Nichtgleichgewicht, Verhalten in äußeren Feldern, kollektive Phänomene*. Springer Berlin Heidelberg, 2017.

[96] T. Stauber, *Analytical expressions for the polarizability of the honeycomb lattice*, *Phys. Rev. B* **82** (2010) 201404.

[97] T. Stauber and G. Gómez-Santos, *Dynamical current-current correlation of the hexagonal lattice and graphene*, *Physical Review B* **82** (2010) .

[98] J. S. Ball and T.-W. Chiu, *Analytic Properties of the Vertex Function in Gauge Theories. 1.*, *Phys. Rev.* **D22** (1980) 2542.

[99] T.-W. Chiu, *Analytic properties of the vertex function in gauge theories. ii*, *Phys. Rev. D* **22** (1980) .

[100] I. F. Herbut, V. Juričić and O. Vafek, *Relativistic mott criticality in graphene*, *Physical Review B* **80** (2009) .

[101] B. Roy, *Multicritical behavior ofz2o(2)gross-neveu-yukawa theory in graphene*, *Physical Review B* **84** (2011) .

[102] Y. Otsuka, S. Yunoki and S. Sorella, *Universal quantum criticality in the metal-insulator transition of two-dimensional interacting dirac electrons*, *Phys. Rev. X* **6** (2016) 011029.

[103] F. Parisen Toldin, M. Hohenadler, F. F. Assaad and I. F. Herbut, *Fermionic quantum criticality in honeycomb and π-flux hubbard models: Finite-size scaling of renormalization-group-invariant observables from quantum monte carlo*, *Phys. Rev. B* **91** (2015) 165108.

[104] M. Hohenadler, F. Parisen Toldin, I. F. Herbut and F. F. Assaad, *Phase diagram of the kane-mele-coulomb model*, *Phys. Rev. B* **90** (2014) 085146.

[105] N. Zerf, L. N. Mihaila, P. Marquard, I. F. Herbut and M. M. Scherer, *Four-loop critical exponents for the gross-neveu-yukawa models*, *Physical Review D* **96** (2017) .

[106] A. Cerjan, M. Xiao, L. Yuan and S. Fan, *Effects of non-hermitian perturbations on weyl hamiltonians with arbitrary topological charges*, *Phys. Rev. B* **97** (2018) 075128.

[107] C. S. Fischer, *Dynamical chiral symmetry breaking in unquenched qed3*, *Phys. Rev.* **D 70** (2004) .

[108] V. P. Gusynin, V. A. Miransky and I. A. Shovkovy, *Dynamical chiral symmetry breaking in qed in a magnetic field: Toward exact results*, *Physical Review Letters* **83** (1999) 1291–1294.

[109] C. S. Fischer, *Qcd at finite temperature and chemical potential from dyson–schwinger equations*, *Progress in Particle and Nuclear Physics* **105** (2019) 1–60.

[110] R. Alkofer and L. von Smekal, *The infrared behaviour of {QCD} green's functions: Confinement, dynamical symmetry breaking, and hadrons as relativistic bound states*, *Physics Reports* **353** (2001) 281 .

[111] E. V. Gorbar, V. P. Gusynin, V. A. Miransky and I. A. Shovkovy, *Magnetic field driven metal-insulator phase transition in planar systems*, *Phys. Rev. B* **66** (2002) 045108.

[112] J. A. Bonnet, *Phase transition in strongly interacting quantum field theories: QED3 vs. QCD*, Ph.D. thesis, Justus-Liebig University Giessen, 2013.

[113] J. Braun, H. Gies, L. Janssen and D. Roscher, *Phase structure of many-flavor* qed_3, *Phys. Rev. D* **90** (2014) 036002.

[114] O. Gamayun, E. Gorbar and V. Gusynin, *Supercritical coulomb center and excitonic instability in graphene*, *Phys. Rev. B* **80** (2009) 165429.

[115] M. Schüler, M. Rösner, T. O. Wehling, A. I. Lichtenstein and M. I. Katsnelson, *Optimal hubbard models for materials with nonlocal coulomb interactions: Graphene, silicene, and benzene*, *Physical Review Letters* **111** (2013) .

[116] J. Negele and H. Orland, *Quantum many-particle systems*, Frontiers in physics. Addison-Wesley Pub. Co., 1988.

[117] J. Hubbard, *Calculation of partition functions*, *Phys. Rev. Lett.* **3** (1959) 77.

[118] J. Kapusta, *Finite-Temperature Field Theory*, Cambridge Monographs on Mathematical Physics. Cambridge University Press, 1993.

[119] A. Nieto, *Evaluating sums over the matsubara frequencies*, *Computer Physics Communications* **92** (1995) 54 .

[120] O. ESPINOSA, *On the evaluation of matsubara sums*, *Mathematics of Computation* **79** (2010) 1709.

[121] M. Laine and A. Vuorinen, *Basics of Thermal Field Theory*, *Lect. Notes Phys.* **925** (2016) pp.1 [1701.01554].

[122] M. L. Bellac, *Thermal Field Theory*, Cambridge Monographs on Mathematical Physics. Cambridge University Press, 2011, 10.1017/CBO9780511721700.

[123] A. Fetter and J. Walecka, *Quantum Theory of Many-particle Systems*, Dover Books on Physics. Dover Publications, 2003.

[124] C. Itzykson and J. Zuber, *Quantum Field Theory*, Dover Books on Physics. Dover Publications, 2012.

[125] W. Greiner and J. Reinhardt, *Feldquantisierung: ein Lehr- und Übungsbuch ; mit zahlreichen Beispielen und Aufgaben mit ausführlichen Lösungen*, Theoretische Physik : ein Lehr- und Übungsbuch. Deutsch, 1993.

[126] W. Armour, S. Hands and C. Strouthos, *Monte carlo simulation of the semimetal-insulator phase transition in monolayer graphene*, *Physical Review B* **81** (2010) 125105.

[127] C. W. J. Beenakker, *Colloquium*, *Rev. Mod. Phys.* **80** (2008) 1337.

[128] B. Dietz, F. Iachello, M. Miski-Oglu, N. Pietralla, A. Richter, L. von Smekal et al., *Lifshitz and excited-state quantum phase transitions in microwave dirac billiards*, *Phys. Rev. B* **88** (2013) 104101.

[129] M. Ebrahimkhas, *Exact diagonalization study of 2d hubbard model on honeycomb lattice: Semi-metal to insulator transition*, *Physics Letters A* **375** (2011) 3223–3227.

[130] A. Emelyanenko and L. Boinovich, *On the effect of discrete charges adsorbed at the interface on nonionic liquid film stability: charges in the film*, *Journal of Physics: Condensed Matter* **20** (2008) 494227.

[131] O. Gamayun, E. Gorbar and V. Gusynin, *Gap generation and semimetal-insulator phase transition in graphene*, *Phys. Rev. B* **81** (2010) 075429.

[132] J. A. Gracey and R. M. Simms, *Renormalization of qcd in the interpolating momentum subtraction scheme at three loops*, *Phys. Rev. D* **97** (2018) 085016.

[133] A. Kormányos, G. Burkard, M. Gmitra, J. Fabian, V. Zólyomi, N. D. Drummond et al., *k·ptheory for two-dimensional transition metal dichalcogenide semiconductors*, *2D Materials* **2** (2015) 022001.

[134] Z.-X. Li, Y.-F. Jiang and H. Yao, *Majorana-time-reversal symmetries: A fundamental principle for sign-problem-free quantum monte carlo simulations*, *Physical Review Letters* **117** (2016) .

[135] Z.-X. Li, Y.-F. Jiang and H. Yao, *Solving the fermion sign problem in quantum monte carlo simulations by majorana representation*, *Physical Review B* **91** (2015) .

[136] V. A. Miransky and K. Yamawaki, *Conformal phase transition in gauge theories*, *Phys. Rev. D* **55** (1997) 5051.

[137] M. R. Pennington, *Swimming with quarks*, *Lecture at the XI. Mexican School of Particles and Fields* (2004) .

[138] R. D. Pisarski, *Chiral-symmetry breaking in three-dimensional electrodynamics*, *Phys. Rev.* **D 29** (1984) .

[139] R. Williams, *Schwinger-Dyson Equations In QED and QCD*, Ph.D. thesis, University of Durham, 2007.

Danksagung

Zunächst möchte ich Prof. Lorenz von Smekal für seine kontinuierliche Unterstützung an meiner Arbeit danken, die stets mit viel Geduld und Humor verbunden war. Außerdem möchte ich mich bei Prof. Christian Fischer für die Übernahme des Zweitgutachtens bedanken. Beiden danke ich für eine schöne und menschliche Arbeitsatmosphäre im Theoretischen Institut.

Des Weiteren will ich mich bei Björn Wellegehausen für eine gelungene und spannende Zusammenarbeit in meiner Anfangszeit als Doktorandin bedanken. Auch bei meinem langjährigen Lieblingsbürokollegen Jan Mühlhans will ich mich für eine tolle und erfolgreiche Zeit bedanken. Hier sollen ebenfalls meine Kollegen Lukas Holicki und Eduard Seifert erwähnt werden, denen ich viele ereignisreiche und bereichernde, aber vor allem lustige Erfahrungen zu verdanken habe.

Schließlich will ich mich vor allem bei meiner Familie für die dauerhafte Hilfe und Unterstützung während meiner Studienzeit und für die vielen guten Ratschläge und Ideen bedanken. Dank gilt hier auch meinen drei Nichten, Loreen, Liz und Anika, die immer für die passende Ablenkung sorgten.

In ganz besonderem Maße will ich meinem Freund Chris danken, der immer für mich da ist, mich immer aufbaut und ermutigt und mit dem jeder Tag einfach unglaublich viel schöner ist.

Erklärung zur Dissertation

Hiermit erkläre ich: Ich habe die vorgelegte Dissertation selbstständig und ohne unerlaubte fremde Hilfe und nur mit den Hilfen angefertigt, die ich in der Dissertation angegeben habe. Alle Textstellen, die wörtlich oder sinngemäß aus veröffentlichten Schriften entnommen sind, und alle Angaben, die auf mündlichen Auskünften beruhen, sind als solche kenntlich gemacht. Ich stimme einer evtl. Überprüfung meiner Dissertation durch eine Antiplagiat-Software zu. Bei den von mir durchgefürten und in der Dissertation erwähnten Untersuchungen habe ich die Grundsätze guter wissenschaftlicher Praxis, wie sie in der „Satzung der Justus-Liebig-Universität Gießen zur Sicherung guter wissenschaftlicher Praxis“ niedergelegt sind, eingehalten.

Ort, Datum

Katja Kleeberg